

THE DEVELOPMENT OF HIGH DIELECTRIC CONSTANT COMPOSITE
MATERIALS AND THEIR APPLICATION IN A COMPACT HIGH POWER
ANTENNA

A Dissertation
presented to
the Faculty of the Graduate School
at the University of Missouri-Columbia

In Partial Fulfillment
of the Requirements for the Degree
Doctor of Philosophy

by
KEVIN A. O'CONNOR
Dr. Randy Curry, Dissertation Supervisor
May 2013

© Copyright by Kevin A. O'Connor 2013

All Rights Reserved

The undersigned, appointed by the dean of the Graduate School, have examined the dissertation entitled

THE DEVELOPMENT OF HIGH DIELECTRIC CONSTANT COMPOSITE MATERIALS AND THEIR APPLICATION IN A COMPACT HIGH POWER ANTENNA

presented by Kevin A. O'Connor, a candidate for the degree of Doctor of Philosophy in Electrical and Computer Engineering,

and hereby certify that, in their opinion, it is worthy of acceptance.

Professor Randy Curry

Professor Robert Druce

Professor Justin Legarsky

Professor Gregory Triplett

Professor Thomas Clevenger

This work is dedicated to the members of the US Armed Forces who served in response
to the terrorist attacks of September 11, 2001.

I am sincerely thankful for the support provided to me by my family and friends throughout this process. In particular, I appreciate the love, support, and patience of my wife, Karen, during the last few years. The support and encouragement offered to me by my immediate and extended families during this effort have been very helpful.

ACKNOWLEDGEMENTS

I first and foremost must express my appreciation to my dissertation supervisor, Dr. Randy Curry. Dr. Curry introduced me to the fields of research in which I have become so deeply involved. He provided guidance, advice, and encouragement when needed while also creating an environment in which independent thought and innovation is supported. The Center for Physical and Power Electronics that Dr. Curry founded and led during my graduate studies has been an excellent institution in which to study, experiment, and cultivate a spirit for innovation.

I would also like to thank the members of my dissertation committee for their service. Each member of the committee has research interests in specific areas relating to this work, so their review and guidance is very much appreciated.

I wish to thank Dan Crosby for managing the chemical lab in which the materials were produced and for his work in preparing many samples both in the materials development and testing phases of the program. Bill Carter, Vicki Edwards, and Mike Fulca provided great logistical support in lab management and equipment procurement. The rest of technical staff at the Center have been very supportive and encouraging, including Dr. Robert Druce, Dr. Ryan Karhi, Dr. David Bryan, and Dr. Dennis Pease. Mr. Lou Ross must be recognized for his assistance with the scanning electron microscope, and Dr. Stephen Lombardo generously provided the use of his laboratory's high temperature furnaces.

I have had the pleasure to work and become friends with many great graduate and undergraduate students during my PhD studies. Although I cannot single out them all, I would like to specifically mention the other PhD students I have studied and worked with, including Peter Norgard, Chris Yeckel, and Adam Lodes. The conversations and shared experiences with these peers have been very valuable.

TABLE OF CONTENTS

LIST OF FIGURES	ix
LIST OF TABLES	xvi
ABSTRACT	xviii
Chapter 1: Introduction	1
1.1 Motivation.....	1
1.1.1 Size Limitation of Antennas	1
1.1.2 Material Requirements.....	5
1.2 Research Goals.....	11
1.3 Overview.....	13
References for Chapter 1	16
Chapter 2: Critical Issues in the Development of Composite Materials Combining High Dielectric Constant and High Dielectric Strength	17
2.1 Complex Permittivity and the Dielectric Constant	17
2.2 The Effective Dielectric Constant of Composites	25
2.2.1 Background on the Effective Dielectric Constant	25
2.2.2 Mathematical Models.....	26
2.2.3 Three-Dimensional Electrostatic Modeling.....	29
2.3 Particle Packing Density	34
2.4 Homogeneity.....	53

2.5 Factors Contributing to High Dielectric Strength.....	62
2.5.1 Voids	62
2.5.2 Air Gaps at Surface Contacts	66
2.5.3 Triple Points.....	68
References for Chapter 2	73
 Chapter 3: Development of High Dielectric Constant Composite Materials	75
3.1 Literature Survey of High Dielectric Constant Composites	75
3.2 Novel Approaches to High Dielectric Constant Composite Development.....	80
3.2.1 Trimodal Particle Packing.....	81
3.2.2 In-situ Polymerization.....	83
3.2.3 Void-Filling with High Dielectric Constant Fluids	85
3.3 Concepts of the Classes of High Dielectric Constant Composites	86
3.3.1 Composite Class 1 – MU45	86
3.3.2 Composite Class 2 – MU100	87
3.3.3 Composite Class 3 – MU550	88
3.4 High Dielectric Constant Ceramics	90
3.4.1 Overview of Perovskite Ceramics	90
3.4.2 Selection of Ceramic Material	94
3.5 Binder Materials.....	96
3.5.1 Cyanoethylated Pullulan	96
3.5.2 Polysilsesquioxanes	97
3.5.3 Agarose	101

3.6 Void Fillers	103
3.6.1 Survey of High Dielectric Constant Fluids	103
3.6.2 Alkylene Carbonates	106
3.7 Examples and Physical Descriptions of Composites	108
References for Chapter 3	113
 Chapter 4: Dielectric Materials Characterization	116
4.1 Introduction.....	116
4.2 Dielectric Spectroscopy	117
4.2.1 Dielectric Spectroscopy Methods	117
4.2.2 Dielectric Spectroscopy Results	125
4.3 Polarization	132
4.3.1 Polarization Methods	132
4.3.2 Polarization Results	136
4.4 Capacitive Discharge	141
4.4.1 Capacitive Discharge Methods	141
4.4.2 Capacitive Discharge Results	144
4.5 Dielectric Strength	147
4.5.1 Dielectric Strength Methods	147
4.5.2 Dielectric Strength Results	156
4.6 Thermogravimetric Analysis	163
4.6.1 Thermogravimetric Analysis Methods	163
4.6.2 Thermogravimetric Analysis Results.....	166

4.7 Scanning Electron Microscopy	169
4.7.1 Scanning Electron Microscopy Methods	169
4.7.2 Scanning Electron Microscopy Results	171
4.8 3D Modeling of High Dielectric Constant Composites	177
4.8.1 3D Model Description.....	177
4.8.2 Model Results	183
References for Chapter 4	190
 Chapter 5: High Power Dielectric Resonator Antenna	191
5.1 Background on Dielectric Resonator Antennas	191
5.2 Coupling Methods.....	193
5.3 Resonant Modes a Cylindrical Dielectric Resonator	197
5.4 Bandwidth Enhancement	208
5.5 DRA Design.....	212
5.6 DRA Evaluation Methods.....	218
5.6.1 Simulation of the Antenna Reflection Coefficient and Radiation Pattern....	218
5.6.2 Low Voltage Measurements	219
5.6.3 Comparison with Fundamental Limits for Electrically Small Antennas	222
5.7 DRA Simulation and Experimental Results	224
5.7.1 Simulation Results	224
5.7.2 Low Power Experimental Results.....	232
5.7.3 Evaluation of Experimental Results against Fundamental Limits	236

References for Chapter 5	239
Chapter 6: High Power Antenna Driver.....	240
6.1 System Overview	240
6.2 Revised FCG Simulator	244
6.2.1 Background and Theory of Operation	244
6.2.2 Magnetic Switches	247
6.2.3 High Power Antenna Driver Construction.....	251
6.3 IES, EEOS, and High Power Oscillator.....	253
6.3.1 Inductive Energy Store	253
6.3.2 Electroexplosive Opening Switch.....	254
6.3.3 High Power Oscillator.....	256
6.3.4 Diagnostics.....	258
6.4 High Power Antenna Driver Simulations	261
6.5 High Power Antenna Driver Results.....	264
6.5.1 CLC-Driven FCG Simulator.....	265
6.5.2 Complete High Power Antenna Driver.....	268
References for Chapter 6	274
Chapter 7: Summary and Future Work.....	276
7.1 Composite Development and Characterization	276
7.1.1 Summary	276
7.1.2 Future Work	286

7.2	Dielectric Resonator Antenna	288
7.2.1	Summary	288
7.2.2	Future Work	291
7.3	High Power Antenna Driver	293
7.3.1	Summary	293
7.3.2	Future Work	295
VITA	298

LIST OF FIGURES

Figure	Page
Figure 1. Relative antenna size compared to vacuum/air and polyethylene vs. relative permittivity.....	4
Figure 2. Energy density vs. dielectric constant for dielectric strengths of 10 MV/m and 100 MV/m.....	8
Figure 3. Power density as a function of the dielectric constant for dielectric strengths of 10 MV/m and 100 MV/m	10
Figure 4. The complex permittivity as a function of frequency showing general trends due to the ionic, dipolar, atomic, and electronic polarization mechanisms. Illustration used under open license [2]......	24
Figure 5. Effective dielectric constant for variable percentage filler and matrix dielectric constant	31
Figure 6. Percentage difference of the simulated effective dielectric constant from calculated values	32
Figure 7. Percentage change in the effective dielectric constant between a composite with and without voids	33
Figure 8. Illustrations of packing (a.) a single particle system, (b.) ideal binary system, and (c.) realistic binary system	37
Figure 9. Possible normalized densities in a binary system with 50% voids in a bed of each component	39
Figure 10. Theoretical specific volume for practical ratios of small to large particle sizes. A bed of each particle size is assumed to be 50% voids by volume.....	45
Figure 11. Volume percentage of voids vs. ratio of particle sizes for particles with 40% voids in a packed bed of each size	49
Figure 12. Volume percentage of voids vs. ratio of particle sizes for particles with 30% voids in a packed bed of each size	50
Figure 13. Large agglomerates formed by 50 nm primary particles.....	55
Figure 14. Uniaxial pressing in a hydraulic press	59
Figure 15. Illustration of transfer of force from friction between composite and die wall	61

Figure 16. Double-ended uniaxial pressing with an isolated die	62
Figure 17. Plot of 3D fields projected onto a 2D cross section of a composite containing high and low dielectric constant fillers	64
Figure 18. 2D plot of the absolute value of the 3D electric field within the matrix material	66
Figure 19. Illustration of microscopic imperfections causing air gaps between surfaces.	67
Figure 20. Reduction of field enhancement from (a) surface electrodes to (b) embedded electrodes	70
Figure 21. Simulated electric field in the sample with high dielectric constant coating (bottom) and without high dielectric constant coating (top).....	72
Figure 22. Example Hysteresis Curve of a Perovskite Material	92
Figure 23. Dielectric constant and dielectric loss of 60/40 barium strontium titanate as a function of temperature and frequency. Data included with permission of TRS Technologies [17]	95
Figure 24. Example of a single polysilsesquioxane network being formed in a void between adjacent barium titanate particles. An actual void would ideally be completely filled with a highly cross-linked network	99
Figure 25. Sample of MU45 produced with a diameter of 11.43 cm	109
Figure 26. A sample of MU45 with a diameter of 2.54 cm showing the mirror-like glossy finish of finely polished MU45	110
Figure 27. 7.62 cm diameter sample cut into rectangular shape as substrate for a microstip transmission line	111
Figure 28. Samples of MU100 with holes drilled along the center axis.....	111
Figure 29. Multiple views of a sample made of MU100. The diameter is 7.62 cm, and the thickness is approximately 1.25 cm. This piece was used as the resonator in the high power DRA described in Chapter 5.....	112
Figure 30. Low voltage permittivity measurement equipment.....	118
Figure 31. Equivalent circuit of a capacitor with air gaps	120
Figure 32. The effects on the capacitance or effective dielectric constant of a discrete air gap over a variable area of the electrode-material interface	121

Figure 33. The dependence of S_{11} with respect to the ratio of the impedance at the MUT and the characteristic impedance of the test fixture. This graph assumes that the impedance at the MUT is purely real. Adapted from figure in [2].	124
Figure 34. Dielectric constant and loss tangent for MU45	126
Figure 35. Dielectric constant and loss tangent for MU100	127
Figure 36. Dielectric constant and loss tangent for MU550	128
Figure 37. Dielectric constant of EC50 at room temperature and greater than 100C	131
Figure 38. Dissipation factor of EC50 at room temperature and greater than 100C	132
Figure 39. Schematic of the modified Sawyer-Tower circuit	133
Figure 40. Polarization vs. electric field of MU45 at low electric field levels from a 100 Hz source	137
Figure 41. Polarization vs. electric field for MU45 under high electric field	138
Figure 42. Polarization vs. electric field for the MU45 composite under electric field strengths greater than 6 MV/m	139
Figure 43. Polarization of MU100 under low electric field conditions	140
Figure 44. Polarization of MU100 under high electric field conditions up to nearly 4 MV/m	140
Figure 45. Polarization of MU100 under high electric field conditions up to more than 10 MV/m	141
Figure 46. Schematic of the High Voltage Capacitive Discharge Test Stand	142
Figure 47. Custom high voltage capacitive discharge test stand	143
Figure 48. Discharge waveform of a capacitor made with MU45	145
Figure 49. Discharge waveform of a capacitor made with MU100	147
Figure 50. Samples prepared for dielectric strength testing. From left to right in sets of six: MU45, MU100, and MU550	150
Figure 51. Dielectric strength test cell	150

Figure 52. Circuit schematic of pulsed dielectric strength test stand	151
Figure 53. Example voltage waveforms from both sides of test cell.....	152
Figure 54. Pulsed voltage across a dielectric sample showing the risetime of the applied voltage.....	152
Figure 55. The PA-80 pulse generator with test cell and diagnostics.....	153
Figure 56. Micrograph of electrode-composite edges	155
Figure 57. Electrode geometry simulated in Maxwell SV for estimation of the field enhancement factor	155
Figure 58. Weibull plot of electric field at breakdown without a dielectric coating and without inclusion of the field enhancement factor.....	158
Figure 59. Weibull plot of electric field at breakdown without a high dielectric constant coating and with the field enhancement factor	160
Figure 60. Weibull plot of electric field at breakdown for MU45 and MU100 samples with high dielectric constant coating around electrode edges but without FEF	162
Figure 61. Large barium titanate pieces before (left) and after (right) sintering treatment. The size scale is 50 μm	172
Figure 62. Large barium titanate pieces before (left) and after (right) sintering treatment. The size scale is 300 μm	172
Figure 63. Milled products of large ceramic pieces without sintering (left) and with sintering (right). The size scale is 500 μm	174
Figure 64. Nanoparticles as received (left) and after milling (right). The size scale on the left is 300 μm , and the size scale on the right is 500 nm.....	175
Figure 65. Intermediate size particles as received. The size scale on the left is 10 μm , and the size scale on the right is 1 μm	176
Figure 66. Cross Sections of composites including a trimodal distribution of particles. The scale on the left is 1mm, and the scale on the right is 500 μm	177
Figure 67. Screen shot of the user interface displaying the control parameters for composite construction	181
Figure 68. Virtual composite filled with 4 types of spherical particles	182

Figure 69. Virtual composite filled with 2 types of cubic particles	182
Figure 70. Particles generated by the macro for the simulation of MU100.....	184
Figure 71. Microstrip coupling	195
Figure 72. Aperture coupling with resonator removed.....	196
Figure 73. Resonant frequency of cylindrical DRA with $\varepsilon_r = 100$ in TM ₁₁₀ mode	200
Figure 74. Resonant frequency of a cylindrical DRA with $\varepsilon_r = 550$ in TM ₁₁₀ mode.....	201
Figure 75. Resonant frequency for cylindrical DRA with $\varepsilon_r = 100$ in TM ₀₁₁ mode	203
Figure 76. Quality factor of cylindrical DRA with $\varepsilon_r = 100$ in TM ₀₁₁ mode	204
Figure 77. Resonant frequency for cylindrical DRA with $\varepsilon_r = 100$ in HE ₁₁₁ mode.....	205
Figure 78. Quality factor for a cylindrical DRA with $\varepsilon_r = 100$ in HE ₁₁₁ mode	206
Figure 79. Resonant frequency of a cylindrical DRA with $\varepsilon_r = 100$ in TE ₀₁₁ mode.....	207
Figure 80. Quality factor of a cylindrical DRA with $\varepsilon_r = 100$ in TE ₀₁₁ mode	208
Figure 81. Dependence of the dielectric loss quality factor and bandwidth with respect to the dielectric losses of the resonator	210
Figure 82. A high power DRA.....	213
Figure 83. Backside of the high power DRA showing the ground plane	213
Figure 84. The DRA with supports to hold the resonator in place and an SMA connector for low voltage characterization.....	215
Figure 85. The DRA was characterized at low power in the anechoic chamber with an LP-80 log periodic antenna from Sunol Sciences.....	220
Figure 86. The simulated DRA with the waveguide port	225
Figure 87. Simulated return loss of the high power DRA	225
Figure 88. Simulated maximum 3D farfield gain of the high power DRA	226
Figure 89. Simulated gain orthogonal to the plane of the DRA substrate ($\theta=\varphi=0^\circ$)	227
Figure 90. 3D plot of the simulated far field gain pattern at 475 MHz	228

Figure 91. Polar plots of the far field gain pattern at 475 MHz.....	228
Figure 92. 3D simulated far field gain pattern at 650 MHz.....	229
Figure 93. Polar plots of the simulated far field gain at 650 MHz	229
Figure 94. Simulated 3D farfield gain pattern at 825 MHz	230
Figure 95. Simulated polar plots of the gain at 825 MHz.....	231
Figure 96. Simulated 3D plot of the gain at 1.2 GHz	232
Figure 97. Simulated polar plots of the gain at 1.2 GHz	232
Figure 98. Return loss of the high power DRA with and without the resonator. The impedance match of the antenna is improved between 475 MHz and 1.5 GHz due to the addition of the resonator.	233
Figure 99. Comparison of the simulated and measured return loss of the high power DRA	234
Figure 100. Measured gain of the high power DRA in oil	235
Figure 101. Comparison of the measured gain and simulated gain at $\theta=\varphi=0^\circ$	236
Figure 102. Measured DRA gain along with the theoretical maximum normal gain for antennas enclosed in a sphere around the full DRA substrate and around only the resonator.....	238
Figure 103. Flow chart for the high power antenna driver	242
Figure 104. Inductive energy storage systems and high power oscillators driving antenna impedance Z_A	244
Figure 105. CLC-Driven FCG Simulator	246
Figure 106. Simulated revised FCG current into 1 uH	247
Figure 107. CLC-driven FCG simulator during evaluation prior to incorporation into the high power antenna driver	252
Figure 108. Three levels of components in the CLC-driven FCG simulator.....	253
Figure 109. Two-section exploding wire fuse	256

Figure 110. High power oscillator	258
Figure 111. Example of the D-Dot signal voltage for calibration on a high voltage transmission line section of the high power oscillator.....	260
Figure 112. Integrated calibration signal for D-dot probe on a high voltage transmission line section of the high power oscillator	260
Figure 113. Full view of simulated voltage at antenna input from high voltage oscillator	262
Figure 114. Detailed view of high frequency content in the simulated voltage signal at the antenna input.....	263
Figure 115. Detailed view of the derivative of the simulated voltage at the input to the antenna	263
Figure 116. FFT of the derivative of the simulated voltage at the antenna input	264
Figure 117. Fully-integrated high power antenna driver in RF-shielded chamber.....	265
Figure 118. Output current of the CLC-driven FCG simulator into an inductive load ..	266
Figure 119. First derivative of the CLC-drive FCG current	267
Figure 120. Second derivative of the CLC-driven FCG simulator current.....	268
Figure 121. Current output of the FCG simulator into the inductive load and electroexplosive opening switch.....	269
Figure 122. Integrated D-dot signal with high frequency oscillations normalized to zero volts.....	270
Figure 123. Detailed view of the first high power oscillations near the antenna feed....	271
Figure 124. FFT of the voltage near the antenna feed	271
Figure 125. A plot of the D-dot signal on the high voltage oscillator near the antenna feed point	272
Figure 126. The FFT of the D-dot signal near antenna feed point	273

LIST OF TABLES

Table	Page
Table 1. Density of compacted beds and particles and the corresponding volume percentages of voids and ceramic	53
Table 2. Notable Previous Works in High Dielectric Constant Composite Materials.....	76
Table 3. Examples of Trialkoxysilanes for Particle Functionalization or Formation of Polysilsequioxane	98
Table 4. High dielectric constant liquids considered for void filler [32-34]	106
Table 5. Summary of Weibull Parameters for Samples without Coating and without FEF Included.....	158
Table 6. Summary of electric field data for samples without a high dielectric constant coating and without inclusion of the field enhancement factor	159
Table 7. Summary of Weibull parameters for samples without a coating and with FEF included.....	160
Table 8. Summary of electric field values for samples without coating and with FEF..	161
Table 9. Summary of Weibull parameters for samples with coating but without FEF ..	162
Table 10. Summary of Electric Field Values for Samples with Coating without FEF...	163
Table 11. Summary of mass loss from each binder	166
Table 12. Basic properties of the samples analyzed through thermogravimetric analysis	167
Table 13. Summary of binder content of composites	168
Table 14. Summary of ceramic content of composites.....	168
Table 15. Summary of void estimates.....	169
Table 16. Summary of EC50 content of MU550	169
Table 17. Summary of dielectric constant values for the ceramic, binder, and voids used in the three composite simulations.....	184
Table 18. Target volume percentages for each component	185

Table 19. The volume percentages of each component reported by the program after automatic generation of the fillers and voids	186
Table 20. The dielectric constant obtained from the simulation, the dielectric constant calculated from Lichtenegger's equation, and the percentage difference	187
Table 21. Resonant frequency calculated for the four modes considered in Section 5.3	217
Table 22. Magnetic Core Parameters.....	250

ABSTRACT

The volume and weight of high power antennas can be a limiting factor for directed energy systems. By integrating high dielectric constant materials into an antenna structure, it is possible to reduce the size of some antenna systems, but conventional high dielectric constant materials do not have adequate dielectric strength and mechanical properties. This work, undertaken to address the material requirements and demonstrate application in a high power antenna, encompasses the following four areas: 1. Development of high dielectric constant composite materials for integration in high power antennas; 2. Characterization of the composite materials through measurements of the permittivity and dielectric strength along with analyses based on thermogravimetry, scanning electron microscopy, and 3D modeling; 3. Design, simulation, and low power measurement of a high peak power antenna including the materials; 4. Design and construction of an antenna driver for high peak power antenna evaluation.

Through novel techniques, including trimodal particle packing, in-situ polymerization, and fluid void filling, three classes of high dielectric constant composites have been developed with dielectric constants of approximately 45, 100, and 550 at 200 MHz. A dielectric resonator antenna has been designed, simulated, and constructed for peak power operation up to 1 GW based on a resonator with a dielectric constant of 100. Antenna simulations and measurements have characterized the antenna performance, showing a primary band of operation between approximately 605 MHz and 1.1 GHz. A high power antenna driver capable of producing a high power damped sinusoidal RF burst was designed and constructed based on an inductive energy storage system that pulse charges the antenna under test and an oscillator to greater than 225 kV.

Chapter 1: Introduction

1.1 Motivation

1.1.1 Size Limitation of Antennas

Pulsed power systems are continually developed with size and weight reduction as a priority to improve their portability and utility. Traditional high energy pulsed power systems are stationary units with volumes of several cubic meters and masses on the order of thousands of kilograms or more. As the range of applications for pulsed power technology grow, the requirements for small and mobile systems have become more stringent. In particular, the increasing functionality of directed energy systems often requires pulsed power drivers that can be quickly transported. Improvements in the materials and technology implemented in new high voltage capacitors, insulation, circuit topologies, switches, and other components have made significant advancements toward minimizing high power drivers. However, for systems driving an antenna load, the system size and weight can be greatly increased by the volume and mass of the antenna.

A high power antenna, as the radiating load of many directed energy systems, is a critical component in a system's implementation. Without proper design, the radiation efficiency, gain, directivity, polarization, frequency bandwidth, or a number of other parameters may be poor, rendering the system ineffective. For these reasons, compromises in antenna design to reduce the size of the antenna can often result in poorly performing systems. Additionally, antennas designed to radiate in the very high frequency (VHF) and ultra high frequency (UHF) bands can be impractically large. Although the specifics of the design of various antenna geometries vary, a general

relationship exists in which the dimension along which a wave propagates along an antenna, l_a [m], is proportional to the wavelength, λ_a [m], at which resonance occurs in the antenna.

$$l_a \propto \lambda_a \quad (1.1)$$

The wavelength is equal to the phase velocity of a wave propagating in the antenna medium divided by the frequency, f_a [Hz], of the wave, as given in equation (1.2) [1].

$$\lambda_a = \frac{v_p}{f_a} \quad (1.2)$$

The phase velocity of a wave traveling in a medium can be calculated as the velocity of light in vacuum divided by the refractive index, n , as given by equation (1.3) [1]. The symbols ϵ_r and μ_r represent the relative permittivity and relative permeability, respectively, of the medium through which the wave travels. It is assumed for the sake of this discussion that the medium is lossless. The symbol c [m/s] represents the speed of light in vacuum.

$$v_p = \frac{c}{n} = \frac{c}{\sqrt{\epsilon_r \mu_r}} = \frac{1}{\sqrt{\epsilon_0 \epsilon_r \mu_0 \mu_r}} \quad (1.3)$$

Thus, in general, the size of an antenna is dependent on the frequency of operation and the properties of the material in which the wave is propagating as shown in equation (1.4).

$$l_a \propto \frac{1}{f_a \sqrt{\epsilon_0 \epsilon_r \mu_0 \mu_r}} \quad (1.4)$$

Since the speed of light in vacuum is a constant, the size of an antenna can generally only be optimized through three factors: the frequency of operation, the relative permittivity of the medium through which the wave travels in the antenna, and the relative permeability of the medium through which the wave travels in the antenna. Compact antennas can

relatively easily be made for antennas of several gigahertz and higher. However, for applications requiring operation in the VHF and UHF bands from 30 MHz to 3 GHz, increasing the frequency to reduce the size of the antenna is not an option. Therefore, in general, the size of the antenna can be reduced by changing the material properties of the medium through which the wave propagates through the antenna, specifically by increasing the relative permittivity and/or the relative permeability of the material. It is noted that the geometry of the antenna also plays a significant role in the relative compactness of the antenna as certain types of antennas are much smaller or better conform to their supporting structure than others.

Either the relative permittivity or the relative permeability can be increased to reduce the phase velocity of waves propagating in an antenna medium and thus decrease the length of the antenna. However, since the medium in which the waves propagate must be electrically insulating, it is impractical to attempt to make a suitable material with a high relative permeability for operation in high electric and magnetic fields. Conventional materials with a high relative permeability, produced from elements such as iron and nickel, are typically conductive and incompatible as insulators in high voltage systems. Additionally, excessive energy losses due to eddy currents and resistive current conduction could significantly reduce the effectiveness of high relative permeability materials as antenna waveguides. Therefore, the most practical way to reduce the size of an antenna in a given frequency bandwidth with conventional materials is by increasing the relative permittivity of the material. The potential for use of metamaterials to produce an effectively high permittivity or permeability is considered in the subsequent subsection.

As described by equation (1.4), the size of an antenna can generally be decreased by a factor of the square root of the relative permittivity. Figure 1 demonstrates the potential for antenna size reduction as the dimension l decreases with increasing values of the relative permittivity. A size reduction factor is plotted for comparison to equivalent antennas incorporating vacuum/air and polyethylene. The size of a dielectric-loaded antenna decreases dramatically at relatively low values of the dielectric constant as the size reduction factor is 5 for a material dielectric constant of 25 in comparison to an antenna with an air dielectric. At a relative permittivity of 100, the antenna size has been reduced to 10% of its air-equivalent size. The antenna size can theoretically be further reduced with ever-increasing values of relative permittivity. However, a situation of diminished returns is evident due to the dependence on the square root of the relative permittivity. Therefore, a point is reached at which further increases in the relative permittivity produce negligible benefits in size reduction.

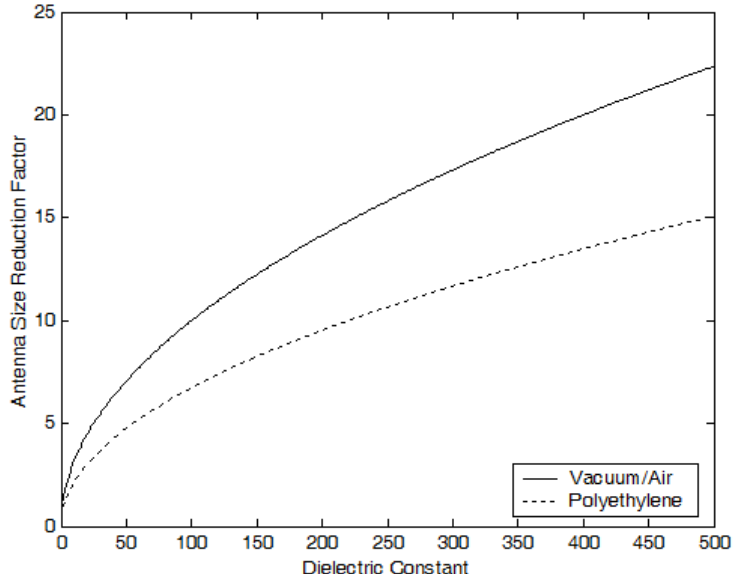


Figure 1. Relative antenna size compared to vacuum/air and polyethylene vs. relative permittivity

Reducing the size of antennas enables not only more compact systems but also arrays of small antennas operating at a much higher output power than a single antenna with a size equivalent to the array. Implementation of an array of compact antennas can reduce the electric field in the air surrounding each antenna element by distributing the power across the array. Further, compact antenna arrays can improve the directionality and beam steering properties over a single antenna system.

While the preceding discussion focused on the theoretical potential for antenna size reduction through the incorporation of materials with high relative permittivity, there are practical limits to antenna size reduction by these means. The limits are often dependent on the specific antenna and the manner in which the dielectric materials are incorporated. In general, electrically small antennas suffer from poor radiation efficiency due to poor impedance matching with the low impedance of the antenna [2]. Impedance matching techniques can be applied, but these solutions are often only effective in a narrowband of frequencies, limiting the antenna bandwidth [2]. With these limitations, an antenna design must be optimized based on the tradeoffs between further antenna minimization and its effects on radiation efficiency, bandwidth, and other performance metrics.

1.1.2 Material Requirements

The preceding discussion describes the potential for reducing the size of high power antennas by incorporating materials with a high relative permittivity. However, at the beginning of this research program, there were few, if any, materials that could meet the requirements to effectively reduce the size of a high power antenna. Although there are well-known materials with a high relative permittivity, these materials do not adequately fulfill the other requirements for incorporation into high power systems. This subsection

will briefly examine the requirements for materials to be incorporated into high power antennas and the properties of some of the currently-available materials.

As the previous section outlined, the relative permittivity is the primary factor that can effectively reduce the size of antennas to operate in a given frequency range. Therefore, a high relative permittivity is the primary criterion for selection of an appropriate material. The criteria for what constitutes a high relative permittivity can be relative in nature and judged based upon the specifications of a given system. A relative permittivity of four can theoretically reduce the size of an antenna by a factor of two, and since most common insulators have a relative permittivity of much less than four, four can in some situations be considered a high relative permittivity. Nevertheless, to provide distinction from some conventional materials with a high relative permittivity, a threshold of 20 has been established in this study for classification of a material as having a high relative permittivity.

Materials with exceptionally high relative permittivity include perovskite ceramics. Although many perovskites have dielectric constants of several thousand, there are significant disadvantages that limit their application in high power systems. First, the dielectric strength of perovskites is generally inadequately low as they are prone to dielectric failure along boundaries within the ceramic. One popular perovskite used in applications demanding a high permittivity, barium titanate, exhibits dielectric strength values typically of less than 10 kV. As one study reported, samples with a thickness of 0.3 mm had dielectric strengths measured from 5-7 MV/m, and thin laminates of 80 μ m were reported to have a dielectric strength up to 30 MV/m [3]. While a dielectric strength of 30 MV/m could meet requirements for some antenna designs, this value is only

associated with material thicknesses that are too thin for application in high voltage systems. Conventional pulsed power dielectrics, such as transformer oils and several plastics, meet the dielectric strength requirements for high power antennas. However, although some high permittivity polymers have been developed, none of these to date have been shown to retain their high permittivity values through the VHF and UHF bands.

Metamaterials, artificial collections of objects on scales smaller than the wavelength of operation, can exhibit effective electrical and magnetic properties on waves interacting with the collection of objects that are very unique from those of conventional materials [4]. High permittivity metamaterials have been produced by stacking silver and conventional dielectric films [5, 6]. Other metamaterials have been effectively implemented into antenna designs to improve the directivity or significantly reduce an antenna's dimensions [7, 8]. However, metamaterials were not considered a viable option for adaptation to this effort. Many metamaterials are formed as small-scale circuit traces, such as split-ring resonators, which could be susceptible to flashover at high power [4]. Similarly, thinly stacked layers of silver and dielectric films could fail at high voltage. Due to their lack of compatibility to high power systems, metamaterials were not investigated in this work.

The peak energy density and power density, due to their dependence on both the dielectric constant and dielectric strength, are a useful figure of merit in comparing candidate materials. The volumetric energy density, W_E [J/m³], of a dielectric material can be calculated from equation (1.5) where the electric field is represented by the symbol E [V/m] [9].

$$W_E = \frac{1}{2} \varepsilon_0 \varepsilon_r E^2 \quad (1.5)$$

The instantaneous power density, S [W/m²], of an electromagnetic wave propagating in a material can be calculated from the electric field and the impedance of the material, Z [Ω], as shown in equation (1.6) [9].

$$S = \frac{E^2}{Z} = \frac{E^2}{\sqrt{\frac{\mu_0 \mu_r}{\varepsilon_0 \varepsilon_r}}} = E^2 \sqrt{\frac{\varepsilon_0 \varepsilon_r}{\mu_0 \mu_r}} \quad (1.6)$$

For both the energy density and power density, the values can be maximized by maximizing both the electric field and the dielectric constant.

Figure 2 shows a plot of the peak energy density vs. dielectric constant for dielectric strength values of 10 MV/m and 100 MV/m.

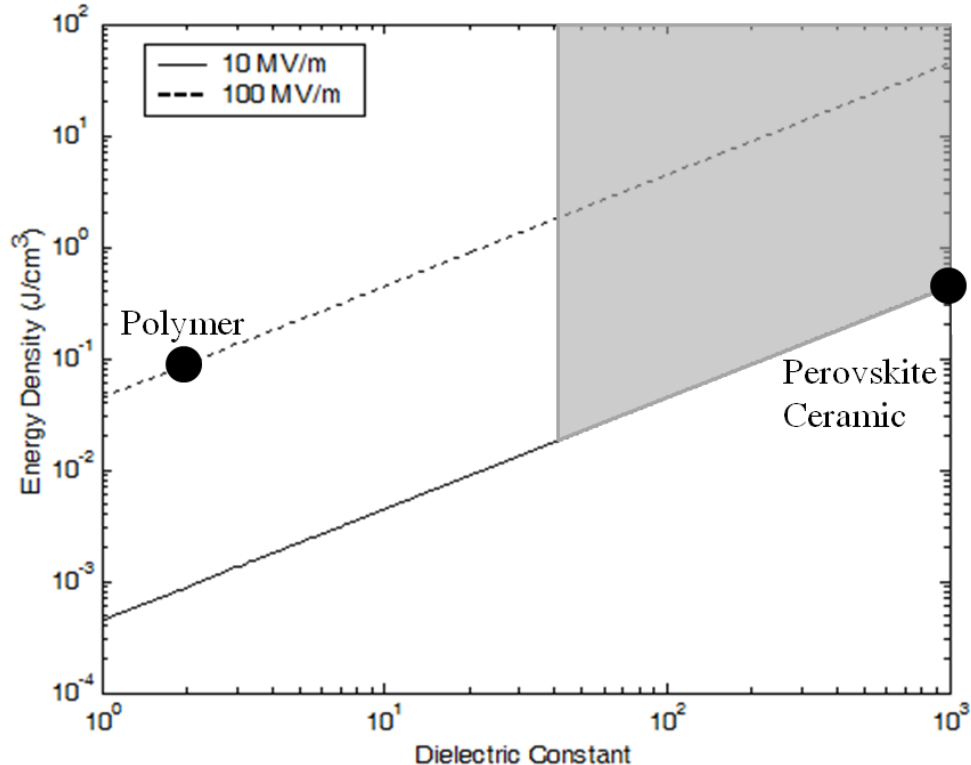


Figure 2. Energy density vs. dielectric constant for dielectric strengths of 10 MV/m and 100 MV/m

The point on the left hand side of the figure represents a typical energy density of a conventional pulsed power dielectric. These dielectrics, such as conventional polymers and insulating oils, typically have a very low dielectric constant of approximately 2.2 and a high dielectric strength on the order of 100 MV/m. Despite the high dielectric strength, the low dielectric constant constrains the peak energy density to a relatively low value, typically less than 0.1 J/cm³. The point at the right of the figure is an example of a perovskite ceramic with a high dielectric constant of 1000 but a low dielectric strength of 10 MV/m, which is representative of that measured for a pure barium titanate sample [10]. In these materials, the low dielectric strength constrains the peak energy density to a value typically less than 1 J/cm³ despite the exceptionally high dielectric constant. The shaded grey region displays a desired range of material properties for high power antennas, combining the benefits of a high dielectric constant and high dielectric strength. The shaded region represents materials with a dielectric constant greater than 40 and a dielectric strength greater than 10 MV/m. While this region includes all dielectric strength values above that cited for typical perovskite ceramics, the dielectric strength would ideally be on the same order or greater than the dielectric strength of polymers. When both a high dielectric constant and high dielectric strength are combined, the energy densities greater than 10 J/cm³ are possible.

Figure 3 displays the power density as a function of the dielectric constant for the typical example dielectric strength values of polymers and perovskite ceramics. The dependence of the power density on the dielectric constant is lower than that for the energy density due to the square root relationship described in equation (1.6). Therefore, the power density capability within a typical polymer is on the order of approximately 5

GW/cm^2 , and the power density calculated for a typical perovskite ceramic is less than $1 \text{ GW}/\text{cm}^2$. By increasing both the dielectric constant and the dielectric strength in the composite material, the power density within the composite would be on the order of $10 \text{ GW}/\text{cm}^2$ to greater than $100 \text{ GW}/\text{cm}^2$. The parameter space of desired material operation, corresponding to a dielectric constant greater than 40 and dielectric strength greater than that of a ceramic at 10 MV/m , is shaded grey in Figure 3. The desired dielectric strength is ideally on the same order of magnitude or greater than that observed for polymers, resulting in power densities greater than $10 \text{ GW}/\text{cm}^2$.

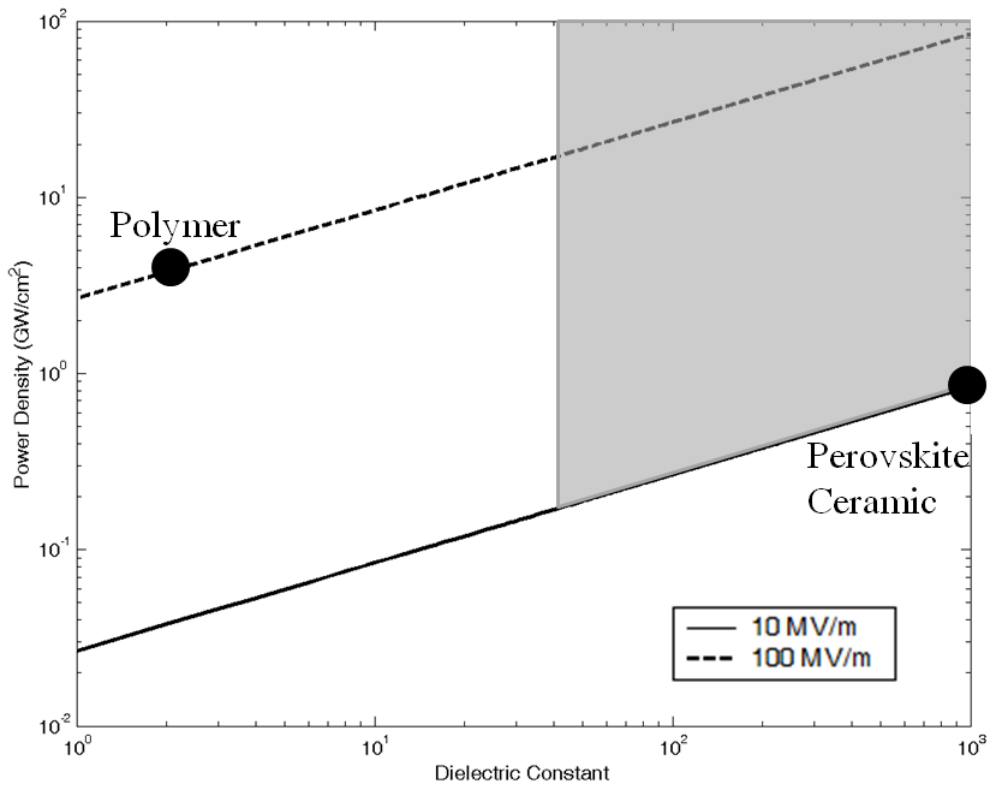


Figure 3. Power density as a function of the dielectric constant for dielectric strengths of 10 MV/m and 100 MV/m

To ensure the material's suitability for implementation in high power antennas and other high voltage components, additional constraints included that the material must be capable of being formed in thicknesses adequate for very high voltage systems, be

machinable to complex geometries, and be manufactured at temperatures much lower than the sintering temperatures used for perovskite ceramics. Conventional materials meeting the previously described requirements for dielectric loading of a high power antenna were unavailable. Therefore, a research effort was necessary to develop a material combining the benefits of a high dielectric constant with a high dielectric strength while also meeting the requirements for size, machinability, and manufacturing conditions.

1.2 Research Goals

The goals of this research include the development of composite materials, dielectric characterization of the composite materials, design, construction, and low power testing of a compact antenna incorporating the composite materials, and development of a high power antenna driver for the dielectric-loaded antenna. These four areas are summarized in the following itemized goals:

1. Develop high dielectric constant composite materials with the following minimum specifications:
 - 1.1 Dielectric constant of greater than 40 at frequencies in the VHF and UHF bands
 - 1.2 Dielectric loss below 0.1 at the frequencies of antenna operation
 - 1.3 Pulsed dielectric strength of greater than 100 MV/m
 - 1.4 Negligible ferroelectric saturation – linear polarization vs. electric field
 - 1.5 Peak energy density of greater than 1 J/cm³
 - 1.6 Capability of being formed into thicknesses greater than 0.5 cm
 - 1.7 Machinability with power and hand tools

2. Characterize the dielectric properties of the composite materials with the following methods:

- 2.1 Dielectric spectroscopy
- 2.2 Polarization
- 2.3 High voltage capacitive discharge
- 2.4 Pulsed dielectric strength
- 2.5 Thermogravimetric analysis
- 2.6 Scanning electron microscopy
- 2.7 3D Electrostatic Simulation

3. Develop a dielectric-loaded compact antenna according to the following minimum specifications:

- 3.1 Operating frequency in the VHF and/or UHF bands
- 3.2 Demonstration of antenna size reduction when compared to conventional antennas operating at similar frequencies
- 3.3 Unity gain or greater at operating frequencies
- 3.4 Peak power capability of 1 GW or greater

4. Develop and test a high power antenna driver with the following specifications:

- 4.1 Driving frequency in the VHF and/or UHF bands at frequencies relevant to the dielectric-loaded antenna
- 4.2 High peak power operation

1.3 Overview

This dissertation is organized along the four tasks outlined in the previous section. Chapters 2 and 3 detail the development of the high dielectric constant composites. Chapter 2 examines the theoretical issues critical to the development of high dielectric constant composites. The range of topics included in Chapter 2 include: a description of the origin of energy storage in dielectric materials; a discussion and analysis of mathematical models describing how the dielectric constant of each material within the composite contributes to the effective dielectric constant of the composite; an analysis of particle packing and how the volume fraction of a component of the composite can be maximized; a discussion on how to improve homogeneity throughout the composite; and lastly how to improve the dielectric strength of the composite. Chapter 3 begins with a brief review of previous notable works in the field of high dielectric constant composites to establish a frame of reference for the current work. The chapter then applies the concepts established in Chapter 2 to discuss the selection of materials, the design of the distribution of the composites' elements, and description of the novel manufacturing methods developed in the course of this work. The three classes of composites developed in this effort, MU45, MU100, and MU550, are briefly described based on their materials and manufacturing concepts.

Chapter 4 includes a full description of the methods and results of the dielectric characterization performed on MU45, MU100, and MU550. The first three characterization methods listed in goal 2 of the previous section, dielectric spectroscopy, polarization, and high voltage capacitive discharge, are complementary methods of determining the dielectric constant and losses under low and high electric field

conditions. Dielectric spectroscopy includes the industry-standard method of network analysis based measurements of the complex permittivity at the frequencies of interest for antenna operation. Since the high dielectric constant composites are intended for high power operation, polarization and high voltage capacitive discharge measurements supplement the low voltage network analysis measurement to account for high electric field effects. Characterization of the dielectric strength is conducted under pulsed conditions to replicate the fast dV/dt of the high frequencies of intended operation. The custom pulsed dielectric test stand is described along with a statistical analysis of dielectric strength measurements on all three composite classes.

Chapter 5 discusses the development and testing of a high power dielectric resonator antenna incorporating one of the high dielectric constant composites. A description of dielectric resonator antennas is provided along with a discussion of coupling methods. An analysis of the resonant modes is provided with models of the resonant frequency based on the properties of the high dielectric constant composites. Due to the narrow bandwidth of many high- Q dielectric resonator antennas, methods to increase the bandwidth are reviewed. The design and construction of a high power dielectric resonator antenna is described, and the results of simulations in CST Microwave Studio are analyzed. Finally, the low power characterization of the antenna is described with results for the return loss and gain.

Chapter 6 covers the design, construction, and testing of a high power antenna driver developed to enable antenna testing at high peak power in transient RF bursts. The high power antenna driver is based on a simulator of a flux compression generator, and a new design for such a simulator is described. The chapter further describes the use of an

exploding wire fuse to interrupt the current in an inductive energy storage system, charging a high power oscillator and the antenna under test to high voltage. The high power damped sinusoid oscillations resulting from discharge of the high power oscillator and antenna provide a high power, high frequency signal that can be radiated by the antenna. This system is described, and results of initial testing of the high power antenna driver are presented.

Chapter 7 provides a summary of the most important results of this work. The outcome of this research is evaluated against the goals established in this chapter. Finally, suggestions for future work are presented in the areas of material development, material characterization, modification of the dielectric-loaded antenna, and high power evaluation of the antenna.

References for Chapter 1

- [1] C. Balanis, *Antenna Theory: Analysis and Design*, 3rd ed. Hoboken, NJ: John Wiley and Sons, 2005.
- [2] G. Breed, "Basic principles of electrically small antennas," in *High Frequency Electronics*: Summit Technical Media, LLC, 2007, pp. 50-503.
- [3] H. Naghib-zadeh, C. Glitsky, I. Dorfel, and T. Rabe, "Low temperature sintering of barium titanate ceramics assisted by addition of lithium fluoride-containing sintering additives," *Journal of the European Chemical Society*, vol. 30, pp. 81-86, 2010.
- [4] D. R. Smith, J. B. Pendry, and M. C. K. Wiltshire, "Metamaterials and negative refractive index," *Science*, vol. 305, pp. 788-792, 2004.
- [5] N. Engheta, "Circuits with light at nanoscales: optical circuits inspired by metamaterials," *Science*, vol. 317, pp. 1698-1702, 2007.
- [6] A. Salandrino and N. Engheta, "Far-field subdiffraction optical microscopy using metamaterial crystals: theory and simulations," *Physical Review B*, vol. 74, 075103, 2006.
- [7] S. Enoch, G. Tayeb, P. Sabouroux, N. Guerin, and P. Vincent, "A metamaterial for directive emission," *Physical Review Letters*, vol. 89, pp. 213902-1 - 213902-4, 2002.
- [8] R. W. Ziolkowski, P. Jin, J. A. Nielsen, M. H. Tanielian, and C. L. Holloway, "Experimental verification of Z antennas at UHF frequencies," *IEEE Antennas and Wireless Propagation Letters*, vol. 8, pp. 1329-1333, 2009.
- [9] C. Balanis, *Advanced Engineering Electromagnetics*. Hoboken, NJ: John Wiley & Sons, Inc., 1989.
- [10] S. Panteny, C. R. Bowen, and R. Stevens, "Characterization of barium titanate-silver composites Part II: Electrical characteristics," *Journal of Materials Science*, vol. 41, pp. 3845-3851, 2006.

Chapter 2: Critical Issues in the Development of Composite Materials Combining High Dielectric Constant and High Dielectric Strength

2.1 Complex Permittivity and the Dielectric Constant

Throughout this work, the terms permittivity and dielectric constant refer to the primary parameter of interest in the composite development. Thus it is important to understand the theoretical basis of this material property and the meaning of these terms. The term dielectric constant generally refers to the real part of the complex permittivity normalized by the permittivity of free space. As will be described, the term dielectric constant is somewhat misleading due to its dependence on a variety of factors, including frequency, temperature, and electric field. Nevertheless, the term dielectric constant is a commonly accepted label used throughout the technical literature, so it is the preferred term used in this work. The following material covers the well-established theory of dielectric materials, and the majority of the remainder of this section is adapted from parts of Balanis' discussion of permittivity [1].

Charges exist in all materials due to the positive charge carried by protons and the negative charge carried by electrons. Separation of charges within a material can occur on a variety of scales, including ions or molecules with a net charge, dipoles in which charge is shared unequally within a molecule or a lattice structure, and dipoles at the atomic scale where the electron cloud can be unsymmetrical with respect to the nucleus. In a perfect dielectric material, these charges or dipoles are completely bound, preventing conduction of current when a constant electric field is applied. The application of a constant electric field, \vec{E} [V/m], can, however, induce alignment of the dipoles with the

electric field, resulting in a net polarization, \vec{P} [C/m²], of the material. As denoted, the electric field and polarization are vectors. To quantify the polarization with respect to individual dipoles, the average dipole moment within the material is defined as the product of the charge being separated in each dipole, q [C], and the average distance the charges in the dipole are separated, $\overrightarrow{l_{av}}$ [m] [1]. This average distance is also a vector in the same direction as the polarization and electric field. The polarization can then be defined based on the number of dipoles per unit volume, N [m⁻³] [1].

$$\vec{P} = Nq\overrightarrow{l_{av}} \quad (2.1)$$

The polarization can be a result of charge separation due to any or all of the mechanisms previously discussed. Even in the absence of a dielectric material, energy can be stored in an electric field in vacuum. The constitutive relation of the electric flux density, \vec{D} [C/m²] to the electric field in a vacuum is given by equation (2.2) [1]. The term ϵ_0 [F/m] represents the fundamental physical constant referred to as the permittivity of free space.

$$\vec{D} = \epsilon_0\vec{E} \quad (2.2)$$

When a dielectric material is present in the electric field, the polarization as calculated in equation (2.1) is additive to the electric flux density of vacuum as described by equation (2.2).

$$\vec{D} = \epsilon_0\vec{E} + \vec{P} \quad (2.3)$$

If a static permittivity is defined as ϵ_s [F/m], equation (2.2) can be rewritten as equation (2.4) [1].

$$\vec{D} = \epsilon_s\vec{E} \quad (2.4)$$

Since $\overrightarrow{l_{av}}$ is a function of the electric field, the polarization is also a function of the electric field based on equation (2.1). Thus it is possible to define the polarization with

respect to the electric field and the permittivity of free space as equation (2.5). To permit this equality, the dimensionless quantity χ is defined as the electric susceptibility [1].

$$\vec{P} = \epsilon_0 \chi \vec{E} \quad (2.5)$$

The electric flux density can be rewritten based on this new definition of the polarization as equation (2.6) [1].

$$\vec{D} = \epsilon_0 \vec{E} + \epsilon_0 \chi \vec{E} = \epsilon_0 \vec{E}(1 + \chi) \quad (2.6)$$

By equating equation (2.6) with equation (2.4), the static permittivity can be defined as equation (2.7) [1].

$$\epsilon_s = \epsilon_0(1 + \chi) \quad (2.7)$$

If the static permittivity is normalized by the permittivity of free space, a new value can be defined that is the relative static permittivity [1]. Since the relative static permittivity is defined relative to the permittivity of free space, it is a dimensionless quantity. This value is the dielectric constant in a static field. However, even in this case of a static field, the term dielectric constant is somewhat misleading based on the common dependence of the value on factors such as temperature and field strength.

$$\epsilon_{sr} = \frac{\epsilon_s}{\epsilon_0} = (1 + \chi) \quad (2.8)$$

The preceding discussion can be extended to the case of alternating electric fields by recognizing that under the influence of an alternative electric field, $\overrightarrow{l_{av}}$ of equation (2.1) becomes a function of time. Thus the separation of charges oscillates with the electric field. The oscillating charges experience both an attractive force pulling the opposite charges together and a damping effect opposing the motion of the charges. This is similar to the mechanical situation in which a mass attached to a spring oscillates with a damping factor due to friction [1]. From an analysis of this oscillating system, the distance

between charges as a function of time, $l^*(t)$ [m], due to an oscillating electric field, $E(t)$ [V/m], can be written as equation (2.9) [1]. The symbol d represents the damping coefficient, and the symbol m [kg] is the effective mass of the charge. The symbol ω [rad/s] is the angular frequency, and the resonant angular frequency of the system is represented as ω_0 [rad/s]. The imaginary unit is represented as i . A superscript asterisk is added to symbolize all quantities that are complex.

$$l^*(t) = \frac{qE^*(t)}{m\left[(\omega_0^2 - \omega^2) + i\omega\left(\frac{d}{m}\right)\right]} \quad (2.9)$$

From equations (2.9), equation (2.1) can be expanded to the time-varying case as equation (2.10) [1].

$$P^*(t) = Nql^*(t) = \frac{Nq^2E^*(t)}{m\left[(\omega_0^2 - \omega^2) + i\omega\left(\frac{d}{m}\right)\right]} \quad (2.10)$$

Applying the same logic used to define the static permittivity through equations (2.4), (2.6), and (2.7), the time-varying permittivity can be determined as equation (2.11) [1]. The permittivity has both real and imaginary parts, so it is now referred to as the complex permittivity [1].

$$\varepsilon^* = \frac{D^*(t)}{E^*(t)} = \varepsilon_0 + \frac{P^*(t)}{E^*(t)} = \varepsilon_0 + \frac{Nq^2}{m\left[(\omega_0^2 - \omega^2) + i\omega\left(\frac{d}{m}\right)\right]} \quad (2.11)$$

Normalizing equation (2.11) by the permittivity of free space provides the complex relative permittivity [1].

$$\varepsilon_r^* = 1 + \frac{Nq^2}{\varepsilon_0 m \left[(\omega_0^2 - \omega^2) + i\omega \left(\frac{d}{m} \right) \right]} \quad (2.12)$$

The complex relative permittivity is often discussed in the context of its real and imaginary parts.

$$\varepsilon_r^* = \varepsilon_r' + i\varepsilon_r'' \quad (2.13)$$

The real and imaginary components of the complex relative permittivity can be separated from equation (2.12) as equations (2.14) and (2.15) [1].

$$\varepsilon_r' = \frac{\frac{Nq^2}{\varepsilon_0 m}(\omega_0^2 - \omega^2)}{(\omega_0^2 - \omega^2)^2 + \left(\omega \frac{d}{m}\right)^2} \quad (2.14)$$

$$\varepsilon_r'' = \frac{Nq^2}{\varepsilon_0 m} \left(\frac{\omega \frac{d}{m}}{(\omega_0^2 - \omega^2)^2 + \left(\omega \frac{d}{m}\right)^2} \right) \quad (2.15)$$

The preceding equations explain the physical origin of the complex relative permittivity and its real and imaginary components. To understand how the quantities of equation (2.14) and (2.15) translate to energy storage and loss, the derivative form of the Maxwell-Ampere equation, which includes the complex permittivity, can be considered [1]. The symbol \vec{H} [A/m] represents the magnetic field, and the symbols \vec{J}_i [A/m²] and \vec{J}_c [A/m²] represent the impressed and conduction current densities, respectively. It should be noted that the permittivity values in equation (2.16) and subsequent equations have not been normalized by the permittivity of free space, so they are equal to the product of ε_0 and the relative values given by equations (2.14) and (2.15).

$$\nabla \times \vec{H} = \vec{J}_i + \vec{J}_c + i\omega(\varepsilon' - i\varepsilon'')\vec{E} \quad (2.16)$$

The conduction current density can be calculated as the product of the static conductivity, σ_s [Ω^{-1}] and the electric field. Applying this relation and simplifying equation (2.16) produces equation (2.17) [1].

$$\nabla \times \vec{H} = \vec{J}_i + (\sigma_s + \omega\varepsilon'')\vec{E} + i\omega\varepsilon'\vec{E} \quad (2.17)$$

As seen in equation (2.17), the imaginary component of the complex permittivity contributes to a real component of the current density, and the real component of the complex permittivity forms the imaginary component of the current density. Further combination of terms in equation (2.17) derives equation (2.18).

$$\nabla \times \vec{H} = \vec{J}_t + i\omega\epsilon' \left(1 - i \frac{\sigma_s + \omega\epsilon''}{\omega\epsilon'} \right) \vec{E} \quad (2.18)$$

In the format of equation (2.18), the loss tangent, $\tan \delta$, is present, as defined by equation (2.19) [1].

$$\tan \delta = \frac{\sigma_s + \omega\epsilon''}{\omega\epsilon'} \quad (2.19)$$

In most good dielectrics, the static conductivity can be neglected. In that case, the loss tangent is simplified to equation (2.20). Since both ϵ'' and ϵ' include the permittivity of free space, the loss tangent can also be written in terms of the ratio of the relative complex permittivity values. The loss tangent is also equivalent to the dissipation factor.

$$\tan \delta \cong \frac{\epsilon''}{\epsilon'} = \frac{\epsilon_r''}{\epsilon_r'} \quad (2.20)$$

Throughout this text, the terms dielectric constant or relative permittivity will be used to refer to the real component of the complex relative permittivity, represented as ϵ_r' or simply ϵ_r . This term is used due to its accepted usage in the technical literature with acknowledgement that the dielectric constant is not constant but rather is a function of frequency, temperature, electric field and other factors. The terms loss tangent or dissipation factor, as well as a general reference to dielectric losses, are used to refer to the losses as a result of time-varying electric fields. When appropriate, losses due to non-negligible conductivity σ_s are referred to separately.

As shown in equations (2.14) and (2.15), the real and imaginary components of the complex relative permittivity have a resonant frequency, ω_0 , around which the complex permittivity undergoes a significant transition. As the polarization of a material can be the result of the multiple polarization mechanisms previously discussed, the material may have multiple resonant frequencies. Figure 4 illustrates the general behavior of the real and imaginary components of the complex permittivity with respect to frequency for the various polarization mechanisms. At the resonant frequency for a particular polarization mechanism, there is significant dispersion in the real part of the complex permittivity, and the imaginary component reaches a maximum. Thus, it is generally disadvantageous to operate a dielectric material near the resonant frequency of the polarization mechanism as it corresponds to a dispersion in the dielectric constant and high dielectric losses. This presents a challenge in this work due to the frequency range of interest for antenna operation in the VHF and UHF bands. In these bands, many materials exhibiting dipolar polarization have high dispersion of the dielectric constant and high dielectric losses. This factor limits the use of highly polar polymers as effective binders as the high dielectric constant of these polymers is much lower in the VHF and UHF bands and the dielectric losses are high.

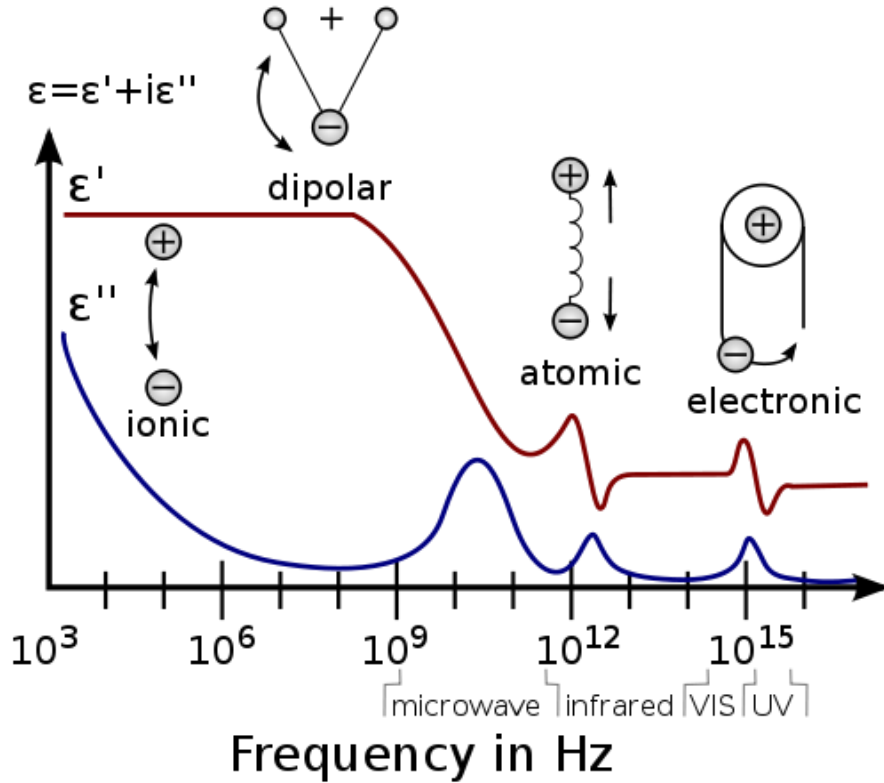


Figure 4. The complex permittivity as a function of frequency showing general trends due to the ionic, dipolar, atomic, and electronic polarization mechanisms. Illustration used under open license [2].

In addition to providing a derivation of the dielectric constant and dielectric losses, the preceding discussion also gives insight to begin the discussion on how a high dielectric constant material can be developed. As described by equation (2.11), increasing the dielectric constant arises from increasing the polarization for a given electric field. The factors determining the polarization apply directly to calculation of the dielectric constant in equation (2.14). Specifically, by increasing the number of dipoles per unit volume, N , and/or the quantity of charge being separated in each dipole, q , the dielectric constant is increased. While the dielectric constant of a given material can be designed and controlled to a certain extent by controlling these parameters, it is not the object of this work to control these parameters in the design of a new material. Rather, the object of this work is to create composites composed of two or more materials which collectively

exhibit the desired properties of high dielectric constant and high dielectric strength. In the process of combining multiple materials into a new composite material, the effective properties of the composite are determined as a weighted average of the properties of the components of the composite. Thus, to develop a high dielectric constant composite material, it is necessary to retain a high average number of dipoles per unit volume, N_{av} , and a high average charge per dipole, q_{av} . The next section discusses models used to calculate the effective dielectric constant of a composite material based on a weighted averaging process of the amount and properties of the composite's component materials.

2.2 The Effective Dielectric Constant of Composites

2.2.1 Background on the Effective Dielectric Constant

Since the high dielectric constant material is developed as a composite, it is by definition composed of more than one material. Since the materials that constitute the composite often have very different physical properties, including electrical properties, prediction and modeling of the effective properties of the composite is dependent on several factors. These factors include the proportions of the individual materials forming the composite, the physical properties of each material, and the coordination of the various materials after being mixed and packed. The multitude of possible combinations of materials and composite arrangements results in a nearly limitless number of potential composite properties, which can make predictive modeling very difficult. However, by limiting the scope of properties of interest to the relative permittivity, it is possible to obtain an approximation that is helpful in designing composites according to the desired specifications.

In high dielectric constant polymer-ceramic composites, the energy storage capabilities of these two main classes of constituent materials are typically very different. Polymers often exhibit excellent dielectric strength, but the dielectric constant is often very low, typically less than 5. Some relatively new classes of polymers exhibit higher dielectric constants, but they are generally only effective at lower frequencies than the VHF and UHF range of interest. Conversely, perovskite ceramic materials, as will be discussed in later sections, are capable of storing very high amounts of electrostatic energy at reduced electric field strengths. These ceramics can have dielectric constants of several hundred to many thousand, depending on the temperature of the material and the frequency of the applied electric fields. Mixing these two very different classes of materials creates a composite with an effective dielectric constant between the two extreme values. Several equations exist to predict the effective dielectric constant of composite systems. To compare the accuracy of the models without the influence of experimental error, a software program was developed to build and simulate three-dimensional dielectric composites.

2.2.2 Mathematical Models

One of the most commonly implemented equations for predicting the effective dielectric constant of dielectric composites is Lichtenecker's logarithmic mixing rule, as given by equation (2.21). Lichtenecker's rule is unique in that it can be applied for an unlimited number of components. It determines the effective dielectric constant of the composite based on the dielectric constant of each component, ε_i , weighted by the volume fraction of the composite that each component occupies, v_i . The effective dielectric constant of the composite is represented as ε_{eff} . As presented in equation (2.21), the

logarithmic terms have a base of ten. The natural logarithm or any other base to the logarithms can be used as long as use of the chosen base is consistent throughout the equation.

$$\log_{10}(\varepsilon_{eff}) = \sum_{i=1}^m v_i \log_{10}(\varepsilon_i) \quad (2.21)$$

Equation (2.22) provides the expanded form of equation (2.21) for a three-component composite consisting of ceramic, polymer, and voids. In this example, the subscript *c* denotes that the corresponding dielectric constant or volume fraction value is for the ceramic content of the composite. Similarly, the subscript *p* represents the polymer contents, and the subscript *void* denotes the values for the voids within the composite.

$$\varepsilon_{eff} = 10^{[v_c \log_{10}(\varepsilon_c) + v_p \log_{10}(\varepsilon_p) + v_{void} \log_{10}(\varepsilon_{void})]} \quad (2.22)$$

Lichtenecker's rule has historically been used extensively due to its correlation with experimental data without a firm theoretical base for its application. However, a recent study derived Lichtenecker's rule from Maxwell's equations based upon conservation of charge for composites with randomly shaped and oriented constituents [3].

There are several other models developed specifically for determining the effective dielectric constant of composites, and the following examples should not be considered an exhaustive list. The following formulas are presented as given in a short review of equations developed for the effective dielectric constant [4]. As will be seen, all of the following models were developed for two-component composites. Unlike the Lichtenecker equation, these models can only account for ceramic and void content, and the common third component consisting of voids is neglected. Following a previously defined variable definition, ε represents the dielectric constant of a particular element,

with the subscripts p , c , and eff indicating that the dielectric constant corresponds to the polymer, ceramic, and effective composite values, respectively [4]. Similarly the symbol v represents the volume fraction of each element as a part of the total composite volume, and the subscripts p and c denote that the volume fraction corresponds to the polymer and ceramic components, respectively. Each of the equations is presented in the following paragraph for reference to the analysis in the next subsection.

Equation (2.23), the Maxwell-Wagner equation, calculates the effective dielectric constant for a two-phase composite, consisting of one ceramic element and one polymeric element.

$$\varepsilon_{eff} = \varepsilon_p \left[\frac{2\varepsilon_p + \varepsilon_c + 2v_c(\varepsilon_c - \varepsilon_p)}{2\varepsilon_p + \varepsilon_c - v_c(\varepsilon_c - \varepsilon_p)} \right] \quad (2.23)$$

Equation (2.24) is the Yamada equation for a polymer-ceramic composite [4, 5]. The variable definitions follow the convention used in the Maxwell-Wagner equation. The variable n is a morphology factor that varies from 0 in the case of all particle connections in parallel to 1 for the case of all connections in series [4].

$$\varepsilon_{eff} = \varepsilon_p \left[1 + \frac{v_c(\varepsilon_c - \varepsilon_p)}{\varepsilon_p + n(\varepsilon_c - \varepsilon_p)(1 - v_c)} \right] \quad (2.24)$$

Finally, the Jayasundere and Smith equation is shown as equation (2.25) [6]. The variables follow the previously-defined convention. The Jayasundere and Smith equation was developed by modifying the Kerner equation to account for interactions between neighboring polarized spheres.

$$\varepsilon_{eff} = \frac{v_p \varepsilon_p + v_c \varepsilon_c \left[\frac{3\varepsilon_p}{\varepsilon_c + 2\varepsilon_p} \right] \left[1 + \frac{3v_c(\varepsilon_c - \varepsilon_p)}{\varepsilon_c + 2\varepsilon_p} \right]}{v_p + v_c \left[\frac{3\varepsilon_p}{\varepsilon_c + 2\varepsilon_p} \right] \left[1 + \frac{3v_c(\varepsilon_c - \varepsilon_p)}{\varepsilon_c + 2\varepsilon_p} \right]} \quad (2.25)$$

Each of these numerical models has been effective in matching the results of specific experimental data. However, variations in the experimental conditions of composite formation and in the minute factors that affect dielectric constant measurements can make comparison of experimental data to numerical models of the effective dielectric constant difficult. Therefore, the implementation of a computer simulation in which all of the factors of composite formation and measurement can be controlled is seen as the advantageous method for comparing numerical models.

2.2.3 Three-Dimensional Electrostatic Modeling

In parallel with the experimental development of high dielectric constant composite materials, a computational effort has been conducted to electrostatically model composites in three dimensions. Due to the many variables that can be adjusted in the development of composite systems, computer models of composites provide a relatively fast method for analysis of the effects of individual variables. In addition to reducing the time needed to predict the properties of a new composite, electrostatic modeling enables the comparison of composites without the effects of experimental or measurement error. Since the accuracy of simulation results can only be as good as the modeling method implemented, the computational and experimental approaches were used in a complementary effort.

A series of simulations were performed to compare the simulated value of the effective dielectric constant with the values calculated from the previously detailed equations. The

virtual composite geometry and constituent material properties were consistent across all simulations. The composite form was defined to be a cylinder with a diameter of 10 μm and a thickness of 5 μm . The filler and void particles were spheres with a radius of 500 nm, so the spherical particles were small enough with respect to the composite form to be able to be randomly placed throughout the volume. Dielectric constants of 1, 1000, and 5 were used for the voids, filler, and matrix materials, respectively. These values were chosen to represent air voids, fillers of a perovskite ceramic, and a polar polymer.

In the first simulations, the volume percentage of the filler was varied from 5 to 50% in steps of 5%. Simulations at volume percentages greater than 50% were not possible due to the packing density limitations of randomly packed spheres. The binder properties were kept constant in each simulation, and no voids were initially included. The simulated data are plotted as points in Figure 5. The curves were plotted by applying equation (2.21) and equations (2.23)-(2.25), including the actual volume data returned for each component after the composite was constructed.

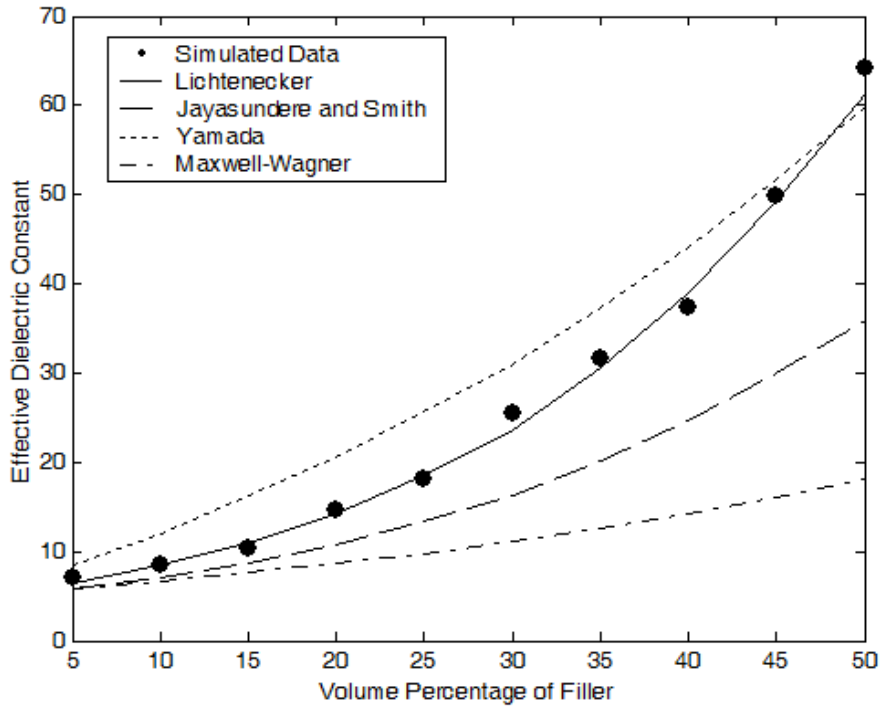


Figure 5. Effective dielectric constant for variable percentage filler and matrix dielectric constant

From Figure 5, it is apparent that the Lichtenecker model closely tracks the simulated data. The Yamada morphology factor of equation (2.23) was selected to match the simulated data as best as possible. The morphology factor used in the Yamada plot of Figure 5 was 0.075. The Jayasundere and Smith model underestimates the effective dielectric constant at all points, and the Maxwell-Wagner equation provides the worst fit for the simulated data. The accuracy of each model is plotted in Figure 6 as the percentage difference of the effective dielectric constant from the simulated data. The Maxwell-Wagner underestimates the simulated data by nearly 70% at high filler loading levels. The Lichtenecker model, however, remains within $\pm 8\%$ through the entire range.

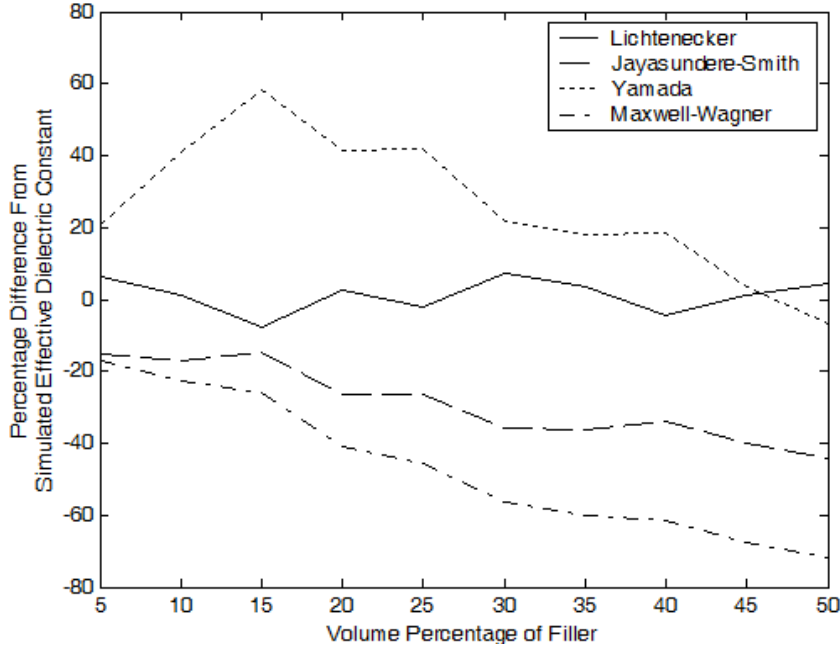


Figure 6. Percentage difference of the simulated effective dielectric constant from calculated values

In general, all of the models except the Lichtenegger model would underestimate the effective dielectric constant from that obtained through simulation. Although the Yamada morphology factor was chosen such that it matches the simulated results near 5% and 50% and overestimates in other areas, a more appropriate morphology factor of 0.5, representing the combination of series and parallel particle connectivity of randomly placed fillers, would also greatly underestimate the simulated results. Some previous experimental studies have found agreement between measured data and the models that do not match the simulated results. One potential explanation for this mismatch between experimental data and the models is the influence of voids, which are unaccounted for in most models. In real polymer-ceramic composites, voids are nearly impossible to completely eliminate. Voids can also be difficult to measure directly, so their presence and significance are often overlooked. Another set of simulations was conducted to demonstrate the effect of voids on the effective dielectric constant of a composite with a

low filler loading. The composite again consisted of a matrix material with a dielectric constant of 5, 500 nm filler particles with a dielectric constant of 1,000, and 500 nm void particles with a dielectric constant of 1. The virtual composite had a thickness of 5 μm and a diameter of 10 μm . The simulation runs varied the volume percentage of voids displacing the matrix material from 0% to nearly 30%. Due to the upper volume limit on the total filler and void content, the volume percentage of fillers with a dielectric constant of 1,000 was kept at 10% in each simulation.

The data were plotted as the percent change in the effective dielectric constant when compared with the baseline case with 0% voids in Figure 7. The absolute value of the percentage change steadily increases with increasing voids to the point that the effective dielectric constant was decreased by more than 20% through the addition of 28.7% by volume voids. The reduction of the effective dielectric constant is just one of the negative effects of voids, along with increasing the potential for dielectric failure due to insulation breakdown.

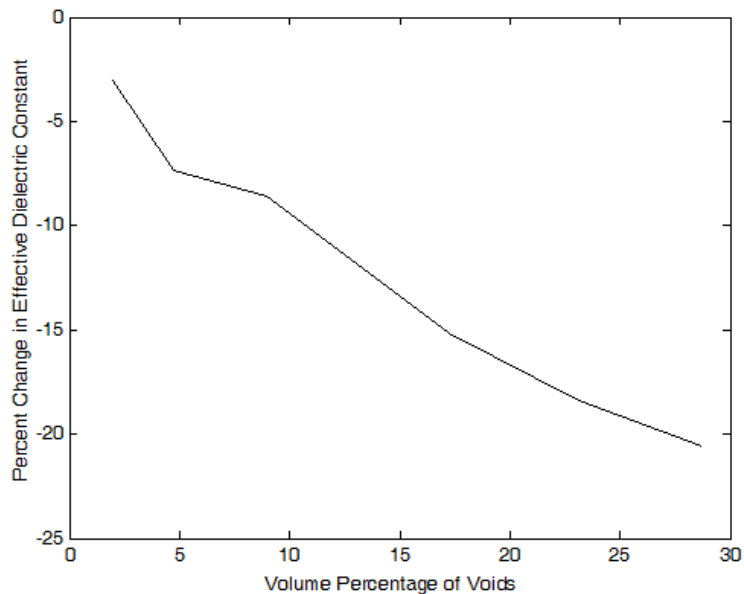


Figure 7. Percentage change in the effective dielectric constant between a composite with and without voids

2.3 Particle Packing Density

As described by Lichtenecker's Rule, the effective dielectric constant of a composite material is equal to the weighted sum of the logarithm of the dielectric constants of each constituent material of the composite [3]. The logarithmic terms are weighted by the volume fraction of the composite occupied by that particular material. Therefore, to maximize the effective dielectric constant of the composite, the material with the highest dielectric constant must occupy the largest possible volume fraction within the composite. Perovskite ceramics are the materials with the highest dielectric constant included in the composite, so the fractional volume of the ceramics must be maximized to obtain the highest effective dielectric constant possible.

The question of how to most tightly pack a number of solids in a given volume has been studied in many theoretical and experimental contexts. Considering the packing of spheres of equal size in a given volume, it has been shown that the greatest density possible through regular packing of spheres is approximately 74.05% [7]. For irregular packing, meaning the compression of spheres added randomly to a given volume, it has been shown that the densest packing of equally-sized spheres is approximately 64% [7]. Since irregular packing best describes the methods by which a composite can be realistically formed, the maximum density that could be achieved with a single size of ceramic spherical particles is 64%. However, the density can be increased further both by the realistic fact that the actual ceramic particles are irregular in shape and through the use of multiple sizes of particles.

The problem of obtaining the maximum density for multiple discrete particle sizes was analyzed mathematically by Furnas in publications from 1929 and 1931 with an

accompanying experimental investigation by Anderegg [8-10]. Most of the following concepts and discussion in this section are based on the analyses presented by Furnas [8, 9]. Some equations have been restructured to solve for the parameters of greatest interest for application in the composites. The issue of mixing multiple particle sizes together to form a final mixture with higher density than any of the individual components alone will first be approached for the bimodal case. In the following definitions and equations, the subscript x is used as any positive number corresponding to a given set of particles. The subscript can only apply to one set of particles for any one equation. By definition, the particle set denoted 1 is the largest particle size, corresponding to a particle dimension d_1 [m], and successively smaller particles are denoted by increasing numbers. Furnas defines particles to be the same size if they cannot be separated through screens differing by a factor of $\sqrt{2}$ [9].

A set of particles of a given size is defined to have a common material density, ρ_{Mx} [kg/m^3]. The material density is the actual density of the material as opposed to the density of multiple packed particles. When the particles are packed into a container, a fraction, v_x , of the total volume of the bed of particles, V_{Tx} [m^3], remains unfilled by particles. Throughout this discussion, reference to a volume fraction of voids refers to the voids within a bed of packed particles. The individual particles themselves are considered fully dense with a density equal to the material density. The lowercase letter v denotes void fractions whereas the capital letter V denotes volumes. The total volume of the bed is partially filled by the particles and partially left unfilled by spaces considered voids. If a mass of particles, m_x [kg], is packed into a container, several relationships can be mathematically defined. First, the volume occupied by the particles themselves, which is

a distinct quantity from the volume filled by the particles and voids, can be defined as V_x [m³].

$$V_x = \frac{m_x}{\rho_{Mx}} \quad (2.26)$$

The void fraction, v_x , is then defined using equation (2.27).

$$v_x = 1 - \frac{V_x}{V_{Tx}} \quad (2.27)$$

Due to the volume occupied by the voids, the apparent density of the bed of particles will be less than the material density. The apparent density or bulk density, ρ_{Bx} [kg/m³], of the bed of particles can thus be defined using equation (2.28).

$$\rho_{Bx} = \frac{m_x}{V_{Tx}} \quad (2.28)$$

The material density and bulk density can be related through the void fraction.

$$\frac{\rho_{Bx}}{\rho_{Mx}} = 1 - v_x \quad (2.29)$$

Consider a bed of packed particles with dimension d_1 [m], material density ρ_{M1} [kg/m³], and void fraction v_1 filling a total volume V_{T1} [m³] as previously defined. If a second, much smaller set of particles with dimension d_2 [m], material density ρ_{M2} [kg/m³], and void fraction v_2 is added to the first bed of particles, the density of the mixture can often be increased, resulting in a smaller void fraction for the mixture. Ideally, the second set of particles would be infinitely small such that they completely fill the voids of the first set of particles. In all real systems, the particles constituting the second set will have finite dimensions, and the packing of the second set of particles will also contain voids. Figure 8 is a simplified illustration of the previously described cases of a bed of large particles and the large bed filled with ideal and realistic smaller particles.

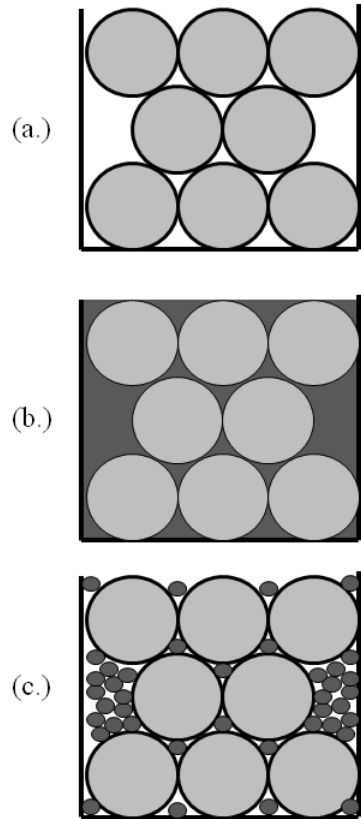


Figure 8. Illustrations of packing (a.) a single particle system, (b.) ideal binary system, and (c.) realistic binary system

To maximize the density of a binary system, the appropriate relative mass percentages of large and small particles must be determined. The relative mass fraction of either the large or small particles is varied from 0 to 1 to cover the range of possible binary combinations. In the following graphical analysis, the void fractions for both large and small particles are arbitrarily defined to be 0.5, and it is assumed that both large and small particles have the same material density. The ratio of small to large particle sizes is 0.0001. The specific volume [m^3/kg] of the composite, which is defined as the reciprocal of the composite density, is used for graphical reasons that will become apparent.

For a composite in which 100% of the mass is from small particles and 0% is from large particles, the specific volume of the mixture will simply be the specific volume of a bed of small particles. This specific volume is equal to the reciprocal of the bulk density

of the small particles and is labeled point 1 on the ordinate of Figure 9. Similarly, if the composite were composed of 100% large particles and 0% small particles, the specific volume of the mixture would be the equal to the reciprocal of the bulk density of the large particles. The specific volume corresponding to 100% large particles is labeled point 3 in Figure 9. Considering a system defined by point 3, if infinitely small particles were gradually added to the voids of the large particles, the total mass of the system would go up without any increase in the total volume. The specific volume would follow the solid line from point 3 towards point 2. The density would reach a maximum when the infinitely small particles had completely filled the voids of the large particles. At this point, the specific volume of the composite would be equal to the reciprocal of the material densities of the two sets of particles. This point is represented by point 2 in the normalized graph of Figure 9. The dependence of the location of point 2 with respect to the fraction of total mass composed of large particles will be described later. The dotted line in Figure 9 connecting points 1 and 2 is analogous to the solid line between points 3 and 2. If a bed of small particles has large particles gradually added to it such that the mass of the system is increased without increasing the system's volume, the specific volume will decrease until it reaches the point at which there are no remaining voids and the specific volume of the composite is equal to the reciprocal of the particles' material density. Whereas the lines between points 1 and 2 and points 2 and 3 represent the idealized case in which the small particles are infinitely smaller than the large particles, the line between points 1 and 3 represents the worst-case scenario in which the small particles are equal in size to the large particles. In this case, since the material and bulk densities of the composites are the same, the addition of particles from one set to a

system composed exclusively of particles from the other set would not alter the specific volume. As mathematically described later, the line between points 1 and 3 is not necessarily parallel to the abscissa. The shaded triangle formed by points 1, 2, and 3 in Figure 9 represents the range of composite densities possible with this binary system.

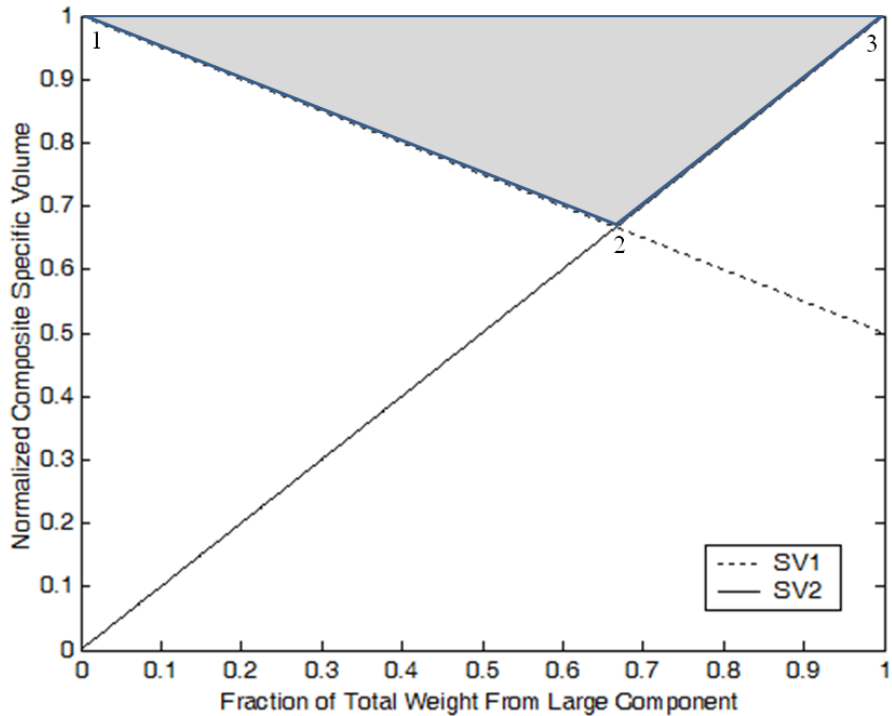


Figure 9. Possible normalized densities in a binary system with 50% voids in a bed of each component

The ideal minimum specific volume represented by point 2 cannot be reached in a real system because any real set of small particles will have finite size and be unable to completely fill the voids of a larger set of particles. However, the fraction of the total mass for each component in an ideal system of maximum density is still very useful to design a real system with an optimized density. To determine the proportions of each component at ideal maximum density, the equations representing the solid and dotted lines of Figure 9 can be used. The mass of the large and small components are defined to

be m_1 [kg] and m_2 [kg], respectively. The fraction of the total weight contributed by the large component can then be defined as Z_1 with equation (2.30) [9].

$$Z_1 = \frac{m_1}{m_1 + m_2} \quad (2.30)$$

The line represented as $SV1$ [m^3/kg] in Figure 9 can be written mathematically based on its previous description. Starting with a composite of 100% small particles, large particles are added such that the volume of the composite does not increase. This describes a line between the reciprocal of the bulk density of the small particles and the reciprocal of the material density of the large particles, as shown in equation (2.31) [8].

$$SV1 = \frac{1 - Z_1}{\rho_{M2}(1 - v_2)} + \frac{Z_1}{\rho_{M1}} \quad (2.31)$$

Equation (2.31) represents an ideal composite and a lower limit of possible specific volume values for low values of Z_1 . However, at some point the line crosses into a region in which it describes a purely theoretical composite. For 100% large particles, $SV1$ predicts a composite specific volume equal to the specific volume of the material without any voids. Since it is known that a bed of all large particles contains voids, this point on $SV1$ is impossible to achieve even in an ideal system. Therefore, $SV2$ [m^3/kg] is necessary to establish a lower limit of possible specific volume values for relatively high values of Z_1 . This lower limit can be drawn as a straight line from the origin to the specific volume at 100% large particles [8]. The line represented as $SV2$ can be described by equation (2.32) [8].

$$SV2 = \frac{Z_1}{\rho_{M1}(1 - v_1)} \quad (2.32)$$

Lines $SV1$ and $SV2$ are the two lower limits for the range of possible specific volume values. The point of maximum density of the ideal system, represented as point 2, can be determined as the intersection of the two lines, as shown in equation (2.33) [8].

$$\frac{1 - Z_1}{\rho_{M2}(1 - \nu_2)} + \frac{Z_1}{\rho_{M1}} = \frac{Z_1}{\rho_{M1}(1 - \nu_1)} \quad (2.33)$$

Equation (2.32) can be solved for the value of Z_1 that creates the ideal composite of maximum density, and the result is given as equation (2.34).

$$Z_1 = \frac{\rho_{M1}(1 - \nu_1)}{\rho_{M1}(1 - \nu_1) + \nu_1 \rho_{M2}(1 - \nu_2)} \quad (2.34)$$

The upper limit of possible specific volume values, represented as the line between points 1 and 3 in Figure 9, can be determined mathematically as a straight line connecting the reciprocals of the bulk densities of the small and large particles. The upper limit, denoted $SV3$ [m^3/kg], can be expressed as equation (2.35). The upper limit is not parallel with the abscissa if the material densities or void fractions of the large and small particles differ [8].

$$SV3 = \frac{1}{\rho_{M2}(1 - \nu_2)} \left[1 + Z_1 \left(\frac{\rho_{M2}(1 - \nu_2)}{\rho_{M1}(1 - \nu_1)} - 1 \right) \right] \quad (2.35)$$

With the limits of all possible values for the specific volume established through analysis of an ideal system in which the ratio of small to large particle dimensions goes to zero, values for real systems can be determined when considering systems with finite ratios of small to large particle dimensions. In the ideal system with infinitely larger large particles than small particles, the voids of the large particles are perfectly filled with small particles without increasing the volume of the composite. As a result of the finite ratio between small and large particles, imperfect packing occurs. Not only are voids present in the filled voids of the large particles, but the volume of the composite can be

increased through the addition of small particles. Furnas introduced a factor y that accounts for the decrease in volume that occurs when two particle sizes are thoroughly mixed with respect to the volume of each of the particle sizes when unmixed [9]. When the particle sizes are equal, y is equal to zero, and the composite volume has been increased by the volume of the bed of small particles. When the smaller particle size is infinitely small with respect to the large particle size, y is equal to 1, and the volume of the composite is equal to the volume of the bed of large particles. There is no known theory to accurately describe how y varies between zero and one, and the variation of y with respect to the ratio of largest to smallest particle size can be dependent on the morphology of the particles. Therefore, equations for y are generally determined experimentally. From experimental data, Furnas obtained equation (2.36) as a curve fit to data obtained on the degree of compaction upon mixing with respect to the ratio of particle sizes [8, 9]. The variable n is defined as one less than the total number of particle sizes included in the composite [9]. For the binary system currently under consideration, the variable n is simply equal to 1. The degree of compaction, y , is a function of the ratio of the smallest particle size, d_{n+1} [m], to the largest particle size, d_1 [m].

$$y = 1 - 2.62 \left(\frac{d_{n+1}}{d_1} \right)^{\frac{1}{n}} + 1.62 \left(\frac{d_{n+1}}{d_1} \right)^{\frac{2}{n}} \quad (2.36)$$

By analyzing the trend line used by Furnas to obtain equation (2.36) with the aid of computational curve fitting, a more precise relationship was obtained, as given in equation (2.37). Additional trend lines have been produced by other researchers for specific particle morphologies. Those trend lines can be interchanged to calculate the factor y when the conditions under which they were measured correspond with the system under design.

$$y = 1 - 2.41 \left(\frac{d_{n+1}}{d_1} \right)^{\frac{1}{n}} + 0.17 \left(\frac{d_{n+1}}{d_1} \right)^{\frac{2}{n}} + 3.26 \left(\frac{d_{n+1}}{d_1} \right)^{\frac{3}{n}} - 2.02 \left(\frac{d_{n+1}}{d_1} \right)^{\frac{4}{n}} \quad (2.37)$$

By including the effects of the ratio of particle sizes on particle packing, it is evident that the real values of composite specific volume vary from the ideal case of the greater value from either equation (2.31) or (2.32) to the maximum specific volume of equation (2.35) by the factor y . Therefore, equations (2.31) and (2.32) can be modified to include the factor y to predict real values of the composite specific volume. Equation (2.31) for $SV1$ can be modified to equation (2.38) [8, 9].

$$SV1 = \frac{1}{\rho_{M2}(1 - v_2)} \left[1 + Z_1 \left(\frac{\rho_{M2}(1 - v_2)}{\rho_{M1}(1 - v_1(1 - y))} - 1 \right) \right] \quad (2.38)$$

When y is equal to 1 as in the ideal situation, equation (2.38) reduces to equation (2.31), and when y is equal to 0 for a system of equal particle sizes, the equation reduces to equation (2.35). Equation (2.32) can similarly be modified to equation (2.39) [8, 9].

$$SV2 = \frac{1}{\rho_{M2}(1 - v_2)} \left[1 - y + Z_1 \left(\frac{\rho_{M2}(1 - v_2)}{\rho_{M1}(1 - v_1)} - 1 + y \right) \right] \quad (2.39)$$

When y is equal to 1 as in the ideal case, equation (2.39) reduces to equation (2.32), and when y is equal to 0 for a system of equal particle sizes, equation (2.39) reduces to equation (2.35). Equations (2.38) and (2.39) can be set equal to each other to determine the value of Z_I for maximum density in systems with non-ideal packing.

$$Z_1 = \frac{y}{\frac{\rho_{M2}(1 - v_2)}{\rho_{M1}} \left[\frac{1}{1 - v_1} - \frac{1}{1 - v_1(1 - y)} \right] + y} \quad (2.40)$$

In the ideal case in the limit as y approaches 1, equation (2.40) reduces to the ideal equation for Z_I presented as equation (2.34). As y is reduced towards the limit of zero, Z_I approaches the value 0.5. This result is intuitive in that as the difference in particle

sizes becomes less and less, each particle size contributes approximately half of the total weight of the composite. Equation (2.40) is undefined for a y value of zero, but it is understood that when the particles are exactly the same size, the relative proportions can be chosen as any possible value.

Implementing equations (2.38) and (2.39), values of the specific volume of practical systems with finite values of $\left(\frac{d_{n+1}}{d_1}\right)$ can be produced for binary systems in any proportion. Figure 10 shows the theoretical results of the same binary system used to produce Figure 9 with specific values for the ratio $\left(\frac{d_{n+1}}{d_1}\right)$. For a very small value of $\left(\frac{d_{n+1}}{d_1}\right)$, 0.0001, the lines approach the lines formed in the ideal case. For intermediate values in which the large particle is only 400%, 200%, or 33% larger than the small particle, the decrease in specific volume achieved by mixing the two component sizes is significantly less than that achieved in the ideal case. Additionally, as the size ratio increases towards 1, the fraction of total weight contributed by the large component tends towards 0. Therefore, to best improve the composite density through multimodal packing, it is generally best to have particle sizes differ by an order of magnitude or more.

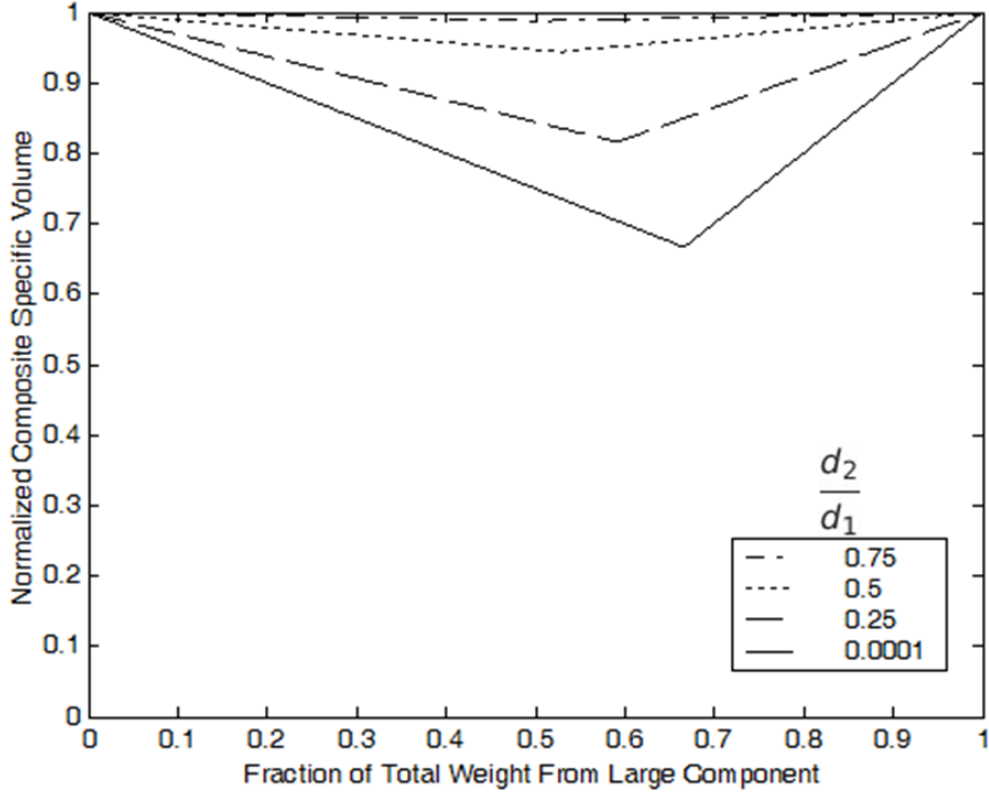


Figure 10. Theoretical specific volume for practical ratios of small to large particle sizes. A bed of each particle size is assumed to be 50% voids by volume.

For simplicity, Furnas' analyses of practical systems concentrate on those in which the void fractions and material densities for the large and small particles are equal [9]. When the material densities of particles of both sizes are equal, the mass fraction and volume fraction of a particle size are identical. For these systems, equation (2.34) reduces to equation (2.41), where v is the common value of the void fractions.

$$Z_1 = \frac{1}{1 + v} \quad (2.41)$$

While previous analysis was limited to a bimodal system. However, Furnas has shown that the analysis can be extended to higher order systems [9]. For a system in which each of the particle sizes has the same volume fraction of voids, the ratio of successive particle sizes for maximum density is the same for all successive particle sizes. This relationship can be mathematically written as equation (2.42) where d_x [m] is the dimension of a

particular particle size [9]. The largest and smallest particle sizes are selected according to the limitations of the application, and the intermediate sized particles can be determined with equation (2.42).

$$\frac{d_3}{d_2} = \frac{d_2}{d_1} = \frac{d_{n+1}}{d_n} \quad (2.42)$$

From equation (2.42), the middle particle size, d_2 , of a trimodal system can be determined from the large, d_1 , and small, d_3 , particle sizes with equation (2.43) [9].

$$d_2 = \sqrt{d_1 d_3} \quad (2.43)$$

In the preceding bimodal discussion, Z_l represented the mass fraction of the large particles. Under the assumption that the material density and void fraction of all particle sizes are the same, the mass fraction is equal to the volume fraction. With this assumption, the mass fraction and volume fraction of the large particles in the bimodal case can both be calculated from equation (2.41), and the mass fraction and volume fraction of the smaller particles is equal to $1-Z_l$. The mass fractions and volume fractions of particle sizes beyond the first two components can be calculated when it is acknowledged that the small particles of a bimodal system will not perfectly fill the voids of the large particles. Again assuming that all of the particle sizes in the multimodal system have the same fraction of voids and material density, it can be shown from Furnas' discussion that the ratios of successive values of Z_l are the same [9]. This relationship is shown in equation (2.44). As seen in the right-hand side of equation (2.44), this ratio can be determined from the previously calculated value for Z_l .

$$\frac{Z_2}{Z_1} = \frac{Z_3}{Z_2} = \frac{Z_{x+1}}{Z_x} = \frac{1 - Z_1}{Z_1} \quad (2.44)$$

Using this ratio and the definitions of Z_1 and Z_2 as described in the previous paragraph, equation (2.45) can be derived for the mass fraction and volume fraction of any component, Z_x .

$$Z_x = (1 - Z_1) \left(\frac{1 - Z_1}{Z_1} \right)^{x-2} \quad (2.45)$$

Furnas has shown through a geometrical progression that the total absolute volume, $V_{1:n+1}$, of all of the particles in the composite can be calculated as equation (2.46) [9]. This volume applied to the particles only and excludes any voids remaining between the particles. Since this is an absolute volume, it is defined on a per unit volume basis and is unitless.

$$V_{1:n+1} = \frac{1 - v^{n+1}}{1 + v^2} \quad (2.46)$$

The total absolute volume including the volume of the voids can be defined as equation (2.47) [9]. The symbols ρ_M [kg/m^3] and ρ_B [kg/m^3] represent the common values of the true material mass density and apparent bulk density, respectively.

$$V_T = \frac{\rho_M}{\rho_B} [V_{1:n+1} - y(V_{1:n+1} - Z_1)] \quad (2.47)$$

The volume fraction of voids, v_{voids} , can be determined based on equations (2.46) and (2.47).

$$v_{voids} = \frac{V_T - V_{1:n+1}}{V_T} \quad (2.48)$$

Since the assumption of a common material mass density and volume fraction is applied to all particle sizes, the absolute volume can also be considered as an absolute mass term. Therefore, the relative mass or volume of any component can be calculated as the ratio of the values determined with equations (2.45) and (2.46). When manufacturing

a composite, it is easiest to determine the mass of each component size, so equation (2.49) is used to calculate the mass of any component relative to the total mass of all particle sizes, m_T [kg]. Since Z_1 is only a function of ν under the assumption of a common material mass density and void fraction, the masses can be calculated based on the volume fraction and total number of particle sizes.

$$\frac{m_x}{m_T} = \frac{(1 - Z_1) \left(\frac{1 - Z_1}{Z_1} \right)^{x-2}}{\frac{1 - \nu^{n+1}}{1 + \nu^2}} \quad (2.49)$$

While the preceding discussion outlines the theoretical framework for multimodal particle packing, the following discussion details how a multimodal particle system can be designed. The first issue examined is whether to implement 2, 3, or 4 particle sizes in the system. The effects of particle sizes can be graphically analyzed by plotting the volume fraction of voids based on equation (2.48). Given the variables of equation (2.48), the volume fraction of voids is ultimately dependent on the volume fraction of voids for all of the components, the particle size ratio $\left(\frac{d_{n+1}}{d_1}\right)$, and the total number of particle sizes $n+1$. Figure 11 shows the volume percentage of voids with respect to the particle size ratio for binary, ternary, and quaternary systems in which the volume percentage of voids in each particle size alone is 40%. Similar graphs can be produced for other initial volume percentages of voids. Figure 11 shows that for a ternary or trimodal particle system with initial voids of 40% at each particle size, the voids can be reduced to approximately 10% by volume when the size ratio of largest to smallest voids is approximately 1,000.

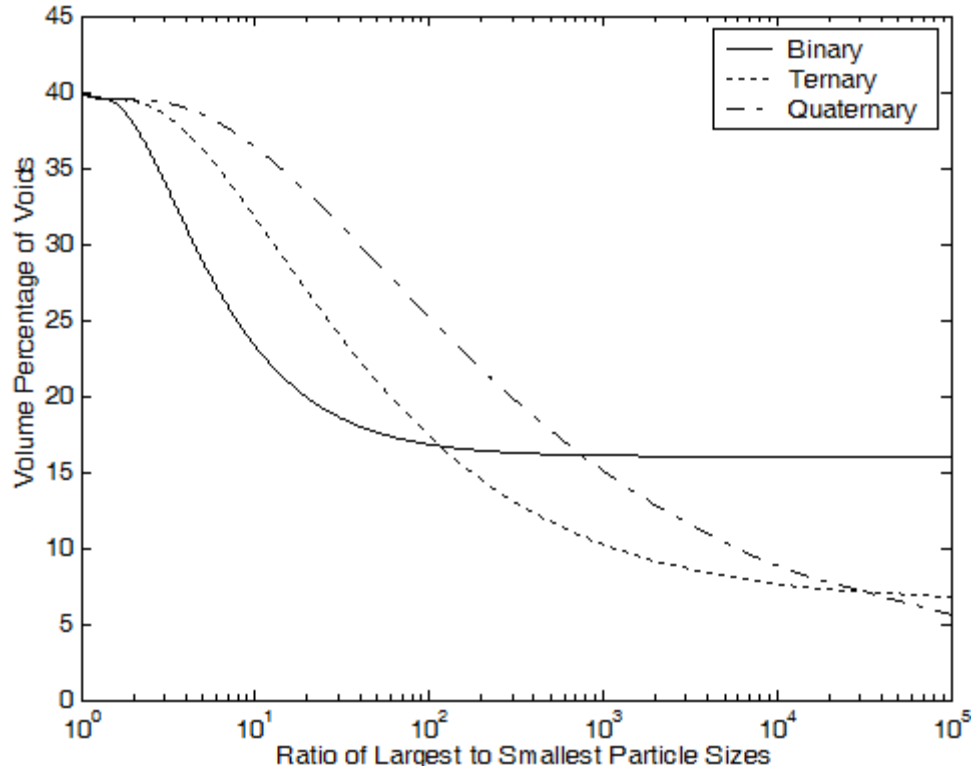


Figure 11. Volume percentage of voids vs. ratio of particle sizes for particles with 40% voids in a packed bed of each size

Figure 12 shows the volume percentage of voids with respect to the ratio of largest to smallest particle sizes for particles with 30% voids by volume. Again the ternary or trimodal particle distribution provides the densest particle packing for ratios of less than 10,000. At a particle size ratio of 1,000, the volume percentage of voids for a trimodal system can theoretically be reduced to nearly 5%.

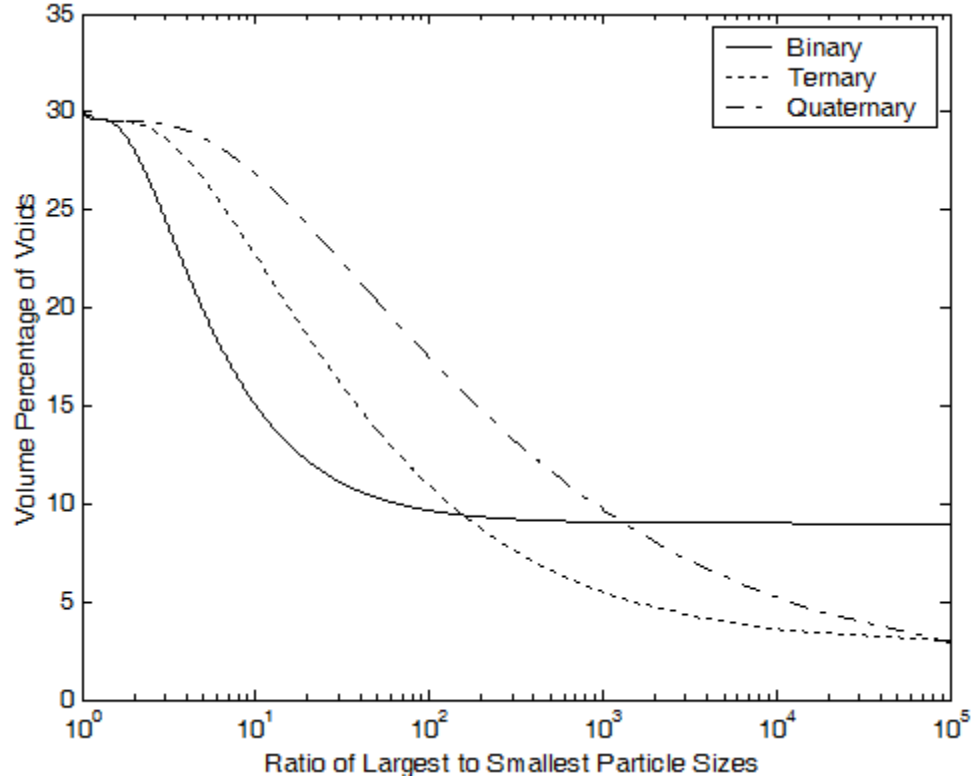


Figure 12. Volume percentage of voids vs. ratio of particle sizes for particles with 30% voids in a packed bed of each size

From Figure 11 and Figure 12, the ratio of largest to smallest particle sizes was chosen to be 1,000. The design of this ratio leveraged one of the unique requirements of this work. Since the composites under development were intended to be produced in relatively large bulk amounts for incorporation into antennas rather than as very thin films, larger particle sizes could be included. Extending the size ratio beyond 1,000 becomes impractical, and the rate of reduction of the void content diminishes when further increasing size ratio.

The lower limit of the smallest particle size is determined by the practical size of nanoparticles that can be kept from agglomerating and effectively incorporated into the composite. The desired nanoparticle size was designed to be 50 nm, but any nanoparticles less than 100 nm would be acceptable. There is little advantage to going to even smaller nanoparticles, and there is evidence that when perovskite nanoparticles are reduced below

a certain level, the lattice structure changes, resulting in a reduction of the nanoparticles' dielectric constant.

With a small particle size set at 50 nm, the designed size ratio dictates that the largest particles should be 50 μm . To determine if particles on the order of 50 μm are reasonable, limitations presented by the dimensions of the composite to be formed and dielectric strength or the wavelength of the waves propagating through the material must be considered. For dielectric strength considerations in thin films, a maximum particle size equal to 1/10th of the film thickness has been chosen such that dielectric failure in a single particle does not cause dielectric failure of the entire film. In thick composites, the size of the largest particles has been limited to a few hundred microns to ensure homogeneity of the composite, especially for use at high frequency. For the composite to appear homogenous to an electromagnetic wave propagating through it, the largest particles should be much smaller than the wavelength of the wave in the material. At the high frequency end of the bands considered, a 3 GHz signal will have a wavelength in free space of approximately 0.1 m. From equation (1.4), the wavelength will be decreased proportionally by the square root of the permittivity. Particle dimensions up to 100 μm are a factor of ten or more smaller than the wavelength of a wave propagating in a material with a dielectric constant up to 10,000. Thus, for the range of dielectric constants and frequencies considered in this work, the restriction on the largest particle size based on dielectric strength considerations is dominant.

The calculated large particle size on the order of 50 μm was determined to be reasonable. For composites with a thickness of 1 mm, a single 50 μm particle only constitutes 5% of the thickness. To maintain homogeneity, a standard was determined

that no single particle should be greater than 10% of the composite thickness. As described in Chapter 4, the manufacturing process of the large particles did not produce a uniform size of particles but rather a distribution of large particle sizes was obtained. Large particles ranging from around 40 μm up to 212 μm were often used.

Implementing equation (2.43), the size of the intermediate particles is calculated to be approximately 1.6 μm . This corresponds to a size ratio of $\sqrt{1,000}$ or 31.6 between particle sizes. The intermediate particles were obtained commercially at a size rated as less than 3 μm . Although the theoretical analysis concentrated on uniform particle sizes for simplicity, a distribution of particle sizes can increase the packing density even further. Thus, the distribution of particle sizes in the large and intermediate sizes was beneficial to the particle packing density.

To determine the volume percentage of voids in a compacted bed of each of the three particle sizes, each particle size was pressed into a disk without binder or any other additive. Although these disks were very fragile, the mass and volume of the disks were determined to calculate the mass density. With the known density of the ceramic, the volume percentages of voids and ceramic were calculated. Table 1 summarizes the results of this experiment. Two sets of large particles were evaluated due to differences in the source material used to produce them. The volume percentages of voids were 25.97% and 33.48%. While 25.97% is a lower volume percentage of voids than expected, the value is likely lowered due to the incorporation of smaller particles as a result of the milling process used to produce the particles. The intermediate size particles and nanoparticles had volume percentages of voids of between 40% and 45%. All of these values fall within a useful range for incorporation in a trimodal distribution. The values around 30%

and 40% volume of voids fit well with the graphs of Figure 11 and Figure 12, which were used to determine the particle size ratio.

Table 1. Density of compacted beds and particles and the corresponding volume percentages of voids and ceramic

	Bulk Density (g/cm ³)	Volume Percentage of Voids	Volume Percentage of Ceramic
Large Particles 1	4.46	25.97%	74.03%
Large Particles 2	4.00	33.48%	66.52%
Intermediate Particles	3.54	41.16%	58.84%
Nanoparticles	3.14	44.72%	55.28%

From the preceding analysis and equation (2.49), the mass percentage of each component was calculated. The calculations assumed that the volume percentage of voids for each individual particle size was 30%, which corresponds to the value calculated for the large particles. The weight percentages of the large, intermediate, and small particles were calculated to be 72%, 21%, and 7%, respectively. This distribution was applied in the trimodal composites reported in this work.

2.4 Homogeneity

For a composite's properties to be consistent throughout the material, the proportions of the constituent materials must be the same in any small volume throughout the composite, the constituent materials must be evenly dispersed, and the constituents must be packed to the same density throughout the composite. A composite in which these conditions are met is considered homogenous, and the composite's properties are the same in any small volume throughout the material. Creating a homogenous composite is required so that the dielectric constant, dielectric strength, and mechanical integrity of the composite are the same throughout the material. If there are significant variations in the

dielectric constant between different regions of the composite, the propagation of electromagnetic waves through a device formed with the composite may be altered in such a way that the device's performance is degraded. This effect could be manifested as scattering due to discontinuities in the impedance of the composite, causing reflections and reducing the radiated output of an antenna. If the dielectric strength of the composite is reduced due to inhomogeneous regions of the composite, the electrically insulating function of a device formed with the composite could catastrophically fail, causing the device to be unusable at high voltage. Lastly, if the mechanical integrity is compromised by inhomogeneous regions, the composite could suffer chipping, flaking, or cracking. For consistency in these three material properties and several others, the homogeneity of the composite is critical to its functions.

The first two conditions, requiring equal proportions of the constituent materials and even dispersion, can both be satisfied through mixing procedures and surface preparation. For adequate mixing, forces strong enough to break the inter-particle attraction caused by the high surface area of very small particles must be overcome. In particular, van der Waals forces between particles can cause attraction between particles that would result in insufficient mixing. When particles group together due to these small-scale forces, agglomerates can form that create inhomogeneous regions and degraded composite properties. Attractive forces between nanoparticles can result in the formation of agglomerates and aggregates [11]. Agglomerates are characterized by the assembly of primary particles that only contact at specific points on their surfaces [11]. The few points of contact between agglomerates result in relatively weak bonds that can be easily broken. However, aggregates are formed when contact between primary particles is made

along an entire surface area, and the strength of aggregate bonds is much greater [11]. This proposal will generally refer to agglomerations formed in loosely-bound clusters, but the methods proposed in the following sections could be applied for aggregates as well. Figure 13 shows a scanning electron micrograph of a large agglomeration. Primary particles with 50 nm dimensions have assembled to agglomerates on the order of tens of microns.

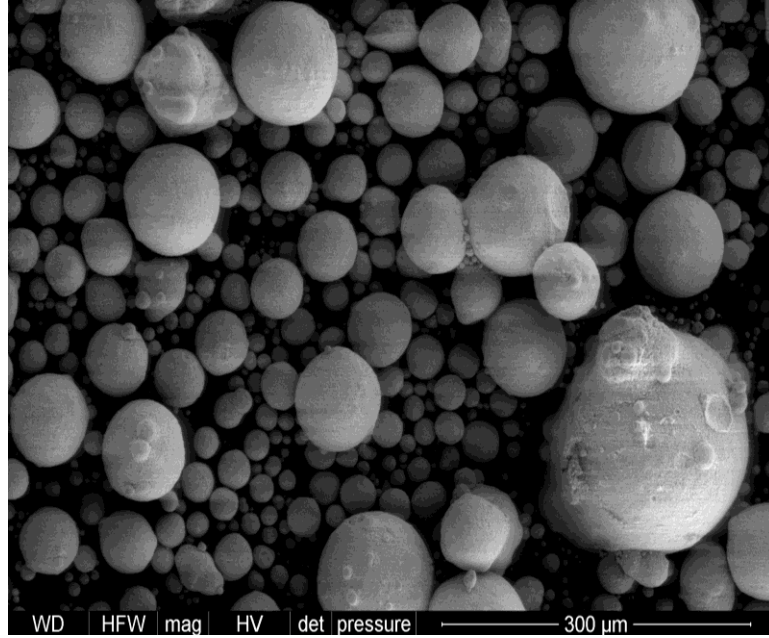


Figure 13. Large agglomerates formed by 50 nm primary particles

The attractive forces that drive the formation of agglomerates are van der Waals forces, which were first detailed during the study of dense gases [12]. The van der Waals force is generally defined as the weak attractive force caused by electric dipole interactions that can lead to stable clusters [13]. The van der Waals force is distinct from stronger types of bonding, such as covalent, ionic, and metallic bonding. The force is often used to describe any weak intermolecular force resulting from permanent dipoles, induced dipoles, and the electromagnetic interaction between two particles and the medium separating them.

The van der Waals force is dependent on the dielectric permittivity of the particles and the medium between the particles [12]. The van der Waals force is present due to electromagnetic interfaces formed as a result of the difference in permittivity between the particles and the medium between particles [12]. Although the particles may be electrically neutral, there will be variations in charge distribution and charge movement due to electron clouds, dipole rotation or vibration, or ion and electron mobility [12]. At small separation distances, the electromagnetic fields created by changes in charge distribution and movement will influence the charge distribution and movement of neighboring particles. The van der Waals force is the result of the lowest system energy occurring when there is mutual charge configuration and movement between the particles [12]. The resonance obtained between the particles' interacting electromagnetic fields is only effective at very small distances due to the small fields and finite speed of wave propagation. Therefore, van der Waals forces are not present on the macroscopic scale.

Several methods have been developed to reduce the size of agglomerates to primary particles and obtain an even dispersion of nanoparticles. The deagglomeration methods share the common goal of mechanically adding energy at a localized level to disrupt the weak bonding between nanoparticles. Deagglomeration is often accompanied by the application of a surfactant or dispersing agent to prevent reagglomeration [14]. Deagglomeration methods include stirring, aerosol impaction, ultrasonic baths, ultrasonic horns, milling, turbulent flow, and homogenization among others [11, 15-17]. Due to the widespread use of milling and ultrasonic horns, their use is described. The principles of operation can be extended to many of the other deagglomeration techniques.

In ball milling, nanoparticle agglomerates are placed in a rotating cylinder with balls. The cylinder and balls are made from a hard material, such as metal or ceramic. As the cylinder rotates, the agglomerates are subjected to forces from the balls and the cylinder walls that break the weak bonds joining the primary particles. The forces can result from static loading, friction, or impact [11]. Milling can be conducted in a wet or dry state, and surfactants are often added to prevent reagglomeration. Milling can reduce particle size down to the dimensions of the primary particle. However, milling is a slow process that can require hours or days to process even relatively small batches of fine particles. Additionally, since the forces on the agglomerates also affect the milling media, it is possible to contaminate the sample with particles from the mill.

Ultrasonic horns apply high frequency pressure waves to a solution containing agglomerates. As a low pressure wave passes through a volume, microscopic bubbles are formed in the solution. When the high pressure wave passes through the same volume, the bubbles abruptly collapse in a process called cavitation [18]. This violent expansion and contraction at very small scales provides energy for the disruption of agglomerates. Surfactants are again often included in the solution to prevent the reagglomeration of nanoparticles [14]. The processing time of ultrasonic horns can vary between tens of seconds to hours. Cavitation at the horn tip can cause erosion of the tip material, contaminating the solution with metal particles.

Although the previously mentioned deagglomeration methods have been successful in reducing agglomerates to primary particles, there are some disadvantages that provide incentive for investigation into novel deagglomeration techniques. First, the processing time can be excessively long to ensure adequate deagglomeration. Due to the very small

scale of the interactions required for deagglomeration of nanoparticles, milling can take many hours or days for most agglomerates to be fragmented. Ultrasonic horns and other methods can also take significant time for all agglomerates to be physically disrupted by the high frequency waves. Second, in conventional deagglomeration methods, the forces acting upon the nanoparticles also act on the surrounding media. The milling media and the ultrasonic horn can be eroded, resulting in contamination of the nanoparticles and degradation of the deagglomeration equipment. Third, conventional methods do not exploit the properties of the nanoparticles to achieve deagglomeration. Milling and other methods have very little refinement from their counterparts in processing larger particles, and all the previously-discussed methods require the source to directly create a mechanical force to disrupt the agglomerate.

The final condition to be considered in producing homogenous composites is equal packing density of the constituent particles. The predominant method employed in this program to form the composites to the desired density was uniaxial pressing. Cold isostatic pressing could also provide the high uniform density required for the composites without exceeding the temperature limits of the program, but due to equipment availability, isostatic pressing is not considered here. Uniaxial pressing is accomplished by compacting the composite material with a compressive force from a single direction. Figure 14 shows a simple illustration of uniaxial pressing. The composite materials are loaded into a die made of thick-walled hardened steel. Two hardened steel pistons, which are machined to close tolerances to fit within a die, hold the composite materials and transfer the compressive force to the composite. The pistons and inner die wall are shown as dashed lines as they are in the center of the cylindrical die. The die and piston

assembly is loaded into a hydraulic press, which applies several tons of compressive force long the axis formed by the pistons and composite material.

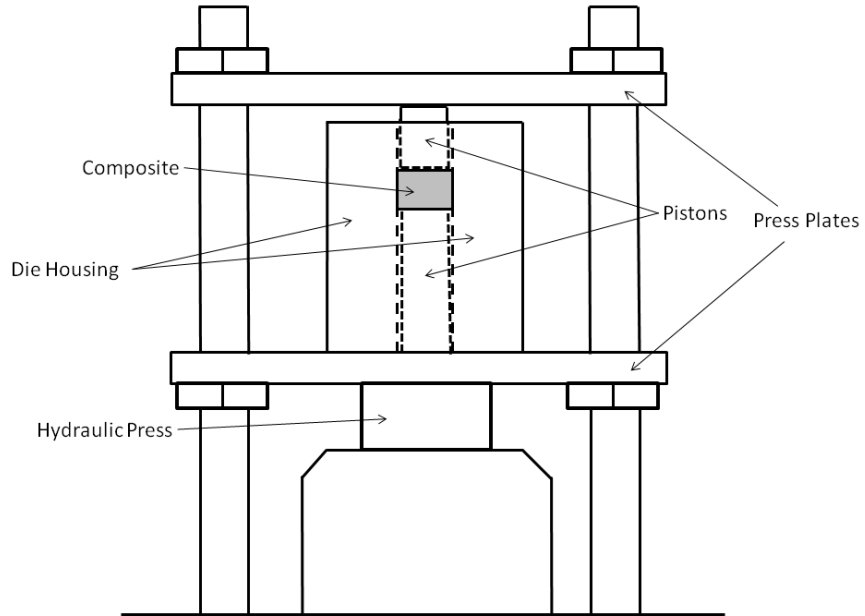


Figure 14. Uniaxial pressing in a hydraulic press

Although uniaxial pressing is very effective at increasing the density of composite materials, it is possible for significant density variation to occur with the composite. In the uniaxial setup shown in Figure 14, the density of the composite can vary significantly due to frictional forces occurring between composite particles and between particles and the walls of the die. These frictional forces act to distribute the compressive force applied by the hydraulic press to the die. If the compressive force from the hydraulic press is partially distributed through the die rather than through the composite material, the density of the composite will be reduced in regions further from the piston that makes sole contact with a plate of the hydraulic press. In the case of Figure 14, only the top piston makes contact with the top plate, but the bottom plate makes contact with both the bottom piston and the die. The top piston experiences the total force of the hydraulic press, and assuming that there is negligible friction between the top piston and the die,

the top piston transfers all of the compressive force applied by the hydraulic press to the top of the composite. The bottom press plate, however, contacts both the bottom piston and the die in Figure 14. This arrangement allows some of the compressive force to be distributed through the die, meaning regions further away from the top of the composite will be compressed to a lower density. Figure 15 illustrates how lines of force can be distributed from the composite to the die through friction between the particles and the die wall. As shown in Figure 15, part of the force applied from the top plate and piston, F , is distributed from the composite through the die wall. The force in the upward direction from the bottom plate acts not only on the bottom piston but also on the die wall. The sum of the three forces shown in Figure 15, A , B , and C , is equal to the force from the top plate on the top piston, F . The forces A and C are applied to the same object, the die, but are shown separately given the nature of the cross-sectional view. Since the force B is by definition less than the force F , the bottom of the composite experiences less compressive force than the top. In summary, the force transferred through the die wall to the bottom plate does not act on the entire composite, causing reduced density of lower regions of the composite.

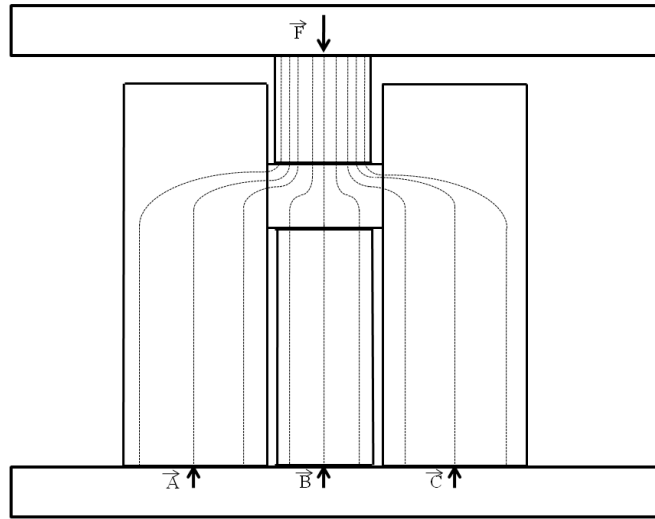


Figure 15. Illustration of transfer of force from friction between composite and die wall

The density of the composite can be significantly improved in uniaxial compression systems by simply isolating the die from the hydraulic press. Isolating the die from the hydraulic press ensures that the forces between the top and bottom press plates cannot be transferred through the die walls. Figure 16 shows another illustration in which the die is isolated from the press by a stand. The stand is supported by the same surface as the hydraulic press as shown by the light gray legs shown in the illustration. The stand supports the weight of the die but is isolated from the compressive force between the press plates. Friction between the particles and the die wall can still lower the compressive force in regions near the center of the composite length, but the degree to which this affects the density is greatly diminished because the lines of force must reenter the composite to transfer the force to the piston rather than the die. Friction between the die and pistons can similarly reduce the density in certain areas of the composite compressive force can be distributed from the composite, through the die wall, and to the piston. To prevent this, the pistons must be able to move freely within the die. It is impossible to eliminate all effects of particle-particle and particle-wall friction, but

additional steps, such as the addition of lubricants during pressing, can also aid in further compacting the composite. If the lubricant is not a constituent material of the composite, its benefits in reducing packing friction may be outweighed by its presence in the final volume of the composite. However, if one of the final constituents of the composite can be added in a form that is lubricating during pressing, the benefits of lubricated compaction can be gained without additional materials.

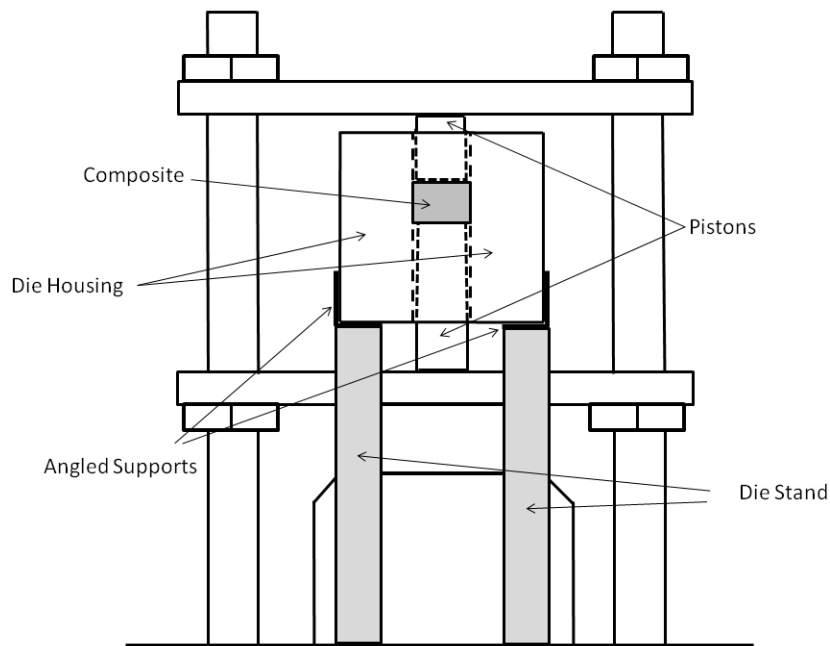


Figure 16. Double-ended uniaxial pressing with an isolated die

2.5 Factors Contributing to High Dielectric Strength

2.5.1 Voids

The presence of voids within a composite can significantly degrade the performance through the potential for electrical failure of the insulation due to the concentration of the electric fields in the void. In a simple model of the electric field distribution between the a void and the surround high dielectric constant material in which a layer comprising the

void and a layer comprising the high dielectric material occupy the volume of a capacitor, a series combination of capacitive layers is effectively formed. The electric displacement through both layers must be continuous. However, the electric field is not distributed equally between the layers of different dielectrics. This can be explained through the constitutive relation describing the electric elasticity without taking into account nonlinear effects as shown in equation (2.50). The magnitude of the electric field is represented as E [V/m], and the electric flux density is represented as D [C/m²]. The permittivity of free space is again ϵ_0 [F/m], and the dielectric constant of the layer is represented as ϵ_r [19].

$$E = \frac{D}{\epsilon_0 \epsilon_r} \quad (2.50)$$

Analysis of equation (2.44) illustrates how if the electric displacement is equal in both layers of the capacitor, the electric field in the void will be greater than the electric field in the high dielectric layer by a factor equal to the ratio of the dielectric constants. This relation is shown in equation (2.51). The electric fields in the void and the high dielectric material are represented as E_{void} and E_{HDM} , respectively.

$$\frac{E_{void}}{E_{HDM}} = \frac{\epsilon_{HDM}}{\epsilon_{void}} \quad (2.51)$$

It is generally assumed here that the composition of the voids is simply air or other similar gases. Since the dielectric constant of air is close to unity, the ratio of the magnitudes of the electric field in the void and in the high dielectric constant material is approximately equal to the dielectric constant of the high dielectric constant material. Thus, use of a high dielectric constant material increases the magnitude of the electric fields in air gaps. This is a risk to the component's functionality and lifetime. If the

electric field in the void is exceeded, there is an increased likelihood of electrical failure of the high dielectric constant material. Failure of the high dielectric constant material could occur due to thermal damage, accelerated ions or electrons in the air gap precipitating breakdown in the high dielectric constant material, or other effects. Therefore, voids must be minimized not only to limit a decrease in the effectiveness of the high dielectric constant material as an energy storage medium but also to prevent accelerated failure of the material as an insulating medium.

Electrostatic simulations of composites generated in CST EM Studio allow the field distribution between the composite's components to be visualized and quantified. Full details on the methods with which the model of the composite was generated and simulated are presented in Chapter 4. Figure 17 shows a plot of the absolute value of the 3D electric field projected onto the 2D surface of a plane intersecting the composite. The colored areas are particle cross sections that intersect with the cutting plane, and the white particles in the background are particles behind the cutting plane. The electric field on the background particles is not shown.

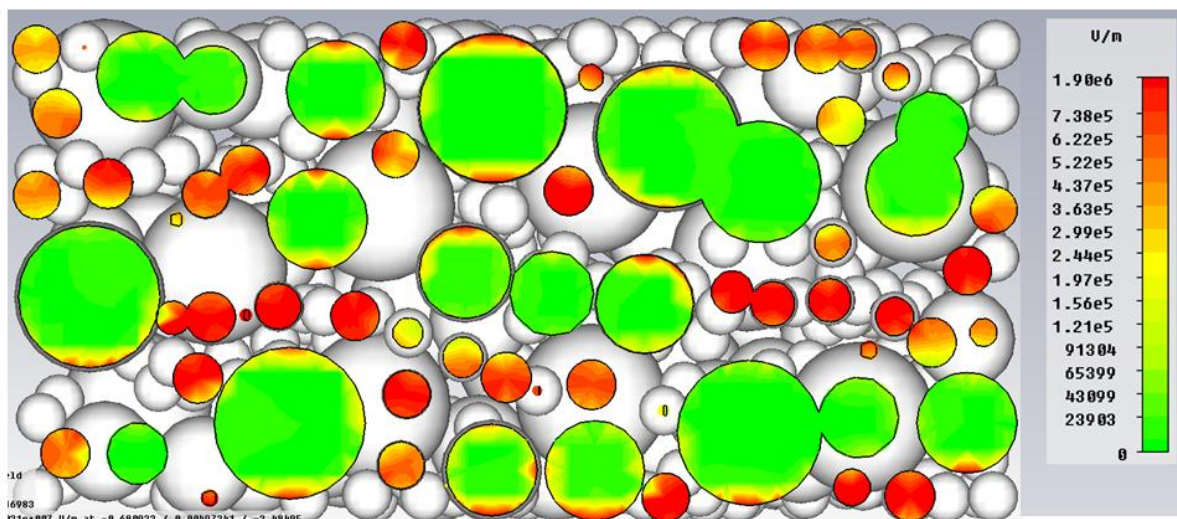


Figure 17. Plot of 3D fields projected onto a 2D cross section of a composite containing high and low dielectric constant fillers

The virtual composite has a diameter of 10 μm and a thickness of 5 μm . The composite volume was filled with large particles with a dielectric constant of 1000 and small particles with a dielectric constant of 1. These values correspond to high dielectric constant ceramic fillers and air voids, respectively. The remaining composite volume not occupied by particles was defined to have a dielectric constant of 5. This matrix material is hidden in Figure 17 to highlight the difference in electric field strength between high dielectric constant filler particles and low dielectric constant voids. Electrodes on the upper and lower surfaces of the composite apply a potential of 1 V across the thickness of the composite. The wide variance in the electric field distribution between particles with different dielectric constants is evident. Most of the area of the small particles with a dielectric constant of 1 is filled with dark orange and red indicating electric fields on the order of 1 MV/m. At the peak electric field value of 1.9 MV/m, the field within the void particles is 9.5 times the field that would be present in a solid material with a constant dielectric constant throughout. The field within the void particles is enhanced due to field concentration by the higher dielectric constant fillers. By contrast, the electric field in the large particles with a high dielectric constant is generally uniform and very low. There is, however, evidence of high electric fields towards the upper and lower edges of the high dielectric constant particles.

Figure 18 shows the same cross-sectional view as Figure 17 with the electric field plotted in the matrix material with a dielectric constant of 5. The concentration of the electric field in regions where filler particles are absent is marked by the dark orange and red regions. The field within this material representing the composite's binder reaches values even higher than those observed in the low dielectric constant filler particles at

4.28 MV/m. The concentration of fields in certain areas of the binder over others is partially due to inhomogeneity in the distribution of the filler particles. Improved homogeneity of the particle distribution will better distribute the electric field within the matrix material to avoid high peak values that can lead to dielectric failure of the composite.

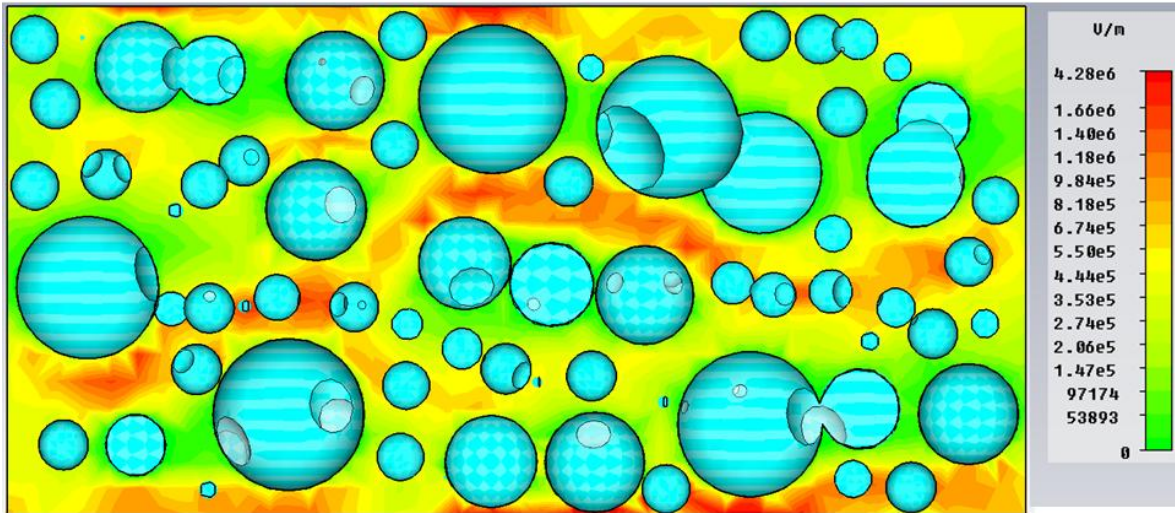


Figure 18. 2D plot of the absolute value of the 3D electric field within the matrix material

2.5.2 Air Gaps at Surface Contacts

Many high power applications of high dielectric constant materials require direct electrical connections to the high dielectric constant material. Implementation of effective electrodes to provide this electrical connection is complicated by two significant issues:

1. The surfaces of the high dielectric constant material and electrode must be prepared to a very high degree of accuracy to eliminate air gaps between the surfaces.
2. Field effect enhancements at the triple point between the high dielectric constant material, electrode, and surrounding medium can be very large as a result of the high dielectric constant of the energy storage material and the geometry of the electrode. Both of these issues are

briefly examined, and a proposed solution to make effective electrical connections to high dielectric constant composite materials is proposed.

For an electrode of a given area, if the interface between the metal of the electrode and the high dielectric constant material is imperfect, the effective dielectric constant of the material can be greatly reduced. Figure 19 illustrates how at a microscopic scale, small imperfections in the surfaces of both the electrodes and high dielectric constant material can cause significant air gaps to form in the energy storage volume of the capacitor.

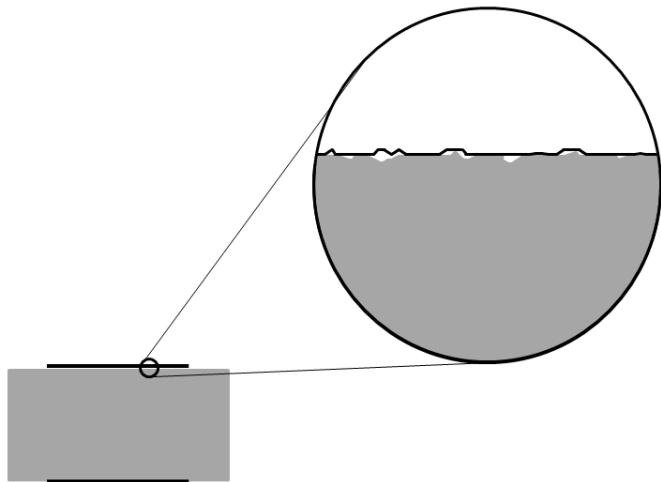


Figure 19. Illustration of microscopic imperfections causing air gaps between surfaces.

An effective way to eliminate most air gaps is to directly apply the electrode material in such a way that will fill all potential areas where an air gap may otherwise form. Several electrode application options exist, including epoxies loaded with silver or other conductive elements and deposition through sputtering. Conductive epoxies have the disadvantage that they contain non-conducting binder materials. At points where the binder makes direct contact with the high dielectric constant material rather than the conductive element, a similar effect to that of an air gap is present at that location. Similarly, if the epoxy is heated to remove the binder elements after application, voids

are left that have effects like those described for air gaps. Therefore, although highly-loaded conductive epoxies can decrease the effects of air gaps, they are not the preferred option. Sputtering, however, can deposit a thin even layer of metal directly on the surface of the high dielectric constant material without the use of binders. If the surface of the high dielectric constant material is prepared with a high grit abrasive prior to sputtering, an even application of metal by sputtering can form an electrode with minimal air gaps. Therefore, it is the preferred method for application of electrodes on the high dielectric material surface. Other steps, including covering the sputtered electrode with a conductive epoxy, are necessary to prevent abrasion of the thin sputtered contact and enable external contacts to be made to the electrode.

2.5.3 Triple Points

Triple points are present along the interface between the highly conductive electrode, the insulating high dielectric constant composite, and the relatively low dielectric constant surrounding air or other surrounding dielectric material. The triple point is present along the entire electrode edge as well as at points along the electrode-composite contact where both ceramic and binder components make contact with the electrode. The magnitude of the field effect enhancement at the triple point is a function of the dielectric constants of the materials involved and the geometry of the interfaces, so the application of the high dielectric constant composites directly contributes to increased field enhancements. The very small radius of the edges of a sputtered electrode can also contribute to field enhancement at these triple points.

Reduction of the field enhancement is critical both to avoid premature failure of the material and to fully utilize the composite's properties in applications requiring direct

electrode connection. The consequences of dielectric failure due to excessively high electric fields are obvious. However, the effects on reducing the effective energy density of the material are less apparent. For a capacitive system with a field enhancement factor of 10, the useful energy density is reduced by a factor of nearly 100 from the peak energy density, which is only present in a very small volume near the triple points. Minimizing field enhancements is necessary to utilize the full volume of the material at high energy densities near its peak capability.

Two approaches have been investigated to address field enhancements due to triple points at the electrode edge. The first approach mechanically alters the sample and electrode geometry to remove the triple point from the high electric field region. Grooves are cut into the composites, forming a reverse mesa structure. The electrodes are then applied within the groove, preferably by sputtering or another application process that eliminates air voids at the contact. The result of this geometry is that the triple point junction of the electrode, high dielectric constant material, and surrounding insulation is in a much lower electric field region. This approach has been investigated previously in high power silicon carbide photo-switches [20]. The effectiveness of the embedded electrodes is demonstrated through simulated electric field plots shown in Figure 20. This simulation compares the geometry in which the electrode contacts the surface of the composite and the geometry in which the electrode is effectively embedded 1 mm within the composite by machining a reverse mesa structure. The electrostatic simulation performed to produce Figure 20 consisted of a 2.1 mm thick composite with a dielectric constant of 100 and copper electrodes with 0.5 mm radii on their outside edge. A voltage of 1 V was applied across the electrodes, and the field levels were compared to those

expected from an infinite parallel plate. The 2D plots of Figure 20 have a radial symmetry around the vertical axis at the left. The triple point in plot (a) corresponds to a field effect enhancement of 10.43 in the composite material, and the peak fields in the surrounding air reach 256 kV/m. By embedding the electrode 1 mm into the composite as in plot (b), the field effect enhancement is reduced to 2.34 in the composite, and the peak field in the surrounding air is less than 100 kV/m.

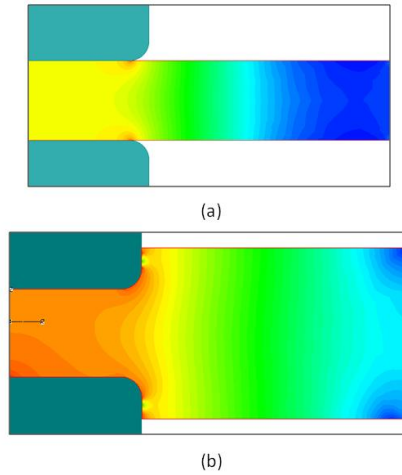


Figure 20. Reduction of field enhancement from (a) surface electrodes to (b) embedded electrodes

A second approach to minimize the field enhancement at the triple points along the electrode edge is a potentially simpler solution as it does not require precision machining of the composites. In the second approach, the electrode edges are coated with a high dielectric constant material that can be applied in a liquid or semi-solid form. By coating with a high dielectric constant material, the difference in dielectric constants between the composite and surrounding material at the electrode edge is reduced, decreasing the field enhancement. This coating approach has also been simulated to evaluate its potential. The 2D plots of Figure 21 have a radial symmetry around the vertical axis at the left. Both plots are the results of simulations of a composite with a thickness of 0.915 mm and a dielectric constant of 100. The electrode had a radius in both simulations of 0.1 mm. The

background material surrounding the structures was simulated to be oil with a dielectric constant of 2.2. The high dielectric constant coating was simulated with a dielectric constant of 40. The plot at the top of Figure 21 does not include a high dielectric constant coating over the electrode edge. The plot at the bottom of the figure has the same sample thickness as in the top, but a high dielectric constant coating has been added to the electrode edge. In both plots, the peak electric field occurs near the triple point of the electrode edge. The peak electric field without the high dielectric constant coating was 10.11 MV/m, and the peak electric field with the high dielectric constant coating was reduced to 2.52 MV/m. The dark orange-red throughout the bulk of the sample between the electrodes in the bottom plot demonstrates how limiting the FEF at the electrode edge enables the field within the bulk of the material to be operated near its peak value. This results in operation with a high electric field in a much greater volume, resulting in a higher maximum stored energy density for a given dielectric strength. These simulations suggest that the field enhancement at the triple point can be adequately reduced with the relatively simple application of a high dielectric constant coating to the electrode edge. However, implementation of the coating is critical, including proper wetting of the coating to the surface and adequate flow of the coating to eliminate any voids.

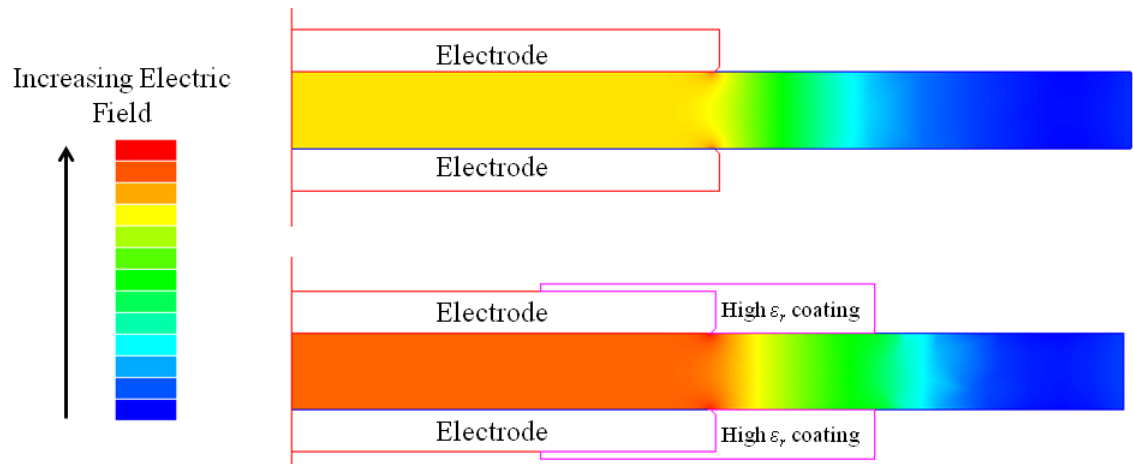


Figure 21. Simulated electric field in the sample with high dielectric constant coating (bottom) and without high dielectric constant coating (top)

References for Chapter 2

- [1] C. Balanis, *Advanced Engineering Electromagnetics*. Hoboken, NJ: John Wiley & Sons, Inc., 1989.
- [2] Archimerged, "Dielectric responses," Wikimedia Commons, 2008.
- [3] R. Simpkin, "A derivation of Lichtenecker's logarithmic mixture formula from Maxwell's equations," *IEEE Transactions on Microwave Theory and Techniques*, vol. 58, pp. 545-550, 2010.
- [4] C. F. Yang, C. C. Wu, C. C. Su, and Y. C. Chen, "The development of prediction method for the permittivity of epoxy/(BaSr)(TiZr)O composites," *Applied Physics A*, vol. 97, pp. 455-460, 2009.
- [5] T. Yamada, T. Ueda, and T. Kitayama, "Piezoelectricity of a high-content lead zirconate titanate/polymer composite," *Journal of Applied Physics*, vol. 53, pp. 4328-4332, 1982.
- [6] N. Jayasundere and B. V. Smith, "Dielectric constant for binary piezoelectric 0-3 composite," *Journal of Applied Physics*, vol. 73, pp. 2462-2466, 1993.
- [7] H. Solomon, "Random packing density," in *Proc. of the 5th Berkely Symposium on Mathematical Statistics and Probability*. vol. 3, L. Lecam and J. Neyman, Eds. Berkely, CA, 1965, pp. 119-134.
- [8] C. C. Furnas, "Flow of gases through beds of broken solids," US Dept. of Commerce Bureau of Mines, Washington, D.C. 1929.
- [9] C. C. Furnas, "Grading aggregates: I-Mathematical relations for beds of broken solids of maximum density," *Industrial and Engineering Chemistry*, vol. 23, pp. 1052-1058, 1931.
- [10] F. O. Anderegg, "Grading aggregates: II-The application of mathematical formulas to mortars," *Industrial and Engineering Chemistry*, vol. 23, pp. 1058-1064, 1931.
- [11] U. Gesenhues, "Substructure of titanium dioxide agglomerates from dry ball-milling experiments," *Journal of Nanoparticle Research*, vol. 1, pp. 223-234, 1999.
- [12] V. A. Parsegian, *Van Der Waals Forces: A Handbook for Biologists, Chemists, Engineers, and Physicists*. New York: Cambridge University Press, 2006.
- [13] "Ceramic Materials for Electronics: Processing, Properties, and Applications," R. C. Buchanan, Ed. New York: Marcel Dekker, Inc., 1986.
- [14] Y. Hwang, J. K. Lee, J. K. Lee, Y. M. Jeong, S. Cheong, Y. C. Ahn, and S. H. Kim, "Production and dispersion stability of nanoparticles in nanofluids," *Powder Technology*, pp. 145-153, 2008.
- [15] S. Y. Yao and Z. H. Xie, "Deagglomeration treatment in the synthesis of doped-ceria nanoparticles via coprecipitation route," *Journal of Materials Processing Technology*, pp. 54-59, 2007.
- [16] A. Voss and W. H. Finlay, "Deagglomeration of dry powder pharmaceutical aerosols," *International Journal of Pharmaceutics*, pp. 39-50, 2002.
- [17] S. Froeschke, S. Kohler, A. P. Weber, and G. Kasper, "Impact fragmentation of nanoparticle agglomerates," *Journal of Aerosol Science*, pp. 275-287, 2003.

- [18] Sonics, Inc. (December 2008). *High Intensity Ultrasonic Processor* [Online]. Available:<http://www.sonics.com/liquid-datasheet/VCX500-VCX750%20new%20micro.pdf>.
- [19] F. T. Ulaby, *Fundamentals of Applied Electromagnetics*. Upper Saddle River, NJ: Prentice Hall, 2001.
- [20] C. M. Fessler, K. Kelkar, W. C. Nunnally, and N. E. Islam, "Investigation of high electric fields at the electrode-SiC interface in photo-switches," in *2007 16th IEEE Inter. Pulsed Power Conf.* Albuquerque, NM, 2007, pp. 114-119.

Chapter 3: Development of High Dielectric Constant Composite Materials

3.1 Literature Survey of High Dielectric Constant Composites

A brief review of notable works in the field of high dielectric constant composites is provided before discussing the critical factors involved in creating high dielectric constant composites and the approaches taken in this program. The majority of research on high dielectric constant composites has focused on thin film applications for very small scale components. Most of these composites have been designed for low power applications, and many of the requirements and constraints differ from the present effort. Nevertheless, the basic effort of developing high dielectric constant polymer-ceramic composite materials is a common goal between these works and the present effort, so an overview is appropriate. The review provided here cannot be considered exhaustive due to the many works on composite materials, but many of the most notable high dielectric constant results are given for comparison to the results achieved in this program. Since the inception of this work, a review of research on composites has been produced for pulse power energy storage applications [1]. While several of the works referenced in that review are noteworthy, energy storage applications often have a priority towards high electric field operation. While high field operation is important in this work as well, a high dielectric constant is necessary to achieve reduction of the antenna size.

Table 2 provides an overview of the works included in this review. The first authors listed in Table 2, excluding Borchardt, are from Georgia Tech University. Their work has concentrated on very thin films for embedded capacitor applications, but it has resulted in many of the highest known dielectric constant composites previously produced.

Table 2. Notable Previous Works in High Dielectric Constant Composite Materials

Researchers	Ceramic Material	Matrix Material	Thickness (mm)	Percentage of Ceramic (vol%)	Frequency of Measurement (MHz)	Dielectric Constant
Rao <i>et al</i> [2]	Bimodal PMN-PT and BTO	High K Epoxy	0.00375	85	1800	140
Windlass <i>et al</i> [3]	Bimodal PMN-PT and BTO	Epoxy	0.003	85	Unspecified	135
Rao <i>et al</i> [4]	Bimodal PMN-PT and BTO	High K Epoxy	0.01	70	100	100
Agarwal <i>et al</i> [5]	Bimodal BTO	Epoxy	~ 0.003	Unspecified	Up to 0.1	74
Ogitani <i>et al</i> [6]	PMN-PT	Photo-definable Epoxy	0.01	71	0.1	70
Borchardt <i>et al</i> [7]	BST	Epoxy	Up to 1.27	Unspecified	Unspecified	50

The first material listed in Table 2 was prepared as a polymer-ceramic composite containing both lead magnesium niobate-lead titanate (PMN-PT) and barium titanate [2]. PMN-PT is noted to have a dielectric constant several times that of barium titanate with the values referenced by Rao *et al* as 19,316 and 3,000, respectively [2]. PMN-PT is often, therefore, a very attractive material for high dielectric constant composites. It should be noted that PMN-PT and other lead-based ceramics were excluded from consideration for the composites developed in this work due to the potential health hazards of lead-based materials. The PMN-PT and barium titanate used by Rao were mixed in a bimodal distribution with particle sizes of 0.9 and 0.05 μm , respectively, resulting in a particle size ratio of 18:1 [2]. The volume ratio of PMN-PT to barium titanate was 4:1. The binder was an epoxy with an enhanced dielectric constant. The binder, Dow Epoxy Resin 661, was modified by 5 wt% cobalt (III) acac, which was used as a curing catalyst to increase the binder's dielectric constant to 6.4 [2]. The ceramic

mixture was loaded into the binder at 85% by volume, and the composite was formed to a thickness of 3.75 μm [2]. The dielectric constant was measured over the frequency range of 10 kHz to 1.8 GHz. The low frequency dielectric constant was measured to be 150, and the dielectric constant remained high at approximately 140 above 1 GHz [2]. The dielectric strength of the composites was measured with a DC supply to reach 17 MV/m [2]. A very similar work by Rao *et al* is listed as the third entry in Table 2. That work was published in the same year as the first table entry, and many of the experimental parameters are the same. The dielectric constant values reported in the second work are slightly lower than the first with a value of 100 at 100 MHz [4]. The difference is likely due to the lower ceramic loading percentage, which was 70% by volume in the measured sample [4]. Other variations in the second work included a barium titanate particle size increase to 0.65 μm and a PMN-PT to barium titanate volume ratio of 3:1. The dielectric constants measured in Rao's work are the highest found for a polymer-ceramic composite and exhibit exceptional stability over a wide frequency range.

The second entry in Table 2 authored by Windlass *et al* primarily discusses issues of ceramic particle treatment, dispersants, and solvents in spin-coated thin film composites for embedded capacitor applications [3]. The article examines the production of a bimodal mixture of PMN-PT and barium titanate. However, the notable dielectric constant reported, 135, is referenced only as a PMN-PT and epoxy composite [3]. The optimal volume percentage of ceramic is noted to be 85% as it is claimed that higher percentages result in porosity due to insufficient filling of the remaining volume with polymers. The author mentions work on films with thicknesses between 2 and 4 microns,

and the dielectric constant value of 135 is believed to be from a 3 μm film. No information is included on the measurement frequency.

Agarwal *et al* reported a work that exhibits the highest previous dielectric constant without lead-based ceramics [5]. The highest dielectric constant measured by Agarwal *et al* was 74 for a bimodal distribution of barium titanate in epoxy [5]. The bimodal distribution was composed of large particles of 200 nm and small particles of 20-30 nm [5]. The frequency of the dielectric constant measurement of 74 was not specifically reported, but it is noted that the measurements were taken with an LCZ meter capable of measurements up to 100 kHz [5]. The volume percentage of ceramic was not reported for the film with a dielectric constant of 74, but the ratio of large to small particles was reported as 5:1. The thin film with a dielectric constant of 74 was formed by dip coating from a colloidal solution of the ceramic and epoxy in methyl ethyl ketone (MEK). The thickness of the film was not specifically reported, but it was noted that thin films were produced. Other films included in the study were reported with a thickness of approximately 3 μm , and that thickness is considered representative for the films in that study [5].

The final thin film high dielectric constant composite described here was reported by Ogitani *et al*. The peak dielectric constant measured in that study was approximately 70 up to 100 kHz [6]. The composites were made from epoxy loaded to 71% by volume with PMN-PT [6]. The ceramics were treated with a phosphoric acid surfactant to improve particle dispersion through an acid-base reaction with the PMN-PT surface [6]. The particle size distributions were centered around 1 μm , but the actual sizes were dependent on the ball mill and surfactant treatment. A final film size of approximately 10 μm was

obtained through spin coating. It was noted that the composite with a dielectric constant of 71% had some negative physical properties due to light scattering by the particles degrading the photo-definable epoxy. Therefore, the particle loading was generally limited to 65%, which resulted in a dielectric constant value of 62 [6].

The notable works reviewed here represent substantial improvements in high dielectric constant composites. However, the applicability of these composite materials to high power systems is very limited. The composites reviewed thus far were developed for embedded capacitors or other thin-film chip-based requirements. The very small thicknesses would not withstand substantial voltages despite the respectable dielectric strength observed by Rao *et al.* Even at a dielectric strength of 17 MV/m, a 3 μm film would fail at 51 V. Therefore, high dielectric constant composites developed specifically for high power applications are required. The amount of previous research into high power composites is much smaller than devoted to embedded capacitor research. Only one notable previous study on high dielectric constant composites for high power applications is known. Borchardt *et al* reported on a high dielectric constant composite built for high energy density capacitors developed in a collaborative effort between Sandia National Laboratories and TPL, Inc. [7]. The article focuses on capacitor development, and relatively little specific information is given on the material. However, it was noted that nanoparticulate ceramics were mixed with a two-part epoxy system to form the composites [7]. The dielectric constant of the material developed by TPL Inc. is reported to be 50, but the frequency of the measurement was not reported [7]. The thicknesses of the composites were reported to typically be between 0.5 mm and 1 mm with a maximum reported thickness of 1.27 mm. While this is not a substantial thickness

for some applications, it is orders of magnitude larger than thin film technology. The highest average dielectric strength reported for single-layer capacitors formed with the material corresponds to 149.6 MV/m. The material energy density at this field reaches nearly 5 J/cm³, but it was noted that capacitors formed with the material had only been shown to operate consistently at 0.6 J/cm³ [7]. Dielectric strength measurements using spherical electrodes with diameters of 16 mm obtained average values corresponding to 334.6 MV/m. Although the dielectric constant of the material developed by TPL Inc. does not reach as high of dielectric constant values as the previously-reviewed thin-film composites, a dielectric constant value of 50 represents a significant milestone for relatively thick substrates of high dielectric constant materials. Along with the high dielectric strength, the material developed by TPL Inc. was the benchmark for comparison of the high dielectric constant composites developed as a part of the effort described in this proposal.

3.2 Novel Approaches to High Dielectric Constant Composite Development

The high dielectric constant composite materials developed in this effort have multiple unique features from previously-developed composites in their composition, fabrication, and properties. The following three points have been singled out for discussion as novel approaches that result in extraordinary dielectric properties.

1. Trimodal Particle Packing: A trimodal distribution of particle sizes in which ceramic particles ranging from less than 100 nm to greater than 100 μm is implemented to increase the ceramic packing factor.

2. In-situ Polymerization of Coupling Agents: Polymerization of the polymer is done in-situ, in which polymer precursors are mixed and compressed with the ceramic particles prior to the onset of polymerization and cross-linking. This method further increases the packing factor and boundary interfaces over composites formed with pre-polymerized macromolecules. While other works have also employed in-situ polymerization, the use of coupling agents as the sole binder in the composite minimizes the volume occupied by the binder and promotes strong binding to the particle surfaces.
3. Void-Filling with High Dielectric Constant Fluids: Dielectric fluid, including high dielectric constant fluids, can be used to replace any remaining composite voids to eliminate space occupied by air, improving the composite dielectric constant and dielectric strength.

3.2.1 Trimodal Particle Packing

As discussed earlier in this chapter, the effective dielectric constant is determined by the volume percentage of the each of the composite's constitutive components. Therefore, for the highest effective dielectric constant, the volume percentage of the components with the highest dielectric constant should be maximized, and the volume percentage can be maximized by efficient packing of the component with the highest dielectric constant by utilizing multiple particle sizes. Bimodal particle distributions have been effectively employed in previous high dielectric constant composites to produce some of the notable works reviewed in Chapter 2 [2-5]. However, the ratio of particle sizes and the relative amount of each particle size were not optimized in those studies for the maximum packing density. The ultra-thin nature of those composites were likely

limiting factors in the ratio of particle sizes, and few details are provided on how the relative amounts of each particle size were obtained. The large thickness requirement of high power composites enables a much larger ratio of particle sizes to be employed, so trimodal distributions are possible in which relatively large particles of many tens or even hundreds of microns can be used. The dielectric strength of the composite is considered to be the limiting factor on the size of the particles. Since defects in the structure of a particle could cause dielectric breakdown of the entire composite if the particle composed a large fraction of the composite's thickness, the maximum dimension of any particle is limited to approximately one-tenth the minimum thickness of the composite.

Due to the processes with which perovskite ceramic powders are manufactured and the common tendency to strictly use nanoparticles or particles with dimensions of only a few microns, powders with dimensions on the order of tens of microns or larger are generally unavailable. Therefore, a method for producing particles in this size range had to be developed. Sintered pieces of the ceramic between 3 and 12 mm, which are traditionally sold for vacuum deposition applications, are purchased commercially. The pieces are then sintered again in air for 3 hours at 1350 C to further improve their density. After sintering, the pieces are milled and sieved to the desired size range.

By combining three particle sizes, the composites have a unique distribution of particle sizes ranging from nanoparticles with dimensions of approximately 50 nm to microparticles with dimensions of 50 μm and greater. To maintain approximately the same ratio between the intermediate-sized particles and small particles and the large particles and intermediate particles, the intermediate sized particles should be approximately 1.6 μm . Such a large range of particle sizes represents a novel

advancement in high dielectric constant composites and enables a higher degree of particle packing and correspondingly larger dielectric constant.

3.2.2 In-situ Polymerization

A binder is necessary to provide the mechanical integrity of a composite made with ceramic particles without sintering. Previous studies of high dielectric constant composites have implemented a wide variety of polymers and epoxy compounds to bind the composite. The approach of mixing polymers with ceramic particles prior to composite formulation generally assumes that the polymers will fill the voids between ceramic particles [3]. This approach appears to be theoretically sound for relatively low loading levels of ceramic particles in which the polymer has ample space to fill between particles. However, when the ceramic particle density is maximized according to the methods previously described, the voids between particles can be much smaller than the dimensions of most polymers. In such a situation, the addition of polymers larger than the voids result in an increase in the size of the composite and a decrease in the ceramic particle density. Therefore, in composites intended to have a very high density of ceramic particles, the design must limit not only the amount of polymer that is added to the system but also the size of the polymer chains.

By definition, polymers are large macromolecules with repeating units. As an example, the typical dimensions of a common polymer implemented in polymer-ceramic composites, polyvinylidene fluoride (PVDF), are considered. PVDF consists of a repeating structure of $(CF_2 - CH_2)_n$ units [8]. The carbon-carbon bond length is approximately 157 pm at an angle of 100 degrees. This corresponds to a unit length of approximately 120 pm. The average molecular weight of commercially-available PVDF

can vary widely, and a recent survey of offerings from Sigma-Aldrich had a low-end value of 180,000. This molecular weight corresponds to approximately 2,800 repeating units and a polymer contour length of slightly greater than 350 nm. The width of the polymer chain is substantially smaller, with a contour width having been measured for poly(2-vinylpyridine) with an atomic force microscope to be approximately 0.4 nm [9]. The polymer chains form coils with different degrees of compactness ranging from being extended chains to compact globules. However, even compact globules formed by poly(2-vinylpyridine) were measured to have a radius of gyration between 20 and 30 nm [9]. The radius of gyration for extended chains was closer to 60 nm [9]. The large contour length and radius of gyration can make them incompatible for filling very small voids. If the polymers being added to a bed of ceramics are on the same size scale as the smallest ceramic particles, the polymers will displace some of the volume that should be occupied by ceramic particles and lower the effective dielectric constant. For polymers to effectively fill the voids between ceramic particles in a packing of maximum density, the polymer dimensions must be much smaller than the dimensions of the smallest ceramic particle. If the smallest ceramic particle size is approximately 50 nm, then the polymer dimensions must be less than 10 nm. Such small dimensions are uncommon for traditional polymers, so a novel approach must be made to form the binder network.

The novel approach developed to minimize binder molecule size and retain a high ceramic particle packing factor has two components, including in-situ polymerization and the selection of unique binder networks. In-situ polymerization is briefly described here, and the unique binders are detailed in the following materials section. In-situ polymerization describes how the formation of polymer chains is delayed until after the

composite has been formed. With this approach, the precursor chemicals needed for polymer formation are mixed into a slurry with the ceramic particles. The slurry is then compacted in a press, so the polymer precursors only remain in the small voids between ceramic particles. After this compaction, polymerization is initiated such that the polymer can only form in the confined spaces of the inter-particle voids. Thus, the decrease in the ceramic particle density resulting from the addition of pre-polymerized macromolecules to the ceramic mixture is avoided.

3.2.3 Void-Filling with High Dielectric Constant Fluids

At the nanometer and sub-nanometer scale, even well-designed, highly-packed composites will have some voids present that cannot be filled with additional ceramic particles or polymers. It is, therefore, beneficial to examine alternative methods for filling the remaining voids. To penetrate to the location of the voids with a small enough chemical structure to fill the sub-nanometer dimensions along particle surfaces, a non-viscous fluid is normally required. The fluid could be either a gas or a liquid. In some limited circumstances in which the composite is used in an air-tight enclosure, filling the voids with sulfur hexafluoride (SF_6) or a high pressure gas could significantly increase the dielectric strength of the composite. However, it is normally much more practical to fill the voids with a liquid, which can remain in the voids for a much longer timeframe than a gas.

Liquid filling of composite voids offers the additional advantages of a wide variety of liquid properties that can be advantageous to add to the composite. Similar to the potential use of SF_6 , dielectric liquids, including oils commonly used for high voltage electrical insulation, can fill the voids to increase the dielectric strength beyond that

obtained with air-filled voids. The higher dielectric constant of the oil can also increase the effective dielectric constant of the composite. While the increase of the effective dielectric constant may only be marginal when using insulating oils, fluids with excellent dielectric strength and very high dielectric constants are available that can substantially increase the effective dielectric constant when used as void fillers. In addition to a high dielectric strength and high dielectric constant, the ideal void-filling fluid has low dielectric losses and a low evaporation rate. A low vapor pressure is necessary for the liquid to be retained in the composite for a suitably long time before the dielectric properties begin to change. The materials identified as good void-filling fluids are described further in the following materials section.

3.3 Concepts of the Classes of High Dielectric Constant Composites

Each of the three composite classes developed in this work is based on a different concept for how the binder enables the effective dielectric constant of the composite to be enhanced. To provide context to the discussion of materials selection, this section first provides a brief description of the concepts behind each of the composite classes.

3.3.1 Composite Class 1 – MU45

MU45 was the first of the three composite classes to be developed, and as such, it employs the most conventional approach of the three high dielectric constant composite classes. The approach to MU45 is conventional in that the dielectric constant is increased by combining perovskite ceramic materials with a highly polar binder. By using a polar binder with a high dielectric constant, both of the major composite components have a high dielectric constant. This approach has been explored many times by other

researchers, and polyvinylidene fluoride is a commonly used polar polymer for this approach. The binder chosen for MU45, cyanoethylated pullulan, has more recently been studied for this approach due to its dielectric constant being approximately 1.75 times higher [10]. Cyanoethylated pullulan has been incorporated into at least two previous polymer-ceramic works on high dielectric constant composites [10, 11].

MU45 is unique compared to previous works incorporating cyanethylated pullulan in two ways. First, MU45 utilizes ceramic particles in three distinct particle size ranges according to the previously discussed trimodal particle packing. The use of trimodal particles significantly increases the particle packing density over that achievable with particles of a single size distribution. The volumetric density of ceramic particles is thus the highest of all materials forming the composite. The polymer content is minimized while ensuring that the mechanical integrity of the composite is maintained. Second, MU45 was produced as a bulk material in contrast to the thin films developed by other researchers. Previous works on composites including cyanoethylated pullulan focused on this films between 100 and 500 μm [10, 11]. MU45 was routinely produced at thicknesses on the order of millimeters up to a few centimeters.

3.3.2 Composite Class 2 – MU100

The MU100 composite class is unique by the choice of the binder material and the in-situ polymerization of the binder after the ceramic particles have been fully compacted. By delaying polymerization of the binder until after the composite materials have been fully compressed, the volumetric polymer content is minimized. This application of in-situ polymerization restricts the polymer content to only filling the natural voids between

ceramic particles ideally without increasing inter-particle distances. In other composites that simply mix ceramic particles with pre-polymerized macromolecules, the packing of the ceramic particles is limited by the space in which the long polymer chains already occupy. With in-situ polymerization, the polymer chain length and volume is limited by the space available between packed ceramic particles.

The binder employed in MU100 is also unique. While many polymer-ceramic composites functionalize the surfaces of the ceramics with a coupling agent to improve particle dispersion and interface to another binder, MU100 eliminates the extra binder and achieves mechanical integrity through the sole use of coupling agents. The binder takes the form of a polysilsesquioxane that directly bonds to the surfaces of the ceramic particles and cross-links into a three-dimensional network.

MU100 also utilizes a trimodal distribution of ceramic particles. As in the first composite class, the three size ranges of ceramic particles allow for a greater volumetric density of the high permittivity material. The volumetric polymer content is minimized through in-situ polymerization and the selection of a polysilsesquioxane binder. Thus, MU100 uses the first two of the three concepts listed in section 2 of this chapter.

3.3.3 Composite Class 3 – MU550

The concepts behind the MU550 composite class make it likely the most novel of the three composite classes. MU550 utilizes the first and third concepts presented in section 2 of this chapter. Of particular importance is that MU550 uses liquid fillers to displace the voids within the composite. By incorporating both solid and liquid phases into its structure, MU550 has a hybrid nature. To facilitate the impregnation of the liquid filler

throughout the composite, a composite formation process has been developed to form a network of small channels along the binder network through which the liquid filler can flow.

The binder for the hybrid composite is a water-gelling thermoreversible polymer. The polymer is added to the ceramic particles while melted in water. The ceramic particles and binder are compacted while the binder is in this melted wet state. As the polymer cools, it forms a gel with the water content that has not been removed during compaction of the mixture. The particle density is able to remain high with this polymer due to the wet pressing technique and the manner in which the gel forms as the mixture is cooled. The composite is then heated to a temperature below the polymer melting temperature to remove the water from the gel. The gel structure does not collapse as the water is removed due to the supporting structure of the ceramic particles, but the removal of the water leaves a substantial number of void channels throughout the binder network that can then be filled with a fluid that does not cause the binder to gel. In this way, the volume of the polymer is minimized by removing the water, and the mechanical integrity of the composite is maintained by replacing the water with a fluid that does not form a gel.

As with the other composite classes, a trimodal size distribution of ceramic particles is used to maximize the particle packing density. The trimodal particle distribution of the MU550 composite is the same as the distribution used in MU45 and MU100. Since the binder is not fully formed while the composite is compressed and excess binder can be squeezed out, the density of the trimodal particle distribution in MU550 can reach approximately the same levels as that obtained in MU100.

3.4 High Dielectric Constant Ceramics

The ceramics incorporated into the composites are the highest dielectric constant material, so the volume percentage of ceramic content is maximized. Some ceramics exhibit extremely large dielectric constant values due to their perovskite structure. This section provides a theoretical background on perovskite ceramics followed by details behind the selection of the ceramic used in the high dielectric constant composites.

3.4.1 Overview of Perovskite Ceramics

Perovskite materials have been of significant interest for more than sixty years. Applications of perovskite materials were first independently studied by several countries during World War II, primarily due to their ferroelectric and piezoelectric properties [12]. Since then, many types of perovskite materials have been created in the laboratory with a wide range of properties and potential applications [12].

Despite the variety of perovskite materials and unique properties that have been developed, perovskite materials with ferroelectric and piezoelectric properties remain of primary interest in electrical engineering for their applications in energy storage, energy transducers, high dielectric constant materials, and sensors. Many researchers have investigated composite materials with perovskites to incorporate their ferroelectric and piezoelectric properties with materials having improved mechanical properties. As the composites have improved, perovskite nanoparticles have been implemented. This section will detail perovskite materials, focusing on their structure, ferroelectric and piezoelectric properties, and two methods of nanoparticle synthesis.

Perovskite materials receive their name from their common structure to calcium titanate (CaTiO_3), which is traditionally referred to as perovskite [13]. Perovskites have the basic chemical formula given in equation (3.1).



The symbols A and B represent positively charged metal cations. The formula of equation (3.1) can become more complex for more exotic perovskites. A solid solution can be formed by two metal cations in ratios that total one for the A component, as given in equation (3.2). The symbol x is a number between zero and one.



More exotic perovskites have been developed with two or more elements represented by B in equation (3.2) [12]. Above the Curie temperature, most perovskites have the cubic structure. In the case of CaTiO_3 , calcium ions are located at the eight corners of the structure. The titanium ion is centered in the cube. Lastly, the oxygen atoms are found at the center of the faces.

One of the perovskites of particular interest due to its ferroelectric and piezoelectric properties is barium titanate, BaTiO_3 . As the similarities of its chemical formula to calcium titanate implies, the calcium ions of calcium titanate are replaced by barium. The coordination of the cations can be determined for barium titanate based upon the unit cell. The titanium ion at the center of the cell is coordinated with the six oxygen ions at the face centers. The barium cations at the corners are coordinated with twelve oxygen atoms.

The cubic structure is useful in describing the arrangement and coordination of barium, titanium, and oxygen atoms, but barium titanate is most often used in

applications with other unit cell structures. Below the Curie temperature, barium titanate takes on a tetragonal structure [12]. The tetragonal structure distorts the symmetry of the cubic structure. One of the side lengths is longer than the other two sides. This distortion results in a loss of charge symmetry and a net electrical dipole. This phenomenon is the basis for the ferroelectric property of perovskite materials.

Perovskites are notable as high dielectric constant materials due to their ferroelectric properties [14]. The spontaneous polarization of ferroelectric materials is responsible for electrostatic energy storage in the electric dipole formed in the material's lattice. The polarization of the material is dependent on the history of the electric field applied to the material. Figure 22 provides an example of a hysteresis loop for a perovskite material.

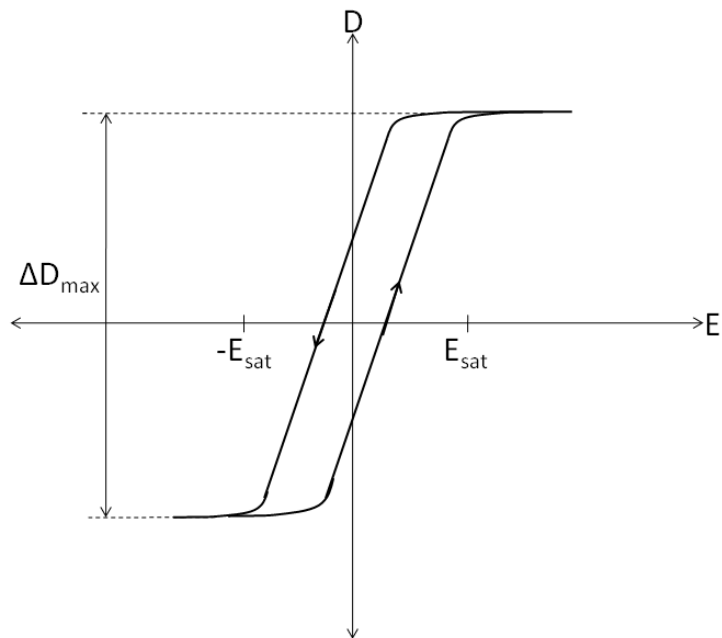


Figure 22. Example Hysteresis Curve of a Perovskite Material

After the electric field, E , applied to the material is removed, the polarization or electric flux density, D , does not go to zero. Instead, ferroelectric materials exhibit a remnant polarization. The polarity and magnitude of the polarization is dependent on the history

of the applied electric field. The similarities of the hysteresis curve to the *B*-*H* curves of ferromagnetic materials influenced the naming of ferroelectric materials [15].

As discussed in Chapter 2, the polarization and the electric field are related by the permittivity. Therefore, the dielectric constant can be taken as the slope of the path followed in Figure 3 when normalized by the permittivity of free space. When the magnitude of the electric field is less than its saturation value, E_{sat} , the slope of the curve and the dielectric constant are very large. This is the normal region of operation of the material in energy storage devices. When the magnitude of the electric field is greater than the saturation value, the material is considered saturated and the dielectric constant is significantly lower. Saturation of the material can be understood as the alignment of all the domains of electrical dipoles in the material. Saturation of the material is avoided in standard applications of ferroelectric materials, such as in capacitors. In addition to the dependence of the dielectric constant to the applied electric field, the dielectric constant has a high dependence on the temperature and frequency of operation.

Another interesting property of some perovskite materials is the piezoelectric effect. The piezoelectric effect relates the strain on the material to the applied or induced voltage [16]. The direct piezoelectric effect describes the voltage induced across the material due to an applied stress, T [Pa]. When no stress is applied, there is no electric displacement induced. However, when a stress is applied to the material, an electric displacement is induced. The presence of a voltage across the material when a stress is applied can be attributed to the distortion of the lattice, causing electric dipoles. In this case of the converse piezoelectric effect, an electric field, E [V/m], is applied to the material. Without the electric field, the induced stress, S [Pa], in the material is zero. However,

when the electric field is applied, a stress is induced in the material. Again the relationship between the electric field and the stress can be attributed to the distortion of the lattice, creating a small change in the material dimensions.

3.4.2 Selection of Ceramic Material

As evidenced by its use in several of the notable works cited at the beginning of this chapter, PMN-PT is an attractive option as the ceramic material. It exhibits a dielectric constant more than six times higher than that of barium titanate [2]. However, PMN-PT and many other lead-based and other perovskites were not considered eligible materials in the development of the composites due to their health risks and the lack of handling equipment to manage those health risks. Since the composites must be machinable, the creation of toxic dusts or flakes when cutting composites with lead or other toxic compounds is unacceptable. If the requirements of a high dielectric constant composite are changed such that the machining capability or the resulting health risk is minimized, replacing the ceramics used in this work with PMN-PT or other perovskites could offer dielectric properties much higher than those achieved in this work.

Another common substitute for barium titanate is the solid solution of barium strontium titanate. The relative amounts of barium and strontium are adjusted to change the Curie temperature between that of pure barium titanate and that of pure strontium titanate. The Curie temperatures for barium titanate and strontium titanate are approximately 120 C and -168 C, respectively. By tuning the Curie temperature to be around the operating temperature of the ceramic, the dielectric constant of the ceramic can be greatly enhanced. An example of tuning the Curie temperature is provided in Figure 23 [17]. The graph shows the dielectric constant and losses with respect to frequency and temperature

for $\text{Ba}_{0.6}\text{Sr}_{0.4}\text{TiO}_3$ produced by TRS Technologies Inc. The added strontium in comparison to barium titanate has the effect of lowering the Curie temperature from around 120 C for barium titanate to around 5-10 C in Figure 23. The peak in the dielectric constant at the Curie temperature is very pronounced as the dielectric constant is more than five times the typical value below the Curie temperature.

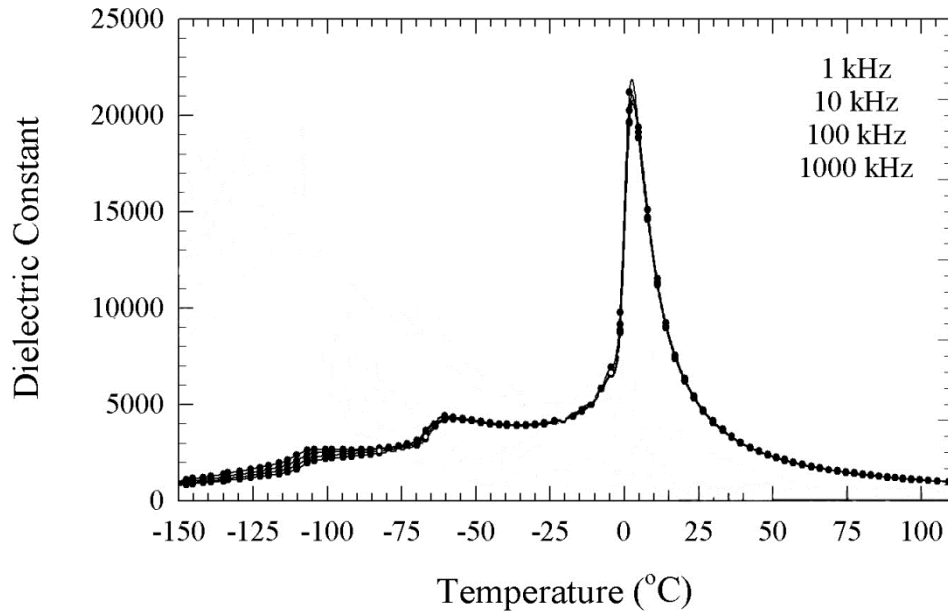


Figure 23. Dielectric constant and dielectric loss of 60/40 barium strontium titrate as a function of temperature and frequency. Data included with permission of TRS Technologies [17]

Despite the significant increase in the dielectric constant, there are two negative aspects of operating near the Curie temperature. As seen in Figure 23, the peak in the dielectric constant is relatively narrow, resulting in a high dependence of the dielectric constant on temperature. Above the Curie temperature, the lattice structure is cubic, and the dielectric constant decreases with increasing temperature. Below the Curie temperature, the lattice structure is tetragonal for a wide temperature range. Although the dielectric constant decreases rapidly from its peak at the Curie temperature, the dielectric constant in the temperature range at which the lattice structure is tetragonal is relatively flat. A second

negative aspect of operating near the Curie temperature is increased dielectric losses. While the losses are highly frequency dependent, a peak in the dielectric losses, denoted by the empty circles in Figure 23, is evident near the Curie temperature.

Since the composites developed in this effort have a requirement for operation over a wide temperature range, barium titanate is used rather than barium strontium titanate to reduce the variation in the composites' properties with temperature. Although this selection reduces the peak effective dielectric constant achievable by the composites, it provides much greater temperature stability and a wider variety of potential applications.

3.5 Binder Materials

Since the three composite classes developed in this work differ significantly in the concepts behind how the dielectric constant is increased, the specific properties desired for the binder in each composite are dependent on the method of composite formation. In general, a low molecular weight was considered advantageous for efficient particle packing as described in Chapter 2. The binders and their properties are significantly different, so each is described independently in the context of its intended application.

3.5.1 Cyanoethylated Pullulan

Cyanoethylated pullulan is the binder used in the MU45 composite. The base of this polymer, pullulan, is a common polysaccharide [18]. The high polarity of the binder arises from the cyanoethylation of the pullulan [11]. Cyanoethylation refers to the chemical addition of acrylonitrile to a compound with a hydroxyl group [19]. Acrylonitrile and nitriles in general contain the cyano functional group, consisting of a carbon-nitrogen triple bond. This carbon-nitrogen triple bond is highly polar due to the

strong electronegativity of the nitrogen atom. The addition of the acrylonitrile groups along the pullulan imparts a net polarity to the binder as a whole.

The cyanoethylated pullulan was obtained commercially through Shin-Etsu Chemical Co., Ltd. Shin-Etsu markets four products as cyanoresins, and the cyanoethylated pullulan is used in this work is referred to as CR-S. A softening point is reported at 90–110 C. CR-S is reported to have a dielectric constant of 18 at 20 C and 1 kHz. The dielectric constant of CR-S has been reported to be 21 at 1 kHz [10]. However, as with all other known highly polar polymers, the dielectric constant decreases significantly with frequency before the VHF and UHF bands. It was noted in the previous study that the peak of the dielectric losses was observed at approximately 4 MHz [10]. This indicates that 4 MHz is a resonant frequency for the polarization mechanism of CR-S, and the dielectric constant decreases significantly above approximately 10 kHz [10]. While CR-S is one of the best polar polymers available to form high dielectric constant composites in a conventional method, the effectiveness of these polar polymers is limited at the high frequencies of interest for antenna applications.

3.5.2 Polysilsesquioxanes

Coupling agents, including silanes and titanates, are commonly applied to particle surfaces in composite systems [20, 21]. The coupling agents are conventionally employed as buffers between the inorganic chemistry of ceramic fillers and the organic chemistry of polymers [20]. Many properties are cited as being improved by uniting the two phases of the composite with a coupling agent, including the particle dispersion, electrical and mechanical properties, rheological control, and particle surface wetting [20]. Titanates are claimed to have additional potential due to the increased number of functional groups

on a titanate compound [21]. However, details are provided here on silane coupling agents only due their more extensive use and more developed technology.

Silanes of particular interest can be classified as organofunctional alkoxysilanes and have the general formula of equation (3.4) [22]. The symbol R' represents an alkoxy moiety, and although the symbol n can be a number between 1 and 4, the class of interest has an n value of 1, representing trialkoxysilanes [22]. The symbol R represents a non-hydrolyzable organic group [22].

$$R_nSiR'_{(4-n)} \quad (3.4)$$

The alkoxy moieties are often methoxy or ethoxy, and these groups easily hydrolyze and later bond to inorganic surfaces containing hydroxyl groups [22]. The organic group represented by R provides compatibility with organic binders and is considered an organofunctional group. Table 3 shows three examples of trialkoxysilanes that can be used as coupling agents.

Table 3. Examples of Trialkoxysilanes for Particle Functionalization or Formation of Polysilsequioxane

<u>Vinyltrimethoxysilane</u>	<u>Vinyltriethoxysilane</u>	<u>Aminopropyltriethoxysilane</u>
R : -CH = CH ₂ vinyl group R' : Me -CH ₃ methyl group	R : -CH = CH ₂ vinyl group R' : Et - CH ₂ -CH ₃ ethyl group	R : -CH ₂ -CH ₂ -CH ₂ -NH ₂ aminopropyl group R' : Et - CH ₂ -CH ₃ ethyl group

Silanes have been effectively implemented as coupling agents in previous composites incorporating barium titanate and barium strontium titanate [23, 24]. It has been shown that a pre-treatment of the particles in hydrogen peroxide can increase the number of hydroxyl groups with which the silanes can bond, creating more sites for coupling between the inorganic and organic phases [25]. Using these methods, silanes have long

been successfully utilized as coupling agents. However, their potential was extended in a novel way in this study by not coupling to a separate binder polymer but rather utilizing the silanes as the composite binder itself.

While the silanes are intended to only form a single functionalized layer on the surface of the particles when acting as coupling agents, the silanes can also form highly networked polymers called polysilsesquioxanes [26]. The polysilsesquioxane forms through the uncontrolled hydrolytic condensation of the organotrialkoxysilane into a three-dimensional gel [26, 27]. The structure of the network can be random or have an ordered ladder, cage, or partial cage structure [28]. Figure 24 illustrates an example of how a polysilsesquioxane network can begin to form in the voids between barium titanate particles.

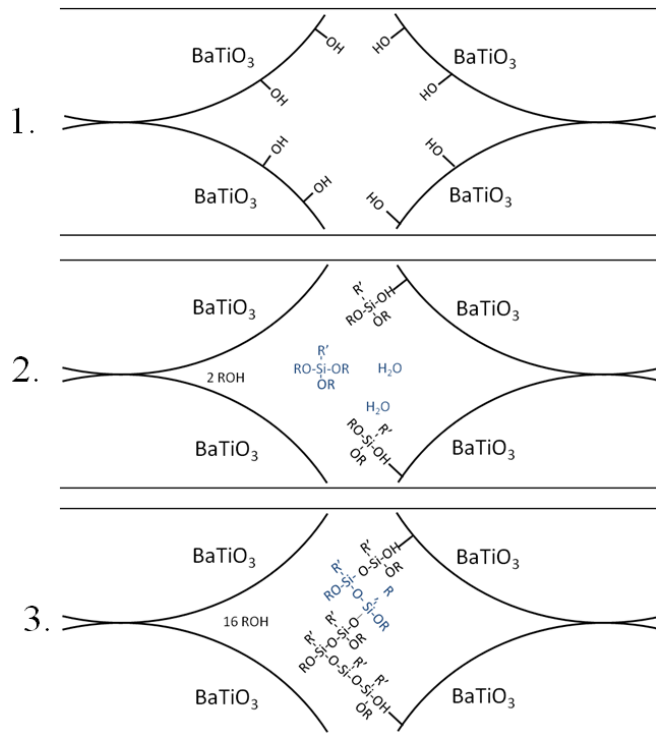


Figure 24. Example of a single polysilsesquioxane network being formed in a void between adjacent barium titanate particles. An actual void would ideally be completely filled with a highly cross-linked network

Many of the hydrolysis and condensation reactions are not shown in the formation of the link between the two particles, but the transition from an empty void with hydroxylated barium titanate surfaces to a single link between two of the four particles is shown. The same process could occur at many sites within the same void, and there are many points at which the alkoxy groups could join to form a more highly linked network.

Polysilsesquioxanes were chosen as the binder for one type of composite due to their perceived advantages over conventional polymers. First, they form covalent bonds along the ceramic surface, providing a stronger bond than polymers that do not directly bond with particles. Second, since the network can be polymerized in-situ, the polymer can be formed within the confines of the voids. By building the polymer up from the particle surfaces into the void, the ceramic packing density is ideally not increased by the inclusion of the binder. Lastly, polysilsesquioxanes can form highly cross-linked networks within the voids, increasing the composite's mechanical strength over composites with the same particle packing density with conventional long chain polymers. The three trialkoxysilanes detailed in Table 3 and some titanate coupling agents were considered for the precursors of the polysilsesquioxane binder. It had been previously shown that thin films could be formed by the polymerization of vinyltrimethoxysilane [27]. The same silane was effectively implemented in this effort as a composite binder. However, due to the methanol vapors released as a byproduct of the hydrolysis reaction, it was not preferred for health reasons. Triethoxyvinylsilane was substituted as the precursor and was found to exhibit similar polymerization behavior as the vinyltrimethoxysilane without producing methanol vapors.

3.5.3 Agarose

In the concept for the MU550 composite class, a gelling polymer is used as the binder. The polymer must be capable of being pressed while in solution with the solvent and forming a gel when cooled. It must be possible to remove the solvent from the gel without degrading the mechanical integrity of the binder. The polymer must also be compatible with the fluid void filler in order to retain its mechanical strength by neither solvating nor swelling when saturated in the filler. A high melting temperature is also desirable to maintain mechanical strength at high temperatures.

Gels can be classified as either chemical gels or physical gels [29]. Chemical gels are characterized by the formation of a network based on covalent bonds, excessive heating of the gel can result in irreversible degradation due to the breaking of the covalent bonds [29]. For example, the formation of the polysilsesquioxane described in the previous subsection is a sol-gel process in which the network is formed through covalent bonds. A physical gel obtains its structure through van der Waals interactions between individual chains, so the attraction between chains can be altered through heating [29]. When the solution is cooled, the van der Waals interactions again dominate chain interaction, reforming the structure [29]. Thus, these physical gels are considered to be thermoreversible [29].

Gels can be formed from either biopolymers or synthetic polymers. Since the intention behind using a gelling polymer as the binder in MU550 is to form small void channels throughout the composites through which a fluid filler can infiltrate, it was considered advantageous to select a polymer that gels with a very high solvent content. Biopolymers are known to be capable of retaining very high relative amounts of solvent with solvent

content above 99% achievable [29]. For this reason, biopolymers were almost exclusively considered for this application. However, it may also be possible to implement the technique behind the MU550 class of composite with a synthetic polymer gel or even chemical gel.

Biopolymer gels that naturally occur in nature unsurprisingly use water as the gel solvent. One of the most common gels is formed from gelatin, which is found in the skin, bones, and other tissues of animals. Other biopolymer gels, including agar and carrageen, can be extracted from seaweed. Carrageen was not extensively considered, but it is unlikely to be the best choice due to being charged [29]. In this work, both gelatin and agar were effectively implemented as the binder in MU550 composites. Agar was the preferred binder due to its melting temperature of 85 C, which allows for a much higher temperature range of operation than the relatively low melting temperature of gelatin at below 35 C. It is interesting to note that these gelling polymers exhibit hysteresis in the melting and gelling temperatures. If an agar gel is melted to a solution at 85 C, it must be cooled again to below 40 C to gel. Agar was also selected due to observation that agar gels were as strong as or stronger than those made with high gelatin concentrations.

Agar is a gelling biopolymer that actually consists of agarose and agarpectin. Agarose is the primary component of agar and is responsible for the gelling capability of agar. While agar containing both agarose and agarpectin was most often used to make MU550, there are advantages to exclusively using agarose, especially for lower frequency investigations. Agarpectin carries a net charge, and it is believed to contribute ions when saturated in a solvent. Although these ions would have negligible effects at the VHF and UHF frequencies of interest in this work, they are incompatible with low

frequency operation as a dielectric. Therefore, it is advantageous to isolate agarose, which is a neutral molecule, from agarpectin, and techniques have been established to perform this separation process [30].

Agarose is a linear polysaccharide [30]. As with other biopolymers that form gels, the polymer chains form helices upon gelling with the structure for agarose as a polysaccharide gel noted to be a double helix [29]. Analysis through electron microscopy has shown the growth of 10 nm diameter fibers composing the gel structure [29]. There is some debate of the process of gelling, specifically whether the polymers in solution are random coils that form the helix upon cooling or the helix is simply bound to a lesser extent when hot and more tightly bound when cooled [29]. The solvent is intercalated within the structure, and hydrogen bonding plays an important role in the retention of water [29]. The molecular weight of the polymers is typically low enough to not limit the ceramic particle packing significantly. For gelatin, experiments have shown average single chain radius of gyration of 17 nm [29]. Other analyses of gelatin have observed fiber diameters ranging from 2 to 20 nm and the radius of gyration calculated at approximately 10.6 nm. These polymer dimensions are considered small enough to fit within the voids remaining of a tightly packed ceramic particle distribution with the smallest ceramic particle dimensions on the scale of 50 nm.

3.6 Void Fillers

3.6.1 Survey of High Dielectric Constant Fluids

When examining high dielectric constant fluids, many highly polar liquids are available. Table 4 is a list of materials that are liquid around room temperature and have a

dielectric constant greater than 40. The dielectric constant and temperature of measurement are given. Due to the multitude of sources of information on these materials, the measurement frequency is inconsistent between materials. Positive attributes are listed for some materials if they are noted to be safe, inexpensive, or have a low evaporation rate. The primary way in which this list is narrowed is by the listed negative attributes as most of the materials have at least one negative attribute that fully disqualifies them. A common disqualifier was toxicity. For example, the fluid with the highest dielectric constant noted in this list, hydrocyanic acid with a dielectric constant of 158, is extremely toxic and considered impractical due to safety issues. It is interesting to note that two of the three highest dielectric constant liquids listed, hydrocyanic acid and hydrogen cyanide, have a high polarity at least partially due to the cyano group. This is similar to the high polarity of the cyanoresin CR-S due to the addition of the cyanoethylation of pullulan.

There are also some very inexpensive and safe chemicals, including water and glycerin, with room temperature dielectric constants of approximately 80 and 47, respectively. Water, however, is disadvantageous as the filler fluid as it swells the agar and weakens the strength of the binder. It also has an unacceptably high evaporation rate for use above room temperature if the composite is not sealed. Glycerin, while having a lower evaporation rate than water, exhibits higher dielectric losses and is slightly too viscous to fully penetrate a composite's voids.

Dimethylsulfoxide (DMSO) is a relatively non-hazardous substance with a high dielectric constant of 48.9 [31]. However, DMSO also has a high freezing temperature just below room temperature at 18.45 C [31]. DMSO could be impregnated into the

composite as a liquid, and subsequent freezing would be unlikely to damage the composite. However, the permittivity with respect to frequency changes significantly when these liquids are frozen. Although the high dielectric constant could likely still be observed while frozen at low frequencies, the relaxation frequency at which the dielectric constant significantly drops will be lowered below the frequency range of interest. A good example of the effects of changes in permittivity when a liquid is frozen is the much lower heating rate of solid ice in comparison to liquid water. Since the resonant frequency of the water dipole has been lowered when frozen, the peak in the losses is lowered below the frequency of microwave heating. While DMSO may be a candidate strictly for applications above room temperature, its high freezing point makes it incompatible with the broad temperature range considered this work.

The remaining candidate materials in Table 4 include glycerin carbonate, ethylene carbonate, propylene carbonate, and butylenes carbonate. As their names suggest, these materials are related by the classification as alkylene carbonates. They feature high dielectric constants, relatively low toxicological hazards, and very low vapor pressures, resulting in low evaporation rates. With the exception of ethylene carbonate, the alkylene carbonates also remain liquid through a wide temperature range around room temperature. Due to the combination of many of the desired properties in a liquid filler, alkylene carbonates were selected as the primary liquid fillers for incorporation into composites, and the following section provides details of their physical and dielectric properties.

Table 4. High dielectric constant liquids considered for void filler [32-34]

Liquid	Dielectric Constant	Temp.	Positive Attributes	Negative Attributes
Hydrocyanic Acid	158	32F		Extremely Toxic
Glycerin Carbonate	111.5	20C	Low Evaporation	Dispersive
Hydrogen Cyanide	95.4	70F		Extremely Toxic
Ethylene Carbonate	90.5	40C	Low Evaporation	Solidifies Below Room Temp
Trimethyl-sulfanilic Acid	89	64F		Hazardous
Hydrogen Peroxide	84.2	32F	Inexpensive	Corrosive
Hydrogen Fluoride	84.2	32F		Very Toxic
Formamide	84	68F		Toxic
Sulfuric Acid	84	68F		Hazardous
Water	80.4	68F	Safe - Inexpensive	High vapor pressure - Swells agar
Deuterium Oxide	78.3	77F		Impractical in comparison to water
Propylene Carbonate	67	20C	Low Evaporation	
Glycerin	47-68	Room Temp	Safe - Inexpensive	High dispersion
Formic Acid	58			Toxic
Butylene Carbonate	57.5	20C	Low Evaporation	
Dimethyl Sulfate	55	68 F		Very Toxic
Dimethylnitroxamine	54	68F		Very Toxic
Hydrazine	52	68F		Very Toxic
Dimethylsulfoxide	47.2			Solid below room temp
Furfural	42	68F		Hazardous
Citraconic Anhydride	40.3	68F		Toxic

3.6.2 Alkylene Carbonates

Alkylene carbonates have been integrated into several processes in the past two decades as reactive components and solvents in industrial applications [35, 36]. They have been cited for their ability to substitute for other chemicals that are hazardous to the health of humans or the environment and are not restricted as volatile organic compounds [36].

The biodegradability and relatively low toxicity make them an attractive choice over much harsher chemicals [36]. The effectiveness of alkylene carbonates as solvents is due to their highly polar chemical structure, which also results in very high dielectric constants. A study of the dielectric properties of ethylene carbonate, propylene carbonate, glycerine carbonate, and butylene carbonate showed properties comparable to and occasionally exceeding those of water [33]. The dielectric constant of butylenes carbonate, propylene carbonate, and glycerine carbonate at 20 °C were measured at 1 MHz to be 57.5, 66.6, and 111.5, respectively [33]. Ethylene carbonate is a solid at room temperature, but its dielectric constant in the liquid state at 40 °C was measured to be 90.5 [33]. While glycerine carbonate exhibits the highest dielectric constant of these four alkylene carbonates, it has been found to be more dispersive and have higher dielectric losses at the high frequencies of interest for antennas. To increase the dielectric constant of propylene carbonate, blends of propylene carbonate and ethylene carbonate are commonly made. Blends with 25%, 50% and 75% ethylene carbonate exhibit a higher dielectric constant than 100% propylene carbonate while remaining liquid at room temperature. A blend of EC50 containing 50% ethylene carbonate and 50% propylene carbonate exhibits dielectric properties similar to water. The freezing temperature of the EC50 blend has been reported to be 4 C [37].

Alkylene carbonates have been seen to be safe and exhibit dielectric properties on par with water. However, compared to water or other common solvents, the evaporation rate of alkylene carbonates is exceptionally low. The vapor pressure of ethylene carbonate and propylene carbonate has been reported to be at or below 2.67 Pa [36]. For comparison, the vapor pressure of acetone is between 13.32 and 53.3 kPa near room

temperature, and the vapor pressure of water is approximately 2.3 kPa at room temperature. The low vapor pressure and correspondingly low evaporation rate result in alkylene carbonates' properties exceeding those of water for integration into high dielectric constant composites. As with any solvent that is used as an insulating material, care must be taken to avoid contamination with potential solutes that could result in increased electrical conductivity. Therefore, the compatibility of other materials for inclusion in composites incorporating alkylene carbonates is dependent upon their solubility in alkylene carbonates. To maintain the electrical and mechanical properties of the composite, the components must be insoluble in the alkylene carbonates and the solvent must not be contaminated with ions.

3.7 Examples and Physical Descriptions of Composites

Before describing the dielectric characterization of the high dielectric constant composites in Chapter 4, this section provides examples of how the composites have met the desired physical characteristics, including the capabilities to be produced in bulk quantities and machined as required for integration into high power antennas. The composites were compacted and formed through high pressure uniaxial pressing in cylindrical dies. The sizes produced through this work ranged from diameters of 1.905 cm (3/4") and 2.54 cm (1") for material characterization up to diameters of 7.62 cm (3") and 11.43 cm (4.5") for the production of resonators and substrates. The maximum diameter that can be produced is only limited by the equipment available, so larger substrates are believed to be possible given the appropriate dies and presses. The composites were typically produced in thicknesses of 2-4 mm for purposes of dielectric evaluation. The lower limit of thickness that the pressing techniques could produce was

not thoroughly investigated, but samples with thicknesses of around 1 mm were produced. While thinner substrates are likely possible, the procedure used to obtain samples of 1 mm or less in this work was to sand and polish thicker samples down to the desired thickness. Thick samples greater than 1 cm were produced with some 1" diameter pieces produced in thicknesses greater than 2 cm. There is no upper limit to the thickness that can be produced, but the effects of increased variation in density as the thickness is increased should be considered.

Figure 25 shows a sample of MU45 with a diameter of 11.43 cm. It was the largest sample of the composites generated in the course of material development, and it is one of many large pieces that demonstrate the capability of producing the high dielectric constant composites in bulk quantities.

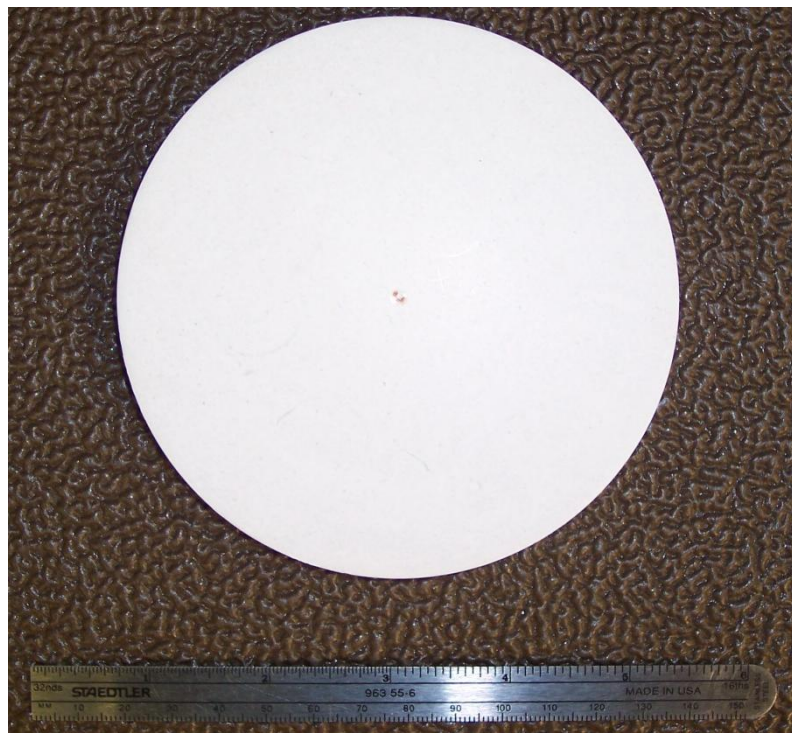


Figure 25. Sample of MU45 produced with a diameter of 11.43 cm

MU45 demonstrated excellent mechanical properties, making it a candidate for the most demanding machining requirements and other applications that put a premium on

robustness over dielectric properties. Due to the relatively high amount of polymer content, machining MU45 is similar to that of conventional plastics, producing flakes and curls of material as it is cut with a low amount of dust. Another example of the higher polymer content can be observed in the polished surfaces of MU45. As shown in Figure 26, a polished surface of MU45 exhibits a mirror-like glossiness that exceeds that of MU100 and MU550.



Figure 26. A sample of MU45 with a diameter of 2.54 cm showing the mirror-like glossy finish of finely polished MU45

The materials have been effectively machined with drills, lathes, mills, and other power cutting and grinding tools. Figure 27 provides an example of a 7.62 cm diameter sample that was cut into a rectangular geometry for testing as a substrate for a microstrip transmission line.



Figure 27. 7.62 cm diameter sample cut into rectangular shape as substrate for a microstrip transmission line

Figure 28 shows a series of 2.54 cm diameter samples of MU100 with holes drilled down the center axis of the cylinders. These holes were cut to mount the samples along the same axis, forming a much longer cylinder. This approach was taken as opposed to pressing one very long cylinder to avoid potential density variation along the length of a single thick pressed cylinder.

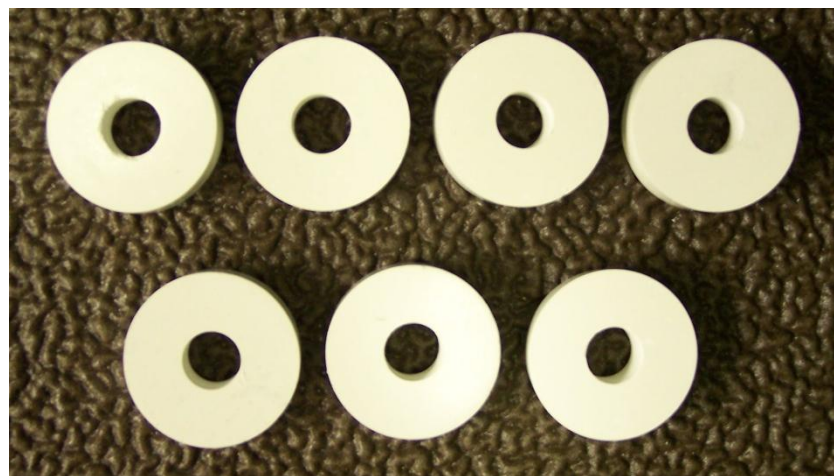


Figure 28. Samples of MU100 with holes drilled along the center axis

Figure 29 shows three views of a sample of MU100 with a diameter of 7.62 cm and a thickness of approximately 1.25 cm. This sample was implemented as a dielectric resonator in the high power antenna driver described in Chapter 5.

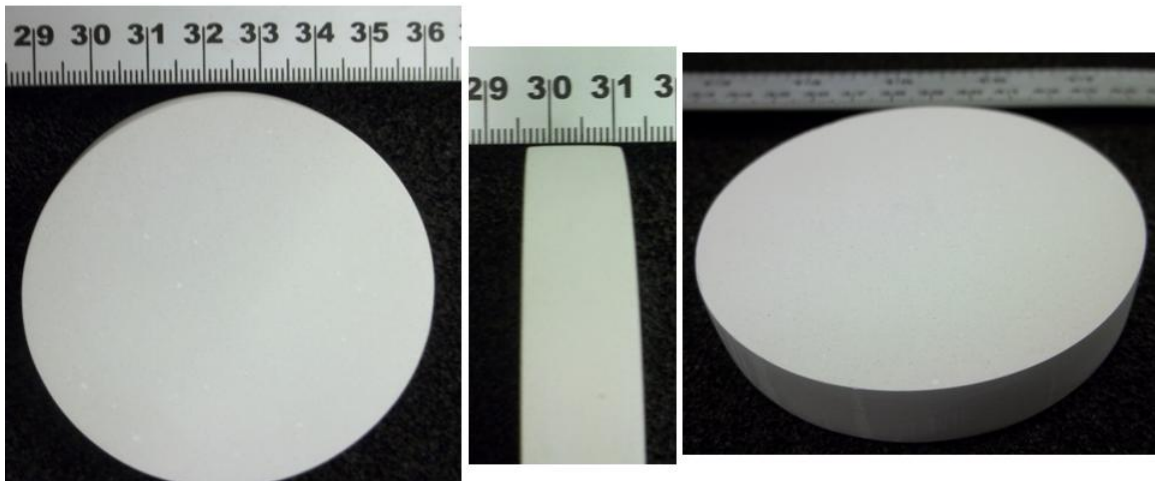


Figure 29. Multiple views of a sample made of MU100. The diameter is 7.62 cm, and the thickness is approximately 1.25 cm. This piece was used as the resonator in the high power DRA described in Chapter 5.

References for Chapter 3

- [1] P. Barber, S. Balasubramanian, Y. Anguchamy, S. Gong, A. Wibowo, H. Gao, H. Ploehn, and H. C. z. Loyer, "Polymer composite and nanocomposite dielectric materials for pulse power energy storage," *Materials*, pp. 1697-1733, 2009.
- [2] Y. Rao, J. Yue, and C. P. Wong, "High-K polymer-ceramic nano-composite development, characterization, and modeling for embedded capacitor RF applications," in *Proc. of the 51st Electronic Components and Technology Conf.* Orlando, FL, 2001.
- [3] H. Windlass, P. M. Raj, D. Balaraman, S. K. Bhattacharya, and R. R. Tummala, "Colloidal processing of polymer ceramic nanocomposite integral capacitors," *IEEE Trans. on Electronics Packaging Manufacturing*, vol. 26, pp. 100-105, 2003.
- [4] Y. Rao, S. Ogutani, P. Kohl, and C. P. Wong, "Novel polymer-ceramic nanocomposite based on high dielectric constant epoxy formula for embedded capacitor application," *Journal of Applied Polymer Science*, vol. 83, pp. 1084-1090, 2001.
- [5] V. Agarwal, P. Chahal, R. R. Tummula, and M. G. Allen, "Improvements and recent advances in nanocomposite capacitors using a colloidal technique," in *Proc. of the 48th Electronic Components and Technology Conf.* Seattle, WA, 1998, pp. 165-170.
- [6] S. Ogutani, S. A. Bidstrup-Allen, and P. Kohl, "Development of high-K photo-definable epoxy composites for embedded capacitors," in *Proc. of the 23rd IEEE/CMPT Int'l Electronics Manufacturing Technology Symp.* Austin, TX, 1998, pp. 199-205.
- [7] J. Borchardt, J. Alexander, K. Slenes, and R. d. l. Fuente, "Ceramic-polymer composite for high energy density capacitors," in *Proc. of the 16th IEEE Int'l Pulsed Power Conf.* Albuquerque, NM, 2007, pp. 294-297.
- [8] W. Eisenmenger, H. Schmidt, and B. Dehlen, "Space charge and dipoles in polyvinylidenefluoride," *Brazilian Journal of Physics*, vol. 29, pp. 295-305, 1999.
- [9] Y. Roiter and S. Minko, "AFM single molecule experiments at the solid-liquid interface: in situ conformation of adsorbed flexible polyelectrolyte chains," *Journal of the American Chemical Society*, vol. 127, pp. 15688-15689, 2005.
- [10] C. K. Chiang and R. Popielarz, "Polymer composites with high dielectric constant," *Ferroelectrics*, vol. 275, pp. 1-9, 2002.
- [11] Y. Suzuki, Y. Kataoka, and H. Matsui, "Electrical properties of composite cyanoethylated pullulan film," *Journal of Wood Science*, vol. 49, pp. 100-103, 2003.
- [12] F. S. Galasso, *Perovskites and High Tc Superconductors*. Amsterdam: Gordon and Breach Science Publishers, 1990.
- [13] T. Wolfram and S. Ellialtioglu, *Electronic and Optical Properties of d-Band Perovskites*. New York: Cambridge University Press, 2006.
- [14] J. M. Herbert, *Ferroelectric Transducers and Sensors* vol. 3: CRS Press, 1982.
- [15] F. S. Galasso, *Structure, Properties and Preparation of Perovskite-Type Compounds*. Oxford: Pergamon Press, 1969.

- [16] A. A. Vives and A. Arnau, *Piezoelectric Transducers and Applications*. Berlin: Springer, 2004.
- [17] TRS Technologies. Obtained through private communication. Used with permission. 2008.
- [18] K. Nishinari, K. Kohyama, P. A. Williams, G. O. Phillips, W. Burchard, and K. Ogino, "Solution properties of pullulan," *Macromolecules*, vol. 24, pp. 5590-5593, 1991.
- [19] H. A. Bruson, "Cyanoethylation," in *Organic Reactions*: John Wiley and Sons, 2011, pp. 79-135.
- [20] K. Weissenbach and H. Mack, "Silane Coupling Agents," in *Functional Fillers for Plastics*, M. Xanthos, Ed. Weinheim, Germany: Wiley-VCH Verlag, 2005.
- [21] S. J. Monte, "Titanate Coupling Agents," in *Functional Fillers for Plastics*, M. Xanthos, Ed. Weinheim, Germany: Wiley-VCH Verlag, 2005.
- [22] G. L. Witucki, "A silane primer: chemistry and applications of alkoxy silanes," *Journal of Coatings Technology*, vol. 65, pp. 57-60, 1993.
- [23] S. Liang, S. R. Chong, and E. P. Giannelis, "Barium titanate/epoxy composite dielectric materials for integrated thin film capacitors," in *Proc. of the 48th Electronic Components and Technology Conf.* Seattle, WA, 1998, pp. 171-175.
- [24] N. Krueson, H. Manuspiya, P. Laoratanakul, and H. Ishida, "Dielectric properties enhancement in polybenzoxazine composite at multi-frequency range," *Advanced Materials Research*, vol. 55-57, pp. 105-108, 2008.
- [25] S. J. Chang, W. S. Liao, C. J. Ciou, J. T. Lee, and C. C. Li, "An efficient approach to derive hydroxyl groups on the surface of barium titanate nanoparticles to improve its chemical modification ability," *Journal of Colloid and Interface Science*, vol. 329, pp. 300-305, 2009.
- [26] I. E. dell'Erba, D. P. Fasce, R. J. J. Williams, R. Erra-Balsells, Y. Fukuyama, and H. Nonami, "Poly(silsesquioxanes) derived from the hydrolytic condensation of organotrialkoxysilanes containing hydroxyl groups," *Journal of Organometallic Chemistry*, pp. 42-51, 2003.
- [27] N. Takamura, T. Gunji, H. Hatano, and Y. Abe, "Preparation and properties of polysilsesquioxanes: polysilsesquioxanes and flexible thin films by acid-catalyzed controll hydrolytic polycondensation of methyl- and vinyltrimethoxsilane," *Journal of Polymer Science: Part A: Polymer Chemistry*, vol. 37, pp. 1017-1026, 1999.
- [28] R. H. Baney, M. Itoh, A. Sakakibara, and T. Suzuki, "Silsesquioxanes," *Chemical Reviews*, vol. 95, pp. 1409-1430, 1995.
- [29] J. M. Guenet, *Thermoreversible Gelation of Polymers and Biopolymers*. San Diego, CA: Academic Press Ltd., 1992.
- [30] Y. J. Jeon, Y. Athukorala, and J. Lee, "Characterization of agarose product from agar using DMSO," *Algae*, vol. 20, pp. 61-67, 2005.
- [31] "Technical Bulletin Reaction Solvent Dimethyl Sulfoxide (DMSO)," Gaylord Chemical Co. LLC, Slidell, LA.
- [32] "Dielectric constants of various materials," Delta Controls 1997.

- [33] Y. Chernyak, "Dielectric constant, dipole moment, and solubility parameters of some cyclic acid esters," *Journal of Chemical Engineering Data*, vol. 51, pp. 416-418, 2006.
- [34] Clipper Controls.(Access Confirmed 2013). Dielectric constant values. [Online]. Available:<http://www.clippercontrols.com/pages/Dielectric-Constant-Values.html>.
- [35] J. H. Clements, "Reactive applications of cyclic alkylene carbonates," *Industrial and Engineering Chemistry Research*, vol. 42, pp. 663-674, 2003.
- [36] H. Klein and T. Marquis, "Cyclic organic carbonates serve as solvents and reactive diluents," in *Coatings World*: Rodman Publishing, May/June 1997.
- [37] "Jeffsol EC-25, EC-50, EC-75," Huntsman Corporation, The Woodlands, TX.

Chapter 4: Dielectric Materials Characterization

4.1 Introduction

Characterization of the high dielectric constant composite materials was focused on the permittivity, dielectric strength, and composition. Examination of the permittivity required multiple methods due to the potential for variation of the permittivity with respect to frequency, applied voltage, and temperature. Since ferroelectric materials exhibit a strong dependence on these factors, their inclusion in the composite at a high volume concentration is likely to manifest many of these dependencies in the composite properties. The permittivity was measured using low voltage dielectric spectroscopy measurements to obtain a standardized measurement at the high frequencies relevant to antenna application. The results from this low voltage measurement method were supplemented with measurements taken under higher electric fields. These high voltage measurements included the measurement of the polarization with respect to electric field and the measurement of the voltage decay in an overdamped RC circuit. While these additional measurement methods provide information on the properties at a higher operating electric field, they are at lower frequencies than those relevant for antenna application. Therefore, the results of the three permittivity measurement methods must be interpreted together to obtain a more complete understanding of the composites' permittivities.

Measurement of the dielectric strength is critical to determine the limits of the electric field levels at which the composites can be effective. Since the composites are intended for high power antennas in which very high frequency content will be present in the

signal applied to the antenna, the measurements were obtained under relatively fast risetime pulse conditions. The fast risetime pulse more closely resembles the conditions of the composites' intended operation in a high power antenna.

Characterization of the composition of the materials utilized both thermogravimetric analysis and scanning electron micrography (SEM). Thermogravimetric analysis enabled the estimation of the relative content of ceramic, binder, voids, and, where applicable, liquid filler. SEM analysis examined the size and morphology of the ceramic particles included in the composite as well as the packing distribution of composite's constituent elements. The results of this compositional characterization informed the input parameters for the final characterization method, 3D simulation.

Finally, virtual composites were built within CST EM Studio using a custom macro introduced in Chapter 2 and described in detail later in this chapter. Incorporating the relative content of each constituent material as determined through the compositional analysis, the dielectric constant values obtained from the 3D analysis were compared with the results of the permittivity measurements. Due to the variety of characterization methods, a summary and discussion section on this topic in Chapter 7 interprets how the many results contribute to an integrated understanding of the composites' properties.

4.2 Dielectric Spectroscopy

4.2.1 Dielectric Spectroscopy Methods

Dielectric spectroscopy refers to the characterization of a material's permittivity with respect to frequency. In the course of this work, two commercially available sets of equipment were utilized for these measurements. A lower frequency band between 100

kHz and 30 MHz was measured using the 16451B Dielectric Test Fixture with the 4285A Precision LCR Meter from Agilent Technologies. A higher frequency range was measured between 200 MHz and 4.5 GHz using another set of Agilent Technologies equipment, including the 85070E Dielectric Probe Kit, the E5071C Network Analyzer, and materials measurement software. This suite of standard low voltage materials measurement equipment is shown in Figure 30.



Figure 30. Low voltage permittivity measurement equipment

The low frequency measurement equipment was used in the initial phases of this work due to its ability to measure thin films with a capacitive air gap method. However, measurements with the capacitive air gap method are very sensitive to the thickness and surface roughness of the sample under test, especially for high dielectric constant materials. Additionally, the upper frequency limit of 30 MHz was below the antenna frequencies of interest in this study. Therefore, no results from the 16451B test fixture are included here.

The high temperature probe of the 85070E dielectric probe kit was used in the measurements reported in the following sub-section. The high temperature probe can measure the permittivity of liquids, soft solids, and select solid materials at frequencies from 200 MHz to 20 GHz [1]. The E5071C network analyzer limited the upper frequency of measurement to 4.5 GHz. The high temperature probe is well-suited to measurement

of flat solid samples due to the relatively large flange of the probe as well as the relatively large 3.5 mm aperture. Additionally, the probe can operate from -40 C to 200 C, enabling material measurements with respect to temperature as well as frequency [1].

There are several material requirements to achieve an accurate measurement with the 85070E high temperature probe. Perhaps most important is the flatness of the sample, which is required to be as flat as the surface of the probe. The probe is reported to be lapped to ± 100 microinches, which corresponds to $\pm 2.54 \mu\text{m}$ [1]. Deviations in the flatness of the sample introduces air gaps between the electrode and the sample. The degrading effects of poor interfaces between electrodes and the high dielectric constant material can be explained directly when considering the case of a capacitor. At points on the electrode surface at which an air gap exists between the electrode and high dielectric constant material, the effective capacitance for that area is a series combination of the capacitance of the air gap and the capacitance of the high dielectric constant material. The series capacitance of these two materials is always less than the smaller capacitance in the series. Thus, the capacitance at these points of imperfect connection is less than the air capacitance, and the benefit of the high dielectric constant material is degraded at these points. A simple equivalent circuit for a capacitor made with a high dielectric material in which air gaps are present is shown in Figure 31. The symbol C_{air} [F] represents the capacitance of air gaps, and C_{HDM1} [F] and C_{HDM2} [F] represent, respectively, the capacitance of the high dielectric constant material in series with the air gaps and the capacitance of the high dielectric constant material in direct contact with the electrodes. The corresponding resistors represent the equivalent series resistance of the capacitive elements and are shown for completeness of the model. Resistive elements are

not included in parallel with the capacitive elements as it is assumed for the purpose of this analysis that there is no current leakage.

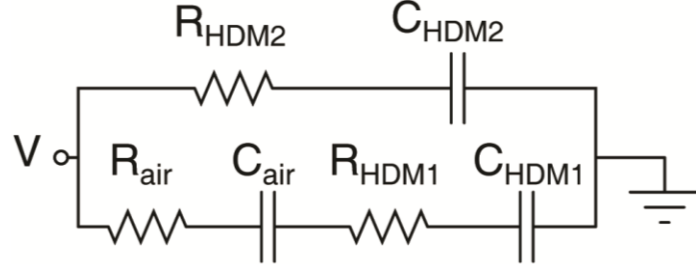


Figure 31. Equivalent circuit of a capacitor with air gaps

To simplify analysis of a capacitor with imperfect electrode and high dielectric material surfaces, it is assumed that the surfaces are relatively smooth such that the air gaps have a single common thickness, t_{gap} [m]. This assumption approximates a condition in which the surfaces are finished to a high degree with an abrasive medium of a single grit size. The total area of the capacitor electrodes will be defined as A [m^2], and the area of the capacitor electrodes at which an air gap exists is represented as A_{gap} [m^2]. Again for simplicity, the total distance between the two capacitor electrodes is considered to be a constant, t [m], at all points. The permittivities of free space, air, and the high dielectric constant material are represented as ϵ_0 , ϵ_{air} , and ϵ_r , respectively. With these definitions, the capacitances in the equivalent circuit of Figure 31 can be determined by equations (4.1) – (4.3) for a parallel plate capacitor with negligible fringe capacitance. Fringe fields are neglected, as their effects are minimal when high dielectric constant capacitor materials are used.

$$C_{air} = \frac{\epsilon_0 \epsilon_{air} A_{gap}}{t_{gap}} \quad (4.1)$$

$$C_{HDM1} = \frac{\epsilon_0 \epsilon_r A_{gap}}{t - t_{gap}} \quad (4.2)$$

$$C_{HDM2} = \frac{\varepsilon_0 \varepsilon_r (A - A_{gap})}{t} \quad (4.3)$$

A numerical analysis can be performed using equations (4.1) – (4.3) to understand the effects of changes to the air gap size and the area of the electrode-dielectric interface with air gaps on the measured capacitance and effective dielectric constant. Figure 32 plots the effects for air gaps with thicknesses of 2, 10, 30, and 125 microns, corresponding approximately to finishes obtained with 12000, 3000, 1500, and 200 grit abrasives, respectively. The capacitor assumed for these calculations has an electrode and dielectric material diameter of 2.54 cm and a thickness of 2 mm. The dielectric constant of the material is assumed to be 300.

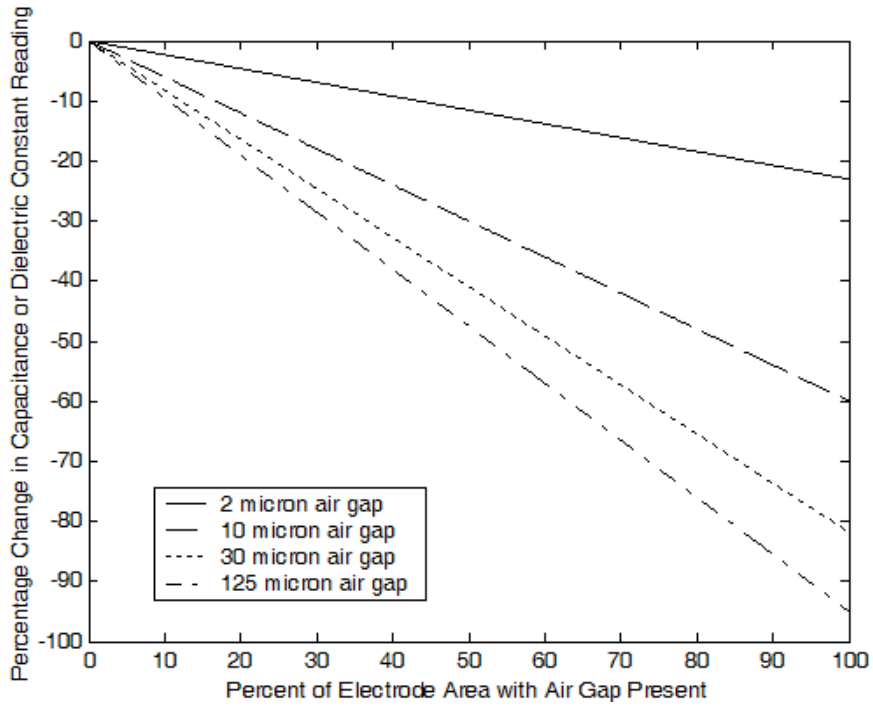


Figure 32. The effects on the capacitance or effective dielectric constant of a discrete air gap over a variable area of the electrode-material interface

As depicted in Figure 32, if the area of the electrode covered by air gaps is very small, less than 5%, the decrease in the capacitance or measured dielectric constant is also minimal. Although larger air gap thicknesses correspond to larger decreases in the

capacitance and effective dielectric constant of the energy storage volume, the decrease is kept minimal for even 125 micron air gaps with small areas. However, as the area covered by air gaps increases, the decrease in capacitance and effective dielectric constant quickly becomes a very significant factor. It is clear from Figure 32 that both the thickness of the air gaps present and the area covered by air gaps must be minimized. The thickness of the air gaps can be minimized by using very fine grit abrasives as small as 2 microns. However, even in this case, the presence of 2 micron abrasive cuts that constitute 50% of the surface area will result in a measured reduction of approximately 10%. The reduction in capacitance and effective dielectric constant measurements are reduced much more drastically for materials with even higher dielectric constants. For example, the same 50% coverage with 2 micron thick air gaps on a dielectric material with a dielectric constant of 1000 would cause approximately a 25% reduction in the measured capacitance and effective dielectric constant. Therefore, the surface preparation of the sample under test is critical to obtaining the best possible measurement.

Since the network analysis measurement method assumes that the material appears approximately infinite to the probe, the diameter must be greater than 20 mm, and the minimum thickness of the material under test, t_{MUT} [m], is given by equation (4.4) [1].

The symbol ϵ_r^* represents the complex relative permittivity.

$$t_{MUT} > \frac{0.02}{\sqrt{|\epsilon_r^*|}} \quad (4.4)$$

The frequency, f [Hz], of measurement is limited by the permittivity being measured as described by equation (4.5) [1]. This restriction is only relevant below 4.5 GHz for materials with an absolute value of complex permittivity above approximately 600.

$$f < \frac{110 \cdot 10^9}{\sqrt{|\epsilon_r^*|}} \quad (4.5)$$

Additional material assumptions for use of the 85070E probes include that the material is non-magnetic, isotropic, and homogenous [1]. Since no magnetic materials are incorporated into the composites and the composites are not polarized, there should be no conflicts with the non-magnetic and isotropic requirements. The composites are ideally also homogenous. However, local variations in the density or relative distribution of materials within the composite can manifest in variance in the permittivity readings across the sample surface.

The high frequency permittivity measurements are made through network analysis techniques, specifically by measuring the S_{11} scattering parameter. The S_{11} scattering parameter is defined in equation (4.6) as the ratio of the voltage of the reflected, negative-traveling wave to the voltage of the incident, forward-traveling wave. Since this is equivalent to the reflection coefficient, the S_{11} can be defined in terms of the characteristic impedance of the test fixture, $Z_0 [\Omega]$, and the impedance encountered at the material under test (MUT), $Z_{@MUT} [\Omega]$ [2].

$$S_{11} = \frac{V^-}{V^+} = \Gamma = \frac{Z_{@MUT} - Z_0}{Z_{@MUT} + Z_0} \quad (4.6)$$

The permittivity of the MUT can then be calculated based upon the impedance inferred from the S_{11} parameter. A disadvantage to this measurement method is that the S_{11} varies nonlinearly with values of $Z_{@MUT}$. Although $Z_{@MUT}$ is in general a complex number, it is assumed for this discussion to be purely real. Under this assumption, Figure 33 illustrates the nonlinear dependence of S_{11} with respect to the ratio of $Z_{@MUT}$ to Z_0 . When the ratio is approximately one order of magnitude greater or less than 1, the slope of the curve

becomes progressively smaller. There is a smaller change in the measured impedance for changes in $Z_{@MUT}$, and the accuracy of the measurement decreases. For larger dielectric constant values of the MUT, the impedance at the MUT decreases. Therefore, when measuring high dielectric constant values, large differences in the dielectric constant result in relatively small changes in the measured S_{II} , reducing the accuracy of the measurement. The typical accuracy for the real, ε_r' , and imaginary, ε_r'' , components of the complex permittivity, ε_r^* , provided by Agilent are given in equations (4.7) and (4.8) [1]. This stated accuracy of $\pm 5\%$ of the absolute value of the complex permittivity does not account for the previously discussed effects of the MUT, including surface roughness and homogeneity.

$$\varepsilon_r' = \varepsilon_r' \pm 0.05|\varepsilon_r^*| \quad (4.7)$$

$$\varepsilon_r'' = \varepsilon_r'' \pm 0.05|\varepsilon_r^*| \quad (4.8)$$

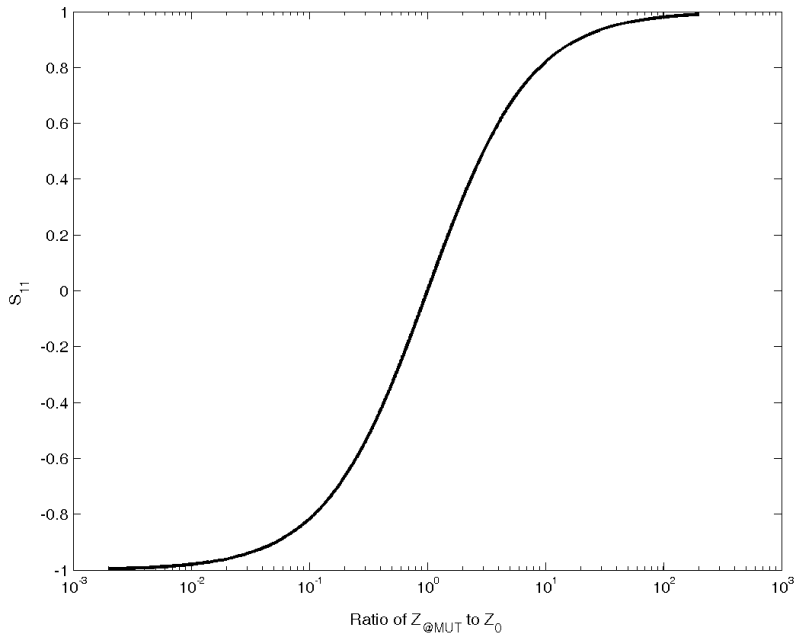


Figure 33. The dependence of S_{II} with respect to the ratio of the impedance at the MUT and the characteristic impedance of the test fixture. This graph assumes that the impedance at the MUT is purely real. Adapted from figure in [2].

With all of the measurement effects accounted for, Agilent recommends use of its 85070E probes for materials with a dielectric constant of less than 100 [1]. The minimum recommended loss tangent is 0.05 [1]. Finally, the probes are not recommended for materials with a loss tangent below 0.5 and a dielectric constant above 5 [1]. These very conservative recommendations require careful consideration when deciding what measurements are appropriate with this system. To limit the error in the measurement, sample preparation is very important, particularly in minimizing the surface roughness. It should be noted that while surface roughness can introduce error, this error has the effect of lowering the dielectric constant measurement. While any measurement error is undesirable, an underestimation of the dielectric constant provides confidence that the actual dielectric constant values are at least as high as the measured values, and the actual values may be even higher. Good judgment is also required when interpreting the results to ensure that the measured values can consistently be measured and the error has been minimized. Despite the limitations of the measurement method presented here, it uses the best-available industry-standard equipment for measurement in this high frequency range. Therefore, the high dielectric constant composites were measured with this technique while minimizing the error presented by surface roughness and material homogeneity.

4.2.2 Dielectric Spectroscopy Results

Figure 34 shows the dielectric constant and losses of the first class of high dielectric constant composite, MU45. At the low end of the measurement range, the dielectric constant peaks at just under 50. The dielectric constant drops with increasing frequency but remains relatively constant between 40 and 45 between 1 and 3 GHz. The dielectric

constant is approximately 40 between 3 and 4.5 GHz. The dielectric losses remain at or below 0.1 up to 2 GHz and peak at 0.14 at approximately 4.25 GHz.

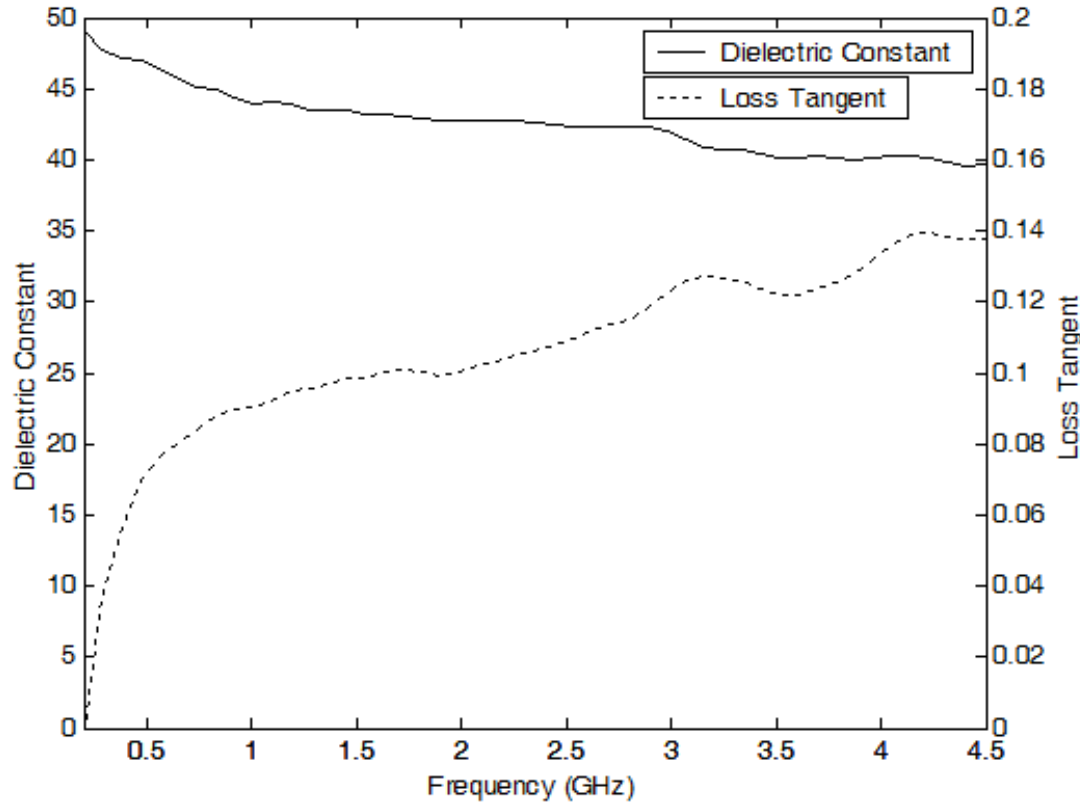


Figure 34. Dielectric constant and loss tangent for MU45

The next composite class, MU100, has a dielectric constant of approximately 105 at 200 MHz, as shown in Figure 35. The dielectric constant slowly drops with increasing frequency, reaching a minimum of 90 at 4.5 GHz. This voltage drop corresponds to less than a 15% reduction over the entire frequency range. The losses of the MU100 composite are less than 0.1 throughout the range except for two peaks at approximately 1.75 and 2.75 GHz where the losses extend to between 0.1 and 0.12. The high dielectric constant and low dispersion of this composite class make it an excellent candidate material for the high power antennas under development.

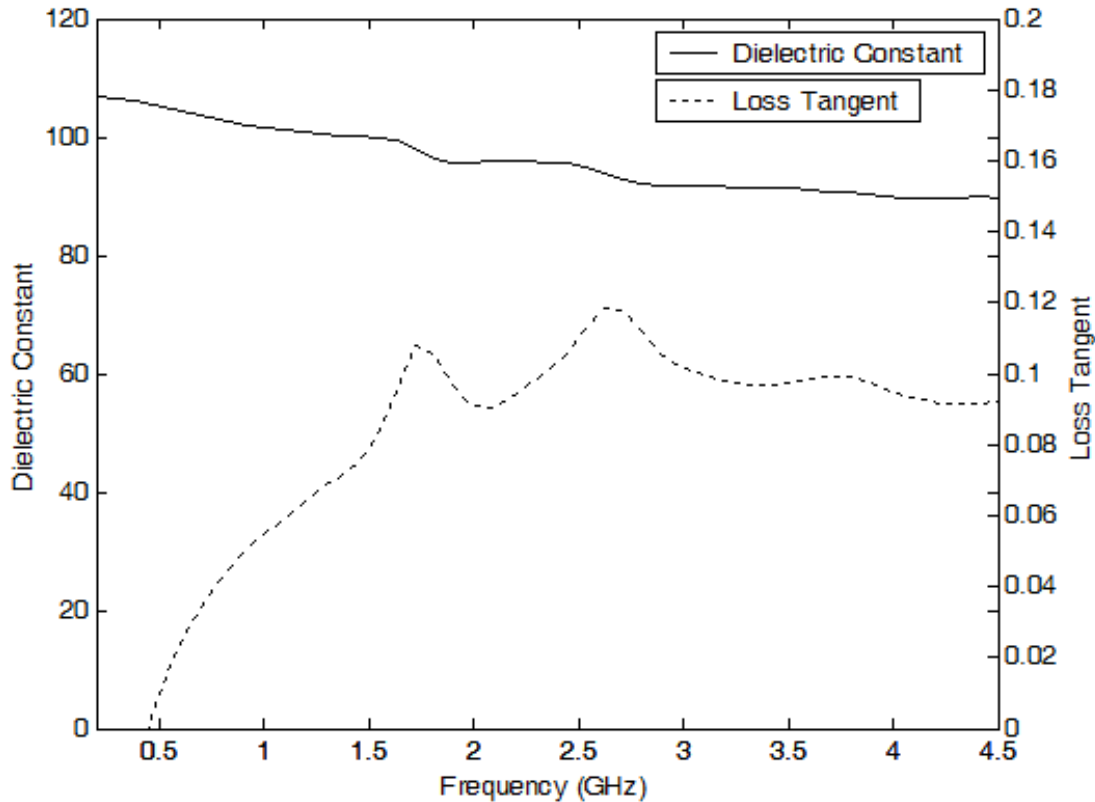


Figure 35. Dielectric constant and loss tangent for MU100

Figure 36 displays the dielectric constant and losses of the composite class with the highest dielectric constant, MU550. The dielectric constant is at its maximum of approximately 550 at 200 MHz. This composite class is also the most dispersive as the dielectric constant drops to a minimum of less than 400 at 4.5 GHz and losses peak at nearly 0.35. The losses remain relatively low below 500 MHz, making this composite class ideal for low frequency applications.

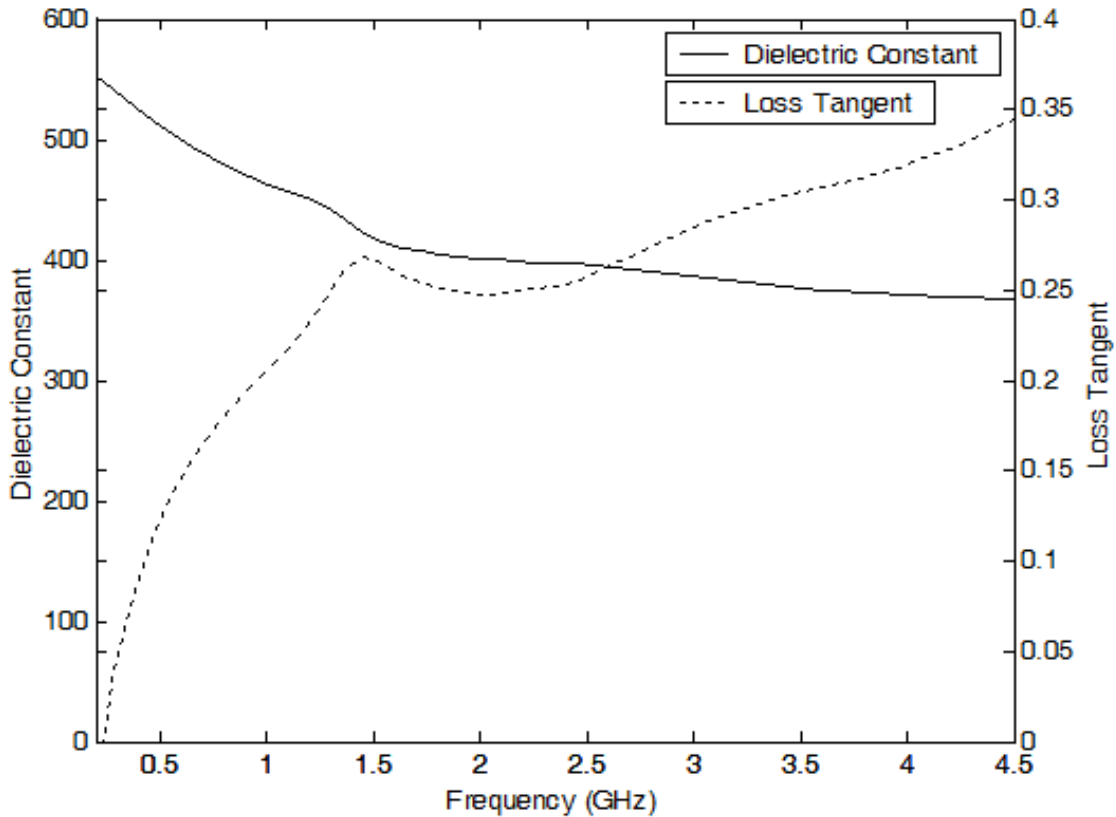


Figure 36. Dielectric constant and loss tangent for MU550

A series of measurements were taken to analyze the temperature dependence of the dielectric constant and losses between -20 C and 120 C. The temperature analysis enabled a qualitative assessment of the useful temperature ranges of the composites and identification of trends. However, since the 85070E high temperature probe is not fully integrated into the oven and freezer used to heat and cool the samples, it is not possible to report specific data for the dielectric constant at specific temperatures. The limitation with assigning the measured data to a specific temperature arises from the time-dependent heating or cooling of the sample towards room temperature when removed from the freezer or oven. The heating and cooling rate of the sample can be rapid when exposed to room temperature, and there is likely a temperature gradient within the

sample. Therefore, the temperature dependence of the samples can only be described from observations of data trends with increasing extremes in temperature.

Since the primary component of all three composites is barium titanate, it can be expected that the temperature variance of the dielectric constant and losses will be heavily dependent on the temperature variance of barium titanate. As described in Chapter 3, one reason for the selection of barium titanate as the ceramic component as opposed to barium strontium titanate or other ferroelectrics with higher room-temperature dielectric constants is that barium titanate has a relatively high Curie temperature of around 120 C. With a relatively high Curie temperature, barium titanate is in the tetragonal phase for nearly all temperatures of interest, and the large temperature dependence of the dielectric constant and losses near the Curie temperature are not present for most temperatures of use. The selection of barium titanate provides a degree of temperature stability of properties compared to other high dielectric constant ceramics. The different binders and other fillers incorporated into the composites can cause a temperature dependence, so the binders and other fillers are discussed separately in the following paragraphs.

The dielectric constant and losses of MU45 were observed to be consistent throughout the wide temperature range of measurement. The temperature dependence of MU45 is likely much lower than that of a similar composite described by Chiang and Popielarz due to the different frequency band of measurement [3]. The previous work incorporating CR-S as the binder in a polymer-ceramic composite observed a strong temperature dependence of the dielectric constant below room temperature at 100 kHz [3]. Based on the frequency-dependent measurements of the dielectric constant of CR-S by Chiang and

Popielarz, 100 kHz is below the relaxation frequency of CR-S. Their data shows that CR-S exhibits a large decrease in the dielectric constant from approximately 20 at 100 kHz to between 10 and 15 at 10 MHz [3]. By lowering the material temperature, the frequency-dependent decrease in the dielectric constant is likely shifted to progressively lower frequencies, resulting in the observed temperature dependence at 100 kHz. However, since the temperature-dependent measurements taken in this study were all above this relaxation frequency, the temperature dependence is not observed between 200 MHz and 4.5 GHz. Although CR-S has a softening temperature of 90-110 C, no polymer flow or loss that could compromise the mechanical integrity of the composite was observed in heating the sample to 120 C.

The dielectric constant and losses of MU100 were also consistent throughout the measured temperature range. This consistency is expected due to the polysilsesquioxane binder. The polysilsesquioxane binder is non-polar and has a low dielectric constant. Thus there is a small margin for change in the dielectric constant of the binder and correspondingly low change in the dielectric constant of the composite. The incorporation of a temperature-stable ceramic and binder result in stable dielectric properties with temperature. Since the polysilsesquioxane can withstand very high temperatures, as described later in this chapter, melting of the polysilsesquioxane is also not an issue.

For MU550, the agar alone is not expected to contribute a strong temperature dependence due to its non-polar structure and relatively low dielectric constant. The effects of the liquid filler are substantially more significant. To demonstrate the temperature dependence of EC50, permittivity measurements were made at room temperature and above 100 C. To take the high temperature measurement, EC50 was

heated to 130 C and removed from the oven. The measurement was taken as the sample was cooling between 120 C and 100 C. As shown in Figure 37, the dielectric constant of high temperature EC50 at the lower end of the measured frequency band is significantly reduced. However, the dispersion of the dielectric constant at high temperature is also reduced, resulting in the high temperature dielectric constant exceeding the room temperature dielectric constant above approximately 2.8 GHz. The relatively flat dielectric constant dependence of the high temperature EC50 is desirable over the very high dispersion present at room temperature.

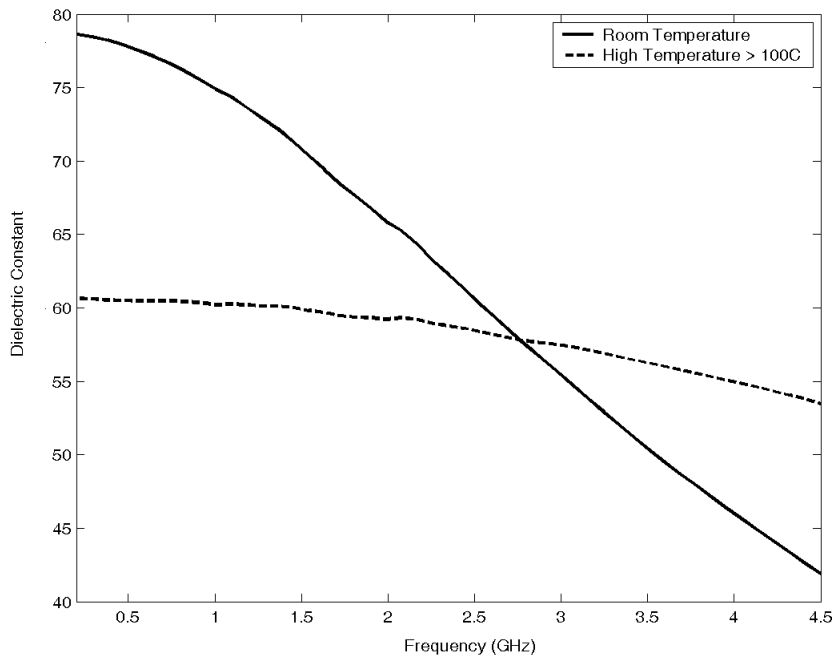


Figure 37. Dielectric constant of EC50 at room temperature and greater than 100C

Figure 36 shows the dissipation factor of EC50 at room temperature and above 100 C. The dissipation factor of the high temperature EC50 is much lower than that of the room temperature EC50. The high temperature trends of lower dispersion in the dielectric constant and much lower losses can provide an advantage to using MU550 in a high temperature application. Although agar has a melting point of approximately 85 C, there

was no sign of polymer flow or softening of the composite that would compromise the mechanical integrity of the composite.

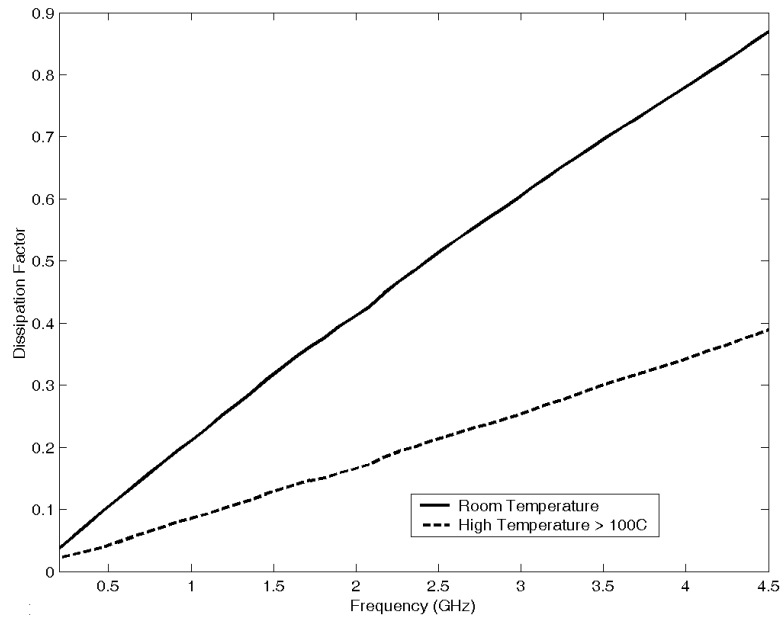


Figure 38. Dissipation factor of EC50 at room temperature and greater than 100C

4.3 Polarization

4.3.1 Polarization Methods

The polarization method facilitates measurement of the dependence of the polarization on the electric field in the material under test. In ferroelectric materials, the dielectric constant is drastically reduced above a saturating electric field. Determining the hysteresis curve for composites containing ferroelectric components can be important to determine if saturation occurs in the composite. If saturation does occur in the composite, the maximum operating electric field may be lower than the dielectric strength to maintain a constant dielectric constant. A second reason for measuring the polarization is to determine the dielectric constant under high electric field conditions. Although the frequency of the polarization measurements is lower than the VHF and UHF bands of

interest, the high electric field dielectric constant measurements provide information on the field dependence of the dielectric constant that low voltage network analysis measurements cannot provide.

The method implemented to measure this relationship is a modification of that used by Sawyer and Tower in 1930 [4]. The schematic of the circuit is shown in Figure 5. An AC voltage, V_{AC} , is applied across two capacitors in series. One of the capacitors, C_T , is made with the dielectric material under test, and the other capacitor, C_0 , has a known capacitance with negligible dependence on the applied electric field. The resistor, R , can be included to limit the current from the high voltage transformer. The resistor can be necessary to limit the current in the secondary circuit for some transformers that will detect a high current as a fault condition.

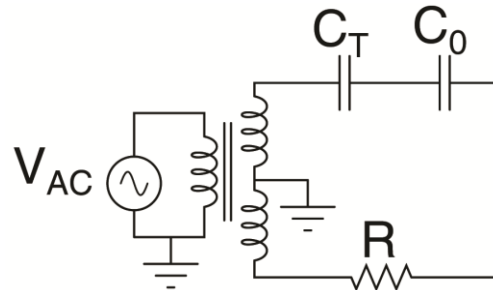


Figure 39. Schematic of the modified Sawyer-Tower circuit

Since the charge, Q [C], on the two capacitors in series is distributed equally, analysis of the voltage across each capacitor results in information on how the polarization changes versus the electric field. As the voltage of the AC source and the electric field in the dielectric material of C_T varies during each cycle, the voltage distribution between C_T and C_0 , is dependent upon the dielectric constant of the material under test. By plotting the variation of the polarization, P [$\mu\text{C}/\text{cm}^2$] or [nC/cm^2], versus the electric field, E [MV/m], in the dielectric material under test, a hysteresis curve is obtained. The hysteresis curve graphically presents the variation of the dielectric constant with respect to the electric

field. To produce the hysteresis curve, the electric field, E_{avg} [V/m], is calculated as the voltage across the test capacitor, V_T [V], divided by the thickness of the material under test, t_{MUT} [m]. This calculation is for the average electric field without consideration of the field effect enhancement at the electrode edges. The charge, Q [C], on each capacitor can be calculated as the product of the voltage across the known capacitor, V_0 [V], and the capacitance of the known capacitor, C_0 [F]. The polarization (C/m^2) is calculated as the stored charge divided by the known area, A [m^2] of the electrodes of the capacitor under test. Using these parameters, the permittivity is calculated by determining the slope from two points along a linear portion of the polarization-electric field curve. By dividing the permittivity by the permittivity of free space, the dielectric constant can be calculated. Equation (4.9) summarizes these calculations and demonstrates how the dielectric constant can be calculated from two data points of voltage across the known and test capacitors.

$$\varepsilon_r = \frac{P_2 - P_1}{\varepsilon_0(E_{avg,2} - E_{avg,1})} = \frac{\frac{Q_2 - Q_1}{A}}{\varepsilon_0\left(\frac{V_{T,2} - V_{T,1}}{t_{MUT}}\right)} = \frac{C_0 t_{MUT}}{\varepsilon_0 A} \left(\frac{V_{0,2} - V_{0,1}}{V_{T,2} - V_{T,1}} \right) \quad (4.9)$$

Polarization measurements were made at both low and high applied voltage. Comparison of the low and high applied voltage measurements provides the most direct means to examine the dependence of the dielectric constant on the electric field. The low voltage source was an LCR meter with a 1 V applied signal at 100 Hz. For this low voltage system, the test leads of the LCR meter were connected directly across the series arrangement of the known and test capacitors. No series resistance was included in the circuit, and since a high voltage transformer with a mid-point ground was not included, one of the test leads was grounded.

The high voltage polarization test stand was implemented with a high voltage transformer that is designed for use with 120 V AC mains power. A variac was used to adjust the voltage amplitude supplied to the high voltage transformer. At the full mains amplitude, the high voltage transformer is capable of supplying an RMS voltage of up to 15 kV at 60 Hz. No series resistor was required to limit the current from the high voltage transformer. The high voltage polarization measurements were conducted in an oil bath to reduce the likelihood of flashover around the sample surfaces.

The capacitors under test were fabricated with 25.4 mm diameter disks of the composite material. The thickness of the composites was less than 1.5 mm, and the surface was sanded and polished to a fine roughness. A platinum electrode with a diameter of approximately 12 mm was sputtered on each side of the composite to form a sample capacitor. Conductive silver paste was applied over the platinum electrode to improve the conductivity of the electrode and to prevent mechanical abrasion of the platinum layer. A thin layer of CM114-14A high dielectric ink with a dielectric constant of approximately 40 was applied around the edges of the electrode in an attempt to minimize the field effect enhancement at the triple point. The sample capacitor was mounted in an acrylic holder, and brass hardware facilitated electrical contact with the capacitor electrodes and external connections.

The results from sample capacitors of MU45 and MU100 are presented here. MU550 is not included due to incompatibility with low frequency measurement methods in its current form. Due to the inclusion of the polar solvent EC50, mobile ions are present in the composite. While the antenna frequencies of interest are too high for charge transport with the ions to occur, low frequency signals do see effects from ion movement. In

particular, a double layer can form at the electrode surface, resulting in very high charge storage that would correspond to dielectric constant values on the order of tens of thousands to millions. However, the separation of charges is no longer the dielectric material's thickness when a double layer is formed. As in the case of ultracapacitors, the double layer is only stable at voltages that are too low to drive the electrochemical oxidation and reduction reactions. Higher voltages result in leakage current within the composite. Therefore, meaningful evaluation of MU550 at low frequency is not possible.

To ensure very little variation of the capacitance of the reference capacitor with respect to the electric field, the reference capacitors were chosen based on the dielectric properties. A high voltage mica capacitor rated at 2 nF was used in the measurements of MU45, and a metalized plastic capacitor measured at 2.48 nF was used in the measurements of MU100.

4.3.2 Polarization Results

Polarization measurements were taken at low electric fields with an LCR meter source. The frequency was 100 Hz as it was the closest frequency to the 60 Hz high electric field source that the LCR meter was capable of producing. Figure 40 shows the hysteresis curve of the MU45 composite at low electric field levels from the 100 Hz source. The dielectric constant corresponding to the slope of the polarization-electric field trace is approximately 109.3. A dashed line in the center of the hysteresis curve with a slope corresponding to a dielectric constant of 109.3 is included for reference. The dielectric constant is much greater than 45 due to the lower frequency of the polarization measurement and the elimination of air gaps by the sputtered electrodes. Due to the low frequency of the measurement, the dielectric constant of the CR-S binder is much higher

than its high frequency value, contributing to the increase in the low voltage dielectric constant value.

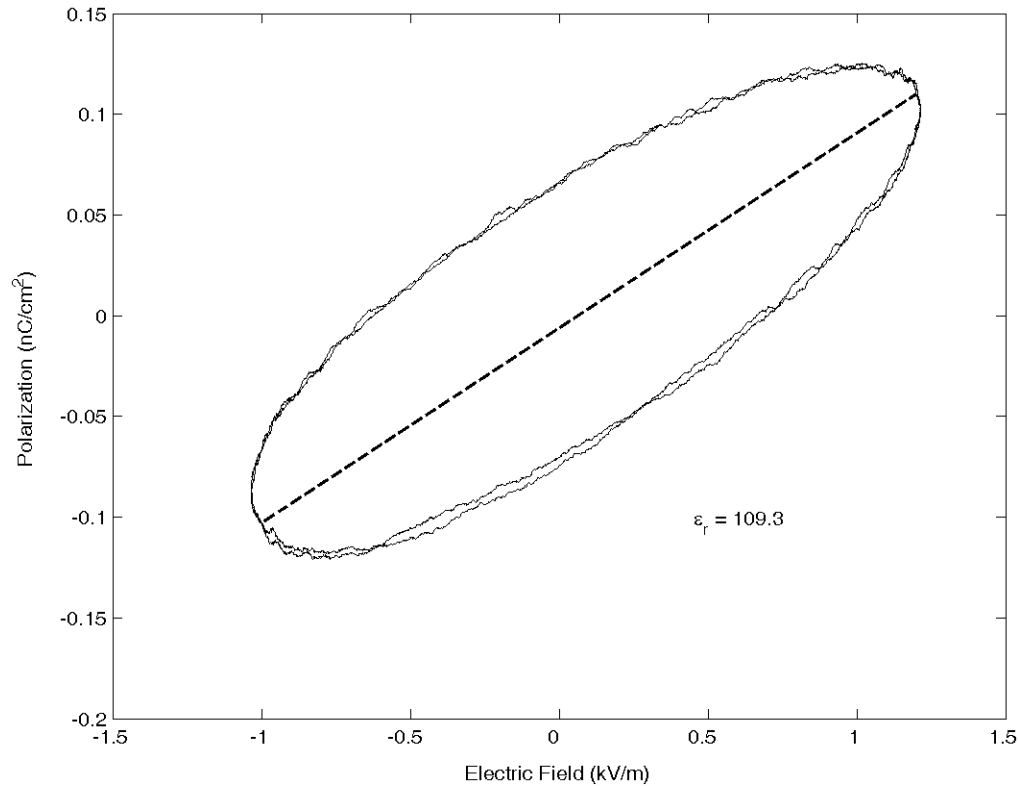


Figure 40. Polarization vs. electric field of MU45 at low electric field levels from a 100 Hz source

Figure 41 shows the hysteresis curve for MU45 measured with the high voltage 60 Hz source. The slope of the curve does not show any signs of saturation up to 2 MV/m. The dielectric constant is estimated from the curve to be approximately 208.6. This is nearly double the value observed from low voltage measurement, suggesting that the effective dielectric constant of MU45 is significantly higher under high electric field conditions.

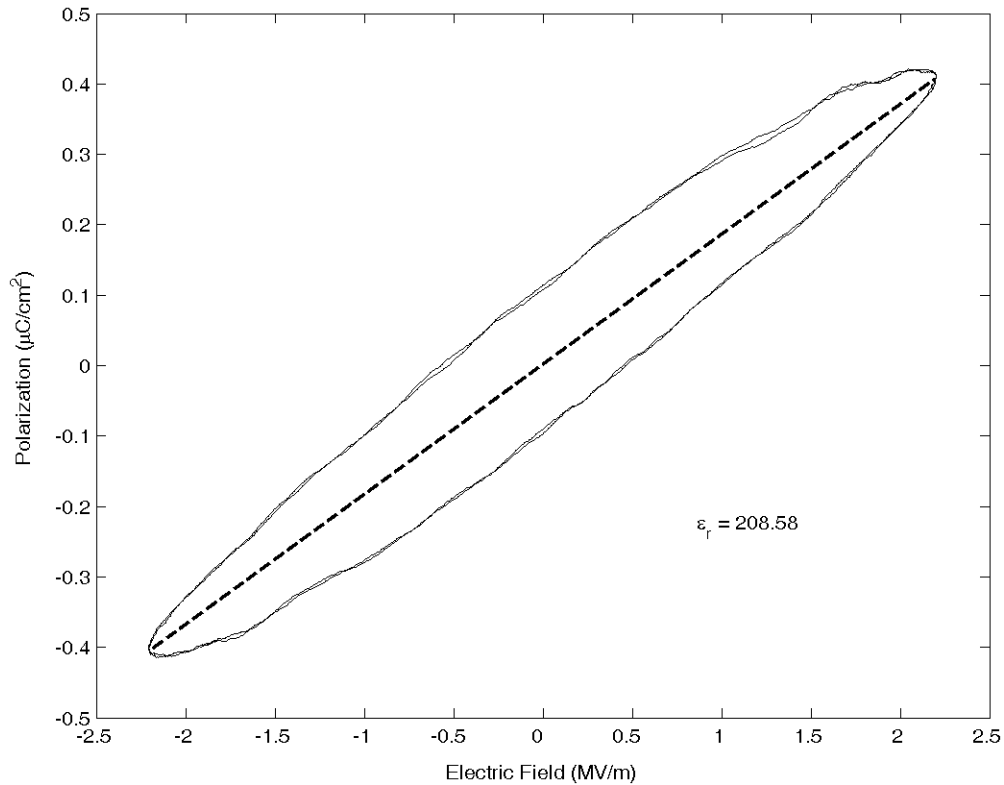


Figure 41. Polarization vs. electric field for MU45 under high electric field

The same MU45 sample was tested to electric field strengths greater than 6 MV/m. As shown in Figure 42, there was no sign of ferroelectric saturation. From the hysteresis curve, the dielectric constant was calculated to be approximately 323.7. This indicates that the dielectric constant continues to increase due to increases in the maximum electric field between 2 and 6 MV/m. It is unknown if the measured dielectric constant would continue to increase at higher electric field levels.

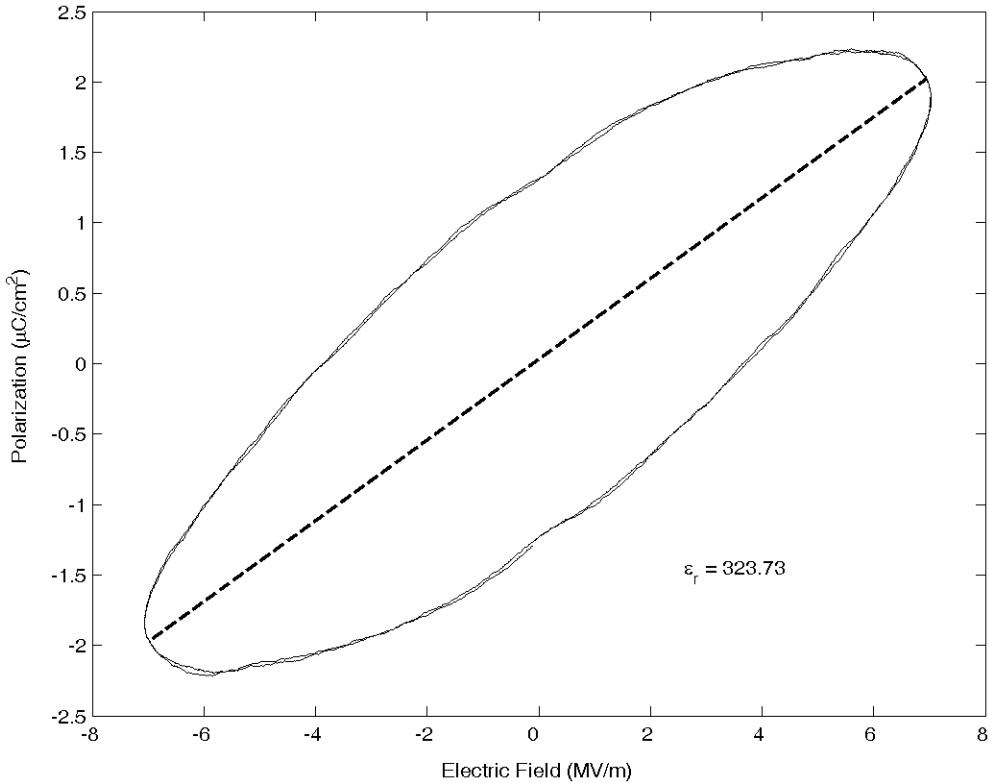


Figure 42. Polarization vs. electric field for the MU45 composite under electric field strengths greater than 6 MV/m

Figure 43 shows the hysteresis curve of MU100 under low electric field conditions. The dielectric constant calculated from the curve is approximately 135.4. Figure 44 shows the hysteresis curve for the same sample under high electric field conditions with the electric field up to nearly 4 MV/m. The dielectric constant calculated from the curve is approximately 308.5. As shown in Figure 45, increasing the electric field further to a peak of more than 10 MV/m corresponds to an increase in the dielectric constant to approximately 387.6. No signs of saturation were evident up to these high field levels. As with MU45, it is unknown what the limit is for increasing the dielectric constant by increasing the operating electric field strength.

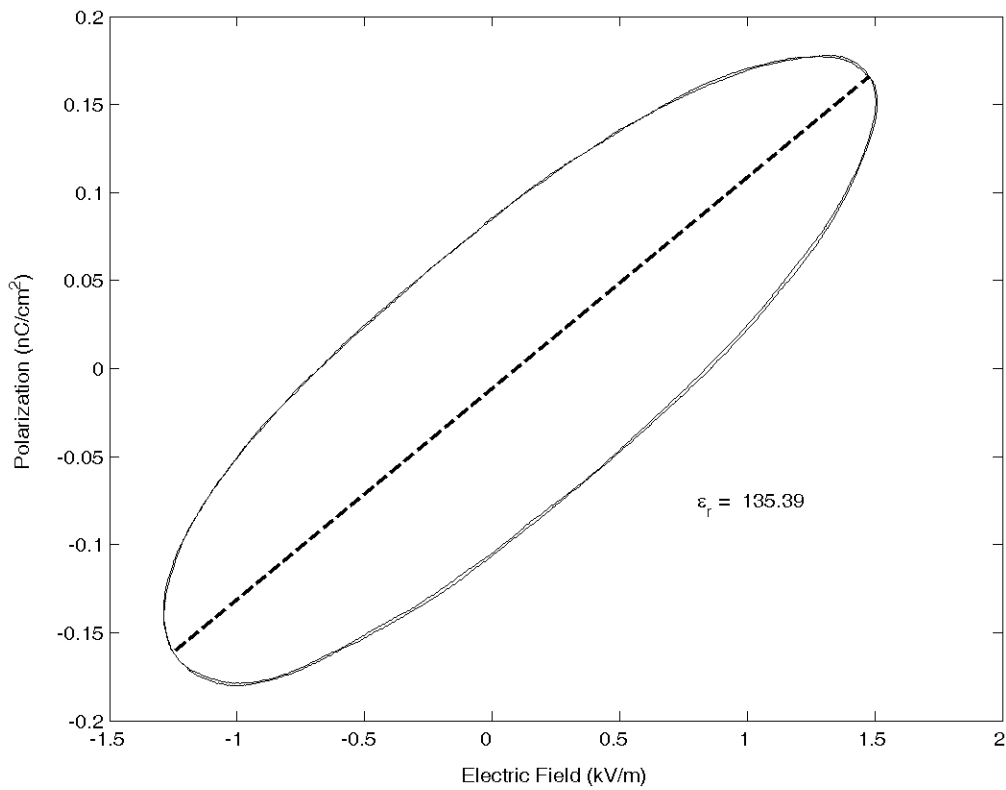


Figure 43. Polarization of MU100 under low electric field conditions

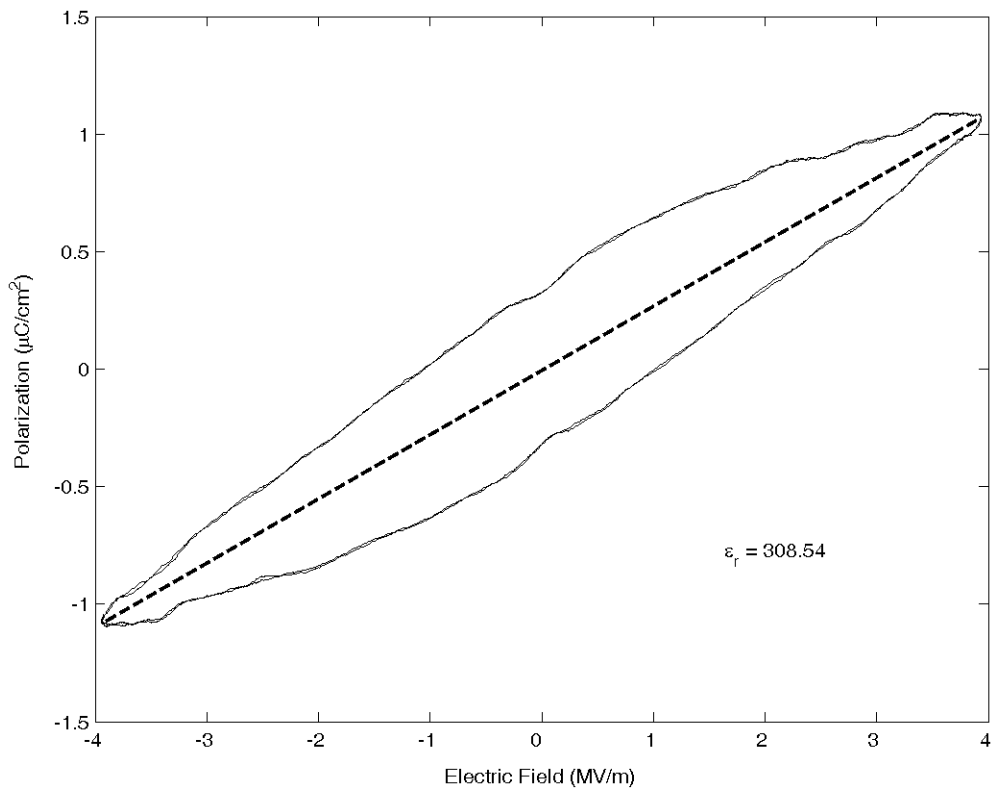


Figure 44. Polarization of MU100 under high electric field conditions up to nearly 4 MV/m

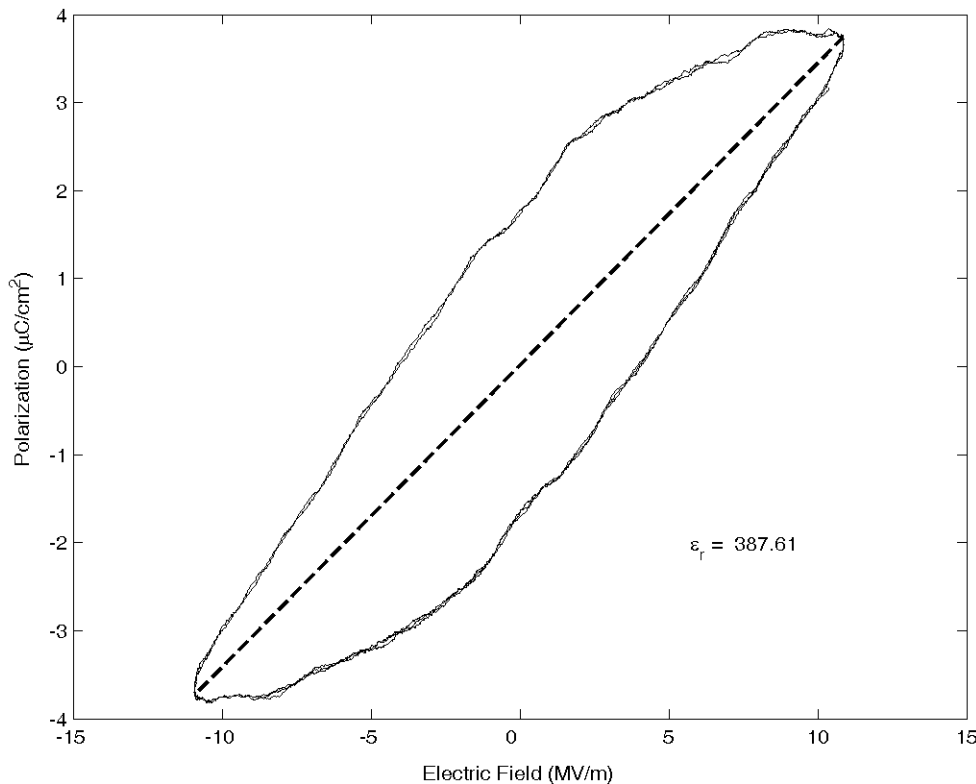


Figure 45. Polarization of MU100 under high electric field conditions up to more than 10 MV/m

4.4 Capacitive Discharge

4.4.1 Capacitive Discharge Methods

A second high voltage diagnostic method in addition to the polarization measurements was implemented in the form of a high voltage capacitive discharge test stand. The high voltage capacitive discharge test stand was used to record the discharge waveform of small capacitors formed with the composite materials into a known resistance. Post-processing of the data enabled the dielectric constant of the material to be estimated while under high voltage conditions. While the frequencies present in the capacitor discharge waveform were generally lower than the application antenna frequencies, the capacitive discharge data provided additional information on the observed increase in the dielectric constant under high voltage conditions.

Figure 46 shows the schematic of the high voltage capacitive discharge test stand. A negative polarity high voltage power supply, V_{DC} , charged the capacitor under test, C , through a charging resistor, R_C . A mechanical safety switch, S_D , was open during charging but was available to dump the charge through resistor R_D . A high voltage IGBT switch stack, S_L , was closed after charging is complete to discharge the capacitor through the load resistor, R_L .

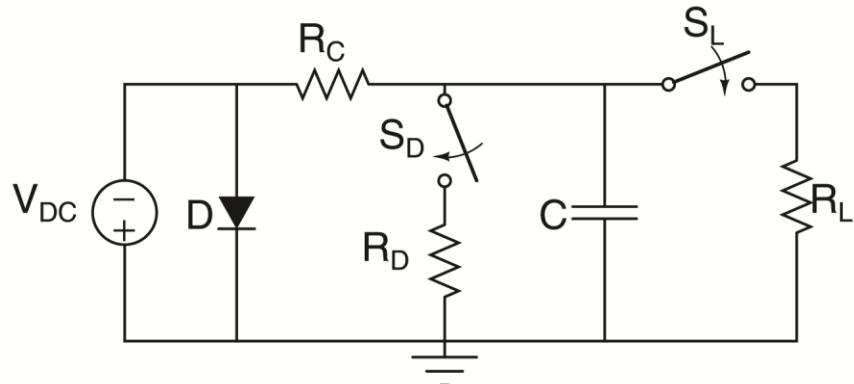


Figure 46. Schematic of the High Voltage Capacitive Discharge Test Stand

The charging voltage was monitored with a Fluke 80K-40 1000:1 voltage probe. The fast discharge of the capacitor was monitored with a Northstar PVM6 1000:1 high voltage probe. The discharge was recorded on a Tektronix TDS 5054B oscilloscope. A custom Matlab program generated a fit to the discharge curve, enabling calculation of the capacitance and effective dielectric constant. Non-inductive resistors were used for the load resistor with values ranging from 1Ω to $105 \text{ k}\Omega$. Figure 47 shows the custom high voltage capacitive discharge test stand.

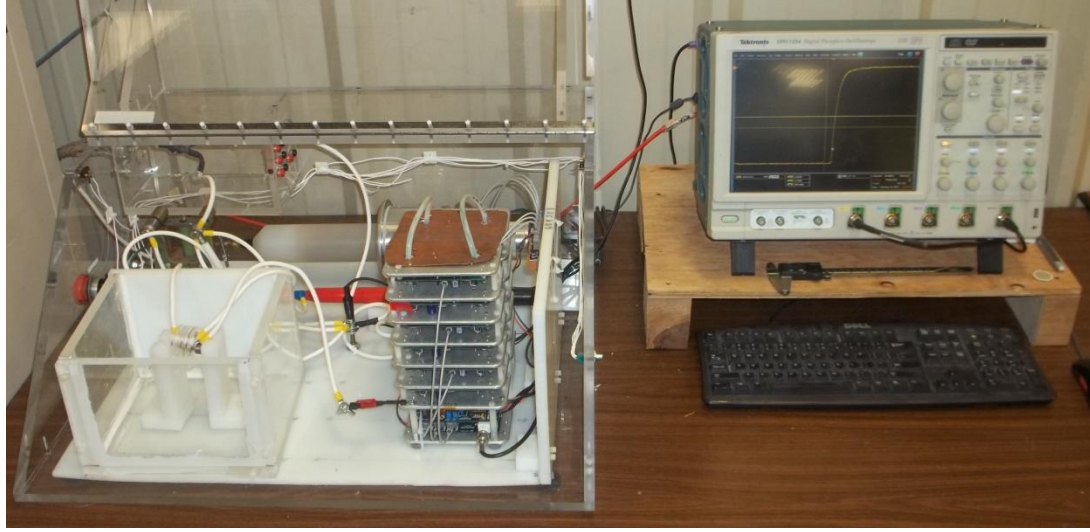


Figure 47. Custom high voltage capacitive discharge test stand

The voltage across the capacitor was monitored during discharge of the capacitor into a low inductance resistor with a known value. From the voltage vs. time plot, it is possible to determine the capacitance of the capacitor under test if the resistance is a known constant. Equation (4.10) describes the time-dependent voltage, $v_c(t)$, across a capacitor, C [F], discharged into an overdamped circuit with resistance R [Ω]. The initial voltage, V_0 [V], is across the capacitor at time, t [s], equal to zero.

$$v_c(t) = V_0 e^{-\frac{t}{RC}} \quad (4.10)$$

Two points along the discharge curve are required to calculate the capacitance. At times t_1 and t_2 , the voltage is defined by variables V_1 and V_2 , respectively. This is represented mathematically as equation (4.11) and equation (4.12).

$$v_c(t_1) = V_1 = V_0 e^{-\frac{t_1}{RC}} \quad (4.11)$$

$$v_c(t_2) = V_2 = V_0 e^{-\frac{t_2}{RC}} \quad (4.12)$$

By dividing by the exponential term in equations (4.11) and (4.12), V_0 is isolated, and equations (4.11) and (4.12) can be equated to each other as shown in equation (4.13).

$$V_0 = V_1 e^{\frac{t_1}{RC}} = V_2 e^{\frac{t_2}{RC}} \quad (4.13)$$

The unknown capacitance can be defined based on the two time and voltage points from the discharge waveform and the known resistance as given by equation (4.14).

$$C = \frac{t_2 - t_1}{R \ln \left(\frac{V_1}{V_2} \right)} \quad (4.14)$$

The effective dielectric constant of the materials was calculated based on the simple equation for a parallel-plate capacitor as shown in equation (4.15). The effect of the fringe fields was ignored as is common in practice as the additional capacitance obtained from fringe fields when measuring a high dielectric constant material are relatively small. In equation (4.15), ϵ_r is the effective dielectric constant of the composite material, and C [F] is the calculated capacitance. The material thickness is again t_{MUT} [m], and A [m^2] is the area of the capacitor electrodes.

$$\epsilon_r = \frac{Cd}{\epsilon_0 A} \quad (4.15)$$

Samples of MU45 and MU100 were prepared as described in the previous subsection with electrodes consisting of sputtered platinum covered with a silver epoxy paste. The measurements were conducted in atmospheric air as opposed to the oil environment used in the polarization measurements.

4.4.2 Capacitive Discharge Results

Figure 48 displays the voltage discharge waveform obtained when discharging a small capacitor made with MU45 from a voltage of approximately -2 kV. The capacitor had electrodes with a diameter of approximately 12 mm, and the thickness of the MU45 material was approximately 1.13 mm. The load resistance was measured to be

approximately 10.4 k Ω . Two empty circles indicate the points along the discharge curve at which the time and voltage was sampled for calculation of the capacitance. From these points, the capacitance was calculated to be 177.1 pF, corresponding to an effective dielectric constant of MU45 of approximately 199.8. For a voltage magnitude of 2 kV and a thickness of 1.13 mm, the average electric field in the composite was approximately 1.77 MV/m. The dielectric constant of 199.8 observed through capacitive discharge with a peak field of 1.77 MV/m agrees very well with the dielectric constant of 208.6 of Figure 41 obtained through polarization measurements at a peak field of slightly more than 2 MV/m. These two measurement methods produced very close dielectric constant measurements at similar peak field strengths. However, it should be noted that the dielectric constant obtained from high voltage discharges of MU45 at higher voltages were also consistently around 200. The dielectric constant calculated from those capacitive discharges did not increase to the same levels observed from very high electric field polarization measurements as in Figure 42.

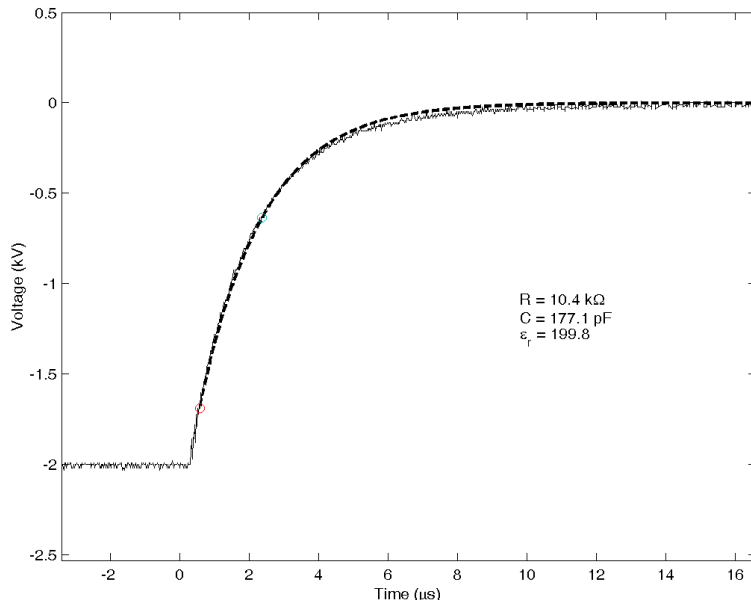


Figure 48. Discharge waveform of a capacitor made with MU45

Figure 49 shows a waveform of a capacitor made from MU100 discharged from approximately -2 kV. The sample capacitor had an electrode diameter of approximately 12 mm and a thickness of approximately 1.27 mm. The load resistance was again 10.4 k Ω . The capacitance calculated from the discharge curve was 272.27 pF, and the corresponding effective dielectric constant was approximately 345.3. Although this capacitive discharge had a lower peak electric field magnitude, the calculated dielectric constant fits between the values obtained at high electric field through polarization measurements as shown in Figure 44 and Figure 45. Different samples of MU100 were used in the polarization measurement and the high voltage capacitive discharge measurement, but the effective dielectric constant at high voltage is similar between samples and measurement methods. As noted for MU45 capacitive discharge measurements, the effective dielectric constants observed for MU100 in capacitive discharge measurements were similar for multiple charge voltage magnitudes, and the dielectric constant did not continue to increase with increasing peak electric field as it did in polarization measurements.

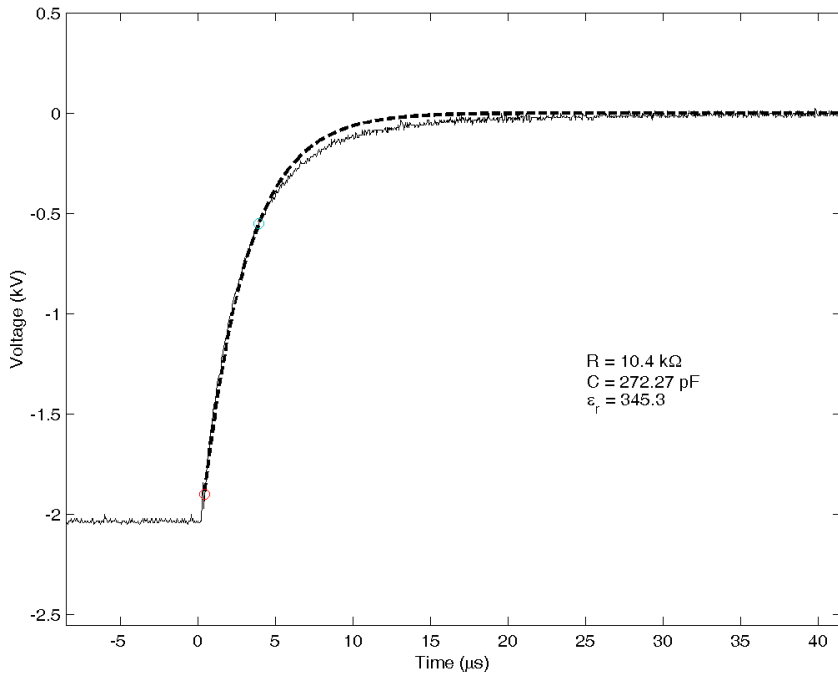


Figure 49. Discharge waveform of a capacitor made with MU100

4.5 Dielectric Strength

4.5.1 Dielectric Strength Methods

In addition to the high dielectric constant of the composites, a high dielectric strength is required to ensure the composites can survive the very high electric fields present in high power antennas. In many cases, the dielectric strength of the composites can be the limiting factor in the power handling capability of the antenna. A high dielectric strength is also critical for compact systems in which a high volumetric energy density is required. Several dielectric strength test methods involve the application of nearly DC voltage or a slowly rising voltage waveform across the sample. In this work, the dielectric strength of the composites was characterized under pulsed conditions. The fast risetime of the applied voltage more accurately replicates the conditions of application in a high power antenna. In particular, a very fast risetime pulse would be applied in an impulse radiating antenna (IRA), so the test method most directly approximates composite incorporation

into an IRA. An antenna driven by a high power resonant signal will also encounter very high dV/dt values, so the test conditions are also relevant for establishing peak electric field values in pulsed ring-down antennas and other transient RF applications. The diagnostics measuring the voltage across the sample limit the practical risetime of the applied pulse. The risetime must be slow enough that the diagnostics can accurately measure the peak voltage across the sample.

A difficult but critical element to analyzing the dielectric strength of high dielectric constant composites is accurately estimating the field enhancement factor (FEF) at the triple point junction of the electrode, the high dielectric constant composite, and the surrounding material. Field enhancement at the triple point can cause the actual electric field in the sample near the electrode edge to be many times the electric field calculated simply from the applied voltage and sample thickness. Since the FEF increases as the difference in the dielectric constants of materials at the junction increases, the FEF must be accounted for when analyzing the dielectric strength of materials with a high dielectric constant to accurately estimate the peak electric field in the material at breakdown.

Sample preparation and electrode contacts are also critical to the measurement of the dielectric strength. Surface roughness of the sample and/or the electrode can result in imperfect contact. One result of imperfect sample-electrode contact is the addition of triple point junctions at each point where the sample-electrode contact is interrupted. The geometry of these extra triple points is unknown, and the resulting FEF may be higher than that estimated at the electrode edge. A second result of imperfect contact is that areas are formed at which the electric field appears across a series arrangement of the background material and the sample. If the background material has a low dielectric

constant in comparison with the material under test, the majority of the electric field will be present in the background material. Breakdown of the background material can contribute to premature breakdown of the sample through effects such as heating and surface ionization from electrons accelerated in the background material.

Based on the field enhancement concerns discussed in the preceding paragraphs, efforts were made to provide a uniform electrode contact and to account for the FEF at the electrode edge. The samples were prepared with extensive sanding and polishing to prepare the surface to a very fine surface roughness. To further improve the sample-electrode contact, the electrodes were applied directly to the sample. As shown in Figure 50, platinum electrodes were sputtered directly onto the sample surfaces. The sputtering masks were prepared to ensure that the electrodes on opposite surfaces were directly adjacent from each other. To prevent mechanical abrasion of the sputtered electrodes and to improve electrode conductivity, a silver-loaded epoxy was applied to the sputtered electrodes. With the electrodes in place on the sample surface, the external electrical contacts applied to the silver-loaded epoxy theoretically should not influence the electric field within the sample. Therefore, electrode surface pitting on the external contacts does not affect the sample-electrode contact. To further ensure that surface pitting does not influence the electrical contact between the external circuit and the silver-loaded epoxy, the external contacts were fitted with replaceable tips in the form of acorn nuts. As shown in Figure 51, the electrode tips were replaced after every three samples to prevent excessive wear from pitting.

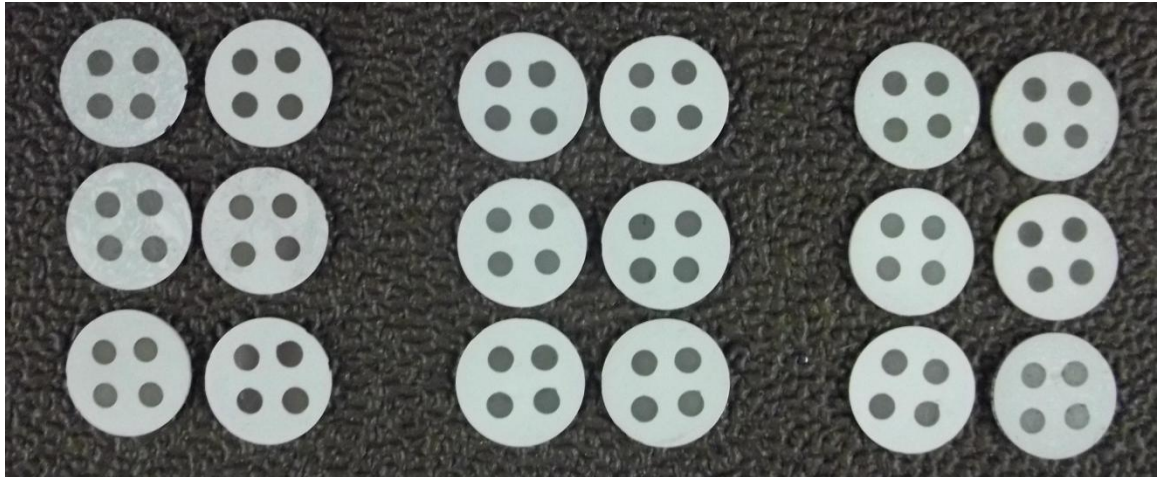


Figure 50. Samples prepared for dielectric strength testing. From left to right in sets of six: MU45, MU100, and MU550

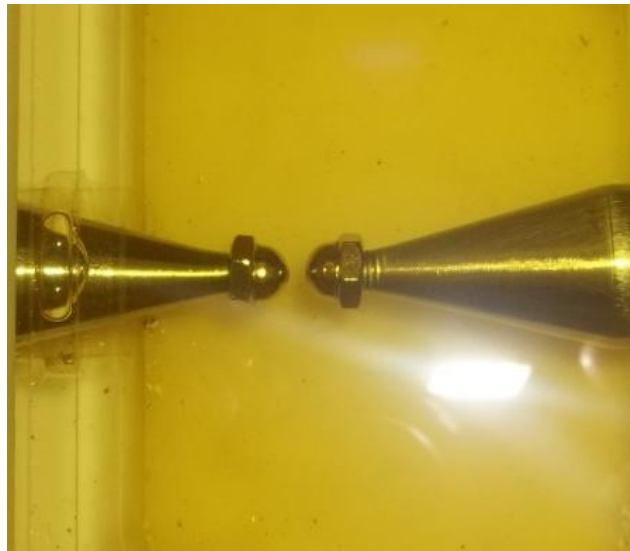


Figure 51. Dielectric strength test cell

Figure 52 shows the circuit of the dielectric strength test stand. A PA-80 pulse generator from L-3 Communications Pulse Sciences was implemented as the high voltage source of the dielectric strength test stand [5]. A 75 nF capacitance, C_S , is resistively charged to between -60 kV and -80 kV from a DC supply. After charging, the switch, S , is triggered by a PT-55, discharging the capacitor into the transmission line, T . Since the capacitor electrode that is initially negatively charged with respect to ground is grounded through switch S , the polarity of the pulse on the transmission line is positive. The

transmission line is a 50Ω cable of RG-218/U. The transmission line is terminated into a load consisting of a parallel arrangement of the dielectric test cell, a capacitance, C_1 , of 0.54 nF , and a resistance, R_1 . Since C_1 is much smaller than C_S , the voltage across the sample can reach a peak up to nearly two times V_{DC} if no breakdown in the sample occurs. In normal operation, the value of R_1 is reduced to between 50 and 100Ω to limit the peak voltage across the test cell to less than 100 kV to prevent damage to the voltage diagnostics. The voltage diagnostics were two PVM-6 high voltage probes monitoring the voltage on each side of the sample under test. The maximum recommended frequency of the PVM-6 is 80 MHz , corresponding to a risetime of between 4 and 5 ns .

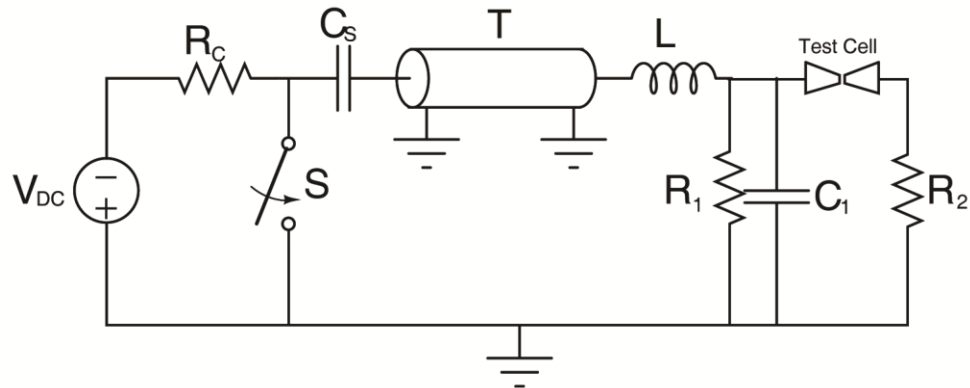


Figure 52. Circuit schematic of pulsed dielectric strength test stand

Figure 53 shows example waveforms recorded during dielectric strength testing. The voltage waveforms were measured from both sides of the dielectric sample. Figure 54 displays the voltage across the dielectric sample. In this example, a peak voltage of nearly 70 kV was applied across the sample before dielectric breakdown. The 10%-90% risetime of Figure 54 is approximately 85 ns .

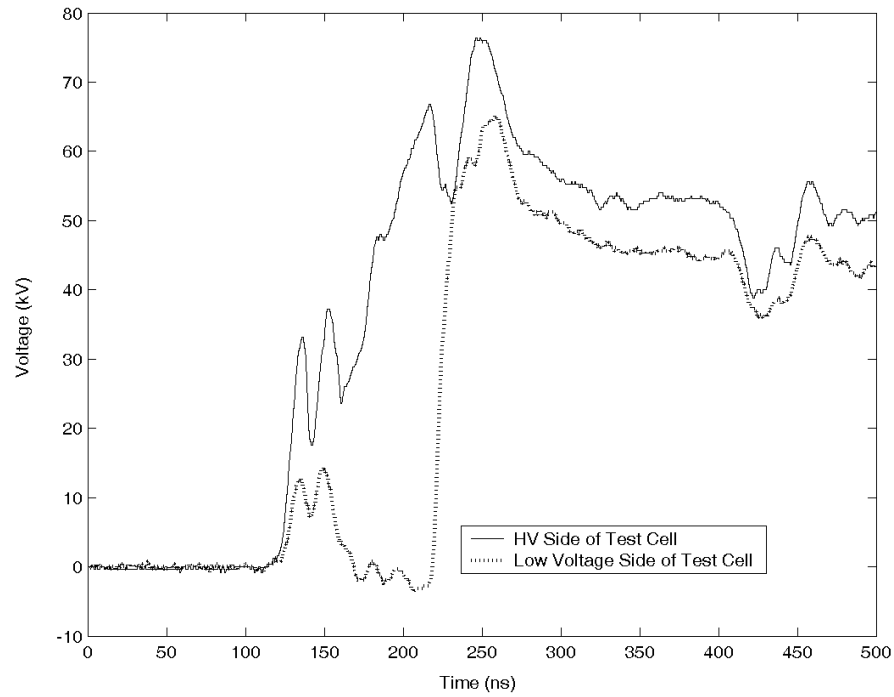


Figure 53. Example voltage waveforms from both sides of test cell

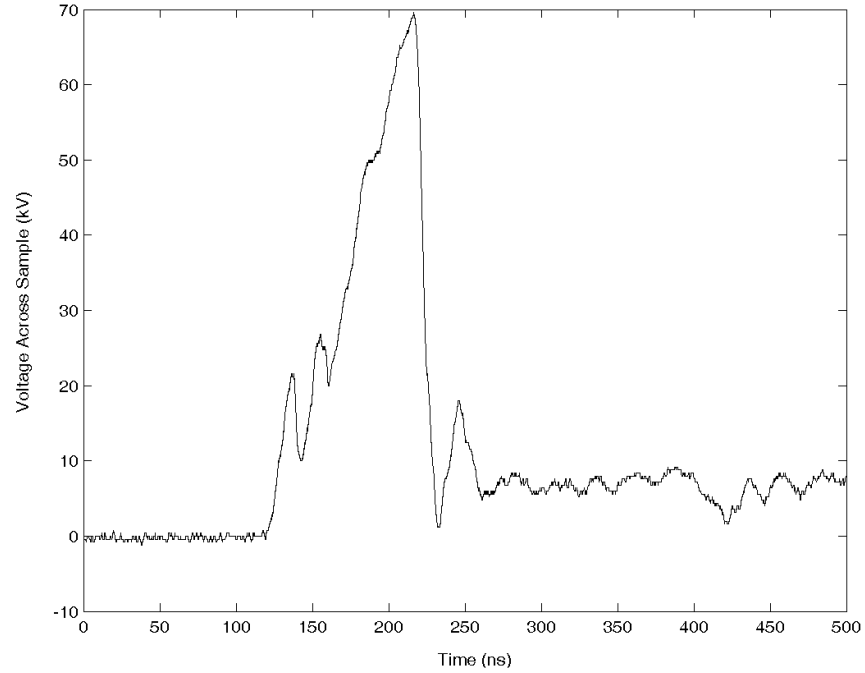


Figure 54. Pulsed voltage across a dielectric sample showing the risetime of the applied voltage

Figure 55 shows the PA-80, transmission line load, and diagnostic arrangement. The experiments were conducted in an oil bath to prevent flashover or arcing around the sample under test.



Figure 55. The PA-80 pulse generator with test cell and diagnostics

Six samples of MU45, MU100, and MU550 were prepared as previously described for dielectric strength testing. Each sample had four measurement sites prepared on it by the application of sputtered platinum electrodes covered with a silver-loaded epoxy for a total of twenty-four potential data points for each class. In addition to the three high dielectric constant composite classes, six Teflon samples with four measurement sites each were also tested for comparison. Of the three classes of high dielectric constant composites, three samples were tested without a high dielectric constant coating around the electrode edge. Three samples were prepared with a coating of CM114-14A high dielectric

constant ink, which has a dielectric constant of 40, around the electrode edge in an attempt to reduce the FEF at the triple point junction. Since Teflon has a relatively low dielectric constant of approximately 2.08, the application of the high dielectric constant ink would have increased the FEF on those samples. Therefore, no Teflon samples were coated with the high dielectric constant ink.

The thickness at each measurement site was measured after the platinum electrodes were sputtered onto the surface but before application of the silver-loaded epoxy. The FEF was estimated through electrostatic simulation in Maxwell SV. A simulation was run for each data point with a unique thickness. The FEF was calculated as the ratio of the peak simulated field to the average field calculated as the applied voltage divided by the thickness at the test site. The high frequency dielectric constants measured through network analysis of 45, 100, and 550 were used in the simulation of each respective composite class. For the dielectric constant of Teflon, the value stored in Maxwell SV of 2.08 was used. The background material was simulated as oil with a dielectric constant of 2.2, and the high dielectric constant coating had a simulated value of 40. To determine the geometry of the electrode edge interface with the composite, the junction was examined through scanning electron micrographs. Figure 56 shows two electrode edges formed from the application of a silver-loaded epoxy over the sputtered platinum contact. These samples were prepared by fracturing the sample to provide a cross-sectional view of the electrode-composite junction. The micrographs shows a good contact along the junction, and the high loading factor of silver particles within the epoxy is evident. The thickness of the electrode gradually decreases towards the electrode edge, forming a curvature with a radius of approximately 100 μm .

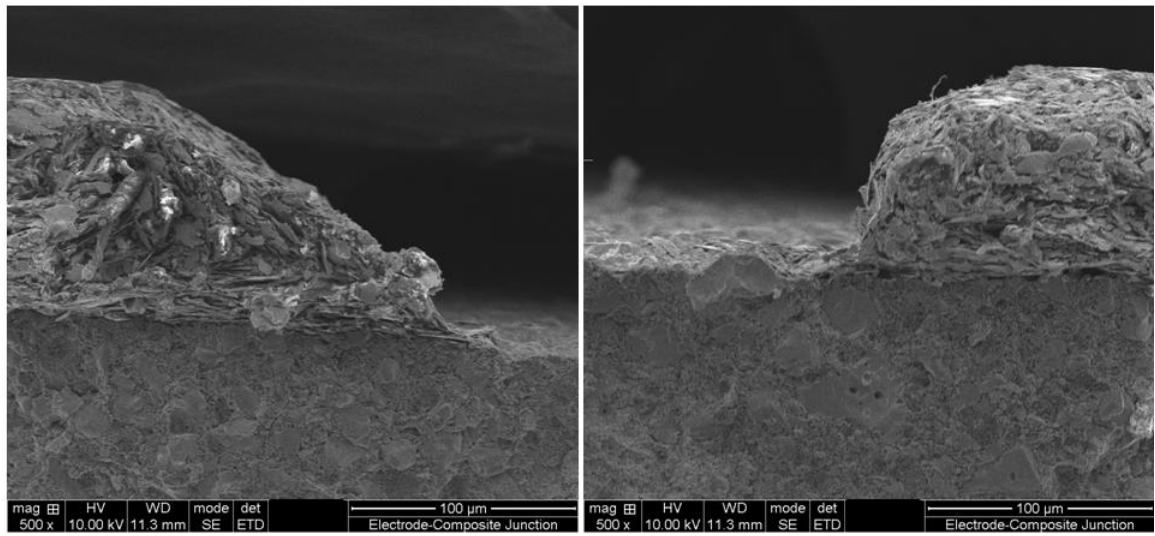


Figure 56. Micrograph of electrode-composite edges

The electrode edge geometry observed in Figure 56 with a radius of curvature of $100 \mu\text{m}$ was implemented in the simulations of the FEF for each data sample. Figure 57 provides an example of the simulated structure from Maxwell SV showing the $100 \mu\text{m}$ thick electrodes on a sample with a dielectric constant of 100. The electrodes are colored red and feature the curvature at the edge with a radius of $100 \mu\text{m}$. In this example, the peak electric field at the triple point was 10.16 MV/m. The field in the bulk of the material to the left of Figure 57 is 1.22 MV/m, so the FEF in this simulation was 8.33.

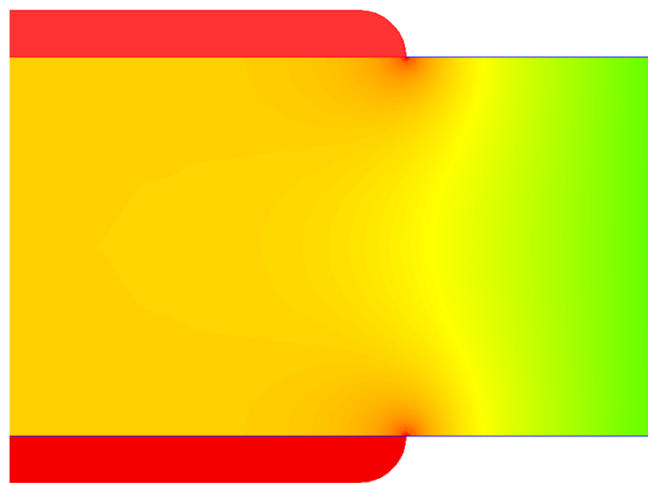


Figure 57. Electrode geometry simulated in Maxwell SV for estimation of the field enhancement factor

Estimating the FEF from electrostatic simulations has some disadvantages. In particular, the peak electric field value is highly dependent on the density of the mesh generated for each simulation. To limit the effects of variations due to mesh density, all of the FEF values were calculated under the same simulation settings. The accuracy of the simulations was run to less than 0.5% error in the energy calculation.

The dielectric strength data is evaluated with the Weibull distribution, which is commonly applied in failure analysis [6]. The cumulative distribution function, F , adapted to this analysis is given as equation (4.16), where E_{peak} is the calculated peak electric field at breakdown, λ_W is the Weibull scale parameter, and k_W is the Weibull shape parameter.

$$F(E_{peak}) = 1 - e^{-\left(\frac{E_{peak}}{\lambda_W}\right)^{k_W}} \quad (4.16)$$

When equation (4.16) is rearranged to the form of equation (4.17), the distribution function can be plotted as a straight line.

$$\ln(-\ln 1 - F(E_{peak})) = k_W \ln(E_{peak}) - k_W \ln(\lambda_W) \quad (4.17)$$

A Weibull plot compares the experimental data to a straight line described by equation (4.17). The Weibull parameters k_W and λ_W can be determined if the data fits to a line described by equation (4.17).

4.5.2 Dielectric Strength Results

The first data set contains the samples without a high dielectric constant coating around the electrode edge. In this data set, the number of data samples for MU45, MU100, MU550, and Teflon number 10, 10, 9, and 23. Of the 12 test sites prepared without a high dielectric constant coating for the MU45, MU100, and MU550 composites and the 24 test

sites prepared for Teflon, the number of data samples for analysis is lower for one of two reasons. First, if a prior data sample caused a fracture in the composite that extended to the electrode edge of another sample, data was not taken on the compromised sample. Second, in rare instances, diagnostic or data collection problems resulted in the loss of a data point.

Figure 58 displays the Weibull plot of samples without a high dielectric constant coating and without inclusion of the field enhancement factor. The field enhancement factor is not included in this first plot to examine if the data initially fits a Weibull distribution before inclusion of triple point effects. The quoted electric fields are the values present in the bulk of the material and are referred to as the average field. The average field varies from 18.8 to 41.8 MV/m for MU45, 45.3 to 51.7 MV/m for MU100, 33.5 to 41.6 MV/m for MU550, and 93.7 to 137 MV/m for Teflon. Table 5 summarizes the Weibull parameters calculated through data analysis in Matlab. The data for MU100, MU550, and Teflon appear to fit the straight line very well. The data for MU45 has the worst fit. It is possible that due to the higher polymer content in MU45, variation in the dispersion and packing density of the particles at different points in the composite is greater than MU100 and MU550, which have lower polymer content. The higher degree of variation found in MU45 could effectively produce an inhomogeneous medium that would not exhibit dielectric strength data with a good fit to the Weibull distribution.

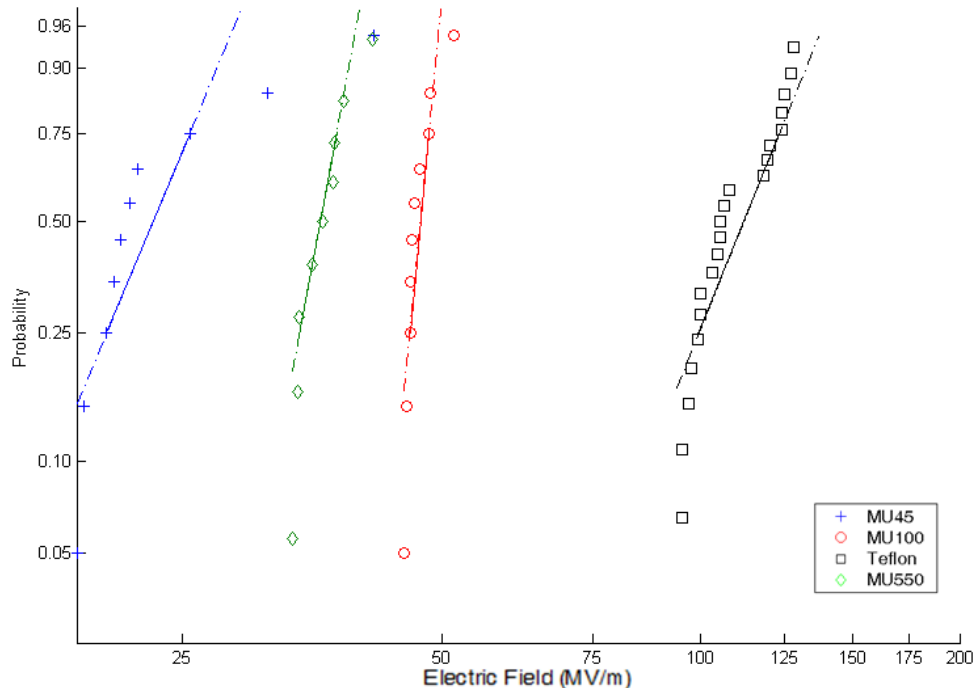


Figure 58. Weibull plot of electric field at breakdown without a dielectric coating and without inclusion of the field enhancement factor

Table 5. Summary of Weibull Parameters for Samples without Coating and without FEF Included

	MU45	MU100	MU550	Teflon
Number of Samples	10	10	9	23
k_W -Shape Parameter	3.48	21.5	14.35	9.05
λ_W - Scale Parameter	26.88	48.1	37.68	116.15

Table 6 summarizes the data for samples without a high dielectric constant coating and without consideration of the field enhancement factor. The relatively large amount of variability in the breakdown data obtained for MU45 results in a significantly lower electric field at 1% probability of breakdown than MU100 and MU550. MU100 and MU550 showed relatively low variation in the electric field at breakdown in the bulk of the material with both composites' values falling within a range of ± 5 MV/m from the median value. Teflon exhibited the highest range of electric fields when the field

enhancement factor is not considered. This is expected due to the relatively low field enhancement factor of Teflon in comparison to the high dielectric constant composites.

Table 6. Summary of electric field data for samples without a high dielectric constant coating and without inclusion of the field enhancement factor

	MU45	MU100	MU550	Teflon
Max Electric Field (MV/m)	41.76	51.73	41.62	137
Min Electric Field (MV/m)	18.82	45.27	33.5	93.7
Electric Field at 1% Probability of Breakdown (MV/m)	7.17	38.84	27.35	69.87

Figure 59 shows a plot of the same data set that produced Figure 58 without a high dielectric constant electrode coating but with inclusion of the field enhancement factor. Including the FEF, the peak field measurements vary from 165.4 to 308.54 MV/m for MU45, 358.76 to 501.32 MV/m for MU100, 276.87 to 419.87 MV/m for MU550, and 259.28 to 379.11 MV/m for Teflon. Inclusion of the field enhancement factor decreased the quality of the fit to a Weibull distribution. This is partially due to the limitations of estimating the field enhancement factor of each sample with electrostatic simulations. Despite the variance that can occur between electrostatic simulations, the FEFs calculated from these simulations provide the best estimate at the actual FEF and give insight to the peak fields present at the electrode edges.

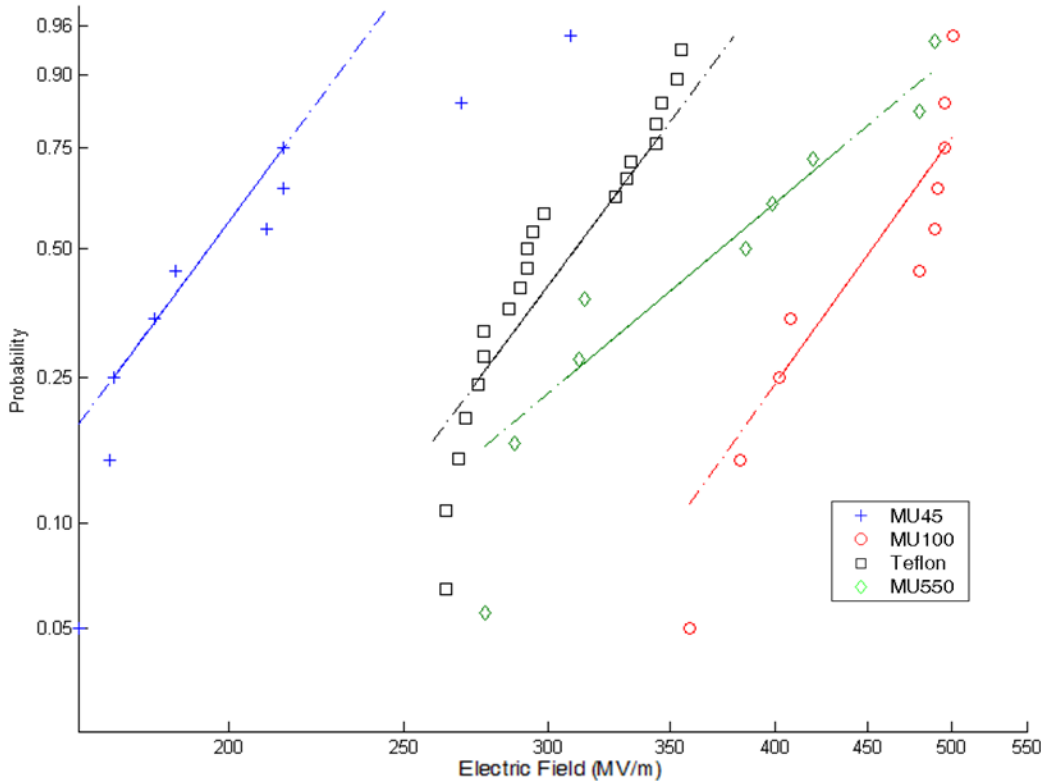


Figure 59. Weibull plot of electric field at breakdown without a high dielectric constant coating and with the field enhancement factor

Table 7. Summary of Weibull parameters for samples without a coating and with FEF included

	MU45	MU100	MU550	Teflon
Number of Samples	10	10	9	23
k_w -Shape Parameter	4.71	11.44	5.48	9.05
λ_w - Scale Parameter	228.05	473.21	405.31	321.39

Table 8 summarizes the electric field data at breakdown. The FEF is much higher for the composites than for Teflon due to the dependence of the FEF on the dielectric constant of the materials. When accounting for the FEF, the peak electric field at breakdown was higher in MU100 than in Teflon. As seen in Figure 59, many of the data points for MU550 with the FEF included were higher than those for Teflon. However, due to the slope of the line fit to the data in the Weibull analysis, the value at 1% probability of breakdown is slightly lower for MU550 than for Teflon. To effectively utilize the high

dielectric strength of the composites, the FEF must be lowered such that the average electric field is not significantly lower than the peak field. As theoretically demonstrated in the simulations described in Chapter 3, one way to potentially lower the FEF to levels at which the average field can be significantly raised is to coat the triple point at the electrode edge with a high dielectric constant material.

Table 8. Summary of electric field values for samples without coating and with FEF

	MU45	MU100	MU550	Teflon
Average Simulated Field Enhancement Factor	8.80	9.60	9.49	2.77
Max Electric Field (MV/m)	308.54	501.32	419.87	379.11
Min Electric Field (MV/m)	165.40	358.76	276.87	259.28
Electric Field at 1% Probability of Breakdown (MV/m)	85.87	316.53	175.07	193.32

Figure 60 shows the Weibull plot of dielectric strength data for MU45 and MU100 with an electrode coating of a high dielectric constant ink. While the FEF is predicted to be reduced to 1.95 and 2.21 for MU45 and MU100, respectively, the FEF is not included in the plot of Figure 60 and the data of Table 9 and Table 10 to enable direct comparison with the average electric values previously presented for samples without a coating. Data for MU550 was unavailable for this coating due to incompatibility of the binder in the high dielectric constant ink with the EC50 component of MU550. The same technique could be applied to MU550 with a high dielectric constant coating that is insoluble in EC50. A total of 12 data points were available for MU45, and 7 data points were obtained for MU100. Table 9 summarizes the Weibull parameters for this data set with a high dielectric constant electrode coating.

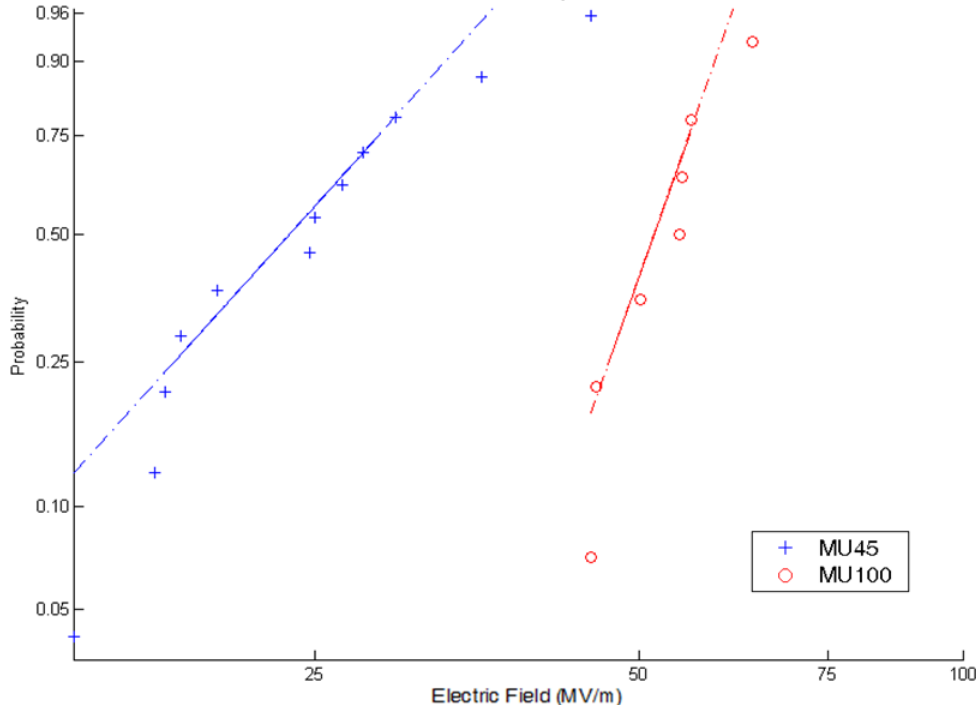


Figure 60. Weibull plot of electric field at breakdown for MU45 and MU100 samples with high dielectric constant coating around electrode edges but without FEF

Table 9. Summary of Weibull parameters for samples with coating but without FEF

	MU45	MU100
Number of Samples	12	7
k_w -Shape Parameter	3.2	9.29
λ_w - Scale Parameter	28.33	55.64

Table 10 summarizes the electric field values observed and calculated from the Weibull analysis. If the coating effectively reduced the FEF to 1.95 and 2.21 for MU45 and MU100, respectively, the electric field observed at breakdown should increase by an average factor of between 4 and 4.5. However, the observed values suggest the coating had either no effect or a somewhat negative. The electric fields at 1% probability of breakdown for the cases with and without the coating are reduced by 6.14% and 12.7% for MU45 and MU100, respectively.

Table 10. Summary of Electric Field Values for Samples with Coating without FEF

	MU45	MU100
Max Electric Field (MV/m)	45.20	63.72
Min Electric Field (MV/m)	14.96	45.19
Electric Field at 1% Probability of Breakdown (MV/m)	6.73	33.91

There are three possibilities that could explain why the coating did not produce the desired effect. The first possibility is that the high dielectric constant coating did not thoroughly coat the triple point junction. This could be due to poor compatibility between the coating and surfaces of the electrode and/or composite, too high viscosity of the coating, trapped gas within the coating, or other factors. The second possibility is that the breakdown was dominated by triple points along the electrode-composite junction away from the edges. The third possibility is that dielectric breakdown is dominated by field concentration with the composite, and effects at the electrode-composite junction do not factor into the dielectric strength. Assuming the FEF due to the electrode-composite junction at the edges does impact the dielectric strength, a larger study is required to develop methods to effectively reduce the FEF. To better implement a high dielectric constant electrode coating, the study must examine issues such as the wettability of the coating to the composite surface, the viscosity of the coating to flow into small features along the electrode edge, the size of filler particles within the coating, and the elimination of gas from the coating.

4.6 Thermogravimetric Analysis

4.6.1 Thermogravimetric Analysis Methods

Thermogravimetric analysis refers to the analysis of the change of a material's mass due to changes in temperature. The technique is often used to generate a continuous curve

of the sample mass as a function of increasing temperature [7]. Identification of mass loss at certain temperatures can provide information on the composition of the sample and the physical processes occurring at particular temperatures [7]. In this work, the analysis was aimed at determining the weight percentage of binder in each of the composite classes. This analysis did not require continuous monitoring of the sample mass as the temperature was raised and lowered. Instead, the sample's mass was determined before and after heat treatment.

One sample of each composite class was prepared for thermogravimetric analysis. The samples were sanded to limit any error that unevenness in the sample thickness would contribute to the calculation of the sample volume. The samples were heated at low temperature for over 24 hours before measurements were taken in an effort to limit the effect of absorbed water from atmospheric exposure on the mass measurement. The thickness, diameter, and mass of each sample were measured before the high temperature treatment. Based on these measurements, the volume and mass density were calculated. For MU550, the mass was measured both dry and after soaking in EC50. Based on the difference in the dry and soaked mass and the density of EC50, the weight and volume percentage of EC50 was calculated. The masses of the composites were measured again after the high temperature treatment. The difference in masses before and after the heat treatment along with information about the binder density and ash content permitted calculation of the remaining parameters of interest.

To determine the ash content of the binders, samples of CR-S, polysilsesquioxane, and agar were included separately during the same high temperature treatment as the composites. The masses of the binders were measured before and after the heat treatment.

The percentage of the initial binder mass remaining after the high temperature treatment was considered the ash content, and this percentage of the binder was assumed to have remained in the composites as well.

Three additional assumptions were required to complete the analysis. First, it was assumed that none of the ceramic mass was lost during the heat treatment. This is a safe assumption due to the temperatures in excess of 1000 C at which barium titanate is routinely processed. The second assumption was that the EC50 soaked into the MU550 sample filled all of the composite's voids. This assumption was necessary due to the unknown mass density and volume of the agar in the composite. While this assumption represents the ideal case and some voids likely remained, the results presented in the following subsection suggest that the assumption is a reasonable approximation. Similarly, the third assumption assumes that the polysilsesquioxane binder of MU100 completely fills the voids between the ceramic particles. This assumption was also due to the unknown mass density and undetermined volume of the polysilsesquioxane. Limited data is available on the mass density of polysilsesquioxanes, and it is believed that the porosity and resulting density of the polysilsesquioxane is dependent on the conditions under which the network forms. In measurement of the mass density from a polysilsesquioxane formed over a long period of time at room temperature and atmospheric pressure, the resulting mass density was so low that the predicted volume of the binder in the composite would have been larger than the composite. The assumption is considered reasonable as the mass density estimated from the calculations is close to the mass density of similar polymers, such as polydimethylsiloxane.

The high temperature treatment was conducted in an ashing furnace. The temperature was increased from room temperature to 400 C at a ramp rate of 10 C/min. The furnace was held at 400 C for 2 hours after which the furnace cooled to room temperature at an unspecified rate.

4.6.2 Thermogravimetric Analysis Results

The results of the thermogravimetric analysis of the binders are summarized in Table 11. As seen in the estimates of the percentage of ash from each binder, more than 83% of the CR-S and more than 87% of the agar masses were lost upon heat treatment, but less than 12% of the polysilsesquioxane was lost. The high remaining amount of PSSQ is due to the low organic content and high thermal stability of the binder used in MU100. The estimated binder densities for the PSSQ and agar were calculated from the estimated mass and volume of the respective binders described later in this section. The estimated density of the CR-S was obtained from data in the literature for pullulan, and this density value was used to calculate the estimated volume occupied by the CR-S in MU45 [8].

Table 11. Summary of mass loss from each binder

	Mass Before Burn (g)	Mass After Burn (g)	Percentage Ash of Binder	Est. Binder Density (g/cm³)
CR-S	1.6200	0.0809	16.18%	1.70 [8]
PSSQ	3.1220	1.7747	88.31%	1.40
Agar	1.2539	0.0214	12.52%	0.85

Table 12 provides a summary of the basic measurements of the composites including the thickness, diameter, and mass before burning. The order of highest to lowest mass density of the composites before heat treatment was MU100, MU550, and MU45. More than 1 g, approximately 13% of the composite mass, was lost upon heat treatment of the MU45 sample.

Table 12. Basic properties of the samples analyzed through thermogravimetric analysis

	Thickness (mm)	Diameter (mm)	Composite Volume (cm³)
MU45	4.05	25.16	2.01
MU100	0.82	25.4	0.42
MU550	2.6	25.4	1.32

	Mass of Composite (g)	Composite Density (g/cm³)	Mass of Binder Lost on Burning (g)
MU45	7.8327	3.8900	1.0158
MU100	1.9581	4.7126	0.0192
MU550	5.4369	4.1269	0.1636

Table 13 summarizes data on the binder content of the composites. The estimated total binder mass was determined from the binder lost during heat treatment of the composites and the percentage ash content observed from the binder alone. The mass percentage was then calculated directly from the binder and composite masses. The estimated volume of the binder was calculated from the mass and density of CR-S for MU45. The volume of MU100 was calculated as the remaining volume unoccupied by the ceramic based on the assumption that the PSSQ filled all of the voids between ceramic particles. The volume of agar in MU550 was calculated as the remaining volume unoccupied after accounting for the volume occupied by the ceramic and EC50. The percentage mass and percentage volume of binder are important results of this analysis. Unsurprisingly due to the lower dielectric constant of MU45, the binder content of MU45 is the highest of the three composites. MU550 had the lowest calculated mass and volume of binder as the agar is intentionally dried from its swelled state during composite formation, reducing its mass through water removal.

Table 13. Summary of binder content of composites

	Est. Total Binder Mass (g)	Est. Percentage Mass of Binder	Est. Volume of Binder (cm³)	Est. Percentage Volume of Binder
MU45	1.2119	15.47	0.7129	35.40%
MU100	0.1642	8.39	0.1175	28.28%
MU550	0.1870	3.44	0.2202	16.72%

Table 14 summarizes the ceramic content in each composite class. For MU45 and MU100, the mass of ceramic was calculated based on the total composite mass and the binder mass of Table 13. With the ceramic mass established, the ceramic volume is calculated based on a mass density for barium titanate of 6.02 g/cm³. MU100 had the highest mass and volume percentage of ceramic followed by MU550 and MU45. The volume percentage of ceramic for MU100 was estimated to be 71.72%, which is only about 5% lower than the measured volume percentage obtained with a trimodal mixture with no binder. All three composite classes have an estimated volume percentage of ceramic greater than 50%, which is due to the high packing density made possible by multimodal ceramic particle sizes. The lower volume percentage of ceramic in MU550 and MU45 is attributed to the larger size of the polymers used in those composites and the polymerization of the binder prior to formation of the composite.

Table 14. Summary of ceramic content of composites

	Est. Mass of Ceramic (g)	Est. Mass Percentage of Ceramic	Est. Volume of Ceramic (cm³)	Est. Volume Percentage of Ceramic
MU45	6.6208	84.53%	1.10	54.62%
MU100	1.7939	91.61%	0.30	71.72%
MU550	4.8944	90.02%	0.81	61.71%

Table 15 provides data on the volume percentage of voids for each composite class. The volume percentage calculated for MU45, approximately 10%, was calculated as the remaining volume after accounting for the ceramic and binder. As previously discussed,

it was assumed that the PSSQ completely fills the voids of MU100. This assumption is necessary because the volume occupied by the PSSQ cannot be calculated due to the unknown density of the PSSQ. Thus the volume percentage is assumed to be the ideal case of 0%. The volume percentage of voids for MU550 is actually the volume percentage occupied by EC50 based on the assumption that EC50 completely fills the composites voids.

Table 15. Summary of void estimates

	Estimated Volume Percentage of Voids (cm³)
MU45	9.98%
MU100	0%
MU550	21.575

Table 16 summarizes how the volume percentage of 21.57% was determined for the EC50. Based on the measured mass gain upon soaking the previously dried MU550 in EC50, the volume was calculated with the known mass density of EC50 of 1.251 g/cm³. Although the volume percentage of voids in MU550 seems high, this volume is filled with a high dielectric constant material, resulting in the highest high frequency dielectric constant values of the three composite classes.

Table 16. Summary of EC50 content of MU550

	Mass of EC50 (g)	Percentage Mass of EC50	Volume of EC50 (cm³)	Percentage Volume of EC50
MU550	0.3555	6.54	28.42	21.57

4.7 Scanning Electron Microscopy

4.7.1 Scanning Electron Microscopy Methods

The primary use of scanning electron microscopy (SEM) was to characterize the ceramic particle size and morphology. Since the ceramic particles were obtained

commercially, the suitability of the particles for the intended use had to be verified. In particular, the large particles and nanoparticles required inspection before use. The large particles were often initially received as very porous pieces of material. Since the large particles would only be effective at contributing towards a high volume fraction of ceramic in the composite if they were non-porous, the SEM analysis revealed that the large particles could not be used as received but rather needed to be further densified through a sintering process. The as-received nanoparticles were revealed to often form large spherical agglomerates. The agglomerates, often measuring several tens of microns in diameter, also were very porous and of low density. Although the primary particles forming the agglomerate were at the size scale rated by the manufacturer, the primary particles could not be adequately mixed into the trimodal composition while in the form of large agglomerates. SEM analysis revealed the agglomerated nature of the nanoparticles, and the nanoparticles were imaged again after a milling and chemical treatment was applied to reduce the agglomerates.

Energy-dispersive X-ray spectroscopy (EDS) was also conducted on some particles and composites to determine the atomic content of the sample. The EDS analysis provided a means of verifying the composition of the particles, and spectral mapping enabled a visual representation of the distribution of elements throughout the surface of the composites.

Scanning electron microscopy produces images at magnification levels greater than conventional light microscopy by directing an electron beam with a small spot size across the sample and detecting the scattered electron and x-ray products of the interaction of the electron beam and material being imaged. The electron beam is scanned across the

entire surface to be imaged, and the data collected at each point is compiled to form an image. Independent detectors can be used to collect information on secondary electrons, back-scattered electrons, and x-rays. All micrographs presented here were obtained on an FEI Quanta 600 Field Emission Gun Extended Vacuum Scanning Electron Microscope. The FEI Quanta 600 can operate under high vacuum and low vacuum conditions. The pressure was varied when necessary to prevent surface charging on the ceramics and composites being imaged. Most samples were imaged with a secondary electron detector to obtain topographical information on the size and morphology of particles.

4.7.2 Scanning Electron Microscopy Results

Figure 61 and Figure 62 each compare micrographs of barium titanate intended for large particles as-received from the manufacturer and after a high temperature treatment to promote sintering and densification. At this stage, the barium titanate was in the form of large pieces between about 3 and 12 mm in diameter. As seen on the left-hand half of each figure, the as-received material was a very porous structure formed from a multitude of primary particles on a size scale of around 1 μm . This indicates that the ceramic pieces were likely manufactured from heat pressing of primary particles on the micron or sub-micron size scale. The heat pressing process did not form a dense structure but rather a hard aggregate. The right-hand half of each figure shows the surface of the pieces after a high temperature sintering treatment at 1350 C for 3 hours. The densification of the ceramic is clearly apparent in the smooth topology of the surface. Boundaries are seen between large particles with dimensions on the order of several tens of microns. These large particles are strongly bonded to one another, but the pieces at this stage are ready for milling to produce large particles with dimensions on the order of tens of microns.

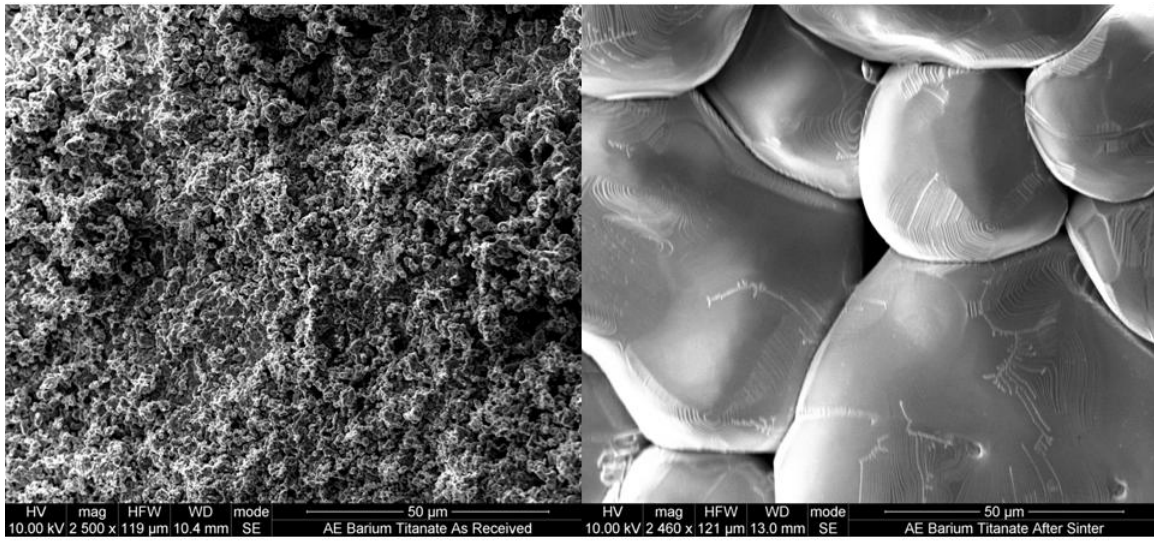


Figure 61. Large barium titanate pieces before (left) and after (right) sintering treatment.
The size scale is 50 μm .

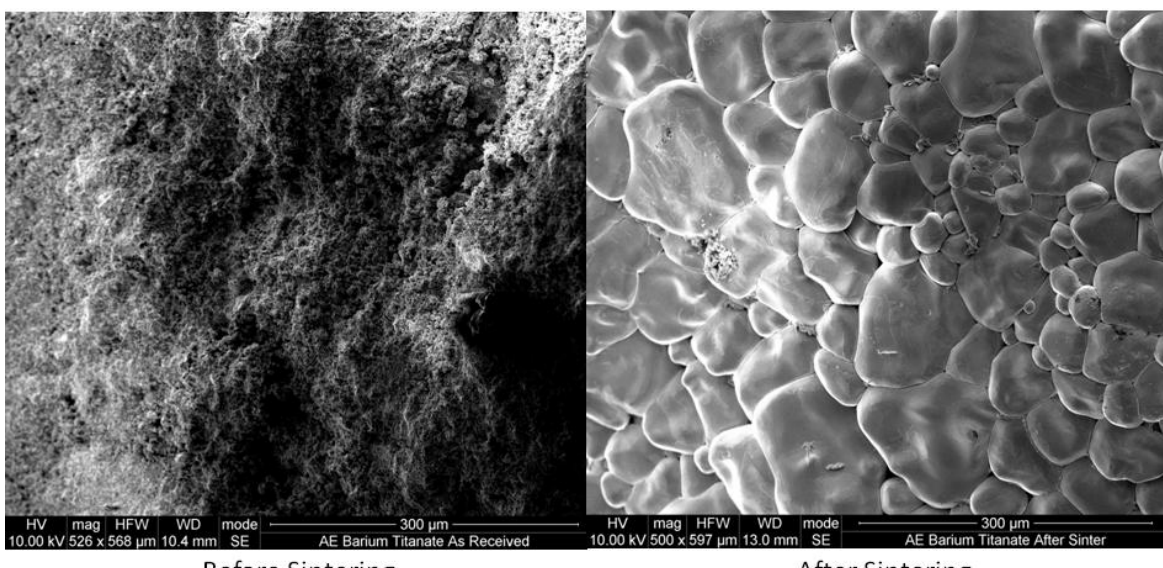


Figure 62. Large barium titanate pieces before (left) and after (right) sintering treatment.
The size scale is 300 μm .

Figure 63 displays the products of milling the ceramic pieces intended for large particles. The left-hand side of the figure shows the products when the large pieces have not been treated at high temperature to further sinter the pieces. Upon milling these hard aggregates, many small particles on a size scale of 1 μm are produced. A relatively small number of large particles appear to be present. However, the density of these large

particles is low, decreasing their effectiveness to increase the volume fraction of ceramic when used in a multimodal distribution. The right-hand side of the figure shows the milled products of ceramic pieces that were treated at high temperature to further sinter the pieces. The products on the right-hand side have also been sieved to greater than 63 μm . Milling the sintered ceramic pieces is effective at producing the large particles required for a multimodal mixture. However, the milling procedure does produce many smaller particles that must be removed through sieving. While these smaller particles could be used for other purposes, they are effectively waste from the large pieces, so excessive milling is avoided to minimize the production of small particles in this process. It can also be seen on the right-hand side of Figure 63 that some of the small particles are adhered to the surfaces of the large particles. These small particles are not necessarily a problem as they can help to fill the voids between the large particles. However, in the interests of consistency and repeatability in the manufacturing process, it is helpful to have full control over the quantity of each size of particle going into the multimodal mixture. Therefore, the small particles adhered to the large particles are unwanted as their size distribution and quantity is unknown. A final note on the large particles is that their shape is highly irregular as a result of the milling process. It is possible that the irregular distribution of particle shapes can factor in increasing the packing density of the particles.

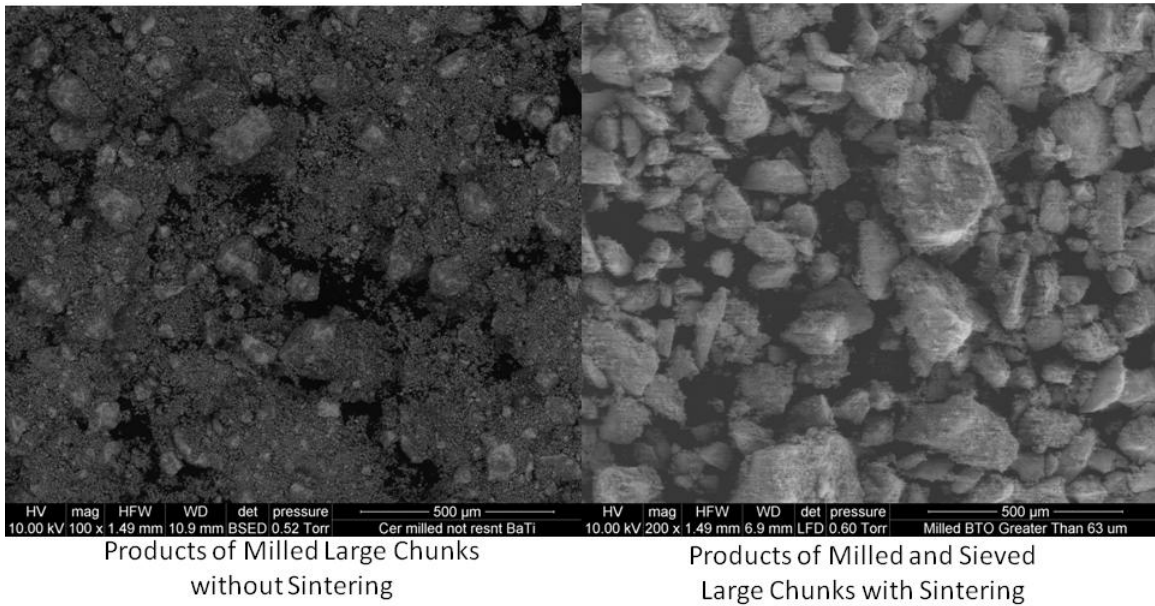


Figure 63. Milled products of large ceramic pieces without sintering (left) and with sintering (right). The size scale is 500 μm .

Figure 64 compares nanoparticles as-received from the manufacturer and after milling.

As seen on the left-hand side of the figure, the nanoparticles have agglomerated into larger structures with dimensions on the order of tens of microns to greater than 100 microns. These soft agglomerates in the shape of spheres hinder effective mixing of the nanoparticles into the voids between the larger particles in a multimodal distribution. Therefore, it is necessary to mill the nanoparticles. The nanoparticles are typically milled in a solvent, optionally with a surfactant to prevent reagglomeration of the nanoparticles. The right-hand side of the figure shows a much higher magnification view of the nanoparticles after the agglomerates have been separated by milling. After milling, it is evident that the primary particles composing the agglomerates are in fact nanoparticles with dimensions of less than 100 nm.

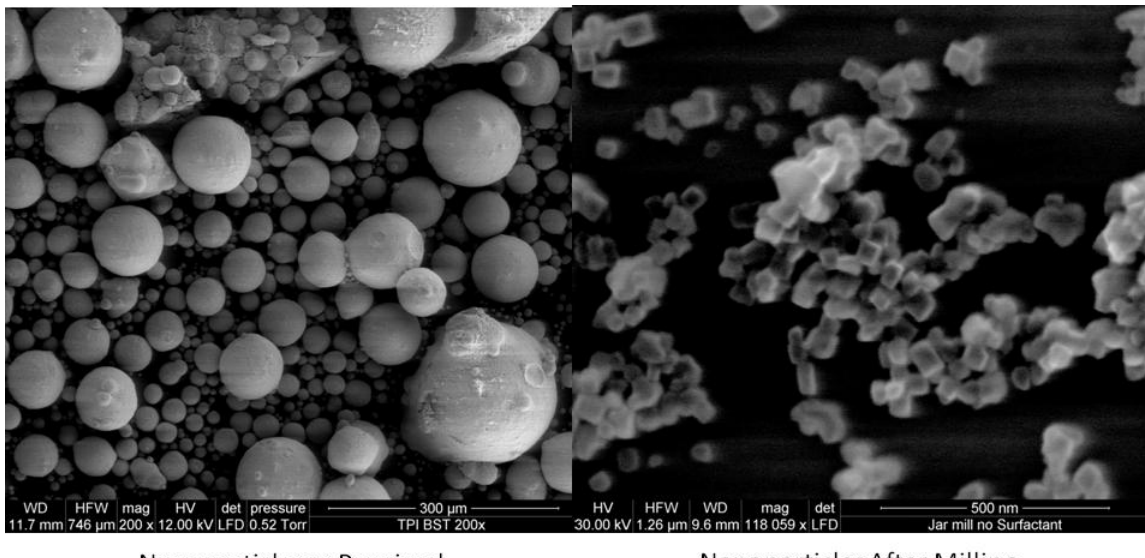
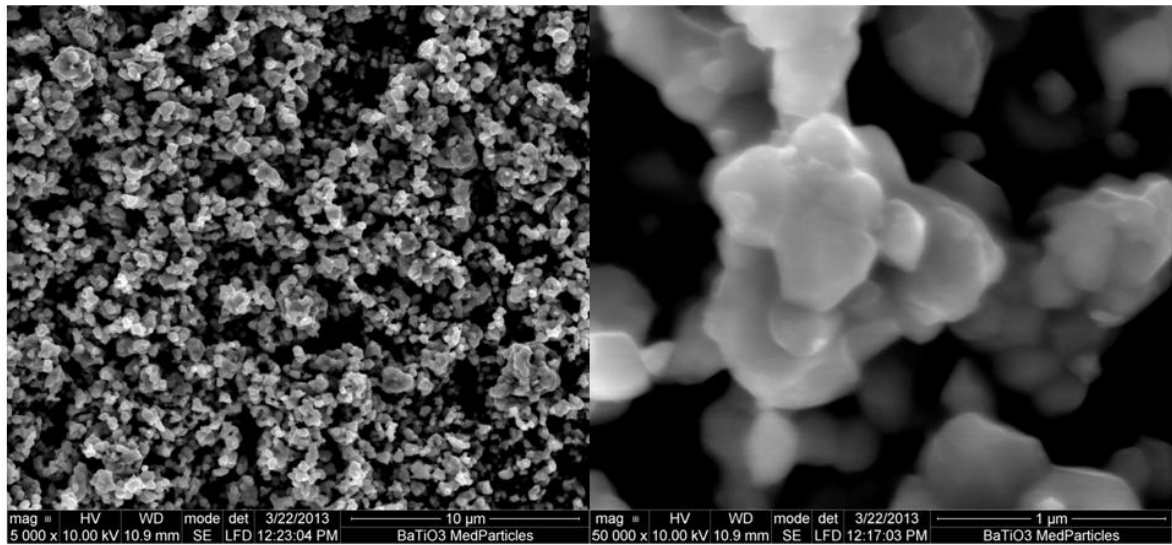


Figure 64. Nanoparticles as received (left) and after milling (right). The size scale on the left is 300 μm , and the size scale on the right is 500 nm.

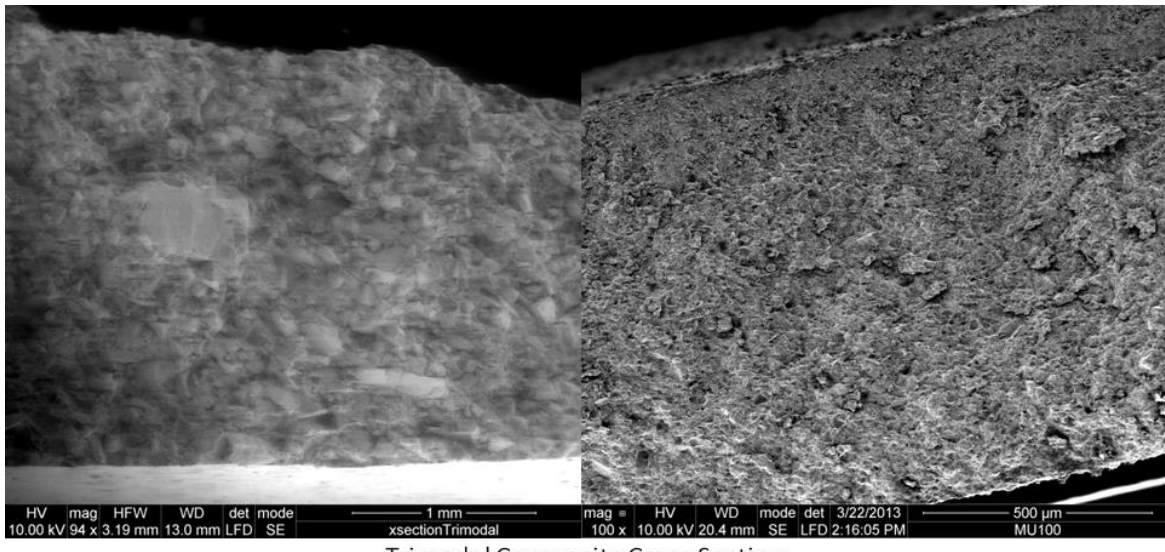
Figure 65 displays micrographs of the intermediate size particles at 5,000 and 50,000 times magnification. The size of these particles is rated to be less than 3 μm . As both sides of the figure show, the particles are within the specification without further treatment, so the particles were used in the composites as received. In the right-hand side of the figure, the particles seem to be formed as a dense formation of smaller primary particles. Since the particles do not appear to be porous, the density of the particles is believed to be adequate. The irregular shape of the particles may increase the particle packing density as in the case of the large particles.



Intermediate Size Particles as Received

Figure 65. Intermediate size particles as received. The size scale on the left is 10 μm , and the size scale on the right is 1 μm .

Figure 66 shows the cross-section of two composites containing a trimodal distribution of particles. These cross-sections were obtained by fracturing the composites, and the surfaces were imaged without polishing, allowing the topography of the fractured surface to be seen. The composite on the left-hand side included large particles that were sized at the high end of particle sizes used in the composites, including particles with dimensions greater than 100 μm . Both cross-sections display the high degree of ceramic particle packing and distribution of particle sizes.



Trimodal Composite Cross Section

Figure 66. Cross Sections of composites including a trimodal distribution of particles.
The scale on the left is 1mm, and the scale on the right is 500 μm .

4.8 3D Modeling of High Dielectric Constant Composites

4.8.1 3D Model Description

The effective dielectric constant of the composite was computationally determined to compare with numerical predictions and experimental results. The effective dielectric constant describes the charge storage capability of the composite based upon the properties of the constituent materials and the manner in which they are mixed. Since the composites of interest contain materials with widely-varying properties, including very high dielectric constant ceramics and relatively low dielectric constant binders, the prediction of the effective dielectric constant of the composite can vary widely between the extreme values of each constituent material. Due to some conflicting evidence of the accuracy of many of the numeric models with respect to a wide range of experimentally-produced composites, the computational model is used for comparison of the competing theories. Computational simulation also enables the analysis of the electric field

distribution between the components comprising the composite. Another result of the widely varying dielectric properties of the composite's constituents is an unequal distribution of the electric field. An understanding of how the electric field is distributed is crucial for prediction of potential failure points due to electrical breakdown. Due to the random nature with which many of the components are arranged in the composite, a detailed analysis of the electric field distribution is effectively impossible without the aid of computer analysis.

The model builds upon the advancements recently made in three-dimensional dielectric composite modeling by other researchers [9, 10]. The model under consideration offers some unique capabilities, including flexibility in the properties of the composite's components, as described in subsequent sections. The program's operation is described, and examples are given of an analysis on the difference between simulated and calculated effective dielectric constant values and the visualization of the electric field distribution.

The modeling program was implemented as a macro in CST EM Studio. The macro provides a user interface to input simulation parameters, check for errors, and automate the process of creating the composite form, filling the composite with ceramic, polymer, and voids, executing the electrostatic simulation, and calculating the parameters of interest from the results of the simulation. This section will describe the flexibility built into the macro in defining the composite parameters.

One of the significant differences between the simulation program being described and similar previously-developed programs is the range of parameters that can be defined. The program is built to accommodate up to six different materials in the composite. The form of the composite is first filled with a solid matrix, which is usually defined with the

properties of a polymer that acts as the composite's binder. Up to four additional materials can be added as fillers, with the default use consisting of between 1 and 3 ceramic fillers and one material defined as voids. The morphology of the particles can be any of the predefined shapes available in CST EM Studio, but cubes and spheres are given as the only default options as they are the most common shapes encountered in real particles.

Figure 67 shows a screen shot of the user interface developed for the program. The input parameters occupy the left side of the interface, and the output from both the particle-filling and electrostatic-modeling functions appears on the right side. For each of the composite materials, the dielectric constant and mass density is entered into the program. For the fillers and voids, the dimensions of the particles to be inserted into the program are also included. The volume percentage of the total composite volume is user-defined for the filler and voids. The user can then define the percentage of each filler towards the total filler volume. Options also allow the composite to be built without fillers and/or voids. The combination of all the parameters allows a substantial amount of flexibility in the range of composites that the program can model.

When filling the composite with filler particles or voids, coordinates are randomly generated, and the volume surrounding the coordinates is checked for other materials, depending on the mode of insertion. Two modes of filler insertion are available based on hard or soft modeling [9, 11]. Hard modeling does not allow two filler particles to intersect. However, soft modeling does allow intersection, forming more complex filler shapes as a new combined particle is effectively formed due to the intersection. Both modeling methods have advantages under certain circumstances. However, in this

program, it has been determined that it is most practical to use hard modeling for generating fillers and soft modeling for generating voids. This practice is intuitive as individual ceramic particles will not be capable of merging without sintering, which is not an option for the composites under development. Voids, often consisting of trapped air, however, will effectively merge if placed adjacent to each other, so soft modeling is appropriate for voids.

There are currently two potential sources for error in calculations of the effective dielectric constant. The first source of error is the inclusion of the fringe capacitance in the value returned by EM Studio in the capacitance matrix. The electrode and composite diameters are equal, so the capacitance value returned by the program will include fringe capacitance due to the surrounding volume occupied by a material with a dielectric constant of 1. Since the fringe capacitance is dependent on the geometry of the composite, it is difficult to precisely account for it. However, the error introduced by the fringe capacitance is lower for a composite with a higher value of effective dielectric constant. Inclusion of a method to account for the fringe capacitance is a potential future improvement to the program. The second source of error is introduced when the edges of neighboring filler particles or filler and void particles overlap. Although the program is designed to model filler-filler and filler-void interactions with a hard model without intersections, a small amount of edge intersections do occasionally occur. When a location is randomly selected for placement of a particle, only a finite number of points on that particle's surface can be analyzed for conflict with other particles already in place. Checking for conflicts at the defined locations along the surface of the new particle prevents placement of particles with a significant overlap but does not always detect

overlapping edges. Although the intersecting volume is relatively small, the exact percentage of overlap is indeterminable. This overlap introduces error during electrostatic simulation as the program can only use the dielectric constant of one of the materials in the overlapping region. Future improvements to the program can be made to either check for conflicts at more surface points before particle placement and/or determine the volume of intersecting edges.

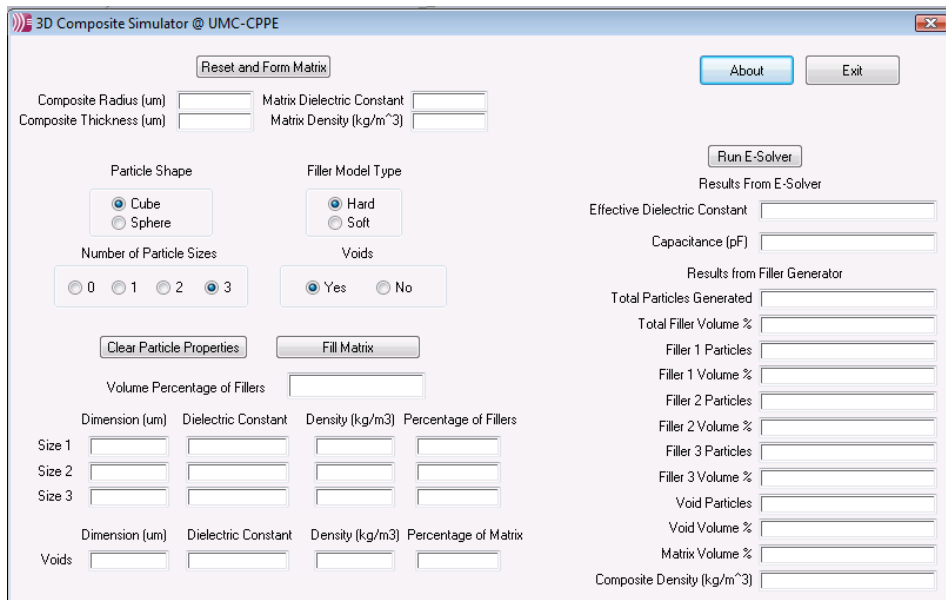


Figure 67. Screen shot of the user interface displaying the control parameters for composite construction

Figure 68 and Figure 69 show examples of composites generated by the macro. The matrix was generated as a cylinder with a relatively low dielectric constant. Perfect electrical conductors, which can be seen as semi-transparent plates in Figure 69, were automatically generated on both sides of the composite to facilitate electrostatic simulation. Spherical fillers were randomly generated and inserted into the matrix volume of Figure 68, and Figure 69 shows a composite filled with cubic particles. Since the simulations are meant to model real composites, partial particles at the edges of the composite are not permitted. Once the composite has been generated through the

automated process according to the user's specifications, an electrostatic analysis can be performed, giving results for the capacitance, effective dielectric constant, and electric field distribution.

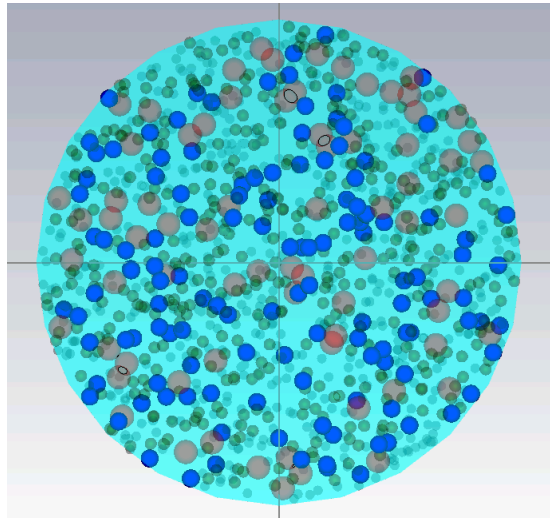


Figure 68. Virtual composite filled with 4 types of spherical particles

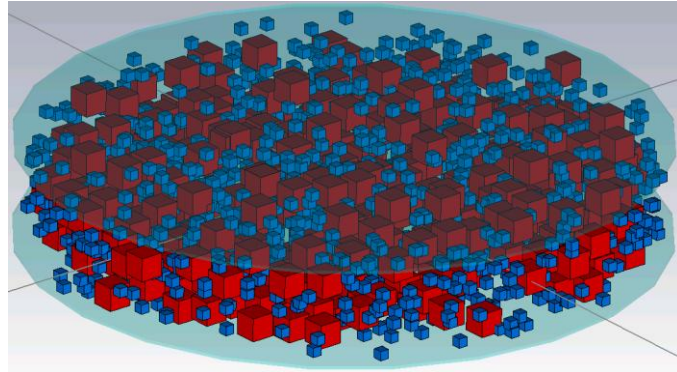


Figure 69. Virtual composite filled with 2 types of cubic particles

A typical composite for a simulation is a cylinder 5 μm thick and 10 μm in diameter. While these dimensions are small in comparison to the large composites produced in this work, the dimensions must be kept on this scale to limit the number of mesh cells generated during the simulation to a practical level of several million. Despite the discrepancy between the sizes of the simulated volume and the physical composites, the concept of simulating a small volume to predict the properties of a larger composite is sound due to the homogeneity of the composites. The simulated dimensions effectively

correspond to simulating a small volume of a much larger composite consisting of many equivalent volumes on the scale of that which is simulated. Two aspects of the composites that cannot be directly replicated in the simulations are the size of the particles and the ratio of the particle sizes. These constraints are also due to the practical limits of the number of mesh cells. If 50 nm particles were to be simulated alongside 1 μm particles, the mesh size would have to be so small to adequately simulate the 50 nm particles that the total mesh count would be unmanageable for a desktop system to simulate. Therefore, the particle sizes are generally kept within a size range between 0.5 and 2 μm . The upper limit ensures that any one particle is less than half the thickness of a 5 μm thick virtual composite. The lower limit of 0.5 μm allows a distribution of particle sizes to be used while keeping the mesh count to a realistic level. A drawback of the limitation in the range of particle sizes is that very high levels of particle loading, typically greater than 70%, are very difficult if not impossible to produce.

4.8.2 Model Results

Three-dimensional models of each of the composite classes were generated and simulated in CST Microwave Studio using the volumetric content calculated from the thermogravimetric analysis data in section 4.7. The composites were simulated as a cylinder with a thickness of 5 μm and a diameter of 10 μm . Two particle sizes, typically 1.5 μm and 0.5 μm , were used to achieve a high volume percentage of filler particles. Figure 70 shows the particles generated by the macro for simulation of MU100. The electrodes and matrix material have been hidden in the figure to allow the particles to be seen more clearly. In this example, the macro generated 1,369 total particles distributed as 110 particles with a diameter of 1.5 μm and 1,259 small particles with a diameter of

0.5 μm . Both particle sizes represented ceramic fillers, and the total volume percentage filled by the particles was approximately 66.8%.

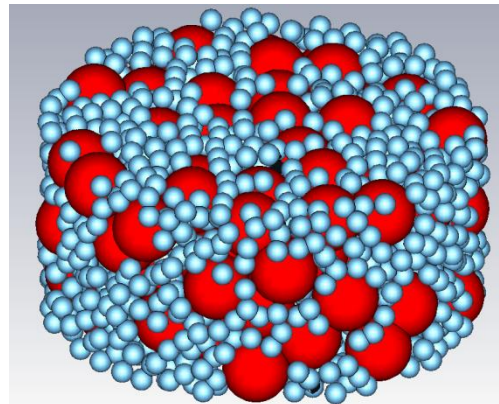


Figure 70. Particles generated by the macro for the simulation of MU100

Table 17 lists the dielectric constant values used in the simulations for the ceramic, binder, and voids in each of the composites. While the dielectric constant of barium titanate can vary depending on the conditions, measurement method, and source of information, a value of 100 was used in these simulations. The dielectric constant of the CR-S in MU45 was estimated to be 5, reflecting the lower value of this polar binder at high frequency. The dielectric constant of the PSSQ was assumed to be 2, which is consistent with measurements of similar low density polysilsesquioxanes. For MU550, it is assumed that the liquid filler is saturated throughout the volume of the binder, so a value of 77 for EC50 was used for both binder and void values.

Table 17. Summary of dielectric constant values for the ceramic, binder, and voids used in the three composite simulations

	Ceramic ϵ_r	Binder ϵ_r	Void ϵ_r
MU45	1000	5	1
MU100	1000	2	1
MU550	1000	77	77

Table 18 lists the target volume percentages of each component. The volume percentages of ceramic are the values calculated from thermogravimetric analysis. For MU45 and

MU100, the volume percentages of binder are also those obtained from thermogravimetric analysis. The volume percentage of binder for MU550 is the sum of the values calculated for the binder and voids. These values were combined because they are assumed to have effectively the same properties due to the saturation of EC50 in both volumes. The target volume percentage of voids for MU550 was accordingly adjusted to zero, so the simulation was simplified somewhat by removing the necessity of adding void particles. The simulation of MU550 required only the generation of ceramic particles, and the matrix material dielectric constant was assigned to 77 to represent the saturated binder and voids. The target void volume percentage was also zero for MU100 to remain consistent with the assumptions taken in the thermogravimetric analysis. The target volume percentage of voids for MU45 was set to 10% to remain consistent with the values of the thermogravimetric analysis.

Table 18. Target volume percentages for each component

	Target Vol. % Ceramic	Target Vol. % Binder	Target Vol. % Void
MU45	55	35	10
MU100	72	28	0
MU550	62	38	0

Table 19 presents the volume percentages reported by the macro after running the automated process of randomly distributing the filler particles and voids throughout the volume of the virtual composite. Some error can be introduced in this process due to either slightly overlapping particle edges or particle edges partially extending out of the composite volume. These overlapping sections introduce error into the reported volume percentage values by counting the volume of the overlapping sections twice. The percent error due to these overlapping sections is also presented in Table 19. This error is minimal for the composites generated for MU100 and MU550 at 0.35% and 0.2 %. The

error is somewhat larger at 3.9% for MU45 due to the additional components added in the form of voids. It should be noted that the volume percentage of ceramic achieved for MU100 was approximately 66.83% or slightly more than 5% lower than the target volume percentage. This discrepancy between the target and achievable value is due to limitations in particle packing density achievable within the constraints of the simulated volume and the practical ratio of particle sizes.

Table 19. The volume percentages of each component reported by the program after automatic generation of the fillers and voids

	Reported Vol. % Ceramic	Reported Vol. % Binder	Reported Vol. % Void	Percent Error in Vol. % Due to Overlap
MU45	52.92	41.73	8.88	3.53
MU100	66.54	33.82	0	0.36
MU550	59.37	40.83	0	0.2

Table 20 lists the simulated dielectric constants obtained from the 3D model along with values calculated using Lichtenecker's equation and the values of Table 17 and Table 19. The percentage difference between the two dielectric constant values is also provided to compare these two modeling techniques. MU550 was the simplest virtual composite due to the common dielectric constant of the matrix material and void regions and the relatively low volume percentage of fillers, both ceramic and voids, required. The agreement between the Lichtenecker model and the simulated value is excellent for MU550 with a percent difference of 3.34%. As the virtual composites become more complex with higher filler loadings, additional error is introduced. The percent difference between the mathematical model and the simulation for MU45 was just under 7%. The percent difference for MU100 reached nearly 17%. This discrepancy is believed to be due to the error introduced by very high filler loadings. As the filler loading reaches the maximum values possible, there is increased overlap of the particle edges. The overlap of

the particle edges would constitute a violation of the assumption of a homogenous mixture of individual particles assumed in the derivation of the Lichtenecker rule by Simpkin [12]. The overlapping particles form a larger percolated mass similar to what might be physically realized through sintering of the particles. Therefore, it is unsurprising that the higher filler loading results in a greater percentage difference as the simulation overestimates the dielectric constant.

Table 20. The dielectric constant obtained from the simulation, the dielectric constant calculated from Lichtenecker's equation, and the percentage difference

	Lichtenecker Predicted ϵ_r From Reported Vol. %	Simulated ϵ_r	% Diff. Between Reported Lichtenecker and Simulated Values
MU45	75.73	70.58	6.80
MU100	125.32	146.14	-16.62
MU550	355.92	367.8	-3.34

The 3D simulations of the effective dielectric constant of composites are most useful for evaluating mathematical models of composites, but some comments can be made on the agreement between the simulated dielectric constant and the measured values. The dielectric constant value for CR-S used in the Lichtenecker model and simulation was 5, corresponding to the high frequency value. The calculated and simulated composite dielectric constants for MU45 of around 70-75 are about 36% higher than the typically measured 45. The discrepancy could be a result of multiple causes. First, due to the imperfect composite-probe contact, it is expected that the high frequency measurement is an underestimation of the actual dielectric constant. Second, the value of 1000 assumed for the dielectric constant of barium titanate may be slightly higher than its actual value in the ceramics used in the composites. If a value of 21 were used as the dielectric constant of CR-S for low frequency applicability, the Lichtenecker equation predicts a dielectric constant of nearly 138. This value is reasonable in consideration of the low

frequency measurements of MU45 in which the dielectric constant was greater than 100 even under low electric field conditions.

Analysis of the calculated, simulated, and measured values of MU100 is very similar to the case of MU45. The calculated and simulated values for MU100 are 19% and 39% higher than the 200 MHz measured value of 105, respectively. The difference again could be due to the imperfect composite-probe contact and the potentially high dielectric constant value used for barium titanate. The theoretical values agree very well with the low frequency measurement of MU100 under low electric field conditions, which was previously reported to be 135.4 in Figure 43.

The discrepancy between the theoretical values of Table 20 and the high frequency measurement of 550 is different than the cases of MU45 and MU100 as the theoretical values are lower than the measured value. This difference is believed to be due to the variation in the volume percentage of ceramic between different samples of MU550. Of the three composites, MU550 exhibited the largest variation in properties from sample to sample. This variance can be caused by several manufacturing issues. The first potential cause is that the agar was allowed to cool and gel prior to the compaction of the composite. With the gel formed, the density of the ceramic particles will be kept below its potential maximum. Second, the solution of agar may have been prepared at too high of a concentration, which also can cause the packing density to be limited. Third, not all of the excess solution may have been pressed out of the slurry during compaction. This is related to the first potential problem but could be due to other issues than premature cooling. It is believed that when MU550 is prepared and pressed to its optimal density, the ceramic density can be as high as a trimodal distribution of particles packed without a

binder. Indeed, if the Lichtenegger equation is evaluated with 77% ceramic and the remaining volume occupied by polymer and voids saturated in EC50, the calculated dielectric constant is approximately 554.5. This value can be measured more accurately with the high frequency probe than MU45 or MU100 because excess EC50 on the surface of the composite fills any voids along the composite-probe junction, limiting the effects of air voids due to the imperfect contact.

References for Chapter 4

- [1] "Agilent 85070E Dielectric Probe Kit Technical Overview," Agilent Technologies 2008.
- [2] "Agilent Technologies Impedance Measurement Handbook," Agilent Technologies 2006.
- [3] C. K. Chiang and R. Popielarz, "Polymer composites with high dielectric constant," *Ferroelectrics*, vol. 275, pp. 1-9, 2002.
- [4] C. B. Sawyer and C. H. Tower, "Rochelle salt as a dielectric," *Physical Review*, vol. 35, pp. 269-275, 1930.
- [5] "PA-80 and PA-100 Trigger Generators," L-3 Communications Pulse Sciences, San Leandro, CA.
- [6] W. Weibull, "A statistical distribution function of wide applicability," *Journal of Applied Mechanics*, vol. 18, pp. 293-297, 1951.
- [7] A. W. Coats and J. P. Redfern, "Thermogravimetric Analysis: A Review," *Analyst*, vol. 88, pp. 906-924, 1963.
- [8] K. Nishinari, K. Kohyama, P. A. Williams, G. O. Phillips, W. Burchard, and K. Ogino, "Solution properties of pullulan," *Macromolecules*, vol. 24, pp. 5590-5593, 1991.
- [9] K. Zhou and S. Boggs, "Effective dielectric constant of a linear matrix filled with linear and nonlinear spherical particles," in *17th IEEE Inter. Pulsed Power Conf.*, Washington, D.C., 2009, pp. 342-345.
- [10] P. Kim, N. M. Doss, J. P. Tillotson, P. J. Hotchkiss, M. J. Pan, S. R. Marder, J. Li, J. P. Calame, and J. W. Perry, "High energy density nanocomposites based on surface-modified barium titanate and a ferroelectric polymer," *ACS Nano*, vol. 3, pp. 2581-2592, 2009.
- [11] D. P. Bentz, E. J. Garboczi, and K. A. Snyder, "A hard core/soft shell microstructural model for studying percolation and transport in three-dimensional composite media," NIST, Gaithersburg, MD 1999.
- [12] R. Simpkin, "A derivation of Lichtenecker's logarithmic mixture formula from Maxwell's equations," *IEEE Transactions on Microwave Theory and Techniques*, vol. 58, pp. 545-550, 2010.

Chapter 5: High Power Dielectric Resonator Antenna

5.1 Background on Dielectric Resonator Antennas

Dielectric resonators were first investigated in the late 1930s and were developed to form compact circuit filters and oscillators [1]. The large difference in the material properties of a high dielectric constant material and the surrounding medium create boundary conditions at the walls of the resonator. These boundary conditions enable standing wave patterns to form within the high dielectric constant material similar to those formed due to the boundary conditions of a metal cavity waveguide [2, 3]. In this way, high dielectric constant materials can form resonators similar to metal cavity waveguides. When applied in filters and oscillators, dielectric resonators are often metalized to prevent electromagnetic radiation from leaking from the circuit. However, the radiating nature of the resonators can be exploited to make compact high frequency antenna elements in the form of dielectric resonator antennas (DRAs). In this study, DRAs are generally limited to cylindrical geometries in which a high dielectric constant material with a dielectric constant of ϵ_r , radius of a [m], and height of h [m] acts as a radiating resonator when excited by being placed on or near a driving circuit.

This work on the development of a dielectric resonator antenna for high power applications in the VHF and UHF bands expands upon the state of the art of dielectric resonator antennas in three significant ways. First, although DRAs have been shown to operate over a large range of frequencies from 1.3 GHz to over 40 GHz, they are less commonly implemented below 1 GHz [3]. Second, the peak power level for DRA design of 1 GW is greater than all known power levels previously used to drive DRAs. The

uniqueness of the gigawatt-level power requirement undertaken in this effort extends the power level orders of magnitude over the levels used in conventional applications. Third, constructing the resonator of the DRA from high dielectric constant composite materials significantly enhances the ability to form the resonator into larger and more complex shapes.

Despite the differences in the frequency and power requirements from what have been previously demonstrated with DRAs, the DRA has multiple factors that make it an ideal choice for a compact, high power, dielectric-loaded antenna. First, the relationship between the dielectric constant of the material forming the resonator and the resonator's dimensions enables the high dielectric constant of the composite materials to directly reduce the size of the antenna with few additional factors influencing the antenna dimensions. The size and weight of the DRA are the primary limiting factors on the minimum operating frequency [3]. Since DRAs have traditionally been made with sintered ceramics or glass-like materials, the size, availability, and manufacturability of the resonators have been limited. By using the newly-developed high dielectric constant composites, the DRAs can more easily be built in the larger sizes required for low frequency operation. Even though the dimensions required for low frequency operation are considered large for DRAs, the dimensions will remain several times smaller than conventional low frequency antennas. Second, due to the flexibility in methods with which the DRA modes can be excited, it is possible to drive the DRA without direct connection between the high voltage metallic feed and the high dielectric constant material. Microstrip, aperture, and even probe coupling techniques can be employed without the conductor making direct contact with the high dielectric constant material.

Since the field enhancements at triple points formed at the edges of interfaces between conductors and high dielectric constant materials can be extremely large, indirect coupling is crucially important to integrating a high dielectric constant material into a very high power system. Large field enhancements can significantly contribute to premature dielectric breakdown in high voltage systems and must be avoided whenever possible. The transmission line feeding the DRA can also be tailored to the high power antenna requirements by utilizing large thicknesses of conventional insulators and adjusting the other transmission line parameters to maintain the desired impedance. For example, for a microstrip feed, the substrate thickness can be increased to withstand the peak high voltage levels while the width of the transmission line can be increased to maintain the characteristic impedance of the line. Thus, the DRA can be driven at very high peak power levels without stressing the dielectrics of the substrate and without making direct electrical contact with the high dielectric constant material. These unique aspects of DRA feeding mechanisms make DRAs an attractive choice for compact high power antennas.

5.2 Coupling Methods

Several options exist for coupling energy to the dielectric resonator, and the coupling method employed can affect the resonant frequency and bandwidth of the antenna. Some of the most common methods for coupling to a DRA include probe coupling, microstrip coupling, aperture coupling, coplanar coupling, and dielectric image guide coupling [3]. Probe coupling involves inserting the end of a microstrip or coaxial probe into or directly onto the surface of the resonator. Since this metal-resonator connection will result in very high field enhancements due to the triple points along the edge of the interface, probe

coupling is not considered a viable option for high power coupling. Coplanar coupling is also excluded due to the potential for flashover between the coplanar strips driving the resonator when driven at very high peak voltage. Lastly, dielectric image guide coupling is generally beneficial to reduce conduction losses that would otherwise occur with microstrip feeds at very high frequencies. Since the antenna will be designed for relatively low frequencies, conduction losses are less of a concern, so dielectric image guide coupling is not well suited for the present application. Microstrip and aperture coupling offer effective means for coupling to the DRA, and both are considered further as the coupling method of choice.

Microstrip transmission lines have been shown to be effective feeds for coupling to DRAs [4]. Microstrip coupling can be achieved through either direct or proximity coupling [3]. In direct coupling, the resonator is placed directly on the end of the microstrip line. Since the direct connection between the microstrip and resonator will also result in high field enhancements, direct coupling is not the preferred embodiment of microstrip coupling. Proximity coupling drives a resonator that is removed from the microstrip by a set distance. To improve the coupling, the resonator should be positioned such that the fields created by the microstrip are incident in the resonator in regions of high fields in the desired resonance mode. Figure 71 shows an example of proximity microstrip coupling. The microstrip is formed by a conductor with a width, w_m [m], over a substrate with a defined dielectric constant, ϵ_{sub} , and thickness, t_{sub} [m]. The distance between the microstrip and the resonator, s [m], can be altered to maximize the coupling. The resonator is separated from the microstrip conductor by a small gap distance, which is not labeled due to the small scale, to prevent direct metal-composite contact.

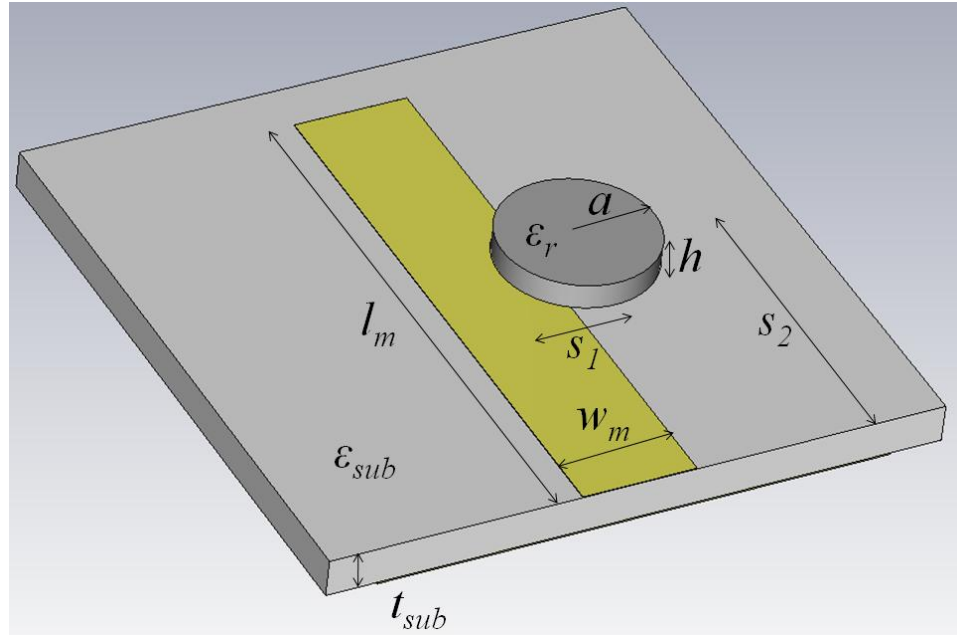


Figure 71. Microstrip coupling

Aperture coupling is similar to microstrip coupling. However, unlike microstrip coupling, the resonator is on the opposite side of the substrate from the transmission line. The antenna can be driven with a microstrip similar to proximity microstrip coupling, or a coaxial cable or other transmission line can be implemented. A microstrip was primarily considered for its advantages in custom fabrication. To couple energy between the microstrip and resonator, an aperture is cut into the ground plane, and the resonator is placed on or near the aperture. Figure 72 shows the critical parameters for designing an aperture-coupled DRA driven by a microstrip. The resonator has been removed from the figure to reveal the aperture and critical dimensions, but the resonator would normally be placed over the aperture to couple to the fields passing through the ground plane. A microstrip, shown on the opposite side of the substrate with dashed lines, again has a width of w_m [m]. The substrate has a thickness of t_{sub} [m] and a dielectric constant of ϵ_{sub} . The rectangular aperture is shown as a slot in the ground plane with a width, w_s [m], and length, l_s [m]. The slot length must be large enough to effectively couple to the resonator

but not so large that a significant back lobe is radiated on the microstrip side of the substrate [3].

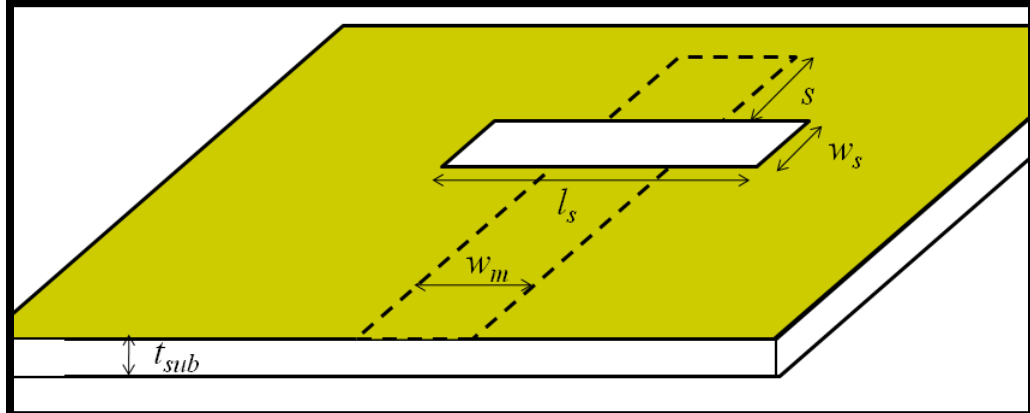


Figure 72. Aperture coupling with resonator removed

Equation (5.1) is recommended as a starting value for the slot length [3].

$$l_s = \frac{0.4\lambda_0}{\sqrt{\varepsilon_e}} \quad (5.1)$$

The symbol ε_e in equation (5.1) is a dielectric constant value calculated as the average of the resonator and substrate dielectric constants. The slot width is also constrained to limit the formation of a back lobe, and a width equal to 20% of the slot length is typical [3]. The microstrip is often extended beyond the aperture by a stub length, s [m], to cancel out the admittance of the aperture and improve the impedance match to the resonator [3]. A recommended initial stub length is a quarter of the guided wavelength of the wave in the substrate, and the stub length can be adjusted to improve impedance matching [3].

One of the advantages to microstrip and aperture coupling is the ability to mechanically tune the antenna to maximize coupling by moving the resonator with respect to the microstrip or aperture without requiring significant alterations to the fixed pieces of the antenna. Additionally, the substrate thickness can be increased as needed to hold off the high voltage signal driving the antenna, and the microstrip width can be increased to

maintain the desired line impedance as the substrate thickness is increased. Both microstrip and aperture coupling have the potential to drive a high permittivity, low profile resonator. However, due to the potentially thick substrates required to hold off the peak voltage at high power, the coupling factor obtained through aperture coupling may be degraded. Therefore, microstrip coupling was chosen as the preferred coupling method.

5.3 Resonant Modes a Cylindrical Dielectric Resonator

Due to the relatively developed state of the design parameters for cylindrical resonators and the convenience of implementing resonators with the same shape formed with cylindrical dry pressing dies, cylindrical dielectric resonator antennas were the primary antenna geometry under consideration. The cylindrical DRA offers a degree of freedom to the designer in which the ratio of the cylinder radius, a [m], to the cylinder height, h [m], can be adjusted to change the resonant frequency [3]. Two values of the ratio will correspond to the same operating frequency but with different Q -factors [3]. Thus, either a relatively short and wide cylinder or a relatively long and thin cylinder can be designed for the same operating frequency depending on constraints due to the Q -factor or form factor of the antenna.

Examination of the lower-order modes of a cylindrical DRA is necessary to determine the resonant frequency, Q -factor, and radiation patterns available for resonators in a range of practical dimensions. The most common radiating modes of the cylindrical DRA, as reported by Petosa, are the $\text{TM}_{01\delta}$ mode, the $\text{TE}_{01\delta}$ mode, and the $\text{HE}_{11\delta}$ mode [3]. The TE and TM designations correspond to transverse electric and transverse magnetic modes, respectively, and the $\text{HE}_{1\delta}$ mode is a hybrid mode in which the E_z component is dominant

over the H_z component [3]. The mode subscripts correspond to field variations in the directions of the cylindrical coordinates of the azimuth, radius, and center axis, respectively. The symbol δ takes a value between zero and one with a higher value corresponding to a higher dielectric constant material comprising the resonator [3]. The equivalent radiating sources of the $\text{TM}_{01\delta}$, $\text{TE}_{01\delta}$, and $\text{HE}_{11\delta}$ modes are a short electric monopole, short magnetic monopole, and a short horizontal magnetic dipole, respectively [3].

The fundamental mode for cylindrical radiators has been cited by some sources to be the TM_{110} mode [5, 6]. The original work on dielectric resonator antennas by Long *et al.* derives the frequency of the fundamental mode of a cylindrical cavity as equation (5.2) [5, 6]. The symbol X_{11} represents the first zero of the Bessel equation describing the fields inside the resonator and is equal to 1.841.

$$f_0 = \frac{c}{2\pi a \sqrt{\epsilon_r}} \sqrt{X_{11}^2 + \left(\frac{\pi a}{2h}\right)^2} \quad (5.2)$$

It is easily shown that when the condition of equation (5.3) is met, the resonant frequency's dependence on the radius is diminished and equation (5.2) is reduced to equation (5.4).

$$\left(\frac{\pi a}{2h}\right) \gg X_{11} \quad (5.3)$$

$$f_0 = \frac{c}{4h\sqrt{\epsilon_r}} \quad (5.4)$$

Equation (5.4) has been shown to be applicable for other low profile antenna shapes, including rectangles and triangles, in which the width dimensions of the antenna are much larger than the thickness [3, 7]. The lack of dependence on the radius or other width

dimension is due to the resonance arising from waves reflections between the top and bottom of the resonator [6].

Plots have been prepared showing the fundamental frequency for radii of 1.27, 3.81, and 5.72 cm. These radii correspond to dry pressing dies that were in use during the course of this work. Figure 73 shows the plot of equation (5.2) for the cylindrical DRA excited in the TM_{110} mode with a resonator dielectric constant of 100. It is clear that for small values of h , which correspond to large values of a/h , the radius of the resonators is negligible. The resonant frequencies of the resonators with all three radii are essentially indistinguishable up to a thickness of at least 5 mm. The frequency of the resonator with the smallest radius quickly loses its independence from the radius as it fails to meet the condition of equation (5.3) as the thickness increases. Although the difference between the frequencies of the resonators with radii of 3.81 cm and 5.72 cm gradually increases, the difference is relatively small due to the weak dependence on the radius when a/h remains large. Both resonators with a large radius have resonant frequencies below 300 MHz at thicknesses below 5 cm. The resonant frequency of the resonator with a radius of 5.72 cm reaches below 200 MHz at a thickness above 5 cm.

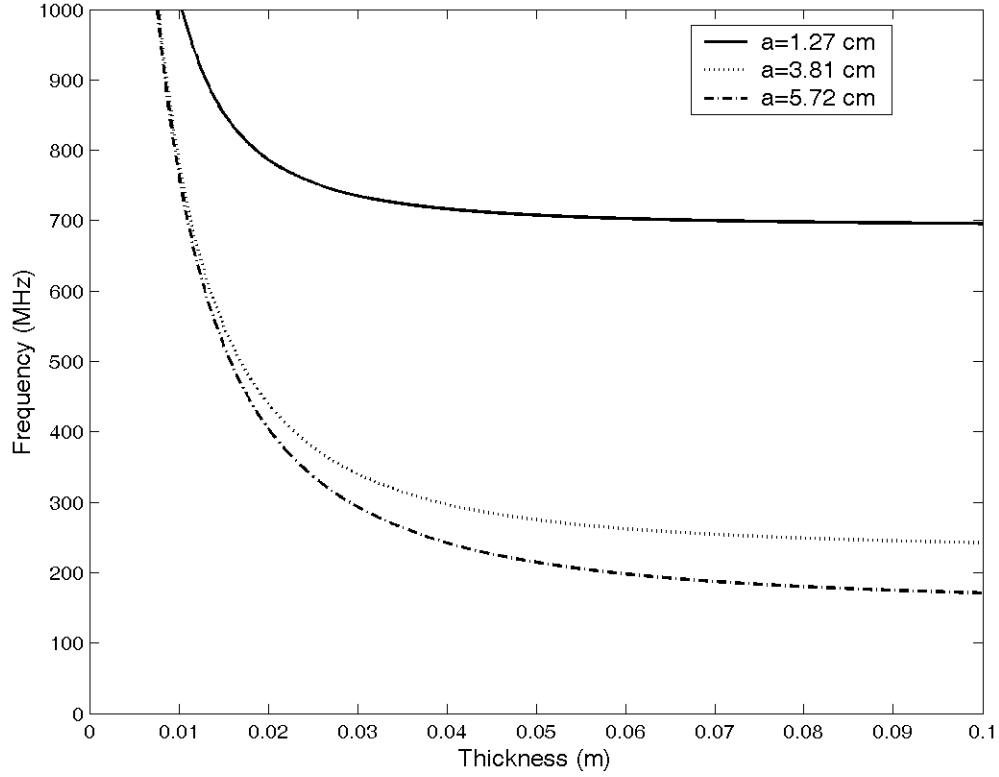


Figure 73. Resonant frequency of cylindrical DRA with $\varepsilon_r = 100$ in TM₁₁₀ mode

Equation (5.2) was also applied for resonators incorporating the MU550 composite as shown in Figure 74. The very high dielectric constant value of 550 results in a frequency reduction to below 200 MHz in resonators with radii of 3.81 cm and 5.72 cm. Even the resonator with a radius of just 1.27 cm extends below 500 MHz with a thickness of just 1 cm. Since equations were unavailable to calculate the quality factor of the TM₁₁₀ mode, it cannot be directly compared to the other resonant modes in this analysis. However, due to the very low frequencies predicted in Figure 73 and Figure 74 and the proven effectiveness of low-profile antennas incorporating high permittivity materials at higher frequencies with this mode, it is a preferred mode for excitation.

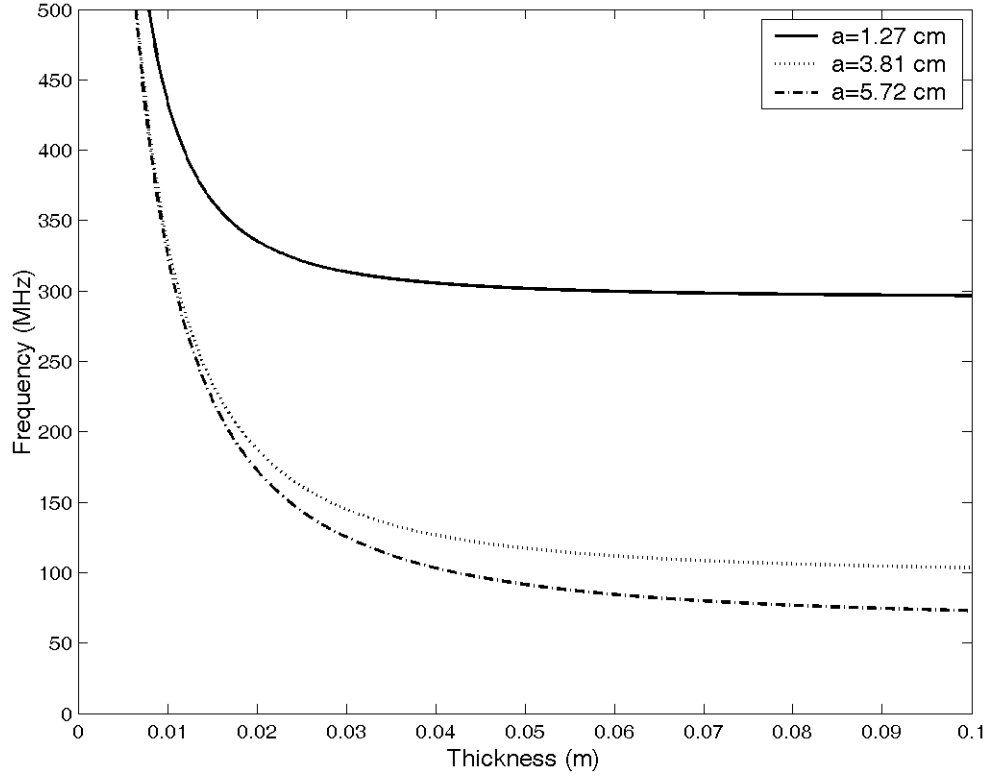


Figure 74. Resonant frequency of a cylindrical DRA with $\varepsilon_r = 550$ in TM_{110} mode

Equation (5.5) describes the relationship between the resonator dimensions and the fundamental wave number, k_0 [m^{-1}], of the $\text{TM}_{01\delta}$ mode [3].

$$k_0 a = \frac{\sqrt{3.83^2 + \left(\frac{\pi a}{2h}\right)^2}}{\sqrt{\varepsilon_r + 2}} \quad (5.5)$$

The fundamental wave number is related to the fundamental wavelength, λ_0 [m], and frequency, f_0 [Hz], according to equation (5.6), in which c [m/s] is the speed of light in vacuum [8].

$$k_0 = \frac{2\pi}{\lambda_0} = \frac{2\pi f_0}{c} \quad (5.6)$$

Equation (5.5) can be used to predict the center frequency of operation for a resonator with chosen radius and height dimensions. The bandwidth is determined by the quality, Q , factor, which is given as equation (5.7) for the $\text{TM}_{01\delta}$ mode [3]. The dielectric constant

of the material comprising the resonator at the center frequency can be used as the value for ε_r .

$$Q = 0.008721\varepsilon_r^{0.888413}e^{0.0397475\varepsilon_r}\left[1 - \left(0.3 - 0.2\frac{a}{h}\right)\left(\frac{38 - \varepsilon_r}{28}\right)\right]\left[9.498186\frac{a}{h} + 2058.33\left(\frac{a}{h}\right)^{4.322261}e^{-3.50099\frac{a}{h}}\right] \quad (5.7)$$

The quality factor is inversely proportional to the bandwidth, Δf , of the antenna as shown in equation (5.8) [2]. Resonators made from very high dielectric constant materials often have higher Q -factor values, so it is imperative to design the antenna to reduce the quality factor to maintain an acceptable bandwidth while maintaining efficiency. Techniques to reduce the quality factor and increase the bandwidth are covered later in this chapter.

$$Q = \frac{f_0}{\Delta f} \quad (5.8)$$

Implementation of very high dielectric constant materials can further increase the Q -factor to impractically high values, so whenever possible, it is advantageous to design for a lower Q -factor.

Figure 75 shows the resonant frequency of the cylindrical DRA excited in the TM_{018} mode. Since the dielectric constant of 100 can be considered high, the mode is likely close to that of the TM_{011} . While the frequency of operation for a DRA with a radius of 1.27 cm remains relatively high with a minimum of approximately 1.5 GHz, the frequency of the DRAs with radii of 3.81 cm and 5.72 cm reach below 500 MHz and 325 MHz, respectively, as the thickness is increased to a few centimeters. The low frequencies of the DRAs with radii of 3.81 and 5.72 cm are within an acceptable range, but the quality factor of these antennas may be impractically high, as shown in Figure 76. Quality factor values of 1000 or greater would result in an impractically-small

bandwidth, which would make the antenna very difficult to drive without a very specific high power source. Therefore, the Q -factor must be appropriately reduced for the TM_{011} mode to be effective in the operation of the DRA.

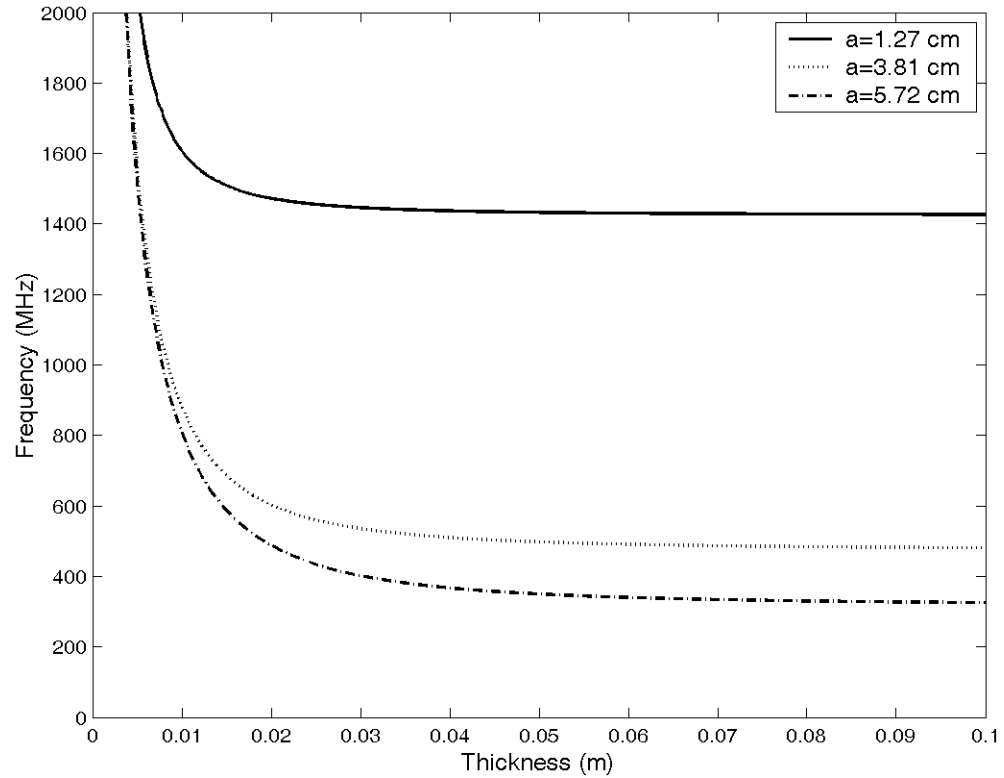


Figure 75. Resonant frequency for cylindrical DRA with $\epsilon_r = 100$ in TM_{011} mode

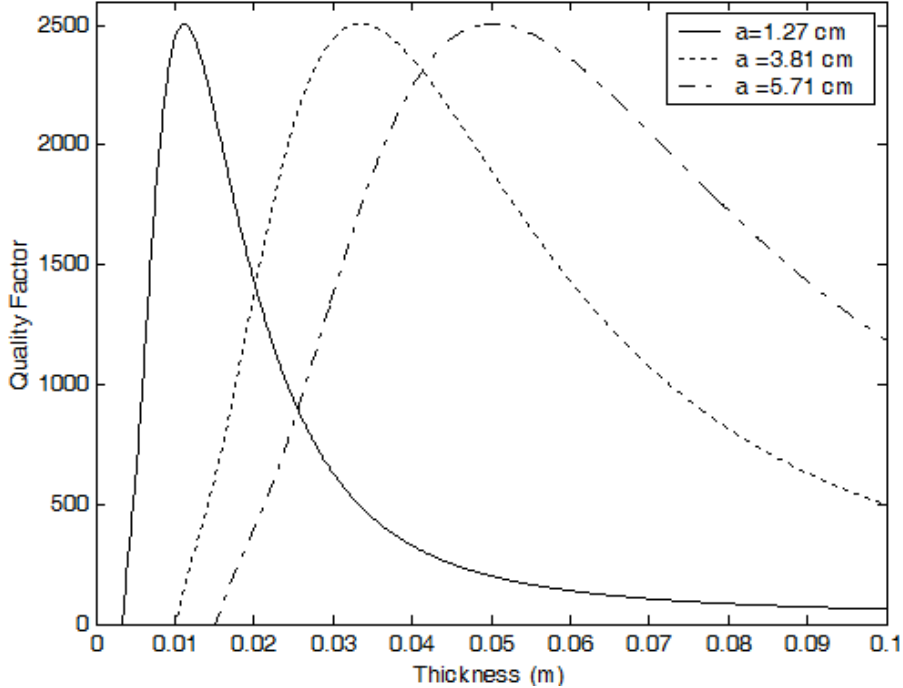


Figure 76. Quality factor of cylindrical DRA with $\epsilon_r = 100$ in TM_{011} mode

Equation (5.9) relates the fundamental wave number and resonator dimensions for the $\text{HE}_{11\delta}$ mode , and the equation for the $\text{HE}_{11\delta}$ Q -factor is given as equation (5.10) [3].

$$k_0 a = \frac{6.324}{\sqrt{\epsilon_r + 2}} \left[0.27 + 0.36 \frac{a}{2h} + 0.02 \left(\frac{a}{2h} \right)^2 \right] \quad (5.9)$$

$$Q = 0.01007 \epsilon_r^{1.3} \frac{a}{h} \left[1 + 100 e^{-2.05 \left(\frac{a}{2h} - \frac{1}{80} \left(\frac{a}{h} \right)^2 \right)} \right] \quad (5.10)$$

A graph of the resonant frequency obtained by applying equation (5.9) for radii of 1.27, 3.81, and 5.72 cm is shown in Figure 77. The shape of the curves is similar to that seen from the TM_{011} mode plot, but the frequencies reach even lower levels at thicknesses larger than 1 cm. The frequency of the 3.81 cm radius resonator dips below 275 MHz at large thicknesses, and the frequency of the 5.72 cm radius resonator extends below 200 MHz as it approaches a thickness of 10 cm. In addition to the lower frequencies achievable in this mode, the quality factor is much lower. The quality factor for the three resonator radii varies between 40 and 160. While these values are higher than desired, the

high quality factor is a given tradeoff when constructing the resonator with a dielectric constant of 100 to reduce its size. Therefore, bandwidth-widening techniques are required with the $HE_{11\delta}$ mode as well to compensate for the high Q -factor.

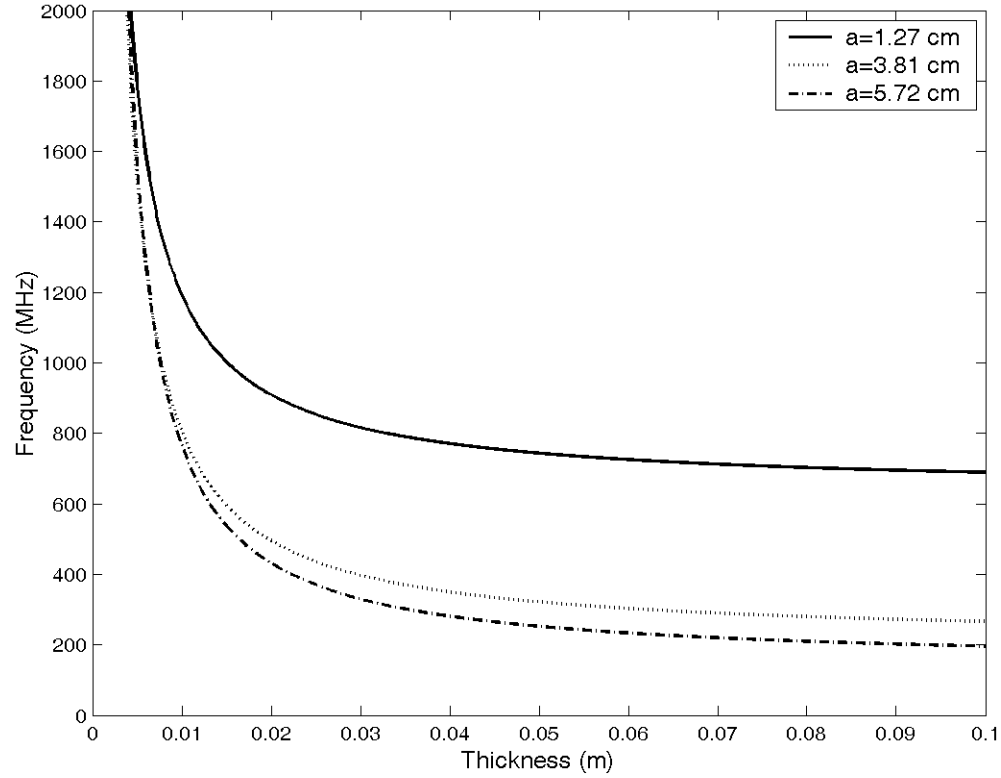


Figure 77. Resonant frequency for cylindrical DRA with $\epsilon_r = 100$ in HE_{111} mode

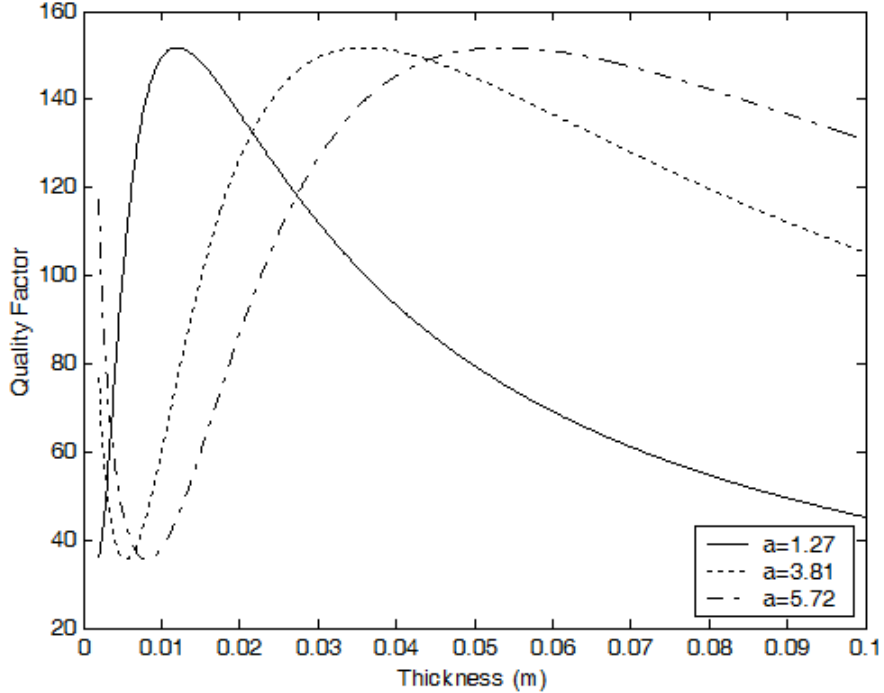


Figure 78. Quality factor for a cylindrical DRA with $\epsilon_r = 100$ in HE_{111} mode

Equations (5.11) and (5.12) show the relationships utilized to determine the resonant frequency and quality factor of a cylindrical resonator excited in the TE_{018} [3].

$$k_0 a = \frac{2.327}{\sqrt{\epsilon_r + 1}} \left[1 + 0.2123 \frac{a}{h} - 0.00898 \left(\frac{a}{h} \right)^2 \right] \quad (5.11)$$

$$Q = 0.078192 \epsilon_r^{1.27} \left[1 + 17.31 \left(\frac{h}{a} \right) - 21.57 \left(\frac{h}{a} \right)^2 + 10.86 \left(\frac{h}{a} \right)^3 - 1.98 \left(\frac{h}{a} \right)^4 \right] \quad (5.12)$$

The graphs of the TE_{018} mode resonant frequency and Q -factor produced with equations (5.11) and (5.12) are shown as Figure 78 and Figure 79, respectively. At large thicknesses, the frequencies of the three resonators are slightly greater than those predicted in Figure 77 for the HE_{111} mode. The most interesting aspect of Figure 79 is how, unlike the previously-considered modes, the resonant frequency decreases at very small thicknesses. This effect is only seen in the resonators with radii of 3.81 and 5.72 cm

as the effect does not occur for the resonator with a 1.27 cm radius in the thickness range considered above 1 mm. It remains to be determined through electromagnetic simulations whether this effect is real or is the result of a breakdown in the equations, which were developed for lower ratios of a/h . Although this behavior in the calculated resonant frequencies for small thicknesses was not investigated further in this work, it is believed that the equations are likely not valid for such small thicknesses and low frequencies with very thin layers are not possible. The Q -factor of the $\text{TE}_{01\delta}$ mode reaches a peak slightly greater than that seen in the $\text{HE}_{11\delta}$ mode. However, the Q -factor is less than 80 in the range of relatively thin thicknesses for which the frequency is predicted to be very low.

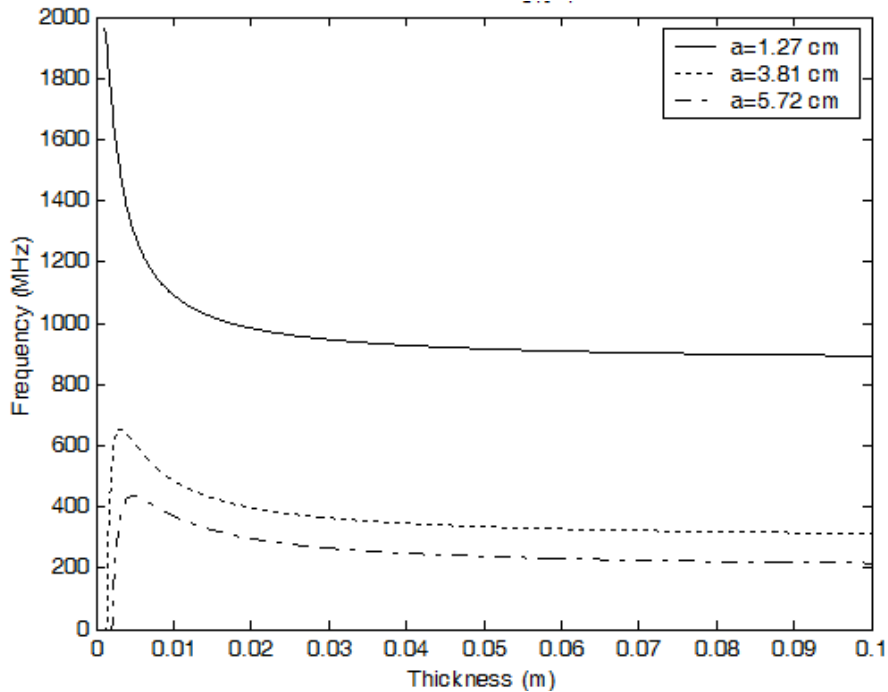


Figure 79. Resonant frequency of a cylindrical DRA with $\epsilon_r = 100$ in TE_{011} mode

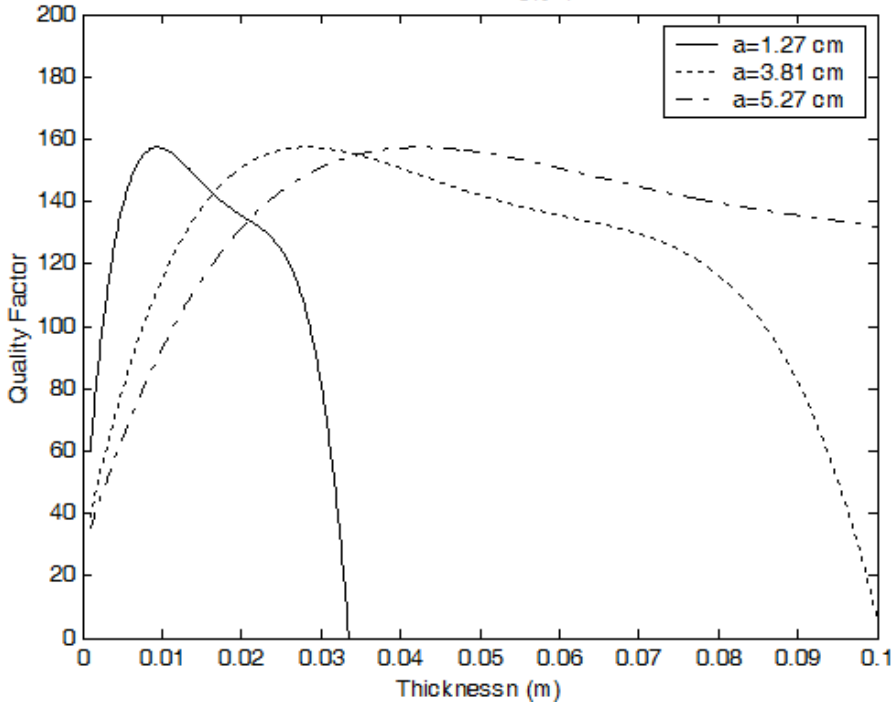


Figure 80. Quality factor of a cylindrical DRA with $\epsilon_r = 100$ in TE₀₁₁ mode

5.4 Bandwidth Enhancement

As previously shown in equation (5.8), the quality factor and the bandwidth of the resonator are inversely related. The utilization of high dielectric constant materials as the resonator can result in a very high Q -factor, so methods have been developed by previous researchers to actively increase the bandwidth. The unloaded Q -factor, Q_0 , can be defined through its contributing factors of the conductor loss quality factor, Q_c , dielectric loss quality factor, Q_d , and radiation loss quality factor, Q_r , as shown in equation (5.13) [2].

$$\frac{1}{Q_0} = \frac{1}{Q_c} + \frac{1}{Q_d} + \frac{1}{Q_r} \quad (5.13)$$

The relationship of equation (5.13) causes the unloaded Q -factor to be limited by the lowest contributing Q -factor. The conductor power loss should be low in the DRA, so Q_c should not be the limiting factor. The radiation loss Q -factor can limit the unloaded Q -factor. The radiation loss Q -factor, given as equation (5.14), is low if the ratio of the peak

stored energy, W [J], to the radiated power, P_r [W], is low [2]. The symbol ω_0 [rad/s] is the resonant angular frequency.

$$Q_r = \frac{\omega_0 W}{P_r} \quad (5.14)$$

When dominated by the radiating loss Q -factor, the bandwidth is usually only a few percent. Therefore, the dielectric loss quality factor or other techniques must be utilized to increase the bandwidth. Although the losses of the high dielectric constant composites are generally kept as low as achievable to limit the amount of wasted energy, some losses in the dielectric can improve the bandwidth significantly. The dielectric loss quality factor, defined by equation (5.15), has an inverse relationship with the dielectric losses. Therefore, a lossy material will result in a low value for Q_c and a relatively low unloaded quality factor [2].

$$Q_d = \frac{1}{\tan\delta} \quad (5.15)$$

The dielectric losses below 500 MHz are relatively low for all three composite materials. The losses can be considered to be within the range of 0.01 and 0.15, which all of the composites have been measured to remain under up to at least 500 MHz. Figure 81 shows the plot of the dielectric loss quality factor and the corresponding bandwidth as functions of the dielectric losses of the resonator.

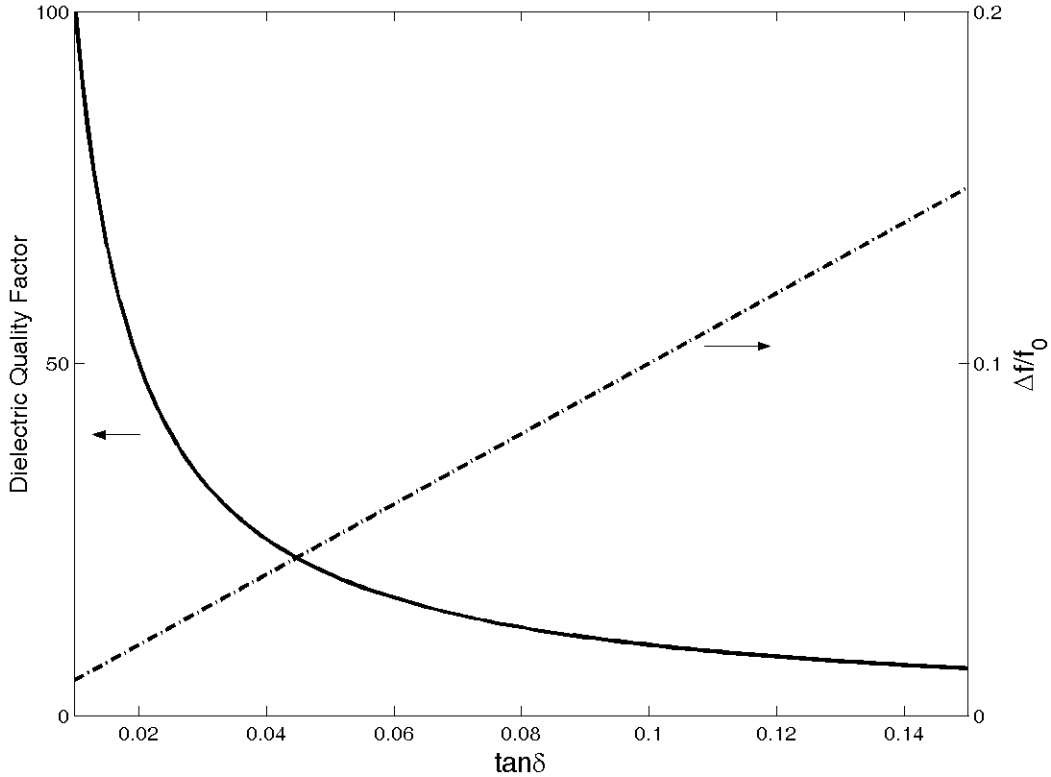


Figure 81. Dependence of the dielectric loss quality factor and bandwidth with respect to the dielectric losses of the resonator

As shown in Figure 81, the dielectric loss values of 0.01 and 0.1 correspond to Q_d factors of 100 and 10, respectively, and bandwidths of 1% and 10%, respectively. If the dielectric losses at the resonant frequency are somewhere in the middle of this range at around 0.05, the unloaded Q -factor will likely be dominated by the dielectric losses, and the bandwidth will be approximately 5%. A bandwidth of 5% is sufficient for many applications and is higher than achieved in many lower permittivity low loss resonators.

Other techniques may be necessary to further increase the bandwidth beyond that predicted from the dielectric loss quality factor to adequately couple the signal from the high power antenna driver. Several bandwidth-enhancement techniques for DRAs have previously been investigated, but the current discussion is limited to multi-mode excitation, multiple resonators, introduction of air gaps, and addition of microstrip stubs. The excitation of multiple modes in the same resonator can broaden the bandwidth

without physically modifying the resonator or microstrip line. An examination of the resonant frequencies of the modes analyzed earlier in this chapter shows that the resonant frequency of some modes are close enough that exciting both modes could result in either wideband or dual-band operation. For the excitation of more than one mode to truly be considered wideband, it is often necessary that the radiation pattern of the two modes be similar [3].

A second relatively straightforward approach to increasing the bandwidth is to include multiple resonators along the same microstrip. If the resonators are made with different dimensions or different materials, they can be designed to have slightly offset resonant frequencies that combine to create an effective wideband antenna. The main disadvantage to this approach is the increased size of the antenna through the addition of multiple resonators. It is possible to minimize the overall size increase by either stacking the resonators or even embedding the resonators within each other [3]. The stacked or embedded resonators can still be individually excited at distinct resonant frequencies that cause the antenna as a whole to operate with an increased bandwidth.

Elevating the resonator to add a gap between the resonator and conductor has also been shown to greatly increase DRA bandwidth [3]. In one study, the bandwidth was increased from 4.2% to 40% through the addition of a 10 mm air gap [3]. The use of a solid foam can effectively add an air gap while providing mechanical support for the resonator since the effective dielectric constant of an air-filled foam is approximately 1 [3].

The final method considered for increasing the bandwidth is adding a microstrip stub. Since the preferred method of coupling has been selected to be microstrip coupling, the addition of a stub to the end of the microstrip line is a simple modification that can

improve the impedance match of the circuit. Both L-shaped and T-shaped stubs have been proven effective by other researchers [3]. By implementing one or more of the bandwidth-widening techniques, the bandwidth can likely be increased above 10% without significantly altering the resonator or feed circuit volume.

5.5 DRA Design

Dielectric resonator antennas were designed and built in this investigation for both low power and high power evaluation. This description will be limited to a high power DRA. To drive the antenna at power levels up to 1 GW with an antenna input impedance of approximately 50Ω , the applied voltage to the antenna must be nearly 225 kV. To withstand these voltage levels, the high power antenna was designed for operation with a very thick dielectric substrate. As shown in photos of the high power DRA of Figure 82 and Figure 83, the substrate was designed to be a 1.91 cm thick piece of polyethylene measuring approximately 30.5 cm by 30.5 cm.

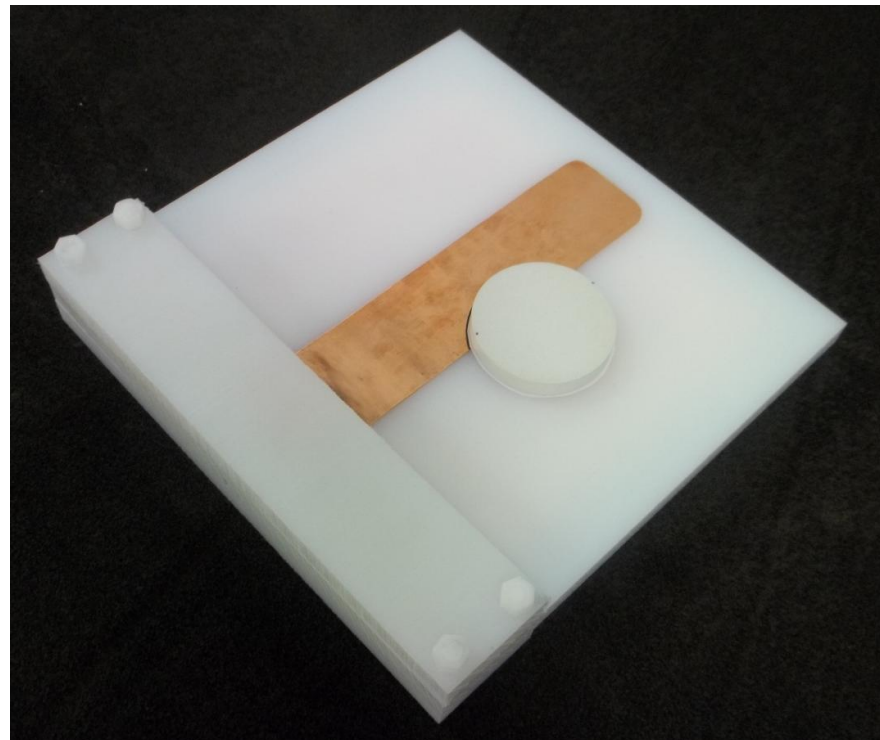


Figure 82. A high power DRA

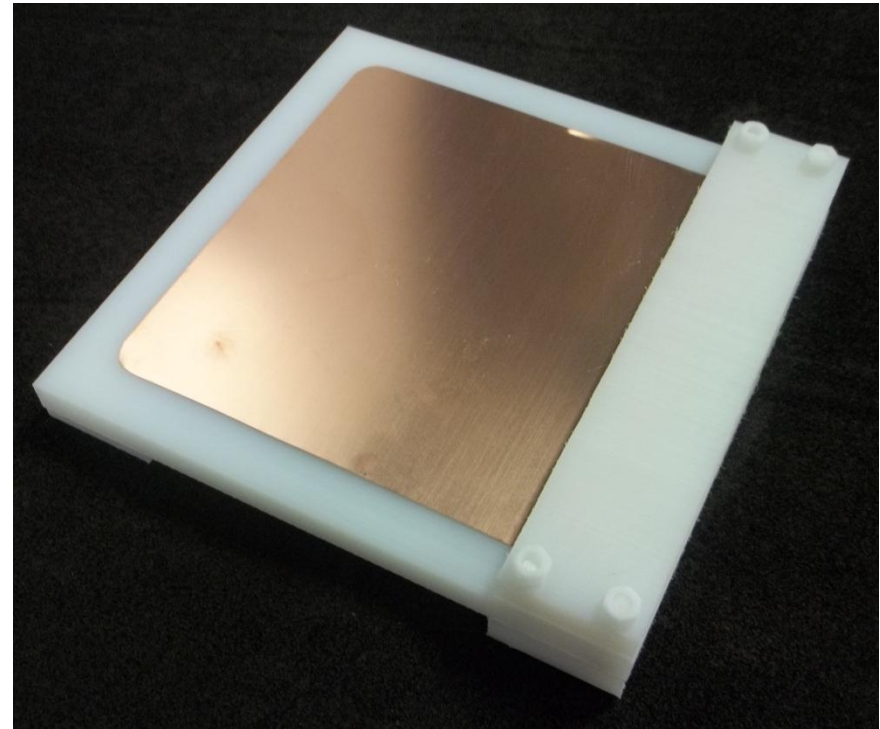


Figure 83. Backside of the high power DRA showing the ground plane

While this large thickness enables operation at high voltage, it also requires an exceptionally wide microstrip to match to the 50Ω cables used for low power characterization without employing additional matching techniques. The dimensions of the microstrip were calculated using Wheeler's formulas shown in equations (5.16) and (5.17) [9]. The characteristic impedance of the microstrip, $Z_0 [\Omega]$, is calculated in equation (5.16) from this semi-empirical equation based on the dielectric constant of the substrate, ϵ_{sub} , the thickness of the substrate, $t_{sub} [m]$, and the effective microstrip width, $w_m' [m]$.

$$Z_0 = \frac{42.4}{\sqrt{\epsilon_{sub} + 1}} \ln \left[1 + \left(\frac{4t_{sub}}{w_m'} \right) \left[\left(\frac{14 + \frac{8}{\epsilon_{sub}}}{11} \right) \left(\frac{4t_{sub}}{w_m'} \right) + \sqrt{\left(\frac{14 + \frac{8}{\epsilon_{sub}}}{11} \right)^2 \left(\frac{4t_{sub}}{w_m'} \right)^2 + \frac{1 + \frac{1}{\epsilon_{sub}}}{2} \pi^2} \right] \right] \quad (5.16)$$

The effective microstrip width is slightly altered from the actual microstrip width, $w_m [m]$, due to effects from the conductor thickness, $t_c [m]$, and the dielectric constant of the substrate. The effective strip width can be calculated from equation (5.17) [9].

$$w_m' = w_m + t_c \frac{1 + \frac{1}{\epsilon_r}}{2\pi} \ln \left[\frac{4e}{\sqrt{\left(\frac{t_c}{t_{sub}} \right)^2 + \left(\frac{1}{\pi} \frac{1}{w_m + \frac{11}{10}} \right)^2}} \right] \quad (5.17)$$

The thickness of the conductor in the design was approximately 406 μm . Using the previously stated substrate dimensions, a substrate dielectric constant value of 2.5, and these two equations, the microstrip width was calculated through an iterative process to obtain a characteristic impedance of approximately 50Ω . The microstrip width was designed to be 5.65 cm, corresponding to a calculated impedance of approximately 50.1Ω . The length of the strip most often used was approximately 28 cm, but similar antenna performance was observed with strip lengths of 25.4 cm and smaller. A ground plane measuring 25.4 cm wide by 25.4 cm long by 0.254 mm thick was positioned on the opposite side of the substrate. Since the resonator is placed partially over the microstrip, a plastic film approximately 0.46 mm thick was placed between the resonator and conductor to prevent direct contact. The high power DRA incorporating plastic supports to hold the DRA in place during testing is shown in Figure 84.

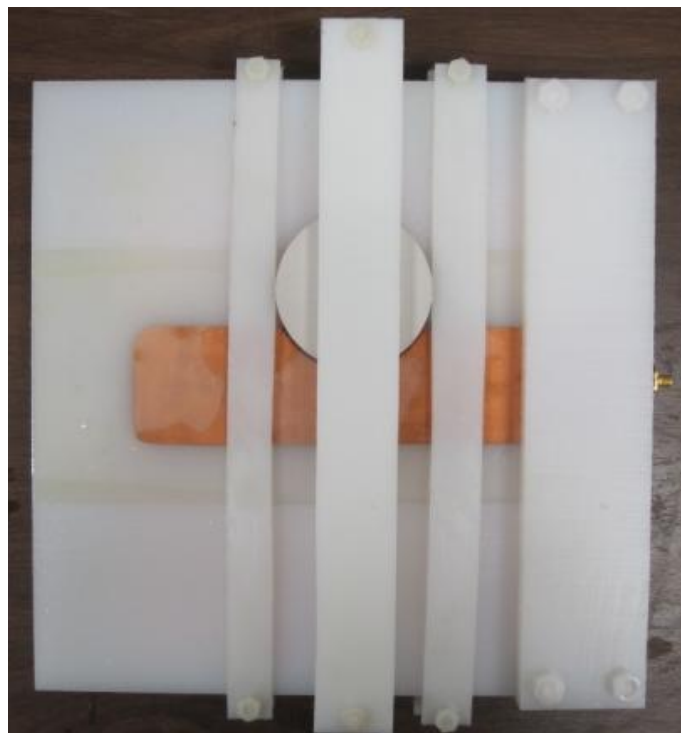


Figure 84. The DRA with supports to hold the resonator in place and an SMA connector for low voltage characterization

The high dielectric constant composite material chosen as the resonator material in the high power DRA was MU100 [10]. MU100 was selected for combining several desirable properties, including a high dielectric constant of approximately 100 in the frequency range of interest, relatively low dielectric losses, high dielectric strength, and robust mechanical strength.

Based on the graphs of the resonant frequencies presented earlier in this chapter, the radius of the resonator was designed to be 3.81 cm. The thickness of the resonator was approximately 1.25 cm. From the equations in Section 5.3, the resonant frequency of a dielectric resonator with fixed dimensions is a function of the permittivity of the resonator. Since the permittivity of the composite is a function of frequency, calculation of the resonant frequency of the resonator is a recursive process. Table 21 summarizes the resonant frequencies calculated for the four modes considered earlier in this chapter when accounting for the slight dependence of the dielectric constant of MU100 with frequency. The lowest resonant frequency was calculated for the TE_{01} mode at 455 MHz. The resonant frequencies of the TM_{110} and HE_{11} modes are only separated by 35 MHz at 650 MHz and 685 MHz, respectively. The highest frequency calculated for these four modes was 770 MHz for the TM_{01} mode. While this analysis has concentrated on these four modes due to reference to these modes in dielectric resonator antenna literature, there are other modes that can potentially be excited within the frequency range covered by these modes and above 770 MHz. It is possible to excite these four modes and others with the same coupling method, so there is significant potential for multimodal operation of the DRA as a bandwidth enhancement method.

Table 21. Resonant frequency calculated for the four modes considered in Section 5.3

Mode	TM ₁₁₀	HE ₁₁	TE ₀₁	TM ₀₁
Resonant Frequency (MHz)	650	685	455	770

The high power DRA was intended to be operated in a bath of transformer oil. High voltage breakdown issues are the primary motivation for the inclusion of transformer oil, but there are additional benefits from incorporation of the oil. First, the dielectric constants of the oil and the polyethylene components comprising the substrate and resonator holders are very similar. The match of these dielectric constants results in the environment around the resonator and microstip appearing to electrically be one material. This continuity of the permittivity around the resonator and microstip minimizes the effects of placing the plastic holders around the DRA to hold it in place. The electric field is distributed around the resonator and conductors as if only a single low dielectric constant material were present. Second, the oil flows into the small gap between the microstrip conductors and the polyethylene substrate to limit the potential for impedance variation along the transmission line due to the imperfections of the conductor-substrate contact. By ensuring consistency of the transmission line impedance, reflections along the line are reduced, and the return loss of the antenna is improved.

The placement of the DRA along the microstrip was determined experimentally by observing the return loss as the resonator position was moved. This tuning process was conducted in an oil bath. The ease with which the DRA can be tuned in this manner is a significant advantage over more permanent antenna designs that require extensive modification to tune the antenna for optimal performance.

5.6 DRA Evaluation Methods

5.6.1 Simulation of the Antenna Reflection Coefficient and Radiation Pattern

The dielectric resonator antenna was simulated using CST Microwave Studio. CST Microwave Studio, like the CST EM Studio package chosen to model particle loading of composites, enables the virtual construction and electromagnetic simulation of components. CST Microwave Studio is specifically suited for performing transient and frequency domain simulations of high frequency problems. The primary simulation parameters of interest are the scattering, S , parameters and the far-field gain and radiation pattern. The simulations were performed in the VHF and UHF bands from 20 MHz to 2 GHz.

The S_{11} parameter provides information on the impedance mismatch of the dielectric resonator antenna and feed structure with an idealized port of known impedance. The S_{11} parameter is determined as the ratio of the reflected, V^- [V], and incident, V^+ [V], voltage magnitudes, as given in equation (5.18) [11].

$$S_{11} = \frac{V^-}{V^+} \quad (5.18)$$

The S_{11} parameter is the primary S-parameter of interest as it determines the input return loss, RL_{in} [dB], according to equation (5.19) [11].

$$RL_{in} = |20 \log_{10}|S_{11}|| \quad (5.19)$$

As the impedance of the DRA is a function of frequency, the S_{11} parameter is also a function of frequency. The S_{11} parameter and input return loss must be minimal at the desired frequencies of operation. Low input return loss indicates matched impedance and efficient energy transfer to the antenna.

In addition to the S -parameters, the far-field gain pattern of the DRA was simulated. The gain, G , in equation (5.20) is an indicator of an antenna's performance in comparison to an antenna standard, which is often an isotropic radiator. The gain is reported in units of dBi, G_{dBi} [dBi], to indicate that the gain is with respect to an isotropic source [12].

$$G_{dBi} = 10 \log_{10}(G) = 10 \log_{10}(e_{antenna} \cdot D) \quad (5.20)$$

The gain calculated from equation (5.20) is sometimes referred to as the realized gain because the efficiency term $e_{antenna}$ includes both the radiation efficiency, e_{rad} , and the mismatch loss due to the return loss. The radiation efficiency accounts for antenna losses, which can include ohmic losses in the conductors or dielectric losses in the high dielectric constant material. The radiation efficiency should be as high as possible, as all antenna losses reduce the radiated power. The directivity, D , represents the ratio of the maximum power density an antenna produces in a particular direction to the average power density in all directions. The desired directivity is dependent on the antenna's application. If the antenna is intended to radiate with a small beam angle in only one direction, the directivity must be high. However, antennas designed to radiate along the horizon in an omnidirectional pattern will require a lower directivity and corresponding lower gain value.

5.6.2 Low Voltage Measurements

Low power measurements were taken with an Agilent E5071C network analyzer in an anechoic chamber. For consistency with the antenna's intended use on high voltage systems, the antenna's performance was characterized with the DRA immersed in oil. The return loss was measured directly with the network analyzer from 20 MHz to 4.5 GHz. The gain was measured in a single direction broadside to the substrate of the DRA

that was identified to be the center of the main lobe from simulations. The gain was calculated from two-port scattering parameter measurements taken with a reference antenna with a flat gain profile over the frequencies of measurement. The reference antenna was selected to be a Sunol Sciences LP-80 log periodic antenna with a reported typical gain of 6 dBi from 80 MHz to 2 GHz [13]. The log periodic antenna and the interior of the anechoic chamber are shown in Figure 85.

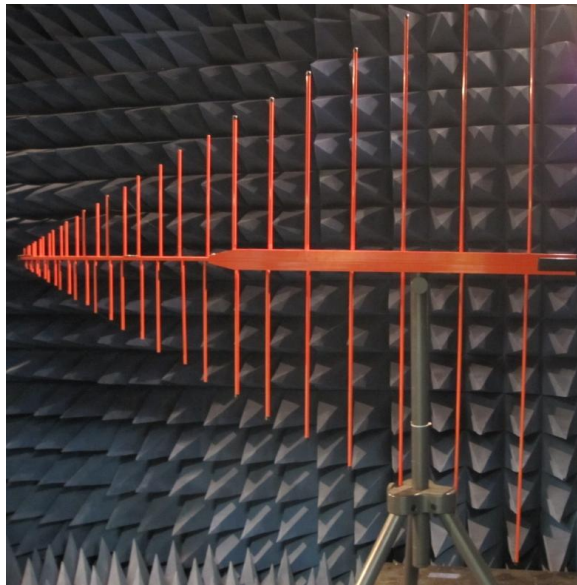


Figure 85. The DRA was characterized at low power in the anechoic chamber with an LP-80 log periodic antenna from Sunol Sciences.

Whereas the LP-80 is linearly polarized, the DRA should be considered elliptically polarized for the purposes of gain measurements. Therefore, any single gain measurement includes polarization mismatch. The polarization mismatch between the log periodic antenna and the DRA were accounted for by taking two measurements with the log periodic antenna maintained at vertical polarization and the DRA rotated 90° between measurements. The ratio of the power received, P_r [W], to the power transmitted, P_t [W], is calculated from the S_{21} [dB] scattering parameter measured by the network analyzer by equation (5.21).

$$\frac{P_r}{P_t} = 10^{\frac{S_{21, dB}}{10}} \quad (5.21)$$

With the known gain of the LP-80 in linear scale, G_{LP80} , the linear gain of the DRA to the vertical polarization of the LP-80, $G_{DRA,pol}$, can be calculated with equation (5.22) based on the Friis transmission formula [8]. The frequency of the measurement and speed of light are represented by f [Hz] and c [m/s], respectively, and the distance between the antennas is represented by R [m].

$$G_{DRA,pol} = \frac{P_r}{P_t G_{LP80}} \left(\frac{4\pi R f}{c} \right)^2 \quad (5.22)$$

These measurements are conducted twice with the DRA rotated by 90° between measurements. The two linear gain values can be added to establish the total gain of the DRA on a linear scale by equation (5.23) [14]. The gain of the DRA can then be converted to decibels with equation (5.20).

$$G_{DRA} = G_{DRA,pol1} + G_{DRA,pol2} \quad (5.23)$$

The feed requirements of the low voltage and high voltage antenna measurements have significant differences. Since the high frequencies measured with the network analyzer can extend up to 4.5 GHz, 50 Ω coaxial cables with SMA connectors were used to connect the network analyzer to the high power antenna. The thick substrate of the microstrip on the high power DRA makes unmodified connection to an SMA connector difficult, but poor coupling of the high frequency cable to the high power microstrip could distort the measurements. A small tab extending from the ground plane and an SMA adapter were added at the microstrip feed for the low power measurements to facilitate connection between the microstrip, the ground plane of the DRA, and the SMA connector of the coaxial cable. For consistency, the grounded tab is also included in the

model used for antenna simulations. The small ground tab and low voltage connectors were removed for high power testing. The antenna feed for high power testing was typically a stripline feed insulated in the oil bath. For optimal operation at full power, the insulator of the stripline feed should be formed from an extension of the same piece of material as the substrate of the antenna to reduce the risk of flashover at the antenna feed.

5.6.3 Comparison with Fundamental Limits for Electrically Small Antennas

Finally, based on the simulated and measured data obtained from the previous two evaluation methods, the performance of the antenna is compared with the theoretical fundamental limits established for electrically small antennas. Practical limits to the minimization of the antenna size arise from degradation of antenna performance factors including efficiency, gain, and bandwidth. The definition of an electrically small antenna is inconsistent between various sources. A common rule-of-thumb definition of an electrically small antenna is that the dimensions of the antenna are less than one-tenth of the free space wavelength, λ [m] [15]. A more rigorous definition from Wheeler proposes that an electrically small antenna has a radius that is a small fraction of the radiansphere with a radius of $\lambda/2\pi^2$ [16]. The near field region is predominantly inside the radiansphere while the far field region is predominantly outside the radiansphere [16]. The product of the free-space wavenumber, k [m^{-1}], and the radius, R [m], of a sphere enclosing an antenna is used as a metric for analysis of antenna size. The free-space wavenumber has previously been defined in equation (5.6).

Wheeler's definition for an electrically small antenna results in the condition that the product of the free-space wavenumber and radius of the sphere circumscribing the antenna be equal to or less than 1 [16]. However, a more strict definition arises from

Wheeler's condition that the largest dimension of an electrically small antenna is less than $1/k$, providing the limit described by equation (5.24) [16].

$$kR \leq 0.5 \quad (5.24)$$

Commonly referenced works by Chu and Harrington derived practical limitations on antenna size [17, 18]. Both works consider theoretical antennas that fit within a sphere of radius R [m]. The radiated fields outside the antenna can be described by the propagating modes within the sphere [19]. When the size of the sphere is decreased to the point at which one or zero modes can propagate within it, fundamental limitations are reached [19]. While it is still possible for the antenna to operate within spheres smaller than these limits, there are significant tradeoffs, including very high fields within the sphere, very high Q and correspondingly low bandwidth, and/or poor efficiency due to impedance mismatch [19].

Chu focused specifically on omnidirectional antennas, analyzing the increase in Q with the decrease of the sphere size circumscribing the antenna [17]. Since the bandwidth can be described as the inverse of Q , electrically small antennas can suffer from very low bandwidth. When kR is much less than 1, Chu's equation for Q is reduced to a dependence on $(kR)^{-3}$ [19]. Therefore, a practical limit is imposed on the minimization of antennas, as evidenced through Chu's analysis of omnidirectional antennas, in which the bandwidth is reduced disproportionately with reduction in antenna size. When the antenna is lossy, the Q is lowered, and the bandwidth is increased at the expense of efficiency [19]. While the radiating field of the DRA considered in this work is not omnidirectional, these concepts apply to the reduction in the antenna size with increasing dielectric constant of the resonator. As the resonator dielectric constant is increased to

reduce the size of the resonator, the Q is increased. The increased Q will limit the bandwidth, and design modifications are necessary to maintain an acceptable bandwidth.

Harrington's work was also derived from analysis of antennas circumscribed by a sphere, but this work is not specific to omnidirectional antennas [18]. A practical limit to the gain achievable by an antenna circumscribed by a sphere with radius R was established by Harrington by considering the point at which fields at the antenna structure would become excessively large to have any practical radiated field [18]. The maximum gain based on this practical limit is defined as the normal gain and given by equation (5.25) [18].

$$G_{max} = (kR)^2 + 2kR \quad (5.25)$$

While it is theoretically possible to achieve gains larger than that predicted by equation (5.25), the fields at the antenna structure would be impractically large [18]. Gain beyond the normal gain is described by the concepts of supergain or superdirectivity [18, 19].

5.7 DRA Simulation and Experimental Results

5.7.1 Simulation Results

The high power DRA was simulated with the transient solver of CST Microwave Studio to predict the return loss, realized gain, and far-field pattern between 200 MHz and 2 GHz. The measured permittivity of MU100 was directly imported into CST to obtain a close numerical fit for simulation of the dielectric resonator's properties. The material around the antenna was defined to be oil for high power operation. Figure 86 shows the high power DRA as it was simulated. The red plane at the antenna feed is the waveguide port used to feed the antenna.

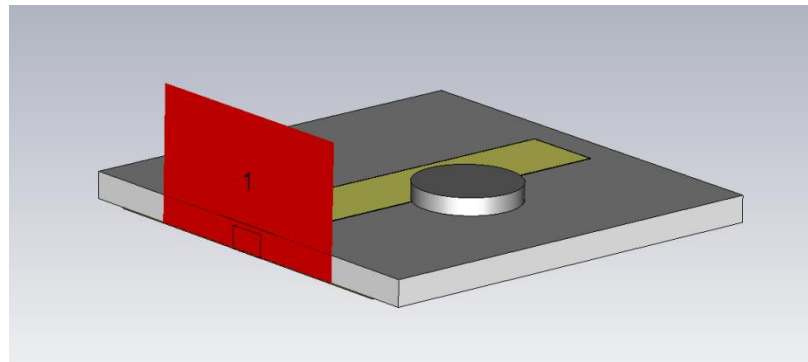


Figure 86. The simulated DRA with the waveguide port

The simulated return loss of the high power DRA is shown in Figure 87. The return loss first dips to nearly -10 dB at approximately 400 MHz, and the lowest simulated return loss value of approximately -21.61 dB occurs at around 816 MHz. The return loss is below -10 dB between approximately 720 and 890 MHz.

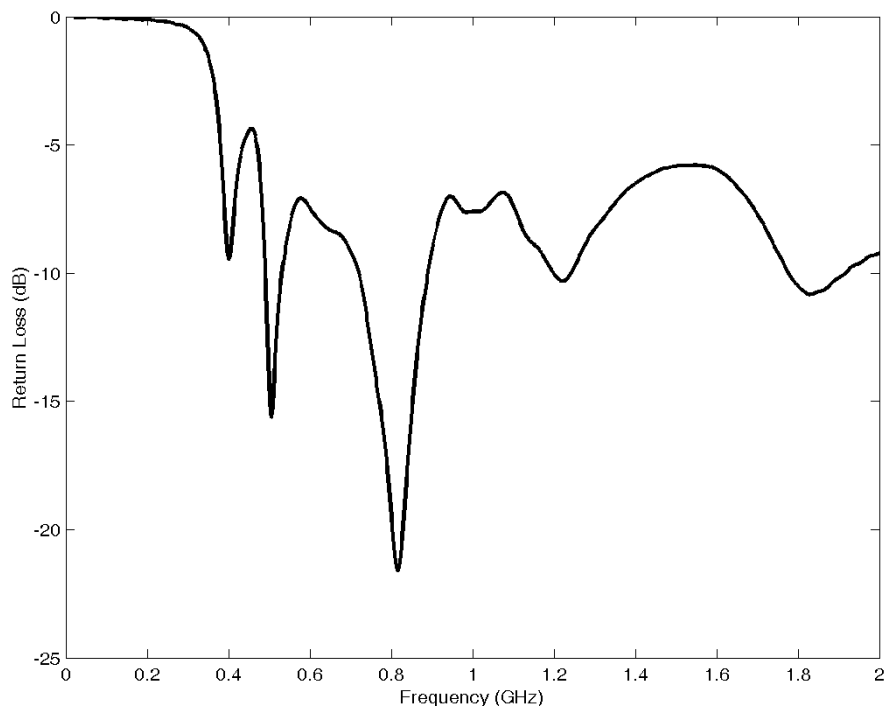


Figure 87. Simulated return loss of the high power DRA

Figure 88 shows the simulated maximum 3D farfield gain as a function of frequency. The first band of greater than unity gain is between approximately 475 and 575 MHz. After

briefly dipping to below unity gain, the gain remains positive above approximately 625 MHz.

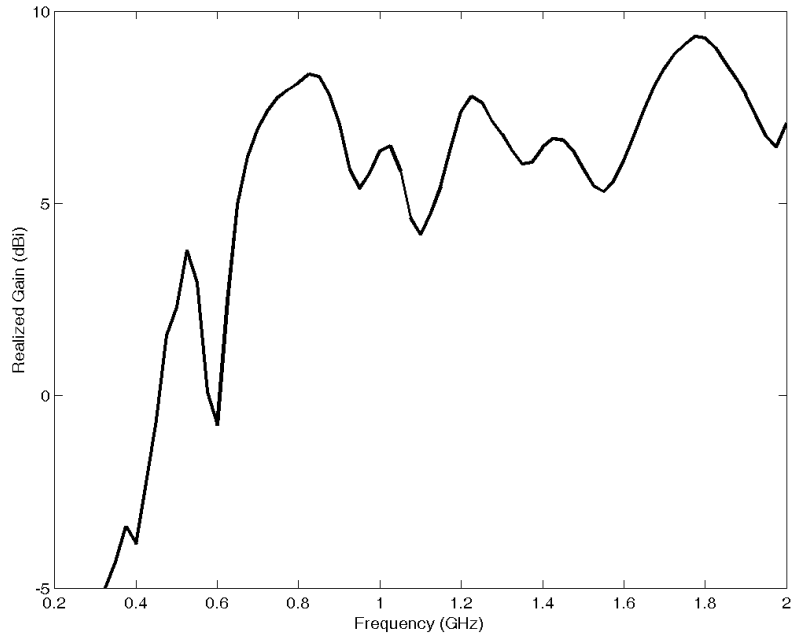


Figure 88. Simulated maximum 3D farfield gain of the high power DRA

While Figure 88 plots the maximum 3D gain, the gain of greatest interest is that which is orthogonal to the plane of the DRA substrate. In the polar coordinates shown in Figure 90, this direction corresponds to $\theta=\varphi=0^\circ$. Figure 89 plots the simulated gain orthogonal to the substrate. The gain is briefly positive between approximately 475 and 525 MHz, and the main band of high gain operation occurs between approximately 625 MHz and 1.05 GHz. The gain is above 5 dBi between approximately 670 and 920 MHz, and the peak gain at $\theta=\varphi=0^\circ$ is simulated to be nearly 7.5 dBi at approximately 829 MHz.

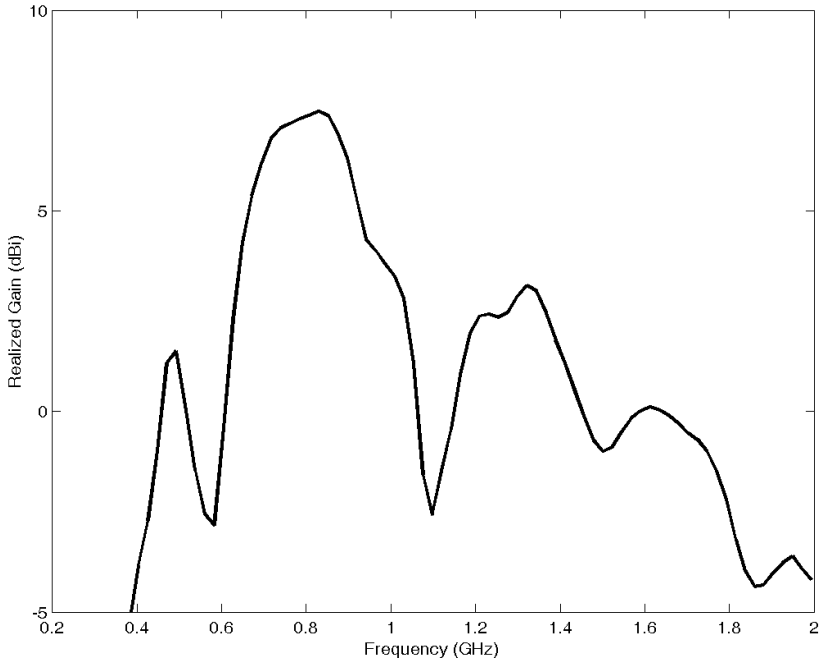


Figure 89. Simulated gain orthogonal to the plane of the DRA substrate ($\theta=\varphi=0^\circ$)

The following four sets of figures illustrate the farfield gain pattern at four frequencies where greater than unity gain was simulated. Both 3D and polar plots are included for 475 MHz, 650 MHz, 825 MHz, and 1,200 MHz. Figure 90 and Figure 91 show the far field gain at 475 MHz. This frequency is at the lower end of the relatively narrow band between 475 and 525 MHz where greater than unity gain is first predicted by the simulations. Neither the radiation efficiency nor the return loss are optimal in this range, resulting in relatively low gain values. The radiation efficiency is simulated to be -2.294 dB or approximately 59%. The maximum 3D gain at 475 MHz is 1.57 dBi, and the main lobe is directly centered at $\theta=0^\circ$ in the $\varphi=90^\circ$ plane and only 5° off in the $\varphi=0^\circ$ plane. The main lobe is relatively wide compared to the pattern at higher frequencies with the 3dB angular beam width measuring 104.4° in the $\varphi=0^\circ$ plane and 52.5° in the $\varphi=90^\circ$ plane.

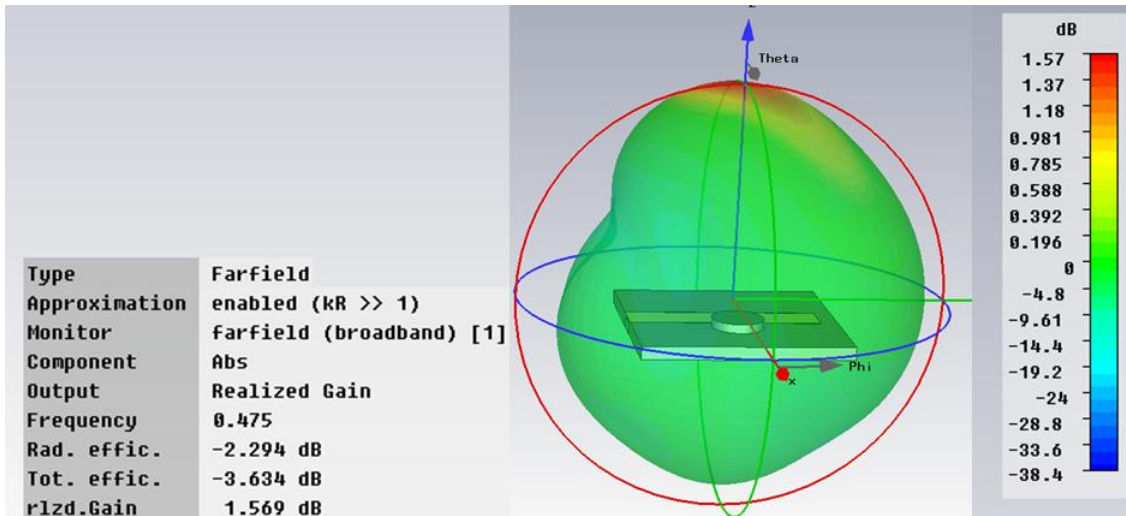
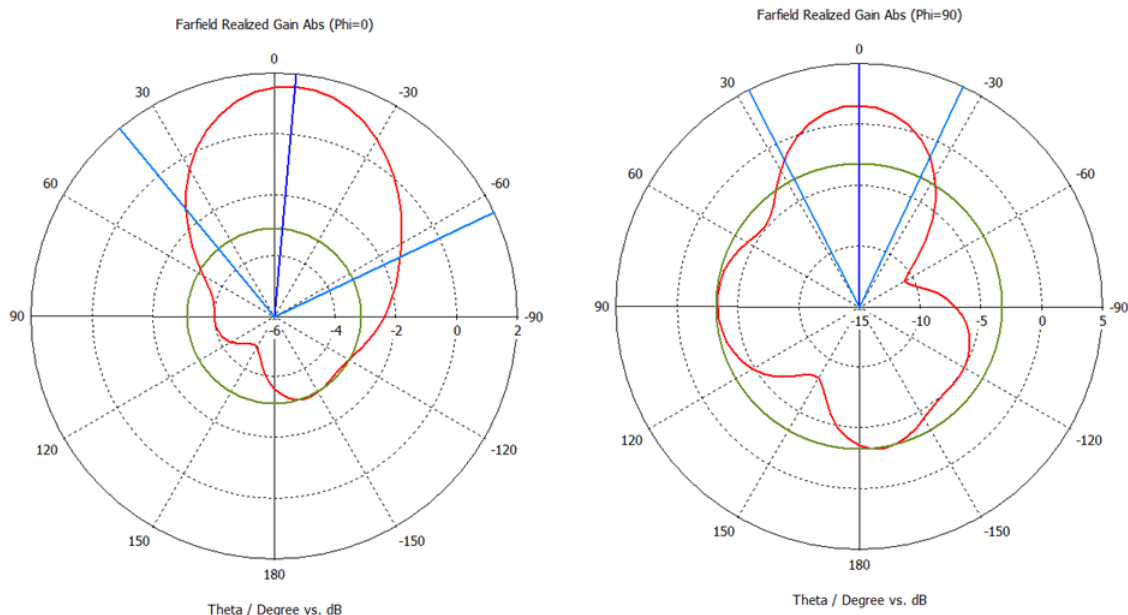


Figure 90. 3D plot of the simulated far field gain pattern at 475 MHz



Frequency = 0.475

Main lobe magnitude = 1.6 dB

Main lobe direction = -5.0 deg.

Angular width (3 dB) = 104.4 deg.

Side lobe level = -4.7 dB

Frequency = 0.475

Main lobe magnitude = 1.5 dB

Main lobe direction = 0.0 deg.

Angular width (3 dB) = 52.5 deg.

Side lobe level = -4.8 dB

Figure 91. Polar plots of the far field gain pattern at 475 MHz

The simulated far field gain pattern is shown at 650 MHz in 3D and polar plots in Figure 92 and Figure 93, respectively. The gain rapidly increases above 600 MHz, reaching a 3D maximum value of nearly 5 dBi at 650 MHz. The main lobe is angled 10° off from $\theta=0^\circ$

in the $\varphi=0^\circ$ plane and 15° off in the $\varphi=90^\circ$ plane. The 3 dB beam width in the $\varphi=0$ plane is narrowed from the 475 MHz case to 60.7° in the $\varphi=0^\circ$ plane but widened to 88.8° in the $\varphi=90^\circ$ plane. The radiation efficiency is -1.9 dB or approximately 64.6%.

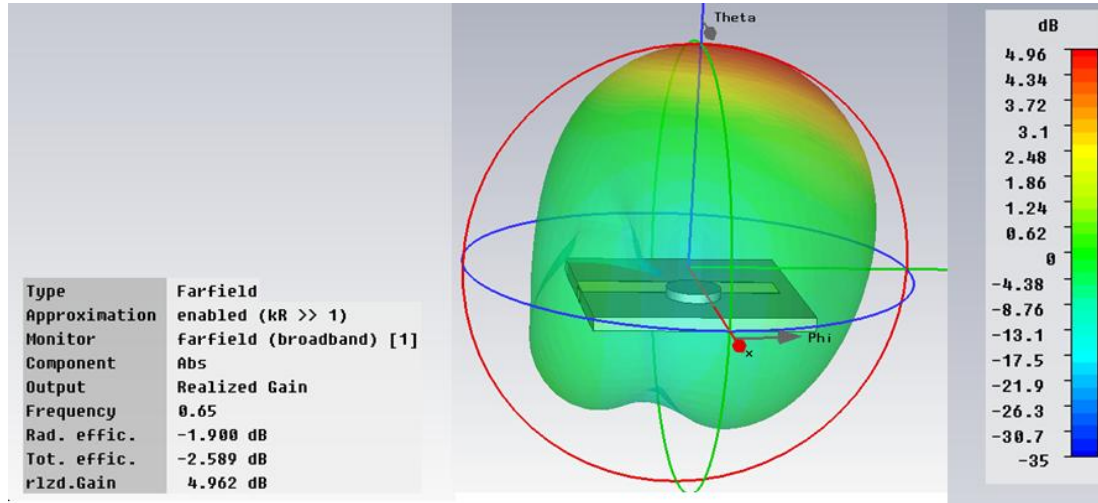


Figure 92. 3D simulated far field gain pattern at 650 MHz

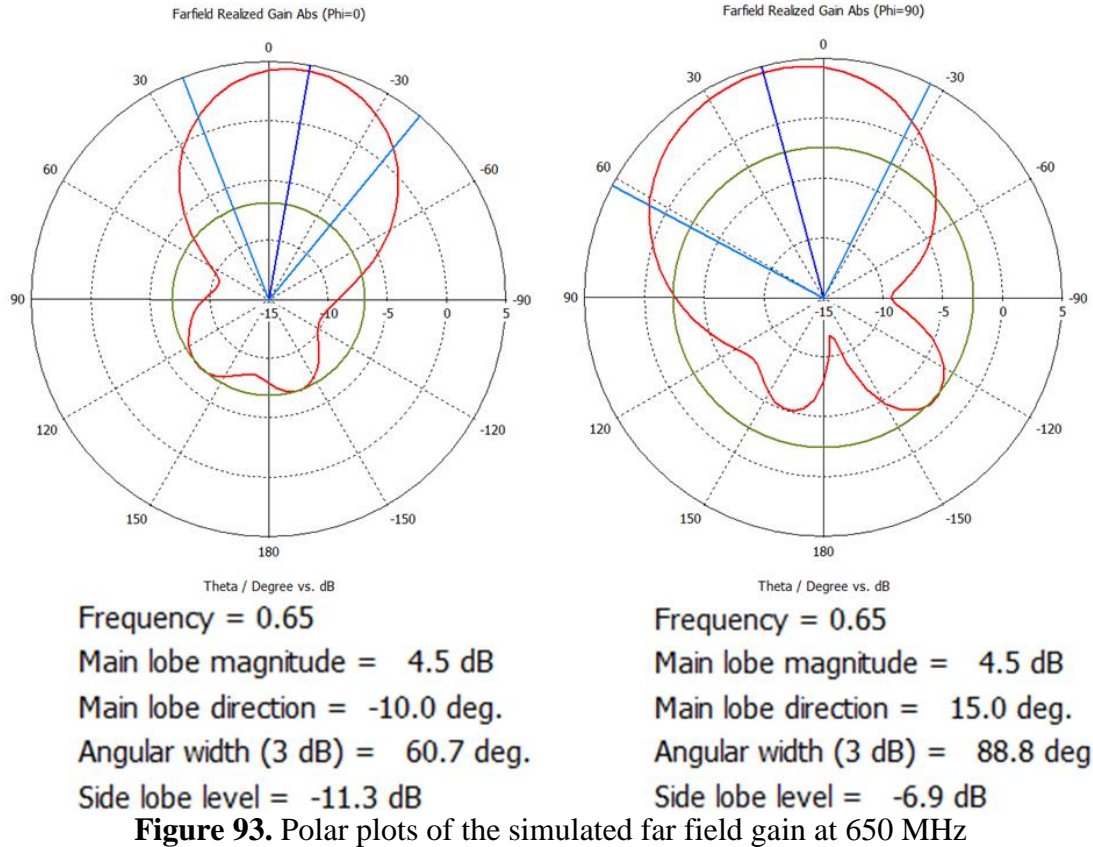


Figure 94 and Figure 95 show the 3D and polar plots of the gain at 825 MHz, respectively. This frequency is near the maximum gain simulated for the $\theta=\varphi=0^\circ$ direction. The maximum gain at 825 MHz is 8.36 dBi, but due to a slight shift off axis, the gain at $\theta=\varphi=0^\circ$ is reduced to approximately 7.5 dBi. The 3 dB angular width of the beam in the $\varphi=0^\circ$ plane is 60.8° , and the beam width in the $\varphi=90^\circ$ plane is 68.7° . The radiation efficiency is calculated to be -0.5275 dB or approximately 88.6%.

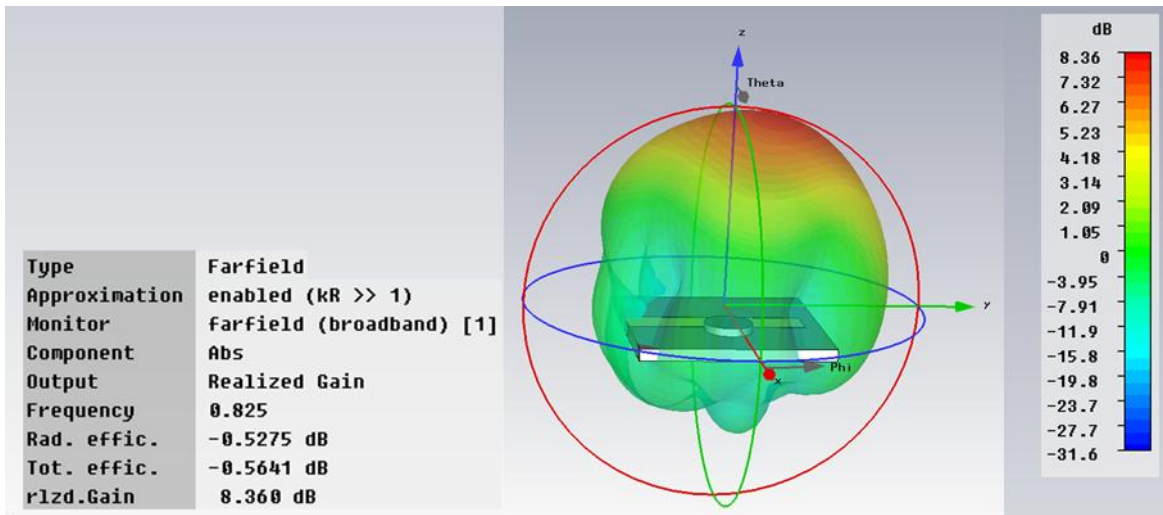
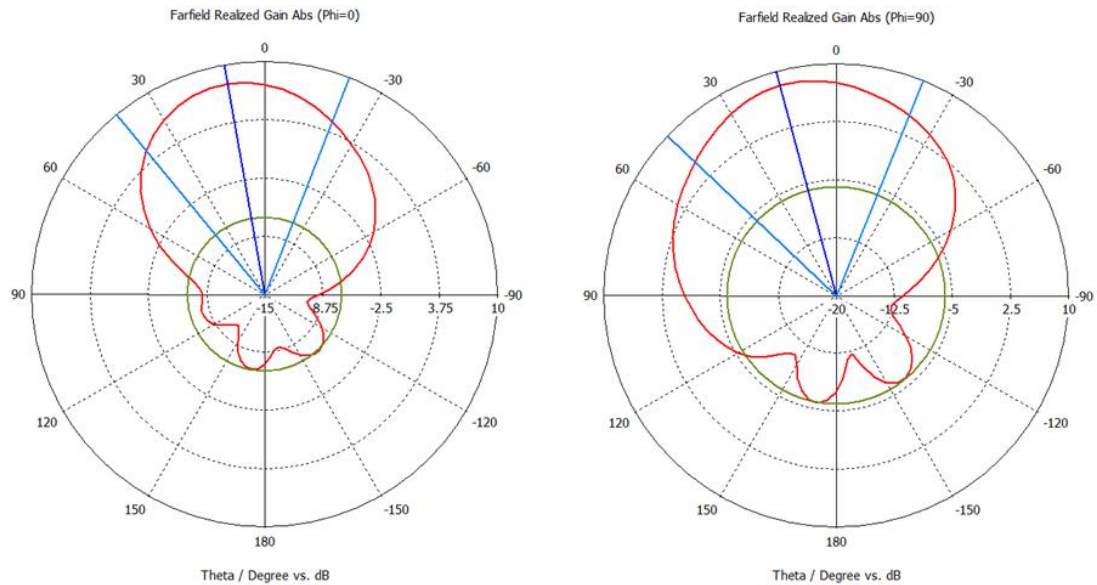


Figure 94. Simulated 3D farfield gain pattern at 825 MHz

Discrepancy between the maximum 3D gain and the gain at $\theta=\varphi=0$ is due to shifting of the main lobe of the farfield pattern. This shifting is more pronounced between approximately 525 and 625 MHz and at most frequencies above 1 GHz.



Frequency = 0.825

Main lobe magnitude = 7.9 dB

Main lobe direction = 10.0 deg.

Angular width (3 dB) = 60.8 deg.

Side lobe level = -14.6 dB

Frequency = 0.825

Main lobe magnitude = 8.1 dB

Main lobe direction = 15.0 deg.

Angular width (3 dB) = 68.7 deg.

Side lobe level = -14.1 dB

Figure 95. Simulated polar plots of the gain at 825 MHz

Figure 96 and Figure 97 demonstrate these shifts in the main lobe at 1.2 GHz. While the peak gain of the antenna at 1.2 GHz is nearly 7.38 dBi, the gain at $\theta=\varphi=0^\circ$ is only approximately 2.4 dBi, primarily due to a 25° shift of the main lobe in the $\varphi=90^\circ$ plane. The main lobe shifts towards progressively larger values of θ in the $\varphi=90^\circ$ plane above 1 GHz. Despite these shifts, the simulations of the high power DRA suggest that there is a wide band of greater than unity gain at $\theta=\varphi=0^\circ$ below 1.05 GHz.

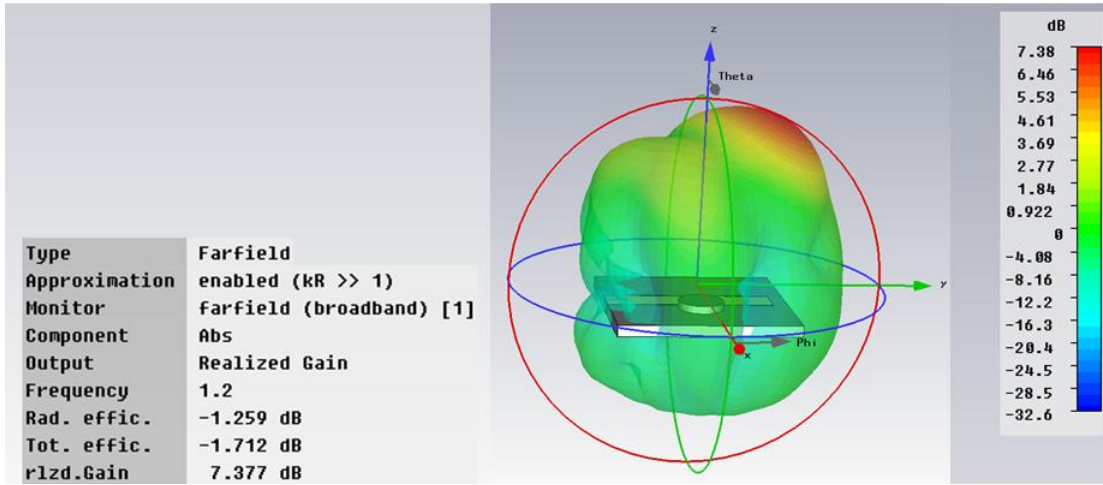
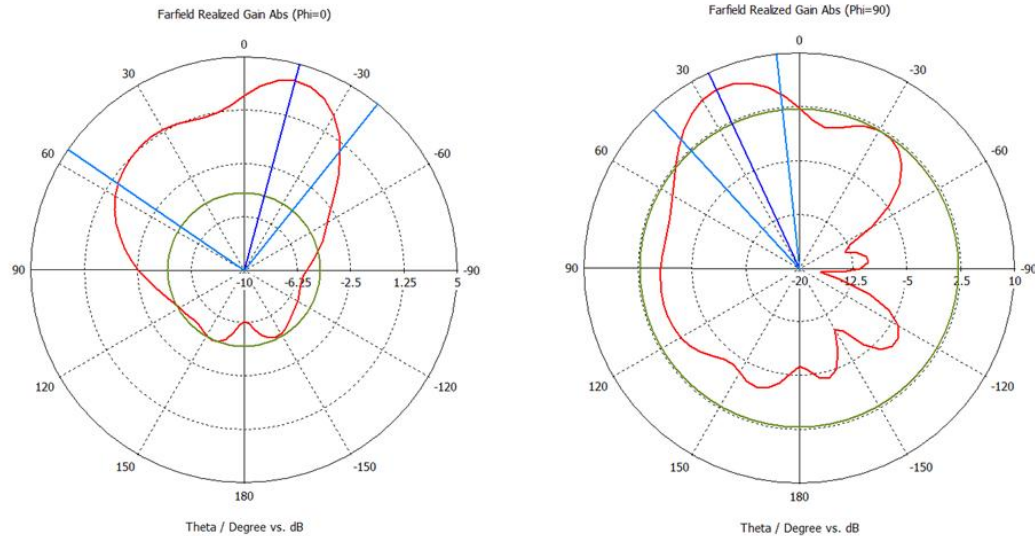


Figure 96. Simulated 3D plot of the gain at 1.2 GHz



Frequency = 1.2
 Main lobe magnitude = 3.8 dB
 Main lobe direction = -15.0 deg.
 Angular width (3 dB) = 94.3 deg.
 Side lobe level = -8.4 dB

Frequency = 1.2
 Main lobe magnitude = 7.4 dB
 Main lobe direction = 25.0 deg.
 Angular width (3 dB) = 36.6 deg.
 Side lobe level = -5.2 dB

Figure 97. Simulated polar plots of the gain at 1.2 GHz

5.7.2 Low Power Experimental Results

Figure 98 shows the measured return loss both with and without the dielectric resonator in place. The effect of the resonator is clearly seen between approximately 475 MHz and 1.5 GHz. Above about 1.5 GHz, the return loss is very similar both with and without the

resonator. The resonator significantly improves the impedance match of the antenna below 1.5 GHz as the return loss is generally below -10 dB down to 475 MHz.

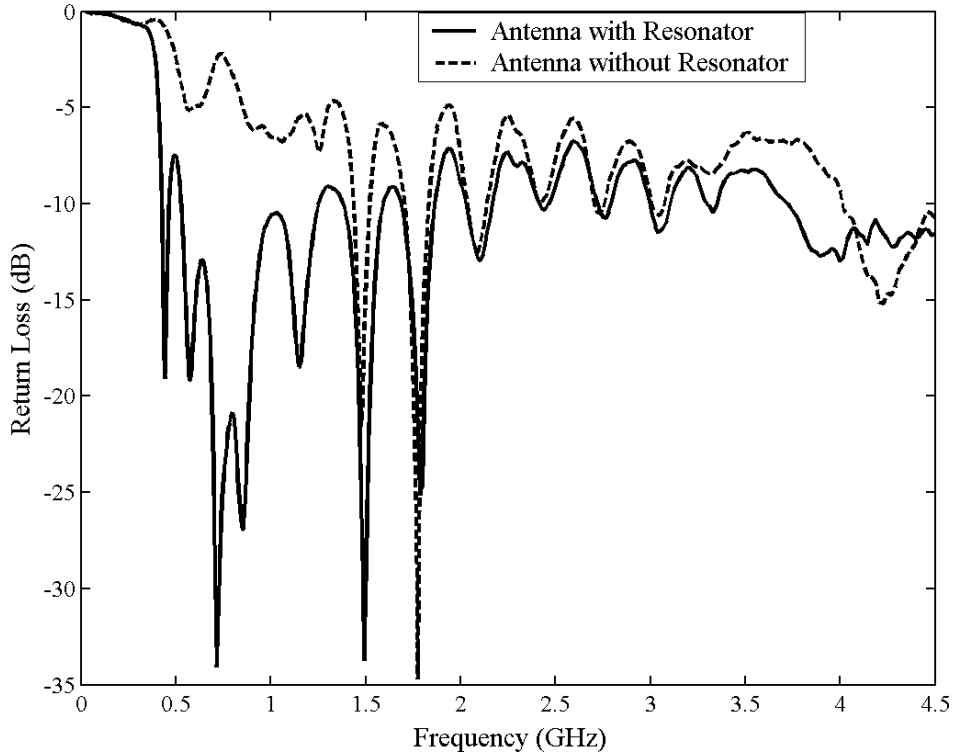


Figure 98. Return loss of the high power DRA with and without the resonator. The impedance match of the antenna is improved between 475 MHz and 1.5 GHz due to the addition of the resonator.

Figure 99 plots the simulated and measured return loss for direct comparison. The first two troughs of the simulated waveform occur at slightly lower frequencies than those measured experimentally, but in general the measured waveform achieves a lower return loss. The measured return loss is believed to be better than the simulated return loss due to the precise tuning that can be done experimentally by moving the resonator along the microstrip. While the simulated resonator should theoretically be in the same position, relatively small adjustments to the location of the simulated resonator could provide improvement to the simulated return loss to the level observed in the experimental measurement. Tuning capability of the resonator position in CST Microwave Studio is

limited due to the simulation time. Despite these differences, the simulated and measured return loss show very similar responses.

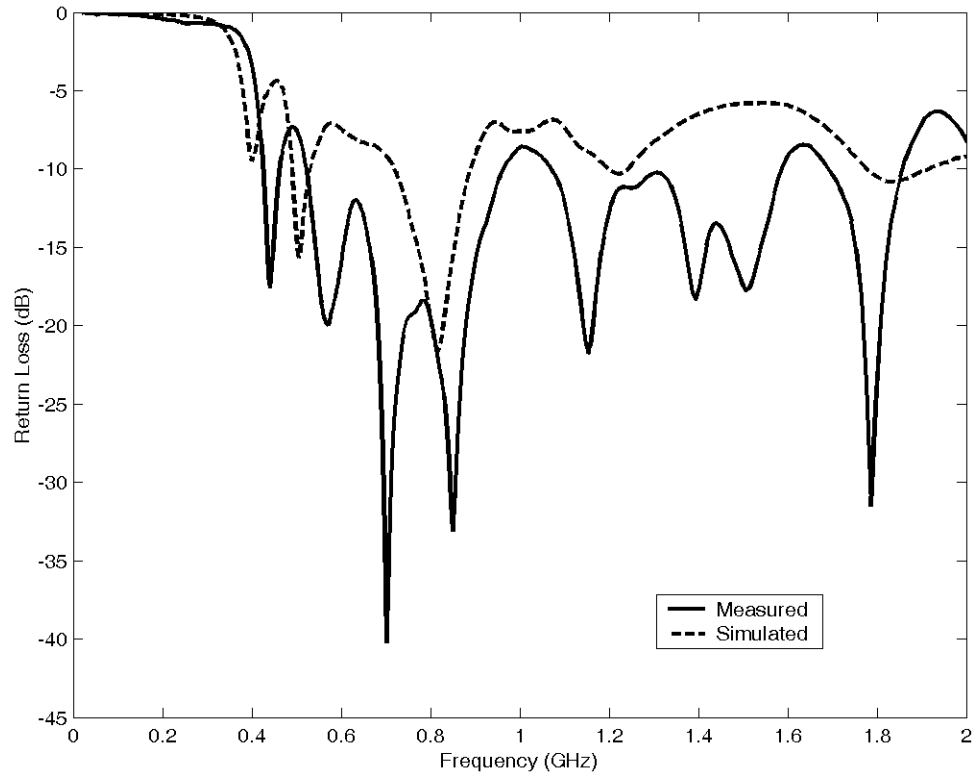


Figure 99. Comparison of the simulated and measured return loss of the high power DRA

Figure 100 shows the measured gain of the high power DRA in oil. While the return loss exhibited good impedance matching down to 475 MHz, the gain is less than unity below approximately 605 MHz. The primary band of operation of the high power DRA was measured between approximately 605 MHz and 1.1 GHz. The peak gain was measured at approximately 700 MHz to be approximately 6 dBi, and the gain reaches a minimum within this band at approximately 890 MHz. Additional bands where positive gain was observed include 1.17-1.32 GHz and 1.4-1.62 GHz. The bandwidth of the high power DRA is larger than that conventionally observed with DRAs.

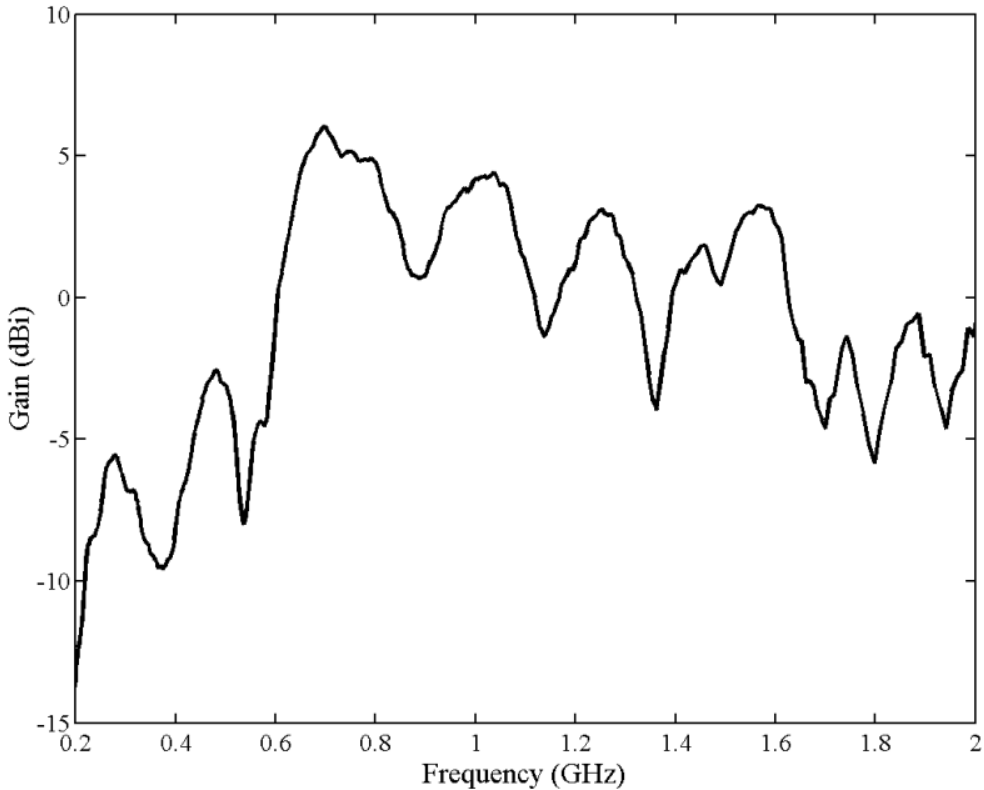


Figure 100. Measured gain of the high power DRA in oil

Figure 101 compares the measured gain to the gain simulated at $\theta=\varphi=0^\circ$. The measured and simulated gains show very similar behavior, and many of the differences below 1 GHz are likely due to slightly shifted maxima in the main lobe of the patterns and somewhat different return loss values. Both gain profiles show a peak near 475 MHz, but the measured gain does not extend above unity gain. This discrepancy may be due to misalignment of the lobe maximum. The gain values are very close between 575 MHz and 700 MHz as the gain rapidly increases. The measured gain peaks at around 700 MHz, and the lower gain seen in the measurements between 700 MHz and 975 MHz is also believed to be due to shifts in the far field gain pattern off axis. The measured gain is greater than the simulated gain between approximately 975 MHz and 1.1 GHz. Although the far field gain pattern was not measured in this work, the agreement between the gain

measured at $\theta=\phi=0^\circ$ provides a level confidence that the features of the simulated gain pattern apply to the constructed antenna.

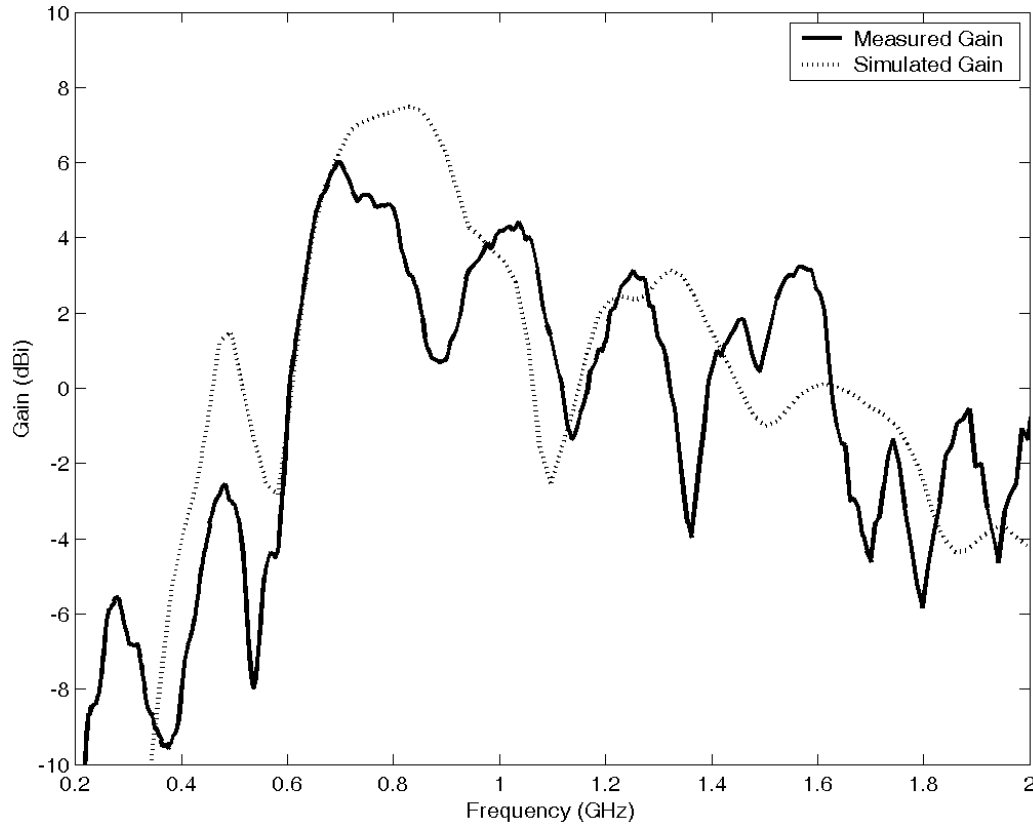


Figure 101. Comparison of the measured gain and simulated gain at $\theta=\phi=0^\circ$

5.7.3 Evaluation of Experimental Results against Fundamental Limits

The measured gain of the high power DRA was compared to the theoretical limits imposed by Harrington's derivation. Figure 102 shows a plot of equation (5.25) for spheres that would approximately circumscribe the dimensions of the DRA substrate and dielectric resonator. The substrate has side dimensions of approximately 30.48 cm, so a sphere radius of 15.24 cm was used in the calculated curve. The diameter of the resonator is approximately 7.62 cm, so a sphere radius of 3.81 cm was used for the second curve. Due to the thickness of the substrate and resonator, spheres completely circumscribing all edges of these structures would be slightly larger than the values used in the calculations.

However, the effect of increasing the sphere radius by a small amount would slightly increase the maximum theoretical gain. Therefore, the curves of Figure 102 represent a slightly underestimated maximum theoretical gain.

As seen in Figure 102, the measured gain is below the theoretical limit. Two important conclusions can be stated from this result. First, the high power DRA is operating within the limits of the normal gain for the size of the antenna as established by Harrington. Second, further antenna minimization through reduction of the substrate and ground plane is possible. Even if the substrate, ground plane, and feed structure were reduced to the circular cross-section of the resonator, the same gain profile as that measured with the large substrate would not be in violation of this practical limit. It should be noted that other practical limitations may limit the reduction of the DRA to this extent, including changes to the radiation pattern as a result of significant changes to the ground plane size. Nevertheless, while the substrate and ground plane size were designed to be relatively large for the requirements of the experiments in this work, including the need for a large microstrip feed capacitance, other applications of the DRA could be minimized to much smaller substrates.

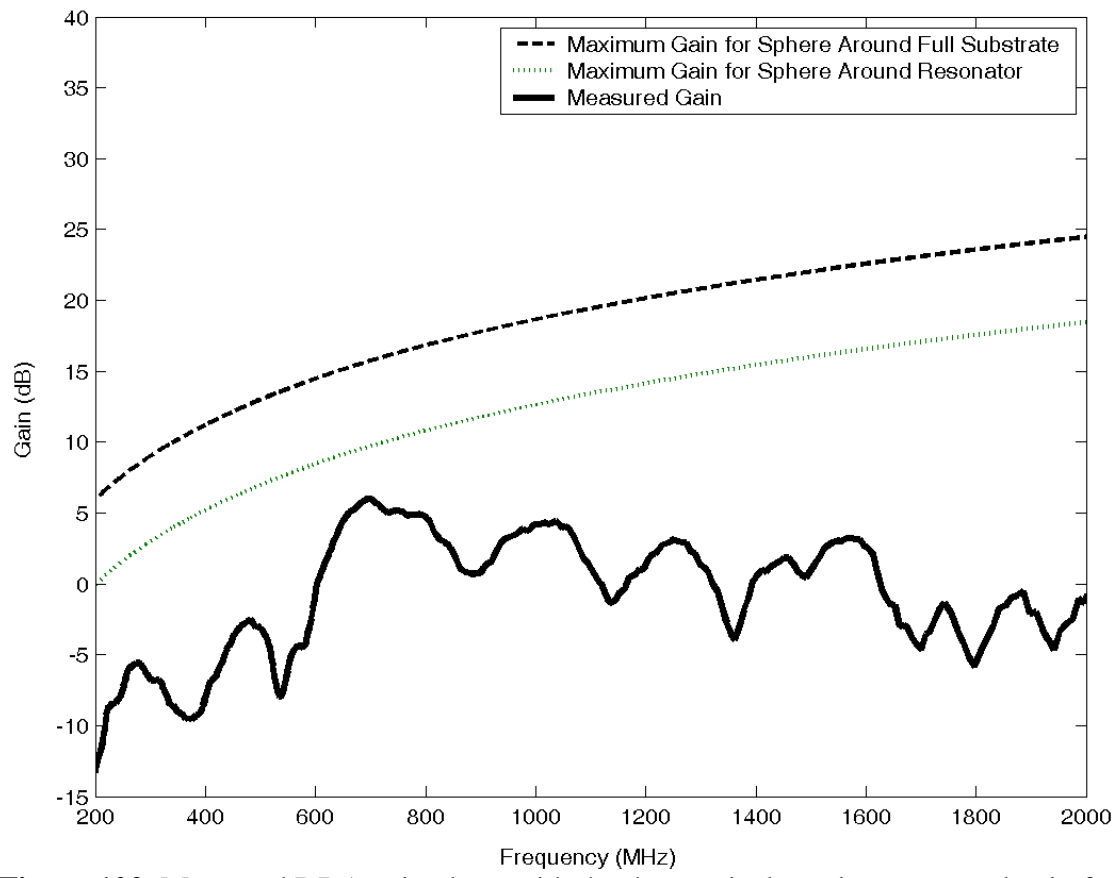


Figure 102. Measured DRA gain along with the theoretical maximum normal gain for antennas enclosed in a sphere around the full DRA substrate and around only the resonator

References for Chapter 5

- [1] R. D. Richtmyer, "Dielectric resonators," *Journal of Applied Physics*, vol. 10, pp. 391-398, 1939.
- [2] D. Kajfez and e. P. Guillon, *Dielectric Resonators*. Norwood, MA: Artech House, 1986.
- [3] A. Petosa, *Dielectric Resonator Antenna Handbook*. Norwood, MA: Artech House, 2008.
- [4] R. A. Krannenburg and S. A. Long, "Microstrip transmission line excitation of dielectric resonator antennas," *Electronics Letters*, vol. 24, pp. 1156-1157, 1988.
- [5] S. A. Long, M. W. McAllister, and L. C. Shen, "The resonant cylindrical dielectric cavity antenna," *IEEE Trans. on Antennas and Propagation*, vol. AP-31, pp. 406-412, 1983.
- [6] K. W. Leung, K. M. Luk, E. K. N. Yung, and S. Lai, "Characteristics of a low-profile circular disk DR antenna with very high permittivity," *Electronics Letters*, vol. 31, pp. 417-418, 1995.
- [7] R. K. Mongia, A. Ittibipoon, and M. Cuhaci, "Low profile dielectric resonator antennas using a very high permittivity material," *Electronics Letters*, vol. 30, pp. 1362-1363, 1994.
- [8] F. T. Ulaby, *Fundamentals of Applied Electromagnetics*. Upper Saddle River, NJ: Prentice Hall, 2001.
- [9] H. A. Wheeler, "Transmission-line properties of a strip on a dielectric sheet on a plane," *IEEE Trans. on Microwave Theory and Techniques*, vol. MTT-25, pp. 631-647, 1977.
- [10] K. A. O'Connor and R. D. Curry, "High dielectric constant composites for high power antennas," in *Proc. 18th IEEE Intl. Pulsed Power Conf.* Chicago, IL, 2011.
- [11] D. Pozar, *Microwave Engineering*, 3rd ed. Hoboken, NJ: John Wiley and Sons, 2005.
- [12] C. Balanis, *Antenna Theory: Analysis and Design*, 3rd ed. Hoboken, NJ: John Wiley and Sons, 2005.
- [13] "Log-periodic antennas LP80: 80MHz-2GHz LP100:100MHz-2GHz," Sunol Sciences, Dublin, CA 2012.
- [14] M. L. Kales and J. I. Bohnert, "Elliptically polarized waves and antennas," Naval Research Laboratory, Washington, D.C. 1950.
- [15] G. Breed, "Basic principles of electrically small antennas," in *High Frequency Electronics*. vol. 6, 2007, pp. 50-53.
- [16] J. Volakis, *Antenna Engineering Handbook*, 4th ed. New York, NY: McGraw-Hill, 2007.
- [17] L. J. Chu, "Physical Limitations of Omnidirectional Antennas," Massachusetts Institute of Technology 1948.
- [18] R. F. Harrington, "On the Gain and Beamwidth of Directional Antennas," *IRE Trans. on Antennas and Propagation*, vol. 6, pp. 218-225, 1958.
- [19] R. C. Hansen, "Physical Limitations in Antennas," *Proc. of the IEEE*, vol. 69, pp. 170-182, 1981.

Chapter 6: High Power Antenna Driver

6.1 System Overview

A high power antenna driver was developed as a final means of experimentally testing the high power DRA and future dielectric-loaded antennas. In addition to the requirement that the antenna developed through this program have reduced dimensions through incorporation of the high dielectric constant composite material, the antenna is intended to be capable of transmitting signals at frequencies below 1 GHz at a peak power level on the order of 1 GW. Thus the antenna driver must be capable of driving the antennas at frequencies on the order of 100s of MHz to 1 GHz at peak power levels on the order of 10s of MW to 1 GW. The driver was designed to be capable of driving a range of prospective antenna impedances at 1 GW or greater. The peak voltage requirement for the antenna driver to achieve 1 GW of applied power can be calculated based on the impedance of the load. For antenna input impedances of 50 to 377 Ω , the voltage requirement varies from approximately 223.6 kV to 614 kV, respectively. Since the high power antenna driver signal applied to the antenna will incorporate significant frequency content at frequencies below the antenna operation frequencies, the power at the frequencies of operation of the antenna will be much less than 1 GW. Nevertheless, the high power antenna driver enables testing of the antenna structures under high peak power conditions.

Two types of high power antenna drivers were considered in this work. The first type of high power antenna driver applies a high voltage pulse to the antenna with a very fast risetime. The frequency content of the signal composing the fast rising voltage signal is

spread over a wide band of frequencies, and this type of antenna driver is used in the research of impulse radiating antennas (IRAs). When a step input with a fast rising edge is applied to an impulse radiating antenna, the radiated field is the derivative of the applied voltage signal. Thus, an IRA radiates an impulse in response to the step input [1]. A high voltage step input has also been applied to other antennas, including a high power helical antenna, under the concept of shock excitation [2]. A Marx generator was implemented as the high voltage source of a fast risetime single in the helical antenna investigation [2]. The PA-80 high voltage trigger generator with a peaking switch to decrease the risetime was considered as a part of this work. While this was determined to be a viable method for performing high power antenna testing with IRAs or other antennas in which the time-domain behavior of the antenna is well characterized, it is not the preferred type of antenna driver for a resonant antenna like a DRA.

The second type of high power antenna driver considered in this study applies a high voltage damped sinusoidal signal to the antenna under test. This type of antenna driver was designed, built, and tested in this work. The high power antenna driver was developed based on a previously investigated system for compact high voltage RF generation with explosive generators, inductive energy storage, exploding wire fuses, and compact ring-down oscillators [3, 4]. Significant modifications were made to the system, including improvement of the simulator of the explosive generator and the capability of generating higher frequency content in the voltage signal applied to the antenna. The following section provides an overview of the high power antenna driver with subsequent sections highlighting new or important design aspects of individual components.

The high power antenna driver can be separated into the three subsystems shown in Figure 103. The subsystems consist of a current source, an inductive energy store, and a high power ring-down oscillator. The flow chart also follows the path of energy delivered to the antenna under test as it is delivered from its source, stored in an intermediate storage element, and diverted to a high power oscillator. The oscillating voltage produced by the high power oscillator directly drives the high power antenna under test.

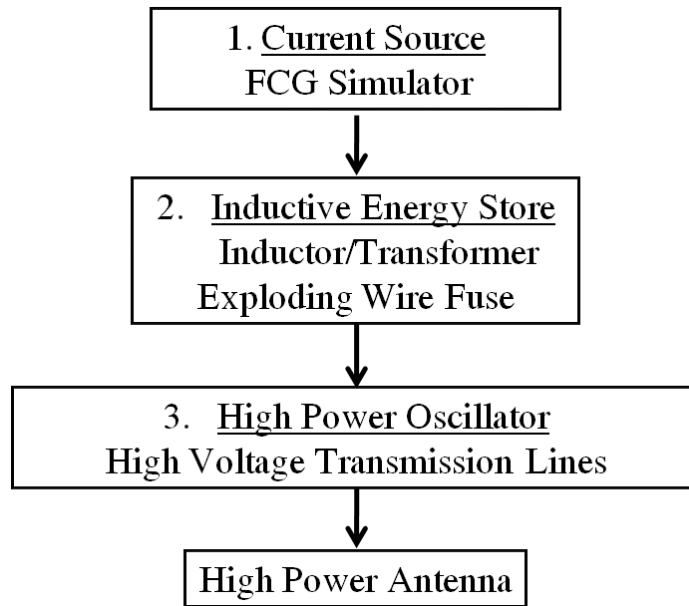


Figure 103. Flow chart for the high power antenna driver

The first subsystem serves as the primary energy storage system and current source. A variety of systems could potentially fulfill the requirements of the current source, but consideration in this study was limited to a flux compression generator (FCG) or a simulator of an FCG. In this case, the FCG or FCG simulator provides an approximately exponentially rising current signal, reaching a peak current on the order of tens of kiloamps after a risetime on the order of several microseconds. The total electromagnetic energy output of the FCG or FCG simulator is on the order of kilojoules.

The second subsystem, the inductive energy storage system, stores energy delivered by the source in its magnetic field. Although the requirements of the source and inductive energy store can vary widely for different systems, the inductance of the storage medium considered here is typically on the order of $1 \mu\text{H}$. For a peak current through this inductive element on the order of tens of kiloamps, the energy inductively stored can vary from a few hundred joules up to a few kilojoules. The inductive energy storage component is typically either a solenoid inductor or the primary winding of a pulse transformer. Figure 104 displays the schematic for the high power antenna driver. The inductive storage element is represented in this schematic by the inductor L_{IS} .

The second component of the inductive energy storage system is the opening switch, which is implemented as an electroexplosive opening switch (EEOS). As the source produces its rising current signal, most of the current passes through the EEOS, represented as R_{EEOS} in Figure 104. As the EEOS resistance rises, energy is transferred to charge the capacitance of the transmission lines, represented by components T_1 and T_2 in Figure 104, charging them to high voltage.

The third subsystem is a high power oscillator consisting of high voltage capacitive transmission lines. The high voltage feed to the antenna under test is made between the two high voltage transmission lines. When the switch S is closed, the transmission lines are shorted through a shunt inductance, and a series of high voltage oscillations along with high frequency content from reflections occur due to mismatching of the transmission lines and antenna impedance. This high power RF signal directly drives the antenna under test, represented by the antenna's impedance, Z_A . The following two

sections describe the design and operation of the driver's subsystems with emphasis on the improvements made to the FCG simulator, EEOS, and high voltage oscillator.

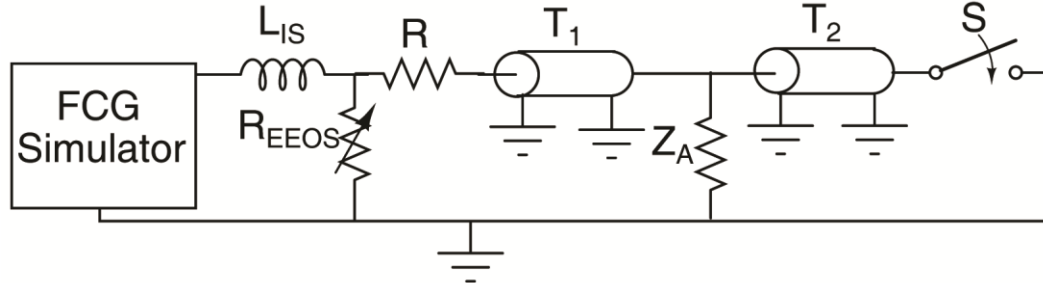


Figure 104. Inductive energy storage systems and high power oscillators driving antenna impedance Z_A

6.2 Revised FCG Simulator

6.2.1 Background and Theory of Operation

The FCG simulators have been developed in the last decade primarily as a means for non-destructive testing of power conditioning components intended for use with FCGs. Previous work by the author has also investigated the use of an FCG simulator to test alternative compact RF generators along with power conditioning components for explosively-driven systems [3, 4]. Although the dielectric-loaded antennas under development are not limited to explosively-driven systems, the addition of the antennas to a modified version of the previously developed components completes the system by radiating the RF signal.

The FCG simulators are distinguished from traditional capacitor-driven sources in that they attempt to replicate the exponentially rising current waveform characteristic of an FCG. Whereas a typical capacitive discharge has its greatest rate of current rise at the very beginning of the discharge, the discharge of an FCG simulator is modified to have an increasing rate of current rise during its operation. In the past, this effect was mainly

achieved through magnetically-switching parallel inductance into the circuit to decrease the circuit inductance in time [5]. An FCG simulator based upon this principle was previously utilized with modifications from the original design, including using a capacitor bank to drive the inductive network rather than a pulse forming network and lowering the inductance to allow the simulator to drive external inductive and system loads [6].

The newly modified FCG simulator developed for the high power antenna driver incorporates two fundamental changes to the previous FCG simulators. Although magnetically switching parallel inductors into the circuit can provide a stepped effect increasing the rate of current rise, the decreasing voltage on the capacitor bank or PFN output in time results in a decreasing rate of current rise between switch closures. A significant modification to the new FCG simulator is to drive the inductive network with a rising voltage in time. This is accomplished by driving the inductor network in parallel with a capacitor-inductor-capacitor (CLC) network, as shown in Figure 105. Capacitor bank C_1 is initially DC charged to high voltage. When the switch S is closed, the voltage across capacitor bank C_2 slowly increases over several microseconds. The rising voltage across capacitor bank C_2 initially drives an increasing current through inductor L_1 while all of the magnetic switches remain closed. The rising voltage across L_1 enables the current through the inductive energy store (IES) to increase smoothly with a derivative similar to that of an FCG. As the rate in the voltage rise on capacitor C_2 reaches its inflection point and begins to decrease, magnetic switches sequentially close to lower the circuit inductance in time. The network of inductors is designed such that $L_1 > L_2 > L_3 > L_4$, and L_4 is the minimal inductance achievable to effectively short out the network of

inductors at the end of the simulator's current rise. Magnetic switches L_{S1} and L_{S2} were arranged in the same manner as previous FCG simulators and were designed to close sequentially. However, unlike the arrangement of previous simulators, magnetic switch L_{S3} and inductor L_4 now form a parallel path with inductor L_1 . This improvement was made to the new simulator to minimize the network's inductance after the closure of magnetic switch L_{S3} . Whereas in the previous design the path through the short circuit inductor L_4 would also include the saturated inductances of all three magnetic switches, the new arrangement only includes the saturated inductance of one magnetic switch. Additionally, since the network of inductors is driven with the slowly rising voltage waveform across capacitor C_2 , the requirements on the size and number of windings on the magnetic switches are reduced, lowering the saturated inductances of the switches. The resistor R_1 is a low resistance load to dissipate the extra energy in the CLC network after operation of the FCG simulator is complete.

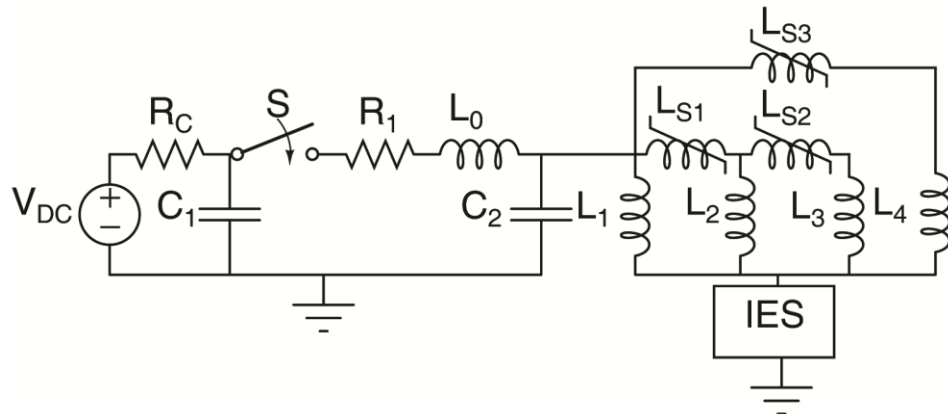


Figure 105. CLC-Driven FCG Simulator

Figure 106 displays the simulated current output of the revised FCG simulator of Figure 105. Both capacitor banks were defined to be $6.6 \mu\text{F}$, and V_{DC} was 35 kV . The values for R_1 and L_0 were 0.25Ω and $5 \mu\text{H}$, respectively. The values for inductors $L_1 - L_4$ were $10 \mu\text{H}$, $10 \mu\text{H}$, $1 \mu\text{H}$, and 10 nH , respectively. Switches $L_{S1} - L_{S3}$ were designed to saturate

due to a flux change of 42 mV·s, 15 mV·s, and 50 mV·s, corresponding to closure times of 8 μ s, 9 μ s, and 9.5 μ s, respectively, after the closure of switch S . The load of the FCG simulator was a 1 μ H inductance with no opening switches in series.

The simulated output of the new FCG simulator produces a current waveform that more closely resembles an exponential rise than previous simulators. The second derivative of the current is positive through the first 8 μ s of operation as the voltage driving the inductor network increases. When the magnetic switches begin closing, the first derivative is increased in large steps to ensure an increased rate of current rise. The simulator current reaches greater than 40 kA after 10 μ s and a peak of approximately 55 kA.

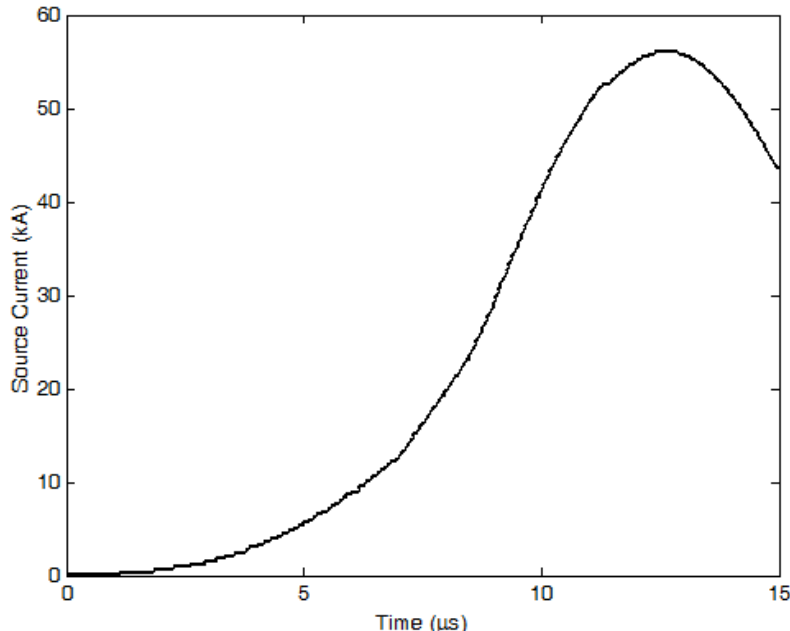


Figure 106. Simulated revised FCG current into 1 uH

6.2.2 Magnetic Switches

One of the critical elements that enable the current of an FCG simulator to be unique from that of a simple capacitive discharge is the decreasing circuit inductance in time.

Magnetic switches have consistently been implemented in FCG simulators for this purpose [3, 7]. Magnetic switches have been a unique option for transient switching since first being described in 1951 [8]. Magnetic switches have found widespread application for laser drivers and accelerators in magnetic pulse compression circuits [9-11]. The magnetic switches of the FCG simulator enable the sequential switching of the fixed parallel inductors, L_1 - L_4 of Figure 105, into the circuit, resulting in a decreasing circuit inductance in time. A simple magnetic switch can be formed by winding a conductor around a magnetic core. Current through the winding creates a magnetic field, which is coupled in the magnetic core. As the magnetic field, H [A/m], is increased, the magnetic flux density, B [T], increases in response [12]. The magnetic field and the magnetic flux density are related by the permeability of the magnetic material, μ [H/m]. The permeability is the product of the permeability of free space, μ_0 [H/m], and the relative permeability of the material, μ_r . Equation (6.1) shows the relation between the magnetic flux density, magnetic field, and permeability [13].

$$B = \mu_0 \mu_r H \quad (6.1)$$

A plot of the magnetic flux density versus the magnetic field is known as a hysteresis loop [13]. The hysteresis loop of a ferromagnetic material is directly analogous to the hysteresis loop previously discussed for ferroelectric materials. A hysteresis loop for a ferromagnetic material can demonstrate saturation of the ferromagnetic material. When the absolute value of the magnetic field in the material is less than the saturation value, H_{sat} [A/m], the magnetic field and magnetic flux density have approximately a linear relation. When below H_{sat} , a small change in the magnetic field results in a large change in the magnetic flux density. This response corresponds to a relative permeability with a

high value when the magnetic core is in an unsaturated state. When the absolute value of the magnetic field is greater than a saturation value, H_{sat} [A/m], the relative permeability approaches 1, and relatively large changes in the magnetic field produce relatively small changes in the magnetic flux density. This response corresponds to the saturated state of the magnetic core. Magnetic switches leverage the difference between the unsaturated and saturated states of the magnetic core to change the impedance of a winding coupled to the core material.

A winding around a magnetic core has an inductive impedance directly proportional to the relative permeability of the magnetic material. The equation for solenoid inductance, L [H], is given as equation (6.2) [14]. The symbol N represents the number of turns. The symbol A [m^2] is the cross-sectional area of the magnetic core, and the length of the solenoid is given as l [m].

$$L = \frac{\mu_0 \mu_r N^2 A}{l} \quad (6.2)$$

When the core is unsaturated, the relative permeability is relatively high, and the inductance of the solenoid is proportionally high. The high impedance of the winding results in a very slow rate of current rise. If a lower impedance parallel current path is present, the current path through the winding can approximately be considered to be open. When the core is saturated, the relative permeability is substantially decreased from the unsaturated value. The inductance is decreased by order of magnitude. The corresponding inductive impedance to current in the winding is proportionally decreased by orders of magnitude, and the current path through the winding can no longer be considered open. This is the closed state of the magnetic switch. Through this change in inductive impedance, the magnetic switch operates as a closing switch [15].

The design of the magnetic switches in the FCG simulator is primarily dependent upon the change in flux density in the magnetic core. The change in flux density, ΔB [Wb/m²], due to a single winding turn is equivalent to the integral of the applied voltage per unit area. Expressing this relationship mathematically, the required area of the core can be determined based upon the maximum change in flux density, the number of turns, and the integral of the applied voltage [10].

$$A = \frac{1}{\Delta BN} \int_0^{t_{sat}} V(t) dt \quad (6.3)$$

The voltage across the inductance is V [V], and the symbol t_{sat} [s] is the time of core saturation. The number of turns on the core is N , and the area of the core is represented as A [m²]. Due to the high voltage applied at the beginning of FCG simulator operation, the cores require a large area and high change in magnetic flux density to remain unsaturated for a time on the order of microseconds. The number of turns could also be increased. However, to minimize the saturated inductance of the winding, the number of turns was minimized. Each of the three magnetic switches was formed from stacks of identical magnetic cores to increase the cross-sectional area. Magnetic switches L_{S1} and L_{S3} were both constructed with two Metglas AMCC1000 cores [14]. Magnetic switch L_{S2} was formed with three square orthonol cores. The parameters of the three saturating magnetic cores are given in Table 22.

Table 22. Magnetic Core Parameters

Switch	N	Area A (m ²)	ΔB (T)	Volt-second product (mVs)
L_{S1}	4	0.0023	3	27.6
L_{S2}	2	0.002044	3	12.3
L_{S3}	2	0.0069	3	41.4

After operation of the FCG simulator, the cores of the magnetic switches will relax to a state such that the maximum ΔB to saturation with the next applied voltage is substantially reduced. Therefore, the cores must be reset, or saturated by a magnetic field with the opposite polarity, to enable the large change in flux density desired in operation of the magnetic switch [16]. The minimum reset current, I_{reset} [A], can be produced in the magnetic switch winding in the opposite direction as the FCG simulator current, or a separate winding can be added to the magnetic switch. The reset current is determined by the number of reset windings, N_r , the magnetic path length of the core, l_m [m], and the saturation magnetic field, H_{sat} [A/m], as shown in equation (6.4) [16].

$$I_{reset} \geq \frac{l_m H_{sat}}{N_r} \quad (6.4)$$

The parameters l_m and H_{sat} are dependent upon the magnetic cores. Since the FCG simulator is not repetitively operated, the number of windings and reset current supply were not critical design factors. A 25 A DC current supply was used as the reset current source.

6.2.3 High Power Antenna Driver Construction

Figure 107 shows the constructed CLC-driven FCG simulator. A second view in Figure 108 shows the three levels of components. This structure was designed to allow the system to fit inside an RF-shielded room while leaving half of the top level open for the remaining high power antenna driver components. The capacitor banks on the bottom level were each composed of 3 2.2 μ F capacitors rated at 100 kV. The second level of the FCG simulator included the main spark gap switch for the CLC circuit, the inductor of the CLC circuit, the low resistance energy dump, and assorted charging and triggering components. The main switch for the system was a T-670 pancake spark gap pressurized

with dry air. The inductor was constructed as an air-core solenoid. The low resistance energy dump included to safely dissipate energy left in the CLC circuit after system operation was implemented as five paralleled $1.25\ \Omega$ resistors. The top level of components consisted of the network of inductors and magnetic switches. The inductors were constructed as air-core solenoids of copper tubing.



Figure 107. CLC-driven FCG simulator during evaluation prior to incorporation into the high power antenna driver

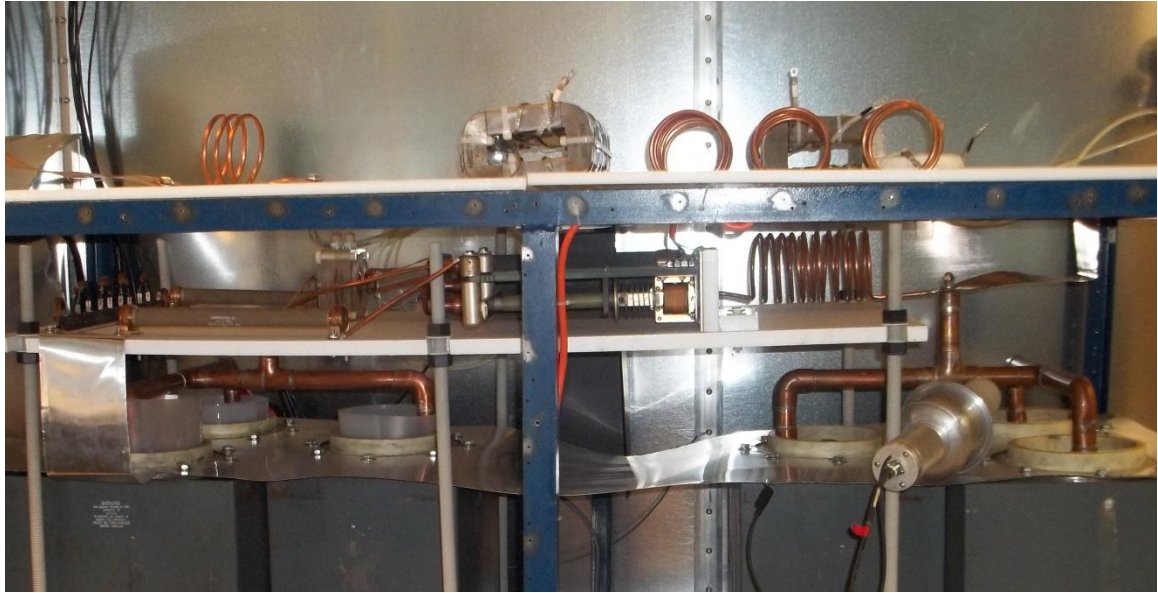


Figure 108. Three levels of components in the CLC-driven FCG simulator

6.3 IES, EEOS, and High Power Oscillator

6.3.1 Inductive Energy Store

An inductive component in series with the output of the FCG simulator is required to magnetically store the energy from the source over its relatively long operating time. Both solenoid inductors and pulse transformers have been used as the inductive energy store in similar systems [3, 17]. A pulse transformer has the advantages of a voltage step up from primary to secondary and electrical isolation of the primary and secondary circuits. An inductor has potential advantages over a pulse transformer in a simpler design and more compact packaging. Previous work by the author has demonstrated the successful integration of a compact spiral-strip pulse transformer in a similar system [3]. In the experiments described in this work, simple non-magnetic-cored solenoids were implemented for simple replacement when changing the inductance of the inductive energy store. The solenoids were immersed in oil to withstand the very high voltages present across the windings when the current is interrupted.

6.3.2 Electroexplosive Opening Switch

A required component in inductive energy storage systems is an opening switch. The opening switch serves to redirect the current from the low impedance path through it while storing the energy inductively to the higher impedance path of the load to the inductive energy storage system. A wide variety of opening switches have been developed for specific conditions. For the high power antenna driver, which requires high currents of tens of kiloamps to be conducted for several microseconds before the current is interrupted in a period of less than one microsecond, the best available opening switch is the electroexplosive opening switch (EEOS) [18]. An EEOS can take the form of an exploding wire fuse or an exploding foil.

An EEOS transitions from a closed to open state through a fast increase of the resistance of its conducting element, either wires or a foil, as the element vaporizes. While the initial cold resistance of the EEOS is often on the order of milliohms, the resistance as the metal vaporizes can rise to several ohms or higher, depending on the dimensions of the EEOS. If enough energy is dissipated in the EEOS after the onset of vaporization, a combination of factors, including expansion of the EEOS conducting material, the electric field across the EEOS, and ionization of the vaporized material can cause the resistance of the EEOS to drop significantly. This drop in EEOS resistivity is commonly termed restrike. In nearly all previously-developed inductive energy storage systems developed, it has been desirable to avoid restrike throughout the system's operation as restrike in those systems represented a failure of the opening function of the switch.

Although restrike causes an EEOS to no longer function as an opening switch, it was noted in a publication on a previous iteration of this type of antenna driver that by the time restrike occurred, the inductive energy storage system had already driven the high power oscillator [19]. The occurrence of restrike did not degrade the operation of that system, but restrike did occur due to inefficiencies in the system. While it was previously noted that these inefficiencies could be eliminated by either driving the system with a lower energy source or driving the load to a higher voltage, a previously-unmentioned third option of driving the load multiple times forms the basis of the approach taken in this system [19].

The time at which an EEOS begins to vaporize is determined using the integral of current action through the EEOS, and the integral of current action at which the EEOS vaporizes can be modified by changing the cross-sectional area of the EEOS conducting medium. Equation (6.5) shows the determination of the integral of current action, h [A^2s], where t_0 [s] is the time at which current begins flowing through the EEOS.

$$h(t) = \int_{t_0}^t i^2(t)dt \quad (6.5)$$

The action limit, h_e [A^2s], is determined by applying equation (6.5) with the limits of the integral from the beginning of current flow to the time at which the EEOS begins to vaporize and its resistance dramatically increases. The cross-sectional area of the EEOS, A [m^2], can be related to the integral of current action at the time at which the EEOS begins to vaporize through equation (6.6) [3]. The symbol α_l [$\text{m}^2/(\text{A}\cdot\text{s}^{0.5})$] is a factor dependent on the materials used and experimental conditions, including the current density and rate of energy dissipation [20]. Values of α_l have been experimentally determined for specific materials [20].

$$A = \alpha_l \sqrt{h_e} \quad (6.6)$$

Figure 109 shows the electroexplosive opening switch, which was implemented as an exploding wire fuse. The switch consists of two sections approximately 12.7 cm each. The fusing element was composed of 40 gauge silver-plated copper wire. The typical number of wires ranged from 15 to 30, depending on the desired action integral at which the fuse was intended to open. The entire assembly was packed in fine glass beads with a rated mesh size of 170-325 to act as a quenching material. Additional details about the exploding wire fuse and analysis of electroexplosive opening switches has been previously published by the author [3, 21, 22].

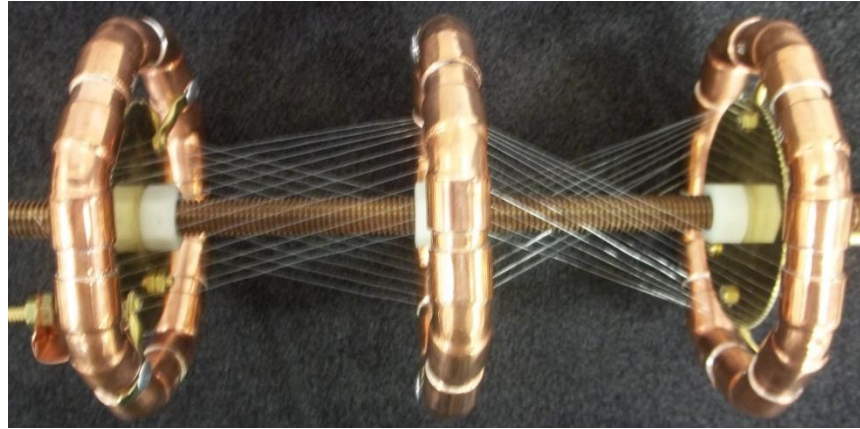


Figure 109. Two-section exploding wire fuse

6.3.3 High Power Oscillator

In the previous version of a high power oscillator driven by an FCG and inductive energy storage system, a high voltage capacitor was charged as the EEOS vaporized until a self-breaking switch closed to form an underdamped oscillator with a low inductance shunt [3, 19]. The operation of the oscillator in this work is similar, but the capacitive element is formed from two high voltage coaxial sections. Both the capacitance and transit time of the transmission line are important to the operation of the oscillator. The

primary function of the element is to serve as the capacitive component of the oscillator. However, due to the low inductance of the circuit when the capacitance is shorted, the transmission line effects of the capacitor cannot be ignored. The reflections from the terminals of the capacitive transmission line can benefit the system by enabling a broader and higher range of frequencies to be applied to the high power antenna. While the two transmission line sections are identical, reflections between the sections are enhanced by feeding the antenna impedance at the junction of the transmission line sections. The microstrip feed of the antenna also acts as a transmission line, introducing additional reflections. The multiple reflections between these short transmission lines cause the frequency content of the signal at the antenna input to spread to much higher frequencies than a simple resonator formed by a capacitance ringing into the inductance of a closing switch.

As shown in Figure 110, the high voltage capacitive transmission lines were constructed from coaxial cylinders of copper. The impedances of the lines were kept low to increase capacitive energy storage while ensuring that they can withstand pulsed voltages on the order of hundreds of kilovolts. The transmission lines are insulated in oil to increase their breakdown strength. The plastic insulators shown in Figure 110 provided mechanical stability to the positioning of the inner cylinders within the grounded outer cylinders. A subsequent modification extended the plastic supports out from the sides of the structure to remove the plastic rods from the high electric field region. This modification prevented surface tracking along the plastic rods.

The outer diameter of the inner copper pipes of the coaxial structures was approximately 19.05 mm, and the inner diameter of the outer copper pipes of the coaxial

structures was approximately 50.8 mm. Since the dielectric constant of the insulating oil was approximately 2.2, the impedance of each coaxial line was approximately 40Ω , and the parallel arrangement of two coaxial lines to form each transmission line produced an impedance of approximately 20Ω . Using a wave velocity in oil of approximately 2.01×10^8 m/s, the electrical length of each transmission line was approximately 0.4 ns.

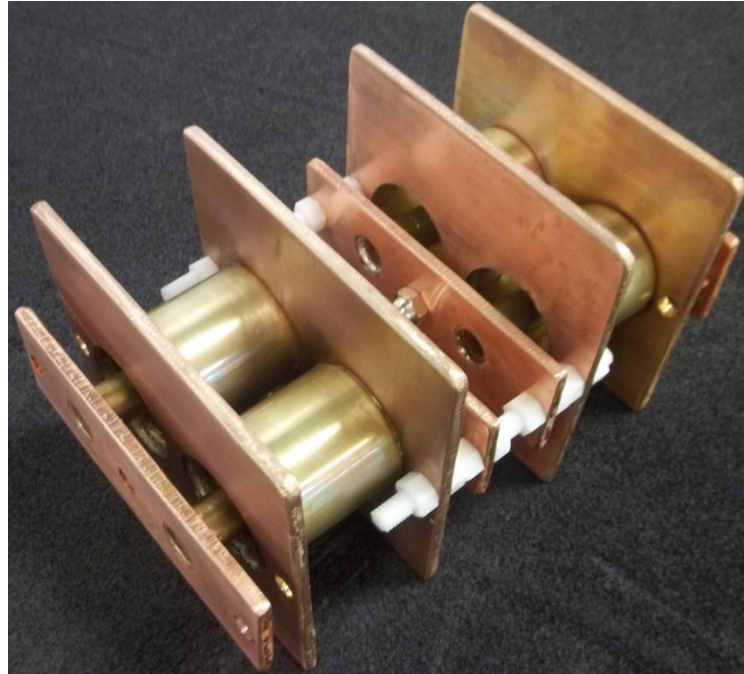


Figure 110. High power oscillator

6.3.4 Diagnostics

The current of the FCG simulator through the inductive energy storage element was measured with a Pearson 301X current monitor. The large core area of the 301X prevents saturation of the monitor during the relatively long current pulse from the FCG simulator. The current-time product of the 301X is 22 A·s, and the peak current capability is 50 kA [23]. The usable pulse risetime is 200 ns [23].

Voltage diagnostics on the high power oscillator presented a significant challenge due to the high voltage and high frequency conditions during the RF burst. The conditions for

measurement of the RF burst were contrasted by the relatively slow change in voltage during charging of the high power oscillator. Since the peak voltage on the high power oscillator can exceed 100 kV and the frequencies in the voltage signal extended well above 80 MHz, commercial high voltage probes based on compensated resistive dividers, such as the PVM-6, were incapable of meeting the measurement requirements. Thus, custom D-dot probes were added to the high voltage oscillator to monitor the voltage along the coax sections near the feed to the antenna. The D-dot probes were fabricated by drilling holes into the outer ground cylinder of each high voltage transmission line section. The flanged connectors for coaxial cables were mounted on the holes with the open faces of the modified connectors pointed towards the inner cylinder of the high voltage transmission lines. The signal of the D-dot probes was proportional to the derivative of the voltage on the transmission lines. The D-dot probes were calibrated by applying a fast-rising pulse to the high voltage transmission lines with a Tektronix Type 109 Pulse Generator with a risetime rated at less than 0.25 ns. Figure 111 shows an example of the signal obtained with the custom D-dot probe, and Figure 112 shows the pulse obtained by integrating the signal of Figure 111 and scaling the amplitude to match the directly measured from the Type 109 Pulse Generator. The large scaling factor on the order of 5.3×10^{11} and the use of attenuators were necessary to be able to measure the large voltage derivative, which is on the order of 10s of TV/s. However, this scaling provided a relative lack of sensitivity for the comparatively low voltage derivative during pulse charging of the high voltage oscillator.

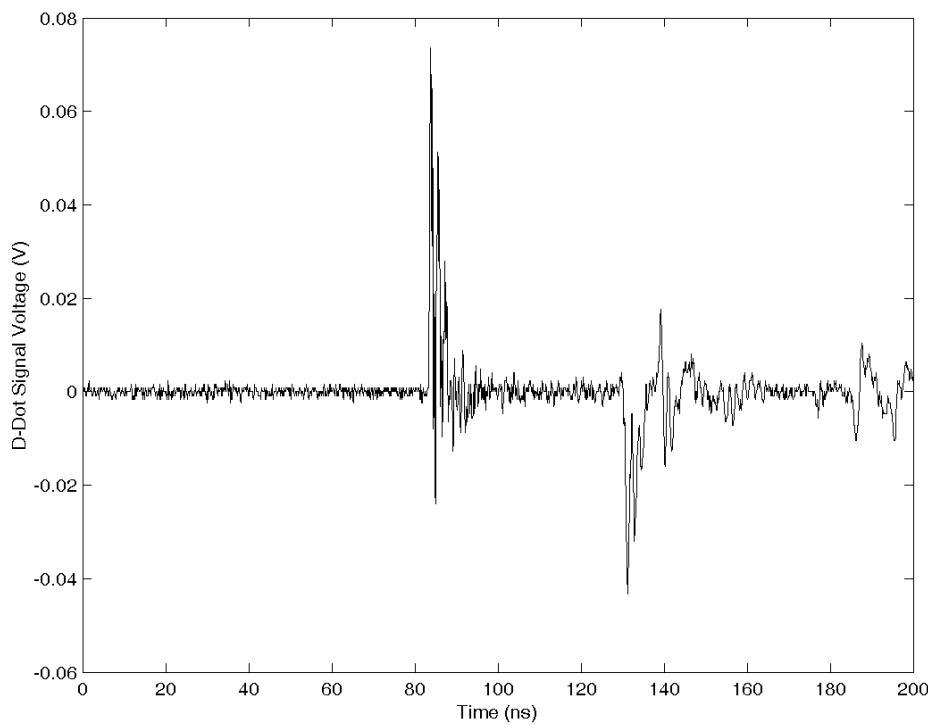


Figure 111. Example of the D-Dot signal voltage for calibration on a high voltage transmission line section of the high power oscillator

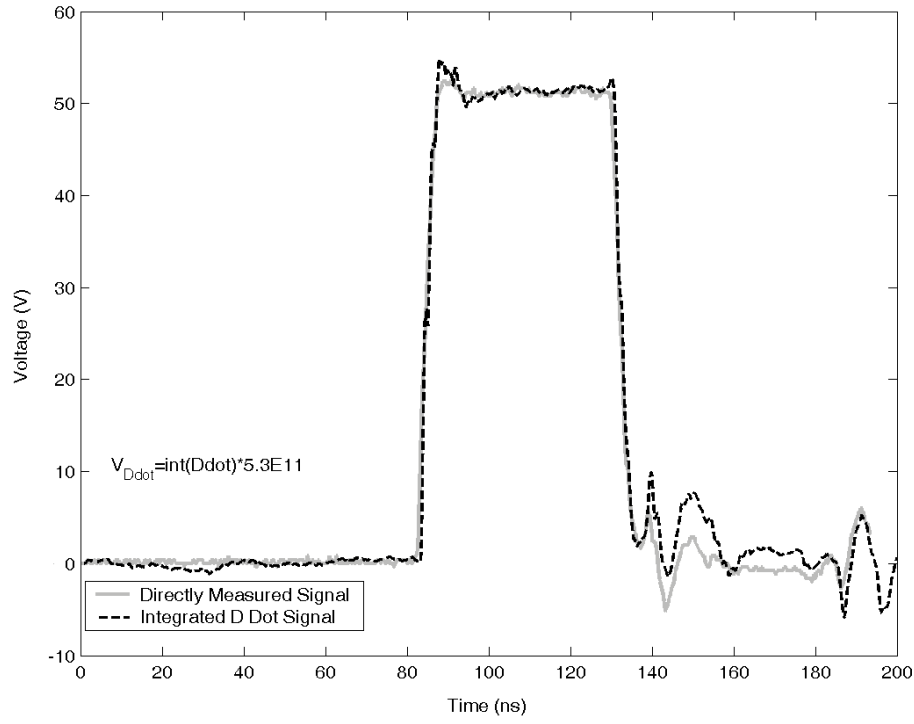


Figure 112. Integrated calibration signal for D-dot probe on a high voltage transmission line section of the high power oscillator

Due to the high power radiated fields anticipated from this system, it was contained in an RF-shielded chamber to protect sensitive equipment in the laboratory. Due to the dimensions of the chamber and the lack of adequate anechoic material to limit internal field reflections, it was not possible to evaluate the antenna's performance during these initial tests of the high power antenna driver. However, the fields produced by the high power DRA and the test stand driving it were monitored to measure the peak field strength and frequency content of the fields within the chamber. These measurements were made with a NanoFast 709-2B E-field monitor and a Fischer Custom Communications F301 H-field monitor. The E-field monitor was rated at 10 kV/m and featured an integrated optical signal transmission system. The use of a fiber optic signal carrier rather than a coaxial cable eliminates the disturbance of the E-field due to coaxial cables and ground loop effects in the signal. The NanoFast E-field monitor was placed approximately 1.5 m above the DRA, and the F301 H-field monitor was placed in the near field of the antenna.

6.4 High Power Antenna Driver Simulations

Simulations were run on an inductive storage system, repetitively-opening switch, and transmission line-based high voltage capacitor. An initial current of 40 kA was assigned to an inductive energy storage inductance of 2 μ H. Referencing Figure 104, both transmission lines were defined to have characteristic impedances of 100 Ω and transit times of 0.5 ns. The switch representing the exploding wire fuse was defined to increase from 400 m Ω to 10 Ω in 300 ns. A series resistance, R in Figure 104, was defined to be 700 Ω . The high power DRA was represented as a lossy transmission line with one end terminated into a high impedance simulating the open end of the microstrip. A switch

performing the function of the switch S in Figure 104 was set to short the high power oscillator into a shunt inductance of 10 nH at 300 ns into the simulation.

Figure 113 displays the simulated voltage waveform at the antenna. The transmission lines representing the high power oscillator and the microstrip of the high power DRA were charged to approximately 250 kV in the 300 ns opening time of the simulated opening switch. Upon shorting the high power oscillator, the first negative voltage peak occurs at nearly -200 kV. The primary oscillations in the signal are quickly damped by the lossy transmission line representing the high power DRA. Figure 114 shows a detailed view of the high frequency content superimposed on the larger voltage oscillations as a result of reflections along the short transmission lines.

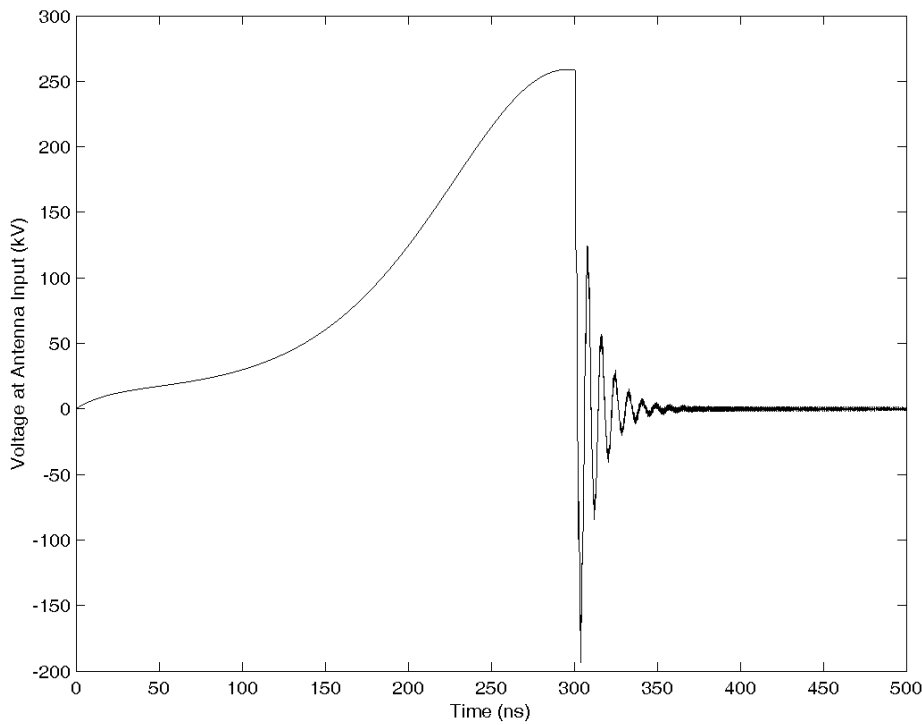


Figure 113. Full view of simulated voltage at antenna input from high voltage oscillator

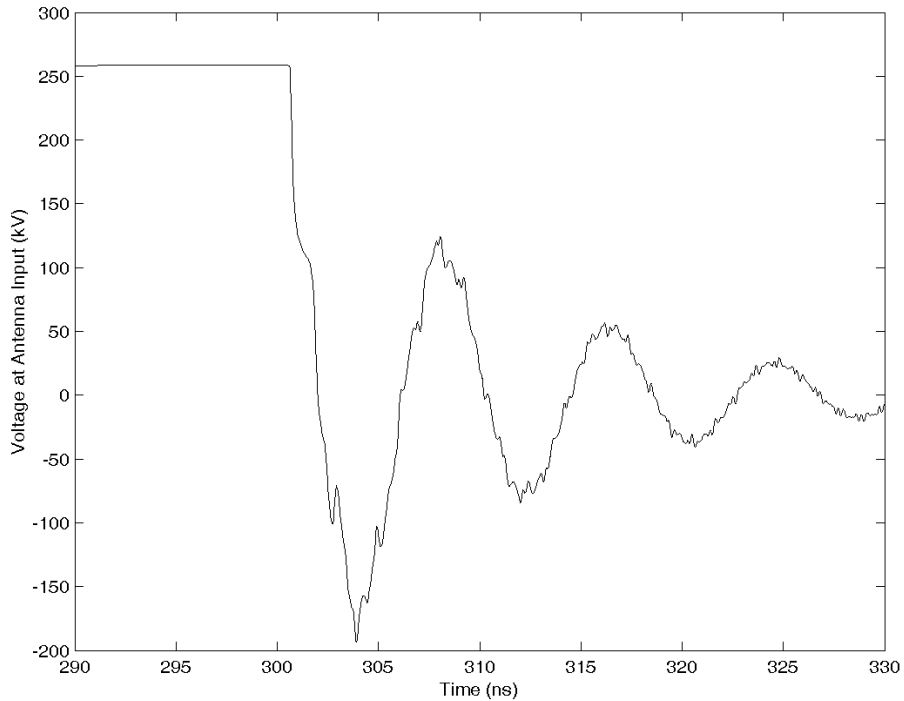


Figure 114. Detailed view of high frequency content in the simulated voltage signal at the antenna input

Figure 115 shows the derivative of the voltage signal of Figure 114. The magnitude of the derivative is on the order of 100s of TV/s. The derivative of the voltage on the high voltage oscillator is monitored in the experiments with the D-dot probe.

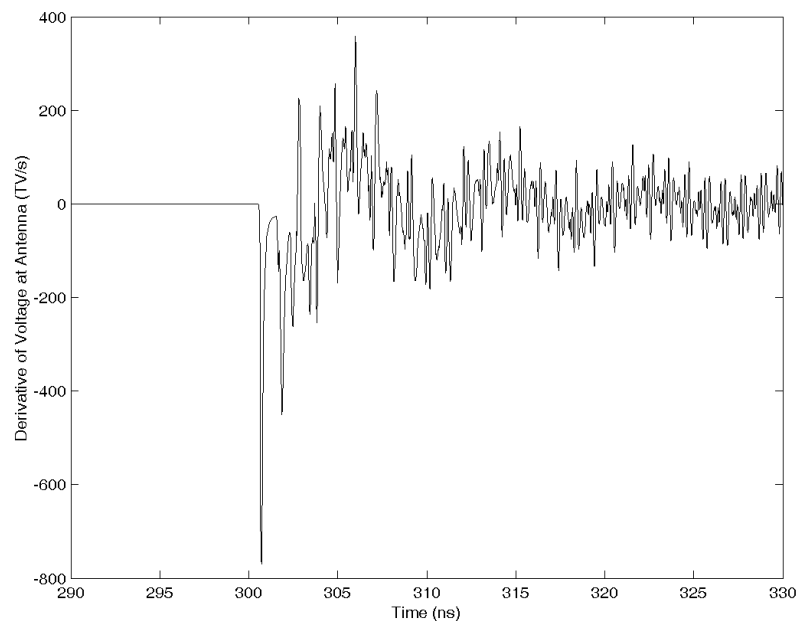


Figure 115. Detailed view of the derivative of the simulated voltage at the input to the antenna

The radiated electric field from the high power antenna is anticipated to be proportional to the derivative of the voltage driving the antenna. Therefore, the frequency content of the derivative of the voltage signal is of interest. Figure 116 shows the fast Fourier transform (FFT) of the derivative of the voltage signal shown in Figure 115. The FFT shows a wide spectrum of frequencies with adequate frequency content between 600 MHz and 1.2 GHz where the DRA exhibits good gain.

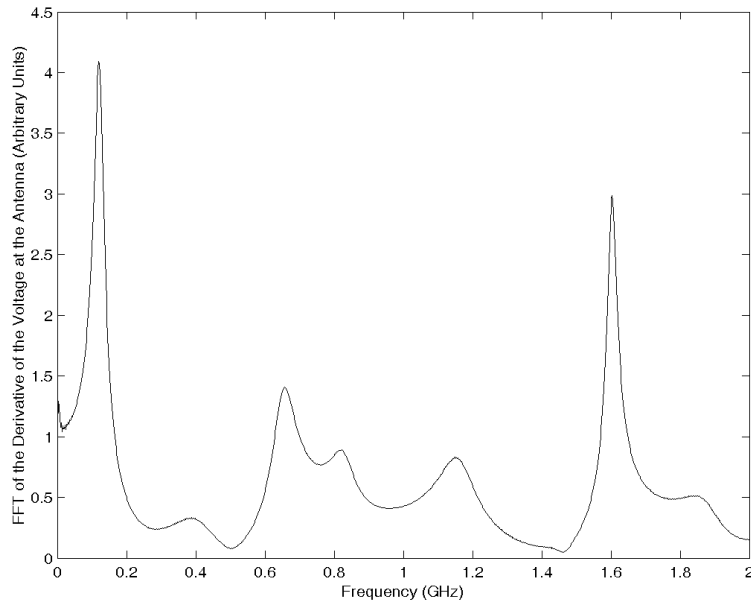


Figure 116. FFT of the derivative of the simulated voltage at the antenna input

6.5 High Power Antenna Driver Results

Figure 117 shows the complete high power antenna driver. The high power oscillator and DRA are located in the oil tank at the back of the test stand. In addition to the network of inductors and magnetic switches on the top level of the test stand, the exploding wire fuse can be seen in a transparent container packed with white glass beads. The NanoFast electric field sensor is positioned above the location of the high power DRA. Anechoic material was placed on both sides of the oil tank in an attempt to limit

the reflected signals observed by the RF sensors and to dissipate some of the energy radiated by the antenna and test stand.



Figure 117. Fully-integrated high power antenna driver in RF-shielded chamber

6.5.1 CLC-Driven FCG Simulator

Prior to testing the fully integrated high power antenna driver, the operation of the CLC-driven FCG simulator was evaluated. The exploding wire fuse, high power oscillator, and DRA were not included in these initial tests. The load of the FCG simulator was a $1 \mu\text{H}$ air-core inductor. The charging voltage of capacitor bank C_1 in this experiment was 35 kV. Figure 118 shows the output current signal into the $1 \mu\text{H}$ load. The slope of the current rise exhibits the desired concave up shape through the first several microseconds before gradually leveling off. The peak current reached 40.8 kA at approximately 14 μs into the waveform. To quantify the analysis of the rate of current

rise, a waveform was generated to fit the curve in Matlab. The curve-fit waveform is shown as the dashed line in Figure 118.

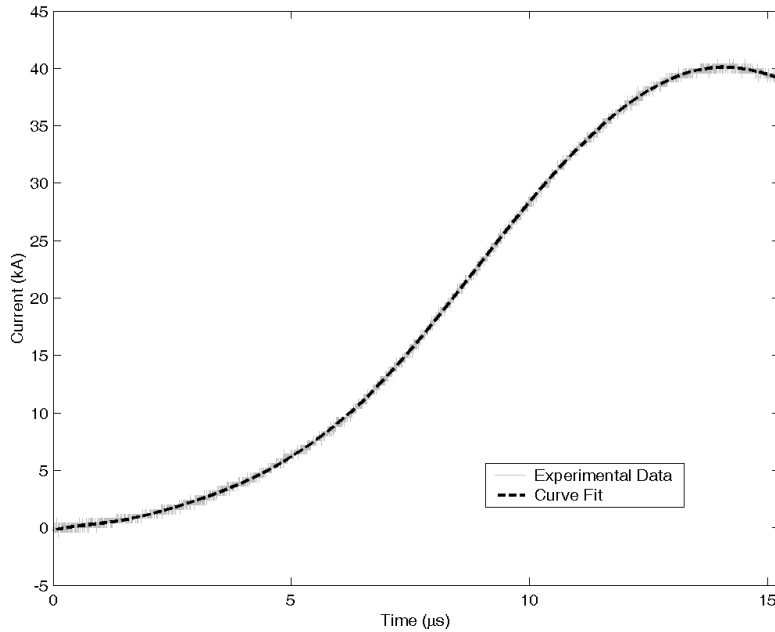


Figure 118. Output current of the CLC-driven FCG simulator into an inductive load

The derivative of the curve-fit waveform of the FCG current is shown in Figure 119. The derivative reaches a maximum of approximately $5.3 \text{ kA}/\mu\text{s}$ at $8.86 \mu\text{s}$ into the signal. The decrease of the first derivative of the current signal in the first microsecond of the simulation is believed to be an artifact of the inaccuracy of the curve fit to the waveform at time close to $t = 0$. It is believed that the actual first derivative is positive throughout the time of interest in the first $10 \mu\text{s}$ of operation.

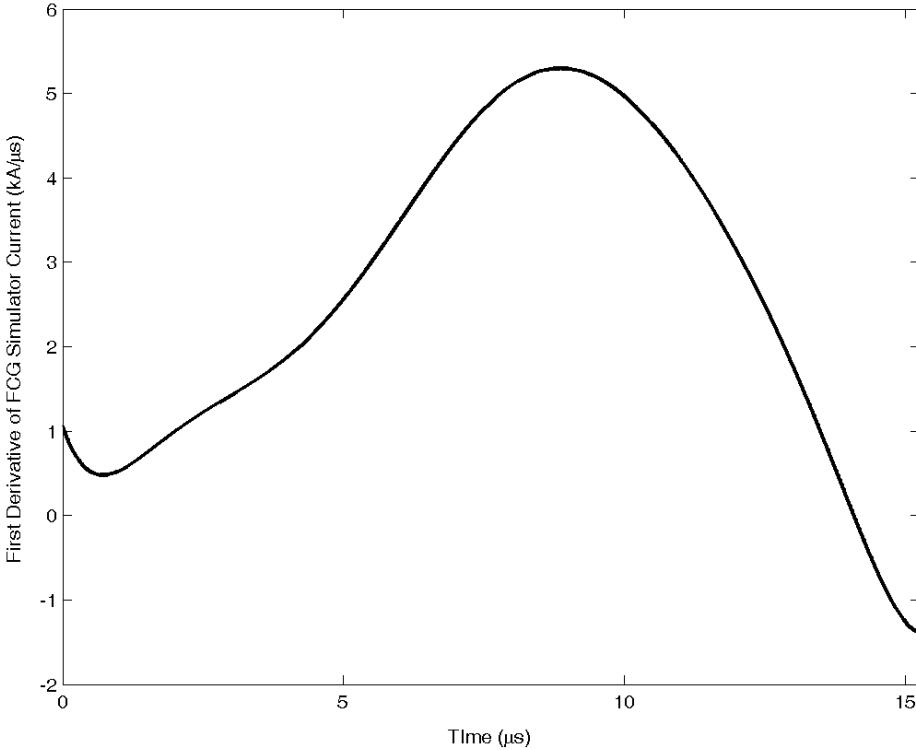


Figure 119. First derivative of the CLC-drive FCG current

Figure 120 shows the second derivative of the current waveform. The second derivative is positive between $0.716 \mu\text{s}$ and $8.86 \mu\text{s}$, causing the concave up shape of the current waveform during this time period. Similar to the exception noted for the first derivative, it is believed that the second derivative is negative for $0 \leq t \leq 0.78 \mu\text{s}$ due to inaccuracy of the curve fit to the simulated waveform near $t = 0$. The peak of the second derivative was at $0.98 \text{ kA}/(\mu\text{s})^2$, occurring approximately $6.08 \mu\text{s}$ into the signal. Achieving a positive second derivative to the current waveform is a significant factor in replicating the current output of an FCG. The second derivative of previous FCG simulators driven by a PFN or a capacitor bank is positive only at the times when the magnetic switches saturate. By shaping the current waveform to have a positive second derivative during nearly the entire first $8.86 \mu\text{s}$ of operation, the output of a CLC-driven FCG simulator more closely matches the quasi-exponential output of an FCG.

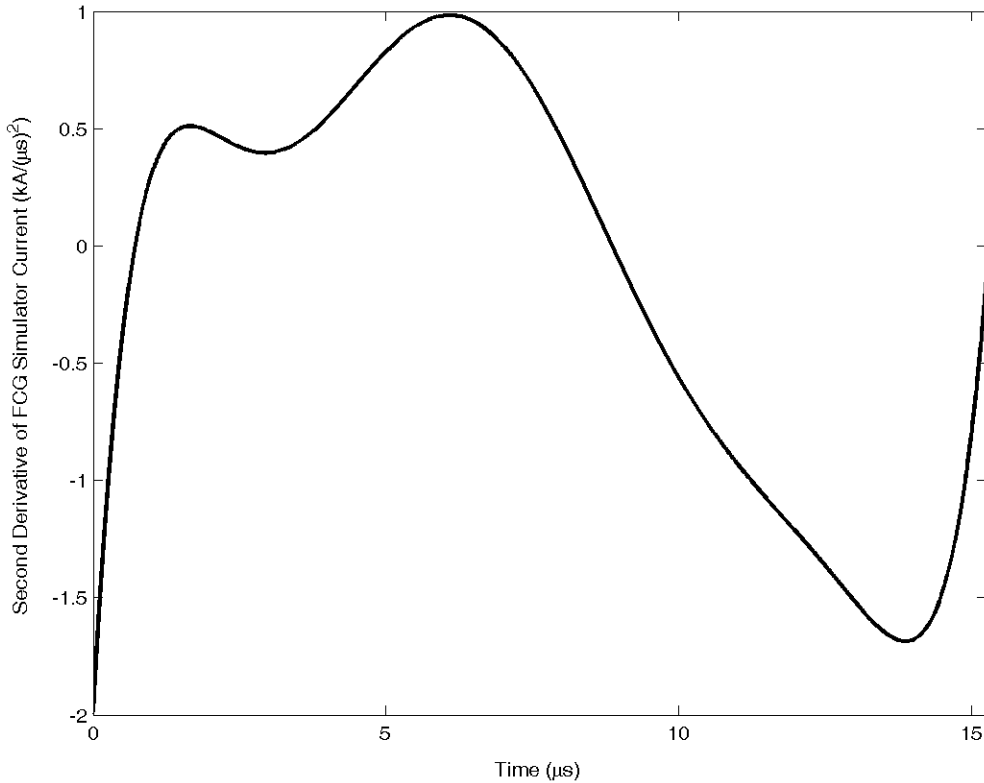


Figure 120. Second derivative of the CLC-driven FCG simulator current

6.5.2 Complete High Power Antenna Driver

Preliminary testing was completed on the fully integrated high power antenna driver with the high power DRA. While testing in the RF-shielded enclosure did not allow the high power characteristics of the antenna to be evaluated, these tests provided information on the feasibility of using the system to conduct high power antenna testing. The results of these tests provide a path forward for full power antenna characterization in either an anechoic chamber or outdoor range. These tests also provided a means to demonstrate the high voltage holdoff of the DRA.

In the experiment reported here, the capacitor bank C_1 was charged to approximately 40 kV. The exploding wire fuse consisted of 34 40-gauge wires. Figure 121 displays the FCG simulator current output into the inductive energy storage element and electroexplosive opening switch. The concave up shape of the current waveform is

evident for the first several microseconds even with the added resistive load of the opening switch. The FCG simulator current reached a peak of nearly 32.8 kA after a risetime of approximately 13.25 μ s. As the current was interrupted due to the rapid increase in the resistance of the electroexplosive opening switch, the RF signal present within the shielded enclosure from operation of the high power oscillator is believed to have coupled to the current monitor and/or signal cable, resulting in the brief burst of noise present in the current waveform. The current was reduced to below 25 kA in less than 300 ns before the onset of the RF noise indicating the operation of the high power oscillator.

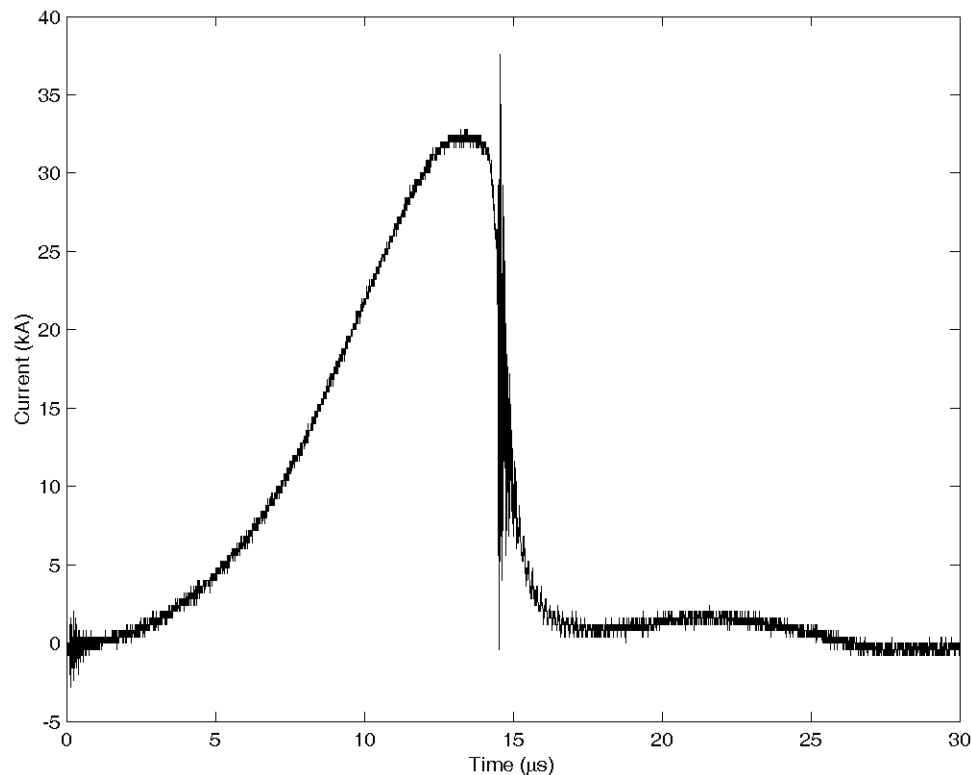


Figure 121. Current output of the FCG simulator into the inductive load and electroexplosive opening switch

Figure 122 shows the voltage signal calculated by integrating the D-dot signal from the high power oscillator near the feed point to the DRA. The discrepancy between the timing of the decrease of the current in Figure 121 and the increase in the voltage on the

high power oscillator in Figure 122 is due to the signals being measured on different oscilloscopes, and it should be noted that these events happen concurrently. Due to the lack of sensitivity of the D-dot probe to the relatively small dV/dt during early stages of the system's operation, the peak charging voltage reached on the high power oscillator and antenna are not definitively known. The voltage displayed in Figure 122 was obtained by normalizing the mid-point of the initial oscillations to zero volts. This is considered a reasonable assumption since the voltage should oscillate with respect to ground after the high power oscillator is shorted. The peak-to-peak voltage from the maximum charge voltage to the maximum negative trough is approximately 70 kV. Figure 123 provides a detailed view of the first high power oscillations, showing the high frequency content of the signal.

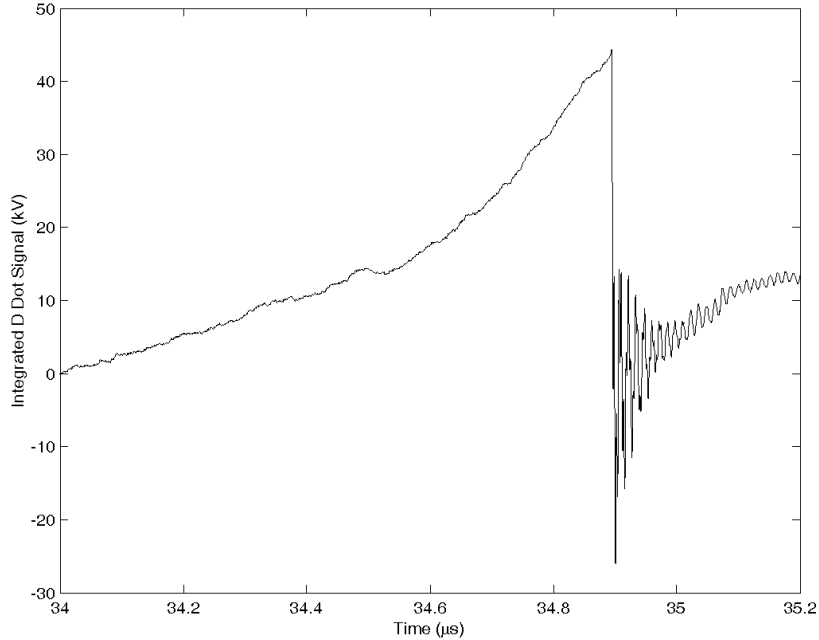


Figure 122. Integrated D-dot signal with high frequency oscillations normalized to zero volts

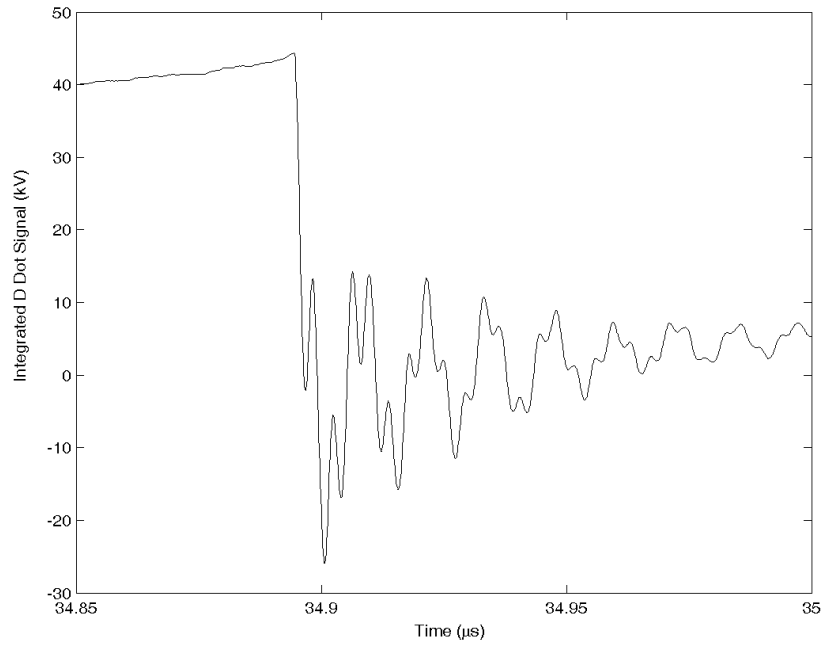


Figure 123. Detailed view of the first high power oscillations near the antenna feed

Figure 124 shows the FFT of the voltage signal of Figure 123. The highest frequency peak in the frequency content of the signal occurs at approximately 250 MHz.

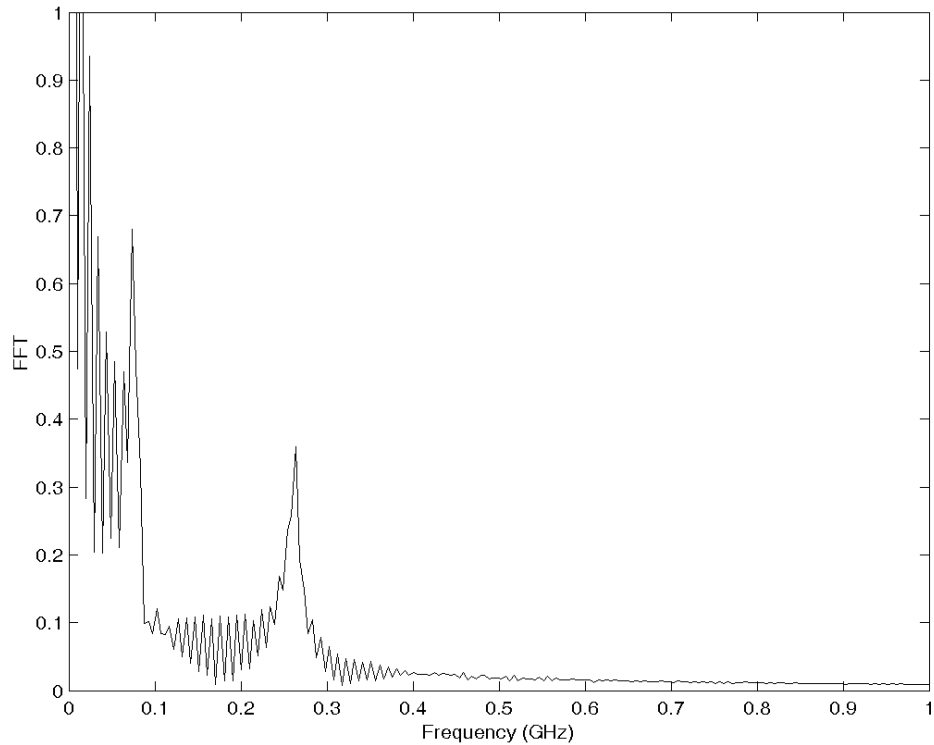


Figure 124. FFT of the voltage near the antenna feed

Figure 125 shows the scaled D-dot signal used to produce Figure 122 and Figure 123. The D-dot signal can be directly analyzed to determine the frequency content expected in the radiated field of an antenna that radiates the derivative of the applied voltage.

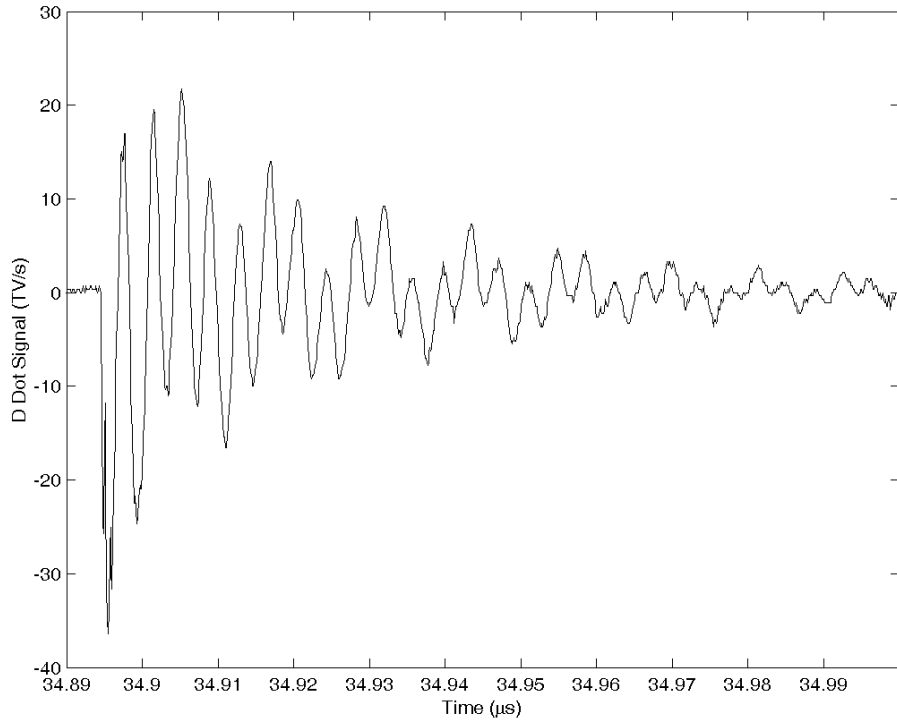


Figure 125. A plot of the D-dot signal on the high voltage oscillator near the antenna feed point

Figure 126 is a plot of the FFT of the D-dot signal of Figure 125. There is a substantial spread in the frequency content between 1 and 2 GHz. As expected, the highest signal content is below 500 MHz, corresponding to the high voltage oscillations of the shorted capacitance of the high power oscillator.

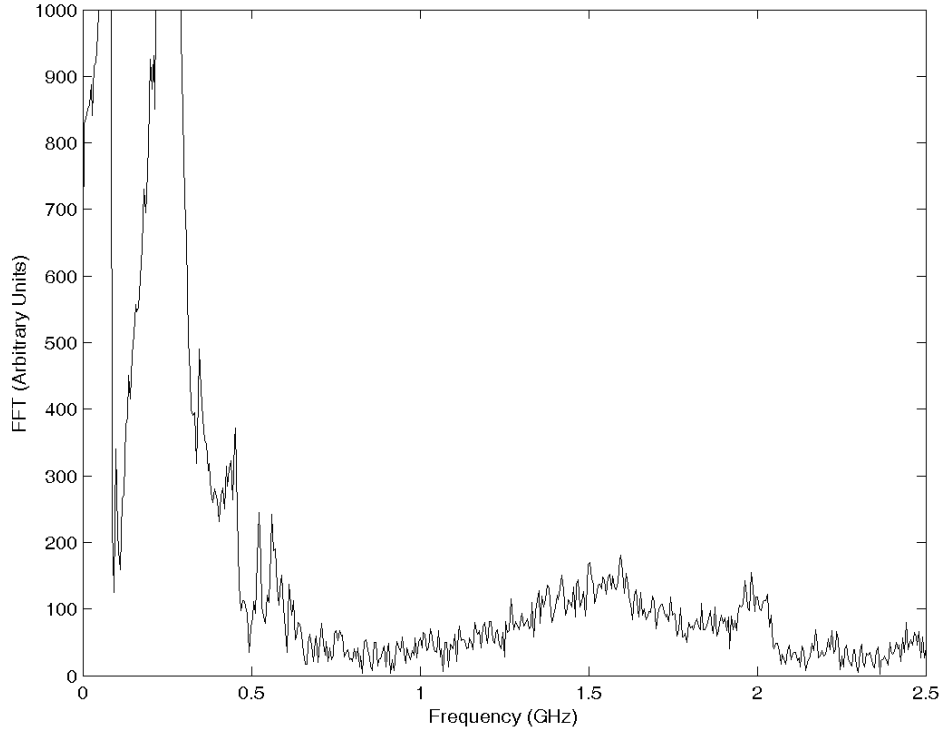


Figure 126. The FFT of the D-dot signal near antenna feed point

The results of this antenna driver testing indicate that the high power antenna driver based on a high voltage sinusoidal decay is best suited for use with antennas transmitting in the VHF band. This type of antenna driver could also potentially drive antennas that radiate the derivative of the applied voltage at lower peak power levels in the UHF band. Further investigation is needed on the time-domain behavior of the antennas to be tested at high power to select the appropriate type of antenna driver and tune the applied frequency to the degree possible. A path forward has been established to transition this high power antenna driver to enable antenna characterization in the anechoic chamber, as described in Section 7.3.

References for Chapter 6

- [1] M. J. Baretela and J. S. Tyo, "Selective trimming of impulse radiating antenna apertures to increase prompt radiated field," *Sensor and Simulation Notes*, pp. 1-27, Note 461, 2001.
- [2] J. R. Mayes, M. G. Mayes, W. C. Nunnally, and C. W. Hatfield, "Helical antennas for high powered RF," in *Proc. of the 2009 IEEE Int'l Pulsed Power Conference* Washington, D.C., 2009, pp. 484-488.
- [3] K. A. O'Connor, "Compact Power Conditioning and RF Systems for a High Power RF Source," M.S. Thesis, Elec. and Comp. Engr., University of Missouri-Columbia, Columbia, MO, 2008.
- [4] L. L. Altgilbers, A. S. Stults, M. Kristiansen, A. Neuber, J. Dickens, A. Young, T. Holt, M. Elsayed, R. Curry, K. O'Connor, J. Baird, S. Shkuratov, B. Freeman, D. Hemmert, F. Rose, Z. Shotts, Z. Roberts, W. Hackenberger, E. Alberta, M. Rader, and A. Dougherty, "Recent advances in explosive pulsed power," *Journal of Directed Energy*, vol. 3, 2009.
- [5] D. Belt, "Non-explosive test bed for flux compression generator fuses," M.S. Thesis, Elec. and Comp. Engr., Texas Tech University, Lubbock, TX, 2006.
- [6] K. A. O'Connor, R. D. Curry, and L. Altgilbers, "Investigation of a high voltage, high frequency power conditioning system for use with flux compression generators," in *Proc. 16th IEEE International Pulsed Power Conference and 34th IEEE International Plasma Science Conf.* vol. 2, E. Schamiloglu and F. Peterkin, Eds. Albuquerque, NM, 2007, pp. 1356-1359.
- [7] D. Belt, J. Mankowski, A. Neuber, J. Dickens, and M. Kristiansen, "Design and implementation of a flux compression generator nonexplosive test bed for electroexplosive fuses," *Review of Scientific Instruments*, vol. 77, pp. 094702-1 - 094702-7, 2006.
- [8] W. S. Melville, "The use of saturable reactors as discharge devices for pulse generators," *IEE Proceedings (London), Part 3: Radio and Communication*, vol. 98, pp. 185-207, 1951.
- [9] H. C. Kirbie, M. A. Newton, and P. D. Siemens, in *International Magnetic Pulse Compression Workshop*. vol. 2, 1991, p. 341.
- [10] W. C. Nunnally, "Stripline magnetic modulators for lasers and accelerators," in *Proc. 3rd IEEE International Pulsed Power Conference* Albuquerque, NM, 1981, pp. 210-213.
- [11] D. Birx, E. Cook, S. Hawkins, S. Poor, L. Reginato, J. Schmidt, and M. W. Smith, "Magnetic switching, final chapter book I: the ATA upgrade prototype," Lawrence Livermore National Laboratory, Livermore, CA 1983.
- [12] D. J. Craik and R. S. Tebble, *Ferromagnetism and Ferromagnetic Domains* vol. 4. New York, NY: John Wiley and Sons, Inc., 1965.
- [13] F. T. Ulaby, *Fundamentals of Applied Electromagnetics*. Upper Saddle River, NJ: Prentice Hall, 2001.
- [14] F. W. Grover, *Inductance Calculations, Working Formulas and Tables*. New York: D. Van Nostrand, 1946.
- [15] W. C. Nunnally, "Magnetic switches and circuits," in *Pulsed Power Lecture Series*: Texas Tech University, 1981.

- [16] D. M. Barrett, "Core reset considerations in magnetic pulse compression networks," in *Proc. of 10th IEEE International Pulsed Power Conference*. vol. 2, 1995, pp. 1160-1165.
- [17] M. Giesselmann, J. Zhang, T. Heeren, E. Kristiansen, J. Dickens, D. Castro, D. Garcia, and M. Kristiansen, "Pulse power conditioning with a transformer for an inductive energy storage system," in *Proc. 12th IEEE International Pulsed Power Conference* Monterey, CA, 1999.
- [18] K. H. Schoenbach, M. Kristiansen, and G. Schaefer, "A review of opening switch technology for inductive energy storage," *Proc. of the IEEE*, vol. 72, pp. 1019-1040, 1984.
- [19] K. A. O'Connor and R. D. Curry, "Experimental results of a high voltage wideband load driven by a pulse transformer and opening switch power conditioning system," in *Conf. Rec. of the 2008 28th IEEE International Power Modulator Symposium* Las Vegas, NV, 2008, pp. 185-188.
- [20] T. Heeren, "Power conditioning for high voltage pulse applications," Ph.D. Dissertation, Elec. and Comp. Engr., Texas Tech University, Lubbock, TX, 2003.
- [21] K. A. O'Connor and R. D. Curry, "The effects of length on electroexplosive opening switch resistance," *Journal of Applied Physics*, To be published, under review 2011.
- [22] K. A. O'Connor and R. D. Curry, "A method for numerically modeling a power-conditioning system with an electroexplosive opening switch," *IEEE Trans. on Plasma Science*, vol. 38, pp. 2520-2530, 2010.
- [23] "Pearson Current Monitor Model 301X," Pearson Electronics, Inc., Palo Alto, CA 1999.

Chapter 7: Summary and Future Work

7.1 Composite Development and Characterization

7.1.1 Summary

Three classes of high dielectric constant composite materials were developed through this work. One of the fundamental principles behind the development the high dielectric constant composites was that the volumetric content of the highest dielectric constant component materials should be maximized while maintaining robust mechanical properties. In all three composite classes, the volumetric content of ferroelectric ceramics was increased through a trimodal distribution of particle sizes designed to increase the ceramic particle packing density. While MU45 took a conventional approach to creating a high dielectric constant composite by incorporating a polar polymer with the ceramics, MU100 and MU550 were designed with innovative concepts to minimize the volume percentage of binder in the composite.

MU100 employed coupling agents, which are conventionally used only to functionalize the surfaces of the ceramic particles, as the sole binder for the composite. The coupling agents form a polysilsesquioxane binder through an in-situ polymerization process after the ceramic components of the composite have been pressed to their final density. The in-situ polymerization of a polysilsesquioxane minimizes any increase to the composite volume due to the addition of the binder while allowing the network formed by the polysilsesquioxane to fill the voids between particles. Since the polysilsesquioxane

directly bonds to the surfaces of the ceramic particles, the composite exhibits good mechanical strength with a relatively low amount of binder.

MU550 leveraged the unique properties of gelling, thermoreversible biopolymers as the binder material. Since the composite was pressed to a high density while the biopolymers were in a solution with a water solvent, excess binder was easily removed from the composite, limiting the increase to the composite volume due to the addition of the binder. Upon cooling of the composite, the biopolymers formed fibers based on helical structures, creating a gel with the remaining water. This gel could then be dehydrated without collapse of the binder network due to the mechanical integrity imparted by the dense packing of the ceramic particles. The dehydrated gel formed a network of channels throughout the ceramic particles through which other fluids could flow. With the selection of a high dielectric constant fluid filler, the voids within the composite were filled in a manner that both increases the dielectric strength of the composite while also significantly increasing the dielectric constant. This concept can be expanded to use of other fluid fillers, allowing the dielectric constant and losses of the composite to be relatively easily adjusted.

Multiple methods were used to characterize the three classes of composite materials, enabling evaluation of the composites against the goals established in Chapter 1. The dielectric constant and losses were primarily measured through dielectric spectroscopy with supplemental information provided by polarization measurements and measurement of high voltage discharges of capacitors formed with the composites. At the low frequency end of the frequencies of interest for antenna operation between 200 MHz and 4.5 GHz, the dielectric constants of the composites correspond with their namesake

values of 45, 100, and 550. MU45 and MU100 exhibit modest dispersion in the dielectric constant as the measurements decrease to approximately 40 and 90 at 4.5 GHz, respectively. The dielectric losses remained at or below 0.1 for MU45 and MU100 up to approximately 2 GHz and 1.75 GHz, respectively. The losses of MU100 remained below 0.1 except for two peaks centered at approximately 1.75 and 2.75 GHz. While these losses could be further decreased with modification to the ceramic content, losses below 0.1 allowed the composites to be integrated into dielectric-loaded antennas. Due to the selection of the ceramic and binder materials incorporated into MU45 and MU100, very little change was observed in the permittivity of these composites at high frequency as a function of temperature between -20 C and 120 C.

MU550 was designed to maximize the dielectric constant, resulting in a maximum value of approximately 550 at 200 MHz. The use of a high dielectric constant liquid filler contributed significant dispersion to the dielectric constant as the value was observed to decrease to less than 400 at 4.5 GHz. The losses are also increased through the use of a highly polar liquid filler, and the losses of MU550 are below 0.1 only at frequencies less than 500 MHz. Observations of the change in the permittivity of the high dielectric constant liquid filler suggest that MU550 may be best suited for low frequency and high temperature antenna applications due to the lower dispersion and losses of the liquid filler at high temperature. While MU550 has not yet been implemented in an antenna, the concepts behind its structure allow the composite to be relatively easily modified to decrease the dispersion and dielectric losses, as described in the next subsection.

Dielectric constant measurements obtained through polarization and high voltage capacitive discharge methods provide insight into the low frequency properties of the

composites under high electric field conditions. In both methods, the dielectric constant is increased in comparison to the value measured through dielectric spectroscopy. This increase is partially due to the elimination of air gaps along the measurement surface due to the direct application of sputtered electrodes to the composite surfaces. The dielectric constant is also increased due to the lower measurement frequency and the higher electric field within the composite. At low electric fields and a frequency of 100 Hz, the dielectric constant of MU45 observed from polarization measurements was approximately 109. At relatively high electric fields around 2 MV/m, the dielectric constant of MU45 was measured with the polarization and high voltage capacitive discharge methods to be approximately 209 and 200, respectively. Increasing the electric field further to levels greater than 6 MV/m resulted in a polarization measurement of the dielectric constant of MU45 at approximately 324. Similar behavior of the dielectric constant increasing with higher electric field levels was observed with MU100. While the dielectric constant observed from low electric field polarization measurements of MU100 was approximately 135.4, the dielectric constant increased to values of approximately 308.5 and 387.6 at electric field strengths on the order of 4 MV/m and 10 MV/m respectively. This increase in the dielectric constant of MU100 under high electric field conditions was also observed through high voltage capacitive discharge measurements. The dielectric constant was calculated to be approximately 345 when discharged from a charging voltage corresponding to an electric field of approximately 1.575 MV/m. The change in the effective dielectric constant with the applied field is consistent with the behavior of capacitors incorporating high dielectric constant ceramics. To account for this dependence on the electric field, the composites should be characterized on a case-by-

case basis under conditions similar to those that will be encountered during application in specific antenna designs.

The dielectric strength of the composites was measured under pulsed conditions with a risetime on the order of tens of nanoseconds. This method most closely replicates the high dV/dt conditions of use in a high power antenna application. The samples were prepared with sputtered platinum electrodes covered with a conductive epoxy paste to minimize the effects of imperfect electrode-composite contact and potential erosion and pitting of the electrode surface after each test. For comparison with a common low dielectric constant high voltage insulator, measurements were also taken on Teflon samples prepared with the same electrodes. Half of the high dielectric constant composite samples were treated with a high dielectric constant coating around the electrode edge in an attempt to reduce the field enhancement factor due to the triple point at the electrode edge. The electric field at breakdown in the untreated samples was examined both with and without inclusion of the field enhancement factor. When the field enhancement factor is not considered, the reported electric field corresponds to the field within the bulk of the material away from the electrode edges. The electric field in the bulk material with no coating calculated for 1% probability of breakdown through Weibull analysis was 7.17, 38.84, 27.35, and 69.87 MV/m for MU45, MU100, MU550, and Teflon, respectively. When including the simulated field enhancement factor around the electrode-composite junction, the peak electric field calculated for 1% probability of breakdown increased to 85.87, 316.53, 175.07, and 193.32 MV/m for MU45, MU100, MU550, and Teflon, respectively. If dielectric breakdown in the composites is dominated by the effects of the electrode contact, antenna designs in which the conductor does not directly contact the

high dielectric constant material may be able to utilize the composites at electric fields in the bulk of the material up to these peak magnitudes. For antenna designs with direct electrode-composite contact, the field enhancement factor due to the electrode edge could be decreased to around 2 with effective implementation of coatings or electrode geometries designed to reduce the field enhancement. If the field enhancement factor were reduced to 2, the practical peak field in the bulk of the material would be half of the peak field calculated at the electrode edge when including the field enhancement factor. From the previously listed values including the field enhancement factor, practical field values in the bulk of the material corresponding to a reduced field enhancement factor of 2 are 42.94, 158.27, and 87.54 MV/m for MU45, MU100, and MU550, respectively. This suggests that much higher electric field levels in the bulk of the material could be realized for cases in which there is either no electrode-composite contact and in which the field enhancement factor at the electrode-composite contact is reduced to around 2. This assumes that the field enhancement is primarily due to the electrode edge and not triple points along the surface at junctions of electrode, ceramic, and binder.

As introduced in Chapter 1, the energy density and power density are useful figures of merit due to their dependence on both the dielectric constant and electric field. The dielectric constant values used in calculations of the peak energy density and peak power density correspond to the values observed around 200 MHz: 45, 100, and 550. Using the field strength at 1% probability of breakdown in the bulk of the material from the dielectric strength measurements reported in Chapter 4 without inclusion of the field enhancement factor, the energy densities of MU100 and MU550 in the bulk of the material were approximately 0.67 and 1.82 J/cm³, respectively. The value calculated for

Teflon was approximately 0.0475 J/cm^3 . In comparison with Teflon, MU100 had a calculated energy density in the bulk of the material that is approximately 14 times the value obtained for Teflon under the same experimental conditions, and the energy density of MU550 in the bulk of the material was calculated to be approximately 38.3 times higher than Teflon. These values are calculated with conservative figures for the dielectric strength, so the energy density could be increased to much higher levels when used in an antenna with a high peak power but low average power. As previously stated, if the field enhancement factor at the electrode edge were reduced to 2, the field in the bulk of the material could be increased to 42.94, 158.27, and 87.54 MV/m for MU45, MU100, and MU550, respectively. Using these field values, the energy density in the bulk of the material would be approximately 0.37, 11.1, and 18.7 J/cm^3 for MU45, MU100, and MU550 respectively. While both the demonstrated and projected energy density values are encouraging for material use in high power antennas, the projected energy densities are also suggestive of the potential for the composite materials to be transitioned to high energy density capacitors. If the composites were to be transitioned to a capacitor application, the selection of the materials composing the composite could be optimized for the application while still using the novel manufacturing techniques developed in this work to further increase the energy density.

The power density is also calculated as a figure of merit using the same dielectric constant and electric field values used in the energy density calculations. Using the field values corresponding to 1% probability of breakdown without inclusion of the field enhancement factor, the power density in the bulk of MU100 is approximately 4 GW/cm^2 , and the power density in the bulk of MU550 is 4.65 GW/cm^2 . Compared to the

corresponding power density calculated for Teflon at 1.92 GW/cm^2 , the power density of MU100 and MU550 are greater by a factor of approximately 2.08 and 2.42, respectively. These power density values also use conservative values for the electric field, so the power density can potentially be increased further when the effects of the field enhancement at the electrode edge are minimized. When the field levels corresponding to reduction of the field enhancement factor to 2 are applied, the power density is projected to increase to approximately 3.28, 66.44, and 47.67 GW/cm^2 for MU45, MU100, and MU550, respectively. While these projected power densities and the previously listed energy density projections have not yet been demonstrated, a path forward is apparent to reduce field enhancements and increase the dielectric strength of the composites.

The masses of the composites were compared before and after a high temperature treatment through which volatile components of the binders were removed. Through this thermogravimetric analysis, the composition of each of the composite classes was estimated based on the mass and volume percentage of each component. The lowest volume percentage of ceramic in the three composite classes was estimated to be slightly less than 55% for MU45. The relatively low volume percentage of ceramic in MU45 is consistent with the lower dielectric constant observed for MU45 and the manufacturing concept that large pre-polymerized binders limit the packing density of ceramic particles. MU45 also had the largest volume percentage of binder, estimated at approximately 35%, and the volume percentage of voids in MU45 was approximately 10%. MU100 had the highest calculated volume percentage of ceramic at approximately 71.72%. The high volume percentage of ceramic is attributed to the in-situ polymerization of the binder, which was assumed to occupy the remaining volume of the composite due to the

unknown mass density of the polysilsesquioxane network. The estimated volume percentage of ceramic in MU550 was calculated to be 61.71%. It is believed that the volume percentage of ceramic in MU550 can be increased to the levels calculated for MU100 when the manufacturing process removes excess binder during pressing and the binder does not fully form until after the ceramic particles are pressed to their final density. Discrepancy between the volume percentage of ceramic observed in this analysis and the values above 70% that are believed to be achievable with MU550 are likely due to excess binder content in the solution and/or cooling of the binder-ceramic slurry prior to pressing. The remaining volume of MU550 composites is considered to be occupied by the liquid filler, which is assumed to penetrate the voids and saturate the areas occupied by the binder.

Scanning electron microscopy was used primarily to examine the size and morphology of ceramic particles contributing to the trimodal distribution. Micrographs identified significant potential problems with particles, including low density of large particles and agglomeration of nanoparticles. Scanning electron microscopy subsequently confirmed that heat treatment of the large particles greatly improved their density and that milling of the nanoparticles broke apart the soft agglomerates. Additional uses of electron microscopy in this work included examination of the distribution of particles from surface and cross-sectional composite views and inspection of the electrode-composite junction.

In conclusion, the goals established for the development and characterization portion of this research were met and often exceeded. The three composite classes have dielectric constants greater than 40 in the VHF and UHF bands of interest. The losses are below 0.1

for MU45 and MU100 below 1.75 GHz. The losses of MU550 are below 0.1 below 500 MHz, and material substitution of the liquid filler could easily permit lower losses with some tradeoff to the dielectric constant. The losses of all three composite classes could likely be further lowered by heat treatment of the ceramic materials. The pulsed dielectric strength at 1% probability of breakdown was calculated to be greater than 100 MV/m for MU100 and MU550 when accounting for the field enhancement factor at the electrode edge. It is believed that reduction of the field enhancement factor to practical values of around 2 could enable operation of the composites at field strengths greater than 100 MV/m within the bulk of the material. No evidence of ferroelectric saturation was observed in polarization measurements. Ferroelectric saturation of the composites is not expected due to the distribution of the electric field between the different materials within the composites. Since the field is concentrated in the lower dielectric constant materials, dielectric failure would be expected before the field levels reached the saturation threshold within the ceramic. The energy density calculated at an electric field strength corresponding to 1% probability of breakdown in the bulk of MU550 was 1.82 J/cm³. The energy density within the bulk at 1% of breakdown for MU100 was approximately 0.67 J/cm³, and this value is projected to increase to more than 11 J/cm³ if the field enhancement factor due to the electrode-composite junction is reduced to 2 and the dielectric strength in the bulk of the material is at least 158.27 MV/m. Finally, all three composites have been manufactured in large thicknesses. Samples have been prepared in a wide range of diameter-to-thickness aspect ratios, and several samples have been machined with power cutting tools. This combination of high dielectric constant, high

dielectric strength, and bulk production/machinability meet the goals required to develop composites suitable for high power antennas.

7.1.2 Future Work

Due to the encouraging results of the composite material development in this effort, work has continued since the end of the development of these three composite classes. The recent work is focused on adapting the materials for other high voltage applications and applying the manufacturing techniques developed for these composites to other types of materials. This work is ongoing and cannot be discussed in detail. However, this section includes suggested areas of work that apply directly to the three types of composites developed for high power antennas.

Perhaps the most important area of improvement for high power antennas incorporating direct electrode-composite contact is the reduction of the field enhancement factor. As analyzed through the dielectric strength measurements and subsequent energy density calculation, effective implementation of the composite materials in high voltage and/or high power applications will require the large field enhancements at this junction to be lowered significantly. Methods to accomplish this reduction include modifying the electrode geometry and the application of high dielectric constant coatings to reduce field enhancement at the electrode edges. As demonstrated through the integration of MU100 in a high power dielectric resonator antenna, it is also possible to avoid limitations presented by triple points by preventing direct electrode-composite contact when possible.

A second area of suggested work is in substitution or modification of the ceramic components. While barium titanate was selected for this work due to its high Curie temperature and perceived relative health safety, substitution of other ceramics could significantly improve the dielectric constant and/or dielectric losses. As discussed in the analysis of notable previous works in Chapter 3, PMN-PT is a common choice of ceramic for its very high dielectric constant. PMN-PT could be directly substituted into the composites developed in this work to further increase the dielectric constant, but this has not yet been done due to the health risks associated with machining lead-based materials. With the continued use of barium titanate, the composite properties can be improved by conditioning the particles of different sizes to exhibit higher dielectric constants and lower losses. The lattice structure can be altered due to particle size and grain size effects, and the entire ceramic volume should be in the tetragonal phase to maximize the dielectric constant. Additionally, heat treatment can relax stresses within the ceramic to reduce losses, so heat treatment of the particles prior to composite formation could potentially benefit both the dielectric constant and losses. The manufacture, sizing, and mixing of particles for the trimodal distribution can continue to be refined to maximize the particle packing density. In particular the production of the large particles can be improved to produce less waste ceramic, and the large particles can be sized with greater accuracy to improve consistency of the size distribution used in every composite. The mixing of the various particle sizes before and after incorporation of the binder can be further improved to increase the homogeneity of the composites.

Finally, the effects of poling the composites should be investigated as a means of increasing the dielectric constant. If the intended use of a composite sample allows the

composite to be polarized along a particular direction, the dielectric constant could be enhanced without requiring any changes to the composite formulas or manufacturing processes.

7.2 Dielectric Resonator Antenna

7.2.1 Summary

A dielectric resonator antenna (DRA) was chosen to provide a proof of concept demonstration of the application of the composite materials developed in this work in high power antennas. The DRA was chosen for reasons ranging from its effective utilization of the high dielectric constants of the composites to the perceived capability of the design to scale to very high power levels. The operating frequency of a DRA is directly dependent on the resonances established with the dielectric resonator, so the size of the resonator could be directly reduced with respect to the square root of the dielectric constant of the resonator material.

The wide variety of DRA designs based on resonator geometry and coupling methods offered a significant amount of design freedom. The geometry of the resonator was selected as cylindrical to both form a low-profile design and require minimal alteration of the composite after its production through high pressure compaction. The coupling methods in particular enabled the DRA to be scaled to very high power levels. By selecting microstrip coupling, the microstrip dimensions could be relatively easily scaled to the dimensions required for high voltage holdoff while maintaining the desired characteristic impedance. The effects of the field enhancement factor at the triple point junction were also mitigated by indirectly coupling the energy from the microstrip to the

resonator without direct conductor-composite contact. The DRA was immersed in oil to enable high peak power operation. The oil insulated the transmission line and improved the return loss due to the closely matched dielectric constant of the oil and polyethylene hardware.

Four modes of resonance were analyzed to predict the frequency of operation and Q -factor of the DRA. The resonant frequencies of these four modes were calculated between 455 MHz and 770 MHz based on a resonator formed from a cylinder of MU100. The resonant mode of a low-profile design in which the resonator radius is much greater than the height was calculated to be 650 MHz. It is possible that all four of these resonant modes and other modes that were not included in the analysis could be excited in a single antenna geometry. This multimodal operation was one of several bandwidth enhancement options considered. The bandwidth enhancement mechanisms that were included into the high power DRA's design and operation included a low dielectric constant spacer between the microstrip and resonator, excitation of multiple modes, and the lower Q factor resulting from the losses of the composite materials forming the resonator.

The high power DRA was designed around a substrate of polyethylene with a thickness of 1.91 cm. The large thickness of the substrate was designed to enable peak signal voltages of at least 225 kV to drive the antenna. To match the microstrip impedance to the network analyzer for low voltage measurement, the microstrip was designed to be 50 Ω . The large thickness of the substrate and relatively low impedance required a wide microstrip of 5.65 cm. The length of the microstrip was designed to be 25.4 cm. This length is longer than that required to drive the resonator, but the microstrip was kept long to increase the capacitance of the antenna for operation in the high voltage ring-down

oscillator. The microstrip and ground plane measuring 25.4 cm by 25.4 cm were mounted on the substrate, which had a cross section of 30.5 cm by 30.5 cm. The resonator consisted of a low-profile cylinder of MU100 with a thickness of 1.25 cm and a radius of 3.81 cm.

The DRA was simulated in CST Microwave Studio, and the results were compared against return loss and gain measurements taken with a network analyzer. In both the simulations and measurements, the first trough of the return loss was between 400 and 500 MHz. The measured return loss was below -10 dB between 475 MHz and 1.5 GHz except for narrow bands centered at approximately 500 MHz and 1.25 GHz. The resonant frequency of the two lowest frequency modes analyzed in the design phase agreed well with observations of the return loss and gain in both simulations and measurements. The two higher resonant frequencies calculated from the resonant modes fall within the main band at which greater than unity gain was observed in both simulations and measurements. This band of greater than unity gain in the direction normal to the plane of the substrate extended up to approximately 1.1 GHz in experimental measurements. The simulated maximum 3D gain was greater than unity at frequencies 625 MHz up to the upper frequency limit of 2 GHz. The gain in the direction normal to the plane of the substrate and resonator differed from the maximum 3D gain due to shifting of the main lobe. While the simulated and measured gain normal to the plane of the substrate and resonator showed good agreement at many frequencies, differences observed in the main band of operation between 700 MHz and 975 MHz are believed to be due to slight shifting of the measured pattern from the direction directly normal to the substrate.

In conclusion, the high power dielectric resonator antenna both demonstrated that antenna dimensions could be reduced through the incorporation of the high dielectric constant composites and the composites could be integrated into a high power antenna design. Given the high dielectric constant of the resonator, the band of frequencies at which greater than unity gain was observed was exceptionally wide. The radiation efficiency was also not excessively low as the simulated values at 650 MHz and 825 MHz were 64.6% and 88.6%, respectively. The relatively wide bandwidth and high radiation efficiency are contrary to conventional behavior of dielectric resonators antennas incorporating resonators with high dielectric constants. However, the agreement between the simulation and measured results and the consistency of the measured results provides ample confidence that the observed performance is legitimate.

7.2.2 Future Work

Future work on the high power DRA should include investigations on the minimization of the substrate size, scaling to lower frequency, and time-domain properties. The dimensions of the substrate used in this work were largely required for the antenna's incorporation in the high power ring-down oscillator. The added capacitance of a long microstrip feed increased the energy stored in the oscillator's high voltage section. However, the microstrip can be much shorter while still properly exciting the resonator modes and maintaining much of the present antenna's performance characteristics. Preliminary measurements of the return loss have confirmed that shorter microstrips can provide very similar coupling. The limiting factor in the minimization of the substrate size may be the ground plane. As the ground plane size is reduced, the approximation of

an infinite ground plane is invalidated, resulting in changes to the farfield gain pattern and other critical parameters. With an adequately sized ground plane for the resonator and microstrip sizes, the relative ease with which the DRA can be experimentally tuned will allow the minimization of the microstrip length and ground plane dimensions to be identified through experimental trial with smaller substrates.

Scaling to lower frequency operation can be achieved with larger resonators, utilization of high dielectric constant materials, or a combination of these approaches. Since the resonant frequencies calculated for dielectric resonators are inversely proportional to the square root of the permittivity of the resonator, there is a case of diminishing returns as the dielectric constant is increased. This situation is one reason why there was relatively little advantage to implementing MU550 as the resonator in this work instead of MU100. Therefore, with a material like MU100 already in use, it may be more practical to increase the dimensions of the resonator to scale to lower frequency. To achieve very low frequencies of operation within volume or weight constraints, innovations in the geometry of the resonator could be made to lower the resonant frequency without necessitating impractically large resonators.

If future work on the high power DRA is directed towards high peak power applications as studied in this work, further investigation on the time-domain behavior of the antenna is needed. The antenna has the potential to reflect a significant amount of power back to the source. This does not present a problem when the antenna is integrated with a ring-down oscillator. However, some high power sources could be damaged or have their operation degraded by energy reflected from the antenna. Further investigation into the time-domain behavior of the antenna will enable better prediction of the transient

fields radiated by the antenna based on the signal applied to the antenna. From a more complete study of the time-domain behavior of the antenna, modifications to the antenna and selection of the high power source can be better informed to enhance transient radiation of high peak power fields.

7.3 High Power Antenna Driver

7.3.1 Summary

A high power antenna driver was designed to drive an antenna with a damped sinusoidal waveform incorporating high frequency signals. The system was based on a concept of an explosive generator as a source driving an inductive energy storage system. The inductive energy storage system pulse charges a high voltage oscillator and the high power antenna. When the oscillator and antenna are switched to ground through a self-breaking spark gap switch, a series of damped oscillations is present on the antenna. High frequency content is superimposed on the main damped sinusoid due to reflections intentionally created on the oscillator through impedance mismatches.

Since the high power antenna driver is intended for high peak power antenna characterization, the driver is based on a simulator of an FCG rather than an actual explosive generator. The FCG simulator was driven by a CLC-network to provide a rising input voltage as a function of time. The rising voltage signal increases the rate at which the current output increases in time. Experiments with the FCG simulator confirmed that not only is the first derivative of the current output positive, but the second derivative of the current output is also positive, indicating that the FCG simulator produces an output more similar to actual FCGs than previous simulators.

The inductive energy storage system consisted of a solenoid inductor and an exploding wire fuse. Upon vaporization of the fuse wires, the energy stored in the solenoid is diverted to charge the high voltage oscillator and antenna structure to high voltage. The high voltage oscillator consisted of coaxial transmission lines with an electrical length of approximately 0.5 ns each. The antenna was driven from a connection point between the transmission line sections. The mismatched impedance due to the addition of the DRA, which also contains a transmission line, resulted in multiple reflections that produce a high frequency signal on top of the high voltage damped sinusoid.

The high power antenna driver was tested in an RF-shielded enclosure due to the potentially high radiated electric fields. The antenna cannot be characterized in this type of enclosure or in the same vicinity as the pulsed power source. Despite the limitations in characterizing the antenna under these conditions, the basic operation of the high power antenna driver was demonstrated. Suggestions on how the high power antenna driver can be transitioned to an environment in which the antenna can be effectively characterized at high power are given in the next subsection.

In conclusion, the high power antenna driver has been shown to be feasible for generating a high power damped sinusoid. However, the effectiveness at applying this type of driver to antennas operating above a few hundred MHz is low. While high frequency signal content in the operating range of the antenna can be generated as a part of the damped sinusoidal signal, the power level of the high frequency signal content is small in comparison to the main components of the signal. Therefore, this type of high power antenna driver is best suited for high power antennas in the VHF band, and alternatives are necessary for antennas in the UHF band.

One potential alternative high power source is a basic high voltage pulser with a fast risetime. The pulser could take the form of a Marx bank, or a simple source such as the PA-80 trigger generator used in dielectric strength testing could be applied with a peaking switch to decrease the risetime. The fast risetime of a high voltage pulse contains high frequency signal content that could be radiated by an antenna. This concept is applied to impulse radiating antennas in which an antenna radiates the derivative of the applied voltage waveform as an impulse of the electric field. The risetime of the voltage signal can be tuned to ensure the frequency content of the signal includes components in the operational bandwidth of the antenna. The peak magnitude of the voltage pulse could also be controlled to drive the antenna at specified peak power levels. This type of system also enables repetitive testing that is not possible with the single-shot antenna driver based on an inductive energy storage system.

7.3.2 Future Work

The antenna driver based on the ring-down oscillator is best suited for antennas in the VHF band. Thus a path forward is needed on how the system could be transitioned to permit actual antenna characterization in the VHF band. The obvious requirement to allow the antennas to be characterized at high power is that the antenna must be tested in an anechoic chamber or outdoor test range where the effects of the radiated fields from the pulsed power system driving the antenna can be minimized. Ideally, the antenna and field measurement devices would be completely isolated from the pulsed power system. The current system could be adapted to enable this isolation if a high voltage transmission line rated to a peak voltage of at least 200 kV were fed into an anechoic

chamber. The high power oscillator would likely need to be integrated directly with the antenna under test within the anechoic chamber to effectively drive it at high frequency. The length of the high voltage transmission line feeding into the anechoic chamber would not negatively affect the performance of the high power oscillator and antenna if the resistor in series with the transmission lines of the high power oscillator were included inside the anechoic chamber at the connection to the high power oscillator.

In the experiments described in the previous chapter, the peak charging voltage of the high power oscillator was below the maximum levels possible with the system. To increase the peak voltage to above 225 kV, the value of the resistor in series with the transmission lines of the high power oscillator should be lowered from 1.4 k Ω to a value of around 700 Ω . To increase the peak voltage further beyond that simulated in section 6.4, the charging voltage of capacitor bank C_1 should be increased above 40 kV, and the number of fuse wires should be increased to allow a higher peak current in the inductive energy store before the fuse opens the circuit.

Future work on high power antenna drivers should also further develop the system based on a fast rise time pulse. While many types of pulse generators could be adapted to serve as a high power antenna driver of this kind, most will require a peaking switch to decrease the rise time of the pulse's leading edge. Preliminary research on an antenna driver of this type was accomplished in this work by using the PA-80 pulse generator with a peaking switch. Future work in this area must be concentrated on lowering the inductance of the peaking switch and improving the switch's connection to the antenna feed. In addition to the development of the peaking switch, the time-domain response of

the antennas under test must be further investigated to optimize the antennas for a fast rise time step input.

VITA

Kevin O'Connor earned the degrees of Master of Science in Electrical Engineering and PhD in Electrical and Computer Engineering from the University of Missouri. His research has focused on the cross-disciplinary fields of pulsed power and materials science. In his masters-level research, Kevin O'Connor investigated a power conditioning and compact RF system for use with flux compression generators. In the course of this research, he focused on the development of compact pulse transformers, exploding wire fuses, a high voltage capacitive-discharge RF generator, and a non-destructive test bed for the simulation of flux compression generators. His PhD-level research has concentrated on the development of high dielectric constant composite materials for high power applications and the design and testing of a compact high power dielectric resonator antenna.

Kevin O'Connor completed an internship with Sandia National Laboratories and KTech Corp. of Albuquerque, NM in 2007. He was a fellow with the National Physical Science Consortium through the sponsorship of Sandia National Laboratories from 2008 to 2011. He was a finalist for the student paper of the year award from the IEEE Nuclear and Plasma Sciences Society at the 2011 IEEE International Pulsed Power Conference, and he was awarded a Tom R. Burkes Outstanding Graduate Student Award at the 2012 IEEE International Power Modulator and High Voltage Conference. While completing his PhD studies, he co-founded NanoElectromagnetics LLC of Columbia, MO to commercialize high dielectric constant composite materials for compact antenna and high energy density storage applications.